Signatures of Majorana Fermions in Hybrid Superconductor-Semiconductor Nanowire Devices

Proefschrift

ter verkrijging van de graad van doctor
aan de Technische Universiteit Delft,
op gezag van de Rector Magnificus prof. ir. K.C.A.M. Luyben,
voorzitter van het College voor Promoties,
in het openbaar te verdedigen op vrijdag 26 februari 2016 om 10:00 uur

door

Kun Zuo

Master of Science
geboren te Anhui, China

en

Vincent Mourik

Natuurkundig ingenieur
geboren te Capelle aan den IJssel.

Dit proefschrift is goedgekeurd door de

promotor: Prof. dr. ir. L.P. Kouwenhoven
promotor: Prof. dr. E.P.A.M. Bakkers

Samenstelling promotiecommissie:

Rector Magnificus,	voorzitter
Prof. dr. ir. L.P. Kouwenhoven,	Technische Universiteit Delft
Prof. dr. E.P.A.M. Bakkers,	Technische Universiteit Delft

Onafhankelijke leden:

Prof. dr. ir. J.E Mooij,	Technische Universiteit Delft
Prof. dr. P. Brouwer,	Freie Universität Berlin
Prof. dr. C.M. Marcus,	University of Copenhagen
Prof. dr. Y.V. Nazarov,	Technische Universiteit Delft
Prof. dr. Y.M. Blanter,	Technische Universiteit Delft, reservelid

Overige leden:

Prof. dr. S.M. Frolov,	University of Pittsburgh

Printed by: Proefschriftmaken.nl || Uitgeverij BOXPress

Copyright © 2016 by K. Zuo & V. Mourik
Casimir PhD series, Delft-Leiden 2016-04

ISBN 978-90-8593-248-2

An electronic version of this dissertation is available at
http://repository.tudelft.nl/.

AUTHOR CONTRIBUTIONS

This thesis contains the research of two doctoral candidates, Vincent Mourik (VM) and Kun Zuo (KZ). Due to a large overlap in the experimental research carried out, a joined thesis has been written. Here we state which person was responsible for a particular part of the research.

A number of chapters in this thesis have a more general character and do not contain a report of actual experimental research carried out by the authors. These chapters are:

- Chapter 1 - Introduction
- Chapter 2 - Theory introduction to Majorana fermions in condensed matter
- Chapter 3 - Experimental methods
- Chapter 6 - Recent developments on Majorana bound states in semiconducting nanowires.

These chapters are written in a truly joined fashion: Both VM and KZ actively contributed to the underlying scientific discussion, both VM and KZ took equal shares in writing a first draft, and the final version is the result of joined writing by both VM and KZ.

The other chapters report experiments carried out as part of the research. Below we specify which of the authors was responsible for conducting a certain part of the research for each chapter. A full list of collaborators to each chapter is included as a footnote on each chapter's title page.

- Chapter 4 - Supercurrent oscillations in InSb nanowires: VM and KZ took equal shares in sample fabrication and measurements. Data analysis and reporting of results were mainly done by VM, with comments and assistance of KZ.
- Chapter 5: - Signatures of Majorana Fermions in Hybrid Superconductor-Semiconductor Nanowire Devices: VM and KZ took equal shares in all aspects of this research (sample fabrication, measurements, data analysis and reporting results).
- Chapter 7 - Tunneling spectroscopy in hybrid superconductor-InSb nanowire devices: VM and KZ took equal shares in sample fabrication and measurements. Data analysis and reporting results were mainly done by VM, with comments and assistance of KZ.

- Chapter 8 - Optimization of superconductor-InSb nanowire interface: KZ contributed to sample fabrication and measurements. VM assisted with measurements. VM and KZ contributed to data analysis. KZ was mainly responsible for reporting of the results, with comments and assistance of VM.
- Chapter 9 - Tunneling spectroscopy in a InSb nanowire device with improved superconducting contacts: KZ performed sample fabrication, measurements and data analysis. KZ was mainly responsible for reporting of the results, with comments and assistance of VM.
- Chapter 10 - Spectroscopy of spin-orbit quantum bits in InSb nanowires: KZ contributed to sample fabrication, measurements, data analysis and reporting of the results. VM was not involved in this research.
- Chapter 11/12 - Outlook, is written separately, independent of the other author, by both VM and KZ. Here the personal, scientific view on the research and its future perspectives is expressed by each author individually.

Except for Chapter 10, in which VM was not involved, and Chapters 11 and 12, which are written independently, both authors take full responsibility for the whole content of this thesis. Although the specific efforts of each author are divided differently over separate chapters, overall this thesis is the result of equal and independent contributions of both authors.

CONTENTS

1

INTRODUCTION

One of the most important scientific achievements to date is the realization that the whole universe is built upon a small collection of basic elementary particles, such as electrons, photons and quarks. These elementary particles can be divided in two types, depending on their spin: fermions, with half integer spin, and bosons, with integer spin.

Upon its invention in 1928, the famous Dirac equation not only captured the quantum behavior of spin-1/2 electrons at relativistic speeds, but also predicted the existence of another type of particle, with equal mass, but opposite properties to the electron [1]. Soon after, in 1932, such a particle was indeed observed in cosmic rays and called 'positron' [2]. This discovery was the first observation of an antimatter particle.

1.1 MAJORANA FERMIONS

More generally, Dirac's equation suggests that all half integer fermions have an antiparticle that is different from themselves. However, this was challenged by Majorana in 1937. Investigating solutions to the Dirac equation, Ettore Majorana found a real solution [3]. Since matter and antimatter solutions to the Dirac equation are related to each other via complex conjugation, this immediately implies that this solution must correspond to a particle equal to its own antiparticle, and that the particle cannot have electrical charge. These hypothetical particles are now known as Majorana fermions. Originally, Majorana envisioned this solution as an explanation for the neutrino, a particle theoretically proposed to exist a few years earlier.

[1] Both Vincent Mourik and Kun Zuo actively contributed to the underlying scientific discussion, both Vincent Mourik and Kun Zuo took equal shares in writing a first draft, and the final version is the result of joined writing by both Vincent Mourik and Kun Zuo.

Searching for Majorana fermions as an elementary particle has been pursued in particle physics ever since. Neutrino's were indeed discovered experimentally two decades later. However, the question if they are Majorana fermions is still unanswered, and until now, no elementary particle that is a Majorana fermions has been detected.

The importance of Majorana fermions in 3+1 space-time dimensions as a new type of elementary particle is potentially immense: except from their relation to the neutrino, they could be present as the lowest energy supersymmetric partner to the standard model, thereby being one of the leading candidates for the origin of dark matter [4, 5]. More relevant to this thesis, however, Majorana fermions posses fascinating properties in reduced dimensions. In 2+1 dimension, such as created in condensed matter, they exhibit non-abelian exchange statistics, thus going beyond the traditional framework of Fermi-Dirac and Boson-Einstein statistics as known from fermions and bosons [6].

Demonstration of non-abelian exchange statistics of Majorana fermions would have a deep impact on fundamental physics, since this peculiar property is the direct consequence of consistently applying the basic concepts of geometry of space and indistinguishability of particles to a specific quantum mechanical context in condensed matter. More beyond that, by exchanging Majorana fermions in a process called 'braiding' a more practical application to the strongly emerging field of quantum computation is anticipated [7].

1.2 TOPOLOGICAL QUANTUM COMPUTATION

Quantum bits (qubits) have by now been developed for nearly two decades since their first realization, and yet they are still significantly suffering from dephasing errors. This is considered to be the biggest obstacle towards the realization of scalable, working quantum computers [8–10]. Many different schemes to eliminate such errors have been investigated, most of them, however, only try to compensate these errors. The best solution of all is to completely isolate the qubits from environmental fluctuations, the main source of dephasing errors. This leads to the idea of so-called topological quantum computation, in which qubits are protected by the system's topology, a global property insensitive to local perturbations [11].

Majorana fermions in two-dimensional condensed matter systems are the prime candidate to implement a form of topological quantum computing. Their absent charge and spin, their topological origin, and the non-local way in which a qubit is encoded in them, makes Majorana fermions a good candidate to build a dephasing free qubit. Interestingly, performing single qubit rotations with Majorana fermions directly relies on their non- abelian exchange statistics [7], giving a strong applied component to this fundamental property. The non-universality of Majorana fermion based quantum computation may be a disadvantage, but by now schemes exist which combine the best of Majorana fermion based qubits with the best of 'conventional' qubits, showing important advantages over schemes based on 'conventional' qubits only [12].

As a consequence, there is currently a strong interest, both from fundamental and applied perspective, to establish and control Majorana fermions in condensed matter.

1.3 ESTABLISHING MAJORANA FERMIONS IN SEMICONDUCTING NANOWIRES

A long development in theoretical physics led to the idea of Majorana fermions in semiconducting nanowires. Relying on earlier work in quantum field theory [13] and Helium-3 theory [14], it was realized in the late nineties that Majorana fermions may emerge as quasi-particles in certain special superconducting systems [15]. The original prediction was that a superconductor with a certain type of unconventional p-wave pairing may host Majorana fermions. In the two-dimensional case this was predicted to happen at defects such as a vortex, in the one-dimonensional case it was predicted for the endpoints of system [16]. As a material, however, this type of superconductor has not been established so far.

An important next step was made in 2008, when it was shown that instead of searching for the material itself, it could be effectively engineered by combining conventional, existing superconductors with certain types of semiconducting materials, known as topological insulators [17]. It is predicted that Majorana fermions emerge in such a system as well. This idea spurred the development of many proposals on a similar basis, in which certain combinations of semiconducting materials with a conventional superconductor give rise to Majorana fermions.

In 2010 independently two different theory collaborations came with the predictions that are the direct initiator of this thesis research [18, 19]. Combining a conventional superconductor with a semiconducting nanowire made of a material with strong spin-orbit interaction, Majorana fermions are predicted to emerge at the ends of the system upon applying strong enough magnetic field. Furthermore, subsequent theory work [20] showed that upon building a quasi two-dimensional network of such nanowires, the system allows for exchange of the Majorana fermions and will exhibit non-abelian statistics, from which topological quantum computing can be derived.

This theory development coincided with a long development in control over nanostructures and materials. Electron beam lithography is by now well established, enabling reliable device fabrication with typical feature size on the order of some ten's of nanometers, more than enough to implement the theory proposal. At the same time, semiconducting nanowires made from group III-V materials such as InAs, InP and InSb are heavily researched and their growth techniques are quite established by now [21, 22]. In particular InAs and InSb nanowires are very attractive for this proposal, since they have a strong spin-orbit interaction and are relatively easy to contact with metals. The research goal of this thesis is therefore to attempt a direct implementation of the nanowire based proposal to engineer Majorana fermions in condensed matter, and to subsequently attempt to detect them.

1

1.4 OUTLINE OF THE THESIS

The structure of this thesis is as follows:

- The theoretical background of Majorana fermions is discussed in chapter 2. Majorana fermions in condensed matter are first introduced, followed by a discussion on how to create Majorana fermions in hybrid superconductor-semiconductor nanowires. Methods to detect Majorana fermions relevant to our experiments are listed. Lastly, a simple estimation of the material parameters is given, which can be used as a reference to engineer Majorana devices using different materials.
- Experimental methods are discussed in chapter 3. Growth of InSb nanowires and fabrication of Majorana devices are first introduced. The measurement setup is discussed in the following section, accompanied with the explanation of tunneling spectroscopy in two and three terminal devices.
- Chapter 4 is on the Josephson effect as a demonstration of inducing supercunductivity in InSb nanowires. New behavior of supercurrent is measured in InSb-NbTiN Josephson junctions in the presence of a moderate to strong magnetic field. These results paved the way for creating and detecting Majorana fermions, as discussed in chapter 5.
- Based on the signatures of Majorana fermions found, as presented in chapter 5, new theory studies were performed in the community, which are summarized in chapter 6. Recommendations for follow up experiments and research directions are outlined in the chapter.
- Tunneling spectroscopy on improved devices based on Ar etched contacts are presented in chapter 7. Here we present reproduction of the main findings shown in in chapter 5 and new behavior is reported. It is found that the interface between superconducting contact and InSb nanowire is crucial. Chapter 8 therefore contains a report on optimizing this interface. Tunneling spectroscopy on devices with these improved contact are reported in chapter 9.
- Chapter 10 reports on spin orbit interaction in InSb as probed in an InSb quantum dot, giving a first estimation of the strength of spin orbit interaction in these nanowires.
- Finally, in chapters 11 and 12, each author concludes this thesis and presents an outlook on possible future research.

REFERENCES

[1] P. A. Dirac, "The quantum theory of the electron," in *Proceedings of the Royal Society of London A: Mathematical, Physical and Engineering Sciences*, vol. 117, pp. 610–624, The Royal Society, 1928.

[2] C. D. Anderson, "The positive electron," *Physical Review*, vol. 43, no. 6, p. 491, 1933.

[3] E. Majorana, "Teoria simmetrica dell'elettrone e del positrone," *Engl. transl [translation from Nuovo Cimento 14, 171 (1937)]F*, vol. 63, p. 149, 1981.

[4] F. Wilczek, "Majorana returns," *Nature Physics*, vol. 5, no. 9, pp. 614–618, 2009.

[5] S. R. Elliott and M. Franz, "*Colloquium* : Majorana fermions in nuclear, particle, and solid-state physics," *Rev. Mod. Phys.*, vol. 87, pp. 137–163, Feb 2015.

[6] A. Stern, "Non-abelian states of matter," *Nature*, vol. 464, no. 7286, pp. 187–193, 2010.

[7] M. Leijnse and K. Flensberg, "Introduction to topological superconductivity and majorana fermions," *Semiconductor Science and Technology*, vol. 27, no. 12, p. 124003, 2012.

[8] D. P. DiVincenzo, "Quantum computation," *Science*, vol. 270, no. 5234, p. 255, 1995.

[9] W. H. Zurek, "Quantum darwinism," *Nature Physics*, vol. 5, no. 3, pp. 181–188, 2009.

[10] T. D. Ladd, F. Jelezko, R. Laflamme, Y. Nakamura, C. Monroe, and J. L. O'Brien, "Quantum computers," *Nature*, vol. 464, no. 7285, pp. 45–53, 2010.

[11] C. Nayak, S. H. Simon, A. Stern, M. Freedman, and S. Das Sarma, "Non-abelian anyons and topological quantum computation," *Rev. Mod. Phys.*, vol. 80, pp. 1083–1159, Sep 2008.

[12] T. Hyart, B. van Heck, I. C. Fulga, M. Burrello, A. R. Akhmerov, and C. W. J. Beenakker, "Flux-controlled quantum computation with majorana fermions," *Phys. Rev. B*, vol. 88, p. 035121, Jul 2013.

[13] R. Jackiw and C. Rebbi, "Solitons with fermion number 1/2," *Physical Review D*, vol. 13, no. 12, p. 3398, 1976.

[14] G. E. Volovik, *The universe in a helium droplet*. Oxford, 2003.

[15] D. A. Ivanov, "Non-abelian statistics of half-quantum vortices in p-wave superconductors," *Physical review letters*, vol. 86, no. 2, p. 268, 2001.

[16] A. Y. Kitaev, "Unpaired majorana fermions in quantum wires," *Physics-Uspekhi*, vol. 44, no. 10S, p. 131, 2001.

[17] L. Fu and C. L. Kane, "Superconducting proximity effect and majorana fermions at the surface of a topological insulator," *Physical review letters*, vol. 100, no. 9, p. 096407, 2008.

[18] R. M. Lutchyn, J. D. Sau, and S. D. Sarma, "Majorana fermions and a topological phase transition in semiconductor-superconductor heterostructures," *Physical review letters*, vol. 105, no. 7, p. 077001, 2010.

[19] Y. Oreg, G. Refael, and F. von Oppen, "Helical liquids and majorana bound states in quantum wires," *Physical review letters*, vol. 105, no. 17, p. 177002, 2010.

[20] J. Alicea, "Majorana fermions in a tunable semiconductor device," *Physical Review B*, vol. 81, no. 12, p. 125318, 2010.

[21] H. Weman and D. Dasa, "Advances in iii-v semiconductor nanowires and nanodevices ed j li," *D Wang and RR LaPierre (Bassum: Bentham Science) pp*, pp. 89–104, 2011.

[22] J. Arbiol and Q. Xiong, *Semiconductor Nanowires: Materials, Synthesis, Characterization and Applications*. Elsevier, 2015.

2

THEORY INTRODUCTION TO MAJORANA FERMIONS IN CONDENSED MATTER

This chapter aims at introducing the topic of Majorana fermions in condensed matter to a nanowire experimentalist audience. In section 2.1, we start with a general introduction of Majorana fermions and their emergence as quasi-particles in certain condensed matter systems. The roles of superconductivity and topology are discussed and we conclude this section with an introduction to non-abelian exchange statistics and braiding. Section 2.2 is about the realization of Majorana bound states in one dimensional systems. The model Hamiltonian is discussed which describes a one dimonesional quantum wire with strong spin orbit interaction and superconducting proximity effect, the system we attempt to realize in the experiments in this thesis. In section 2.3, we describe possible experiments resulting in detection of Majorana bound states. Lastly, in section 2.4, realistic parameters and corresponding materials are discussed.

[1] Both Vincent Mourik and Kun Zuo actively contributed to the underlying scientific discussion, both Vincent Mourik and Kun Zuo took equal shares in writing a first draft, and the final version is the result of joined writing by both Vincent Mourik and Kun Zuo.

2.1 MAJORANA FERMIONS IN CONDENSED MATTER

This section aims at introducing the necessary concepts to understand the importance of Majorana fermions to condensed matter physics. Starting from a historical perspective (2.1.1), Majorana operators are introduced (2.1.2). The roles of superconductivity and topology in creating Majorana bound states are discussed (2.1.3 and 2.1.4). Finally we introduce and discuss the concept of non-abelian statistics and its implications for quantum computation (2.1.5).

2.1.1 HISTORICAL BACKGROUND

Historically the Majorana fermion has its origin in the relativistic wave equation for electrons postulated by Dirac in 1928 [1]. In solving his equation Dirac found the famous set of matrices whose entries contain both real and imaginary numbers. As a consequence the corresponding field ψ is a complex field. This is a necessity following from the fact that the electron has electrical charge, a property which can only be captured in a complex field. Furthermore, in the case of a complex field ψ the complex conjugate field ψ^* is also a solution to the equation. Whereas ψ creates an electron, it turned out that ψ^* creates a positron. The theoretical prediction of the positron by Dirac and its subsequent discovery [2] a few years later was the first occasion of the more general principle of what is now known as a particle and anti-particle corresponding to a field and its complex conjugate field respectively. The innovative question asked by Majorana in 1937 [3] was if it is a true necessity to involve imaginary numbers in describing spin 1/2 fields with the Dirac equation. As an answer Majorana found a set of matrices with entries containing imaginary numbers only which therefore correspond to a real field. Direct consequences of this finding are that such particles do not have electrical charge and are equal to their own anti-particle. These type of particles are known today as Majorana fermions. Originally Majorana speculated that neutrinos might be described in this way. Though actively pursued, this question is still not answered today. Introductory reviews of the role of Majorana fermions in particle physics and quantum field theory can be found in [4–7].

2.1.2 MAJORANA FERMIONS AS CONDENSED MATTER QUASI-PARTICLES

Majorana fermions may not only exist as elementary particles, but also as emergent quasi-particles in certain condensed matter systems. In condensed matter, a good analogy to electron and positron as particle and anti-particle pair is the electron and hole pair: creating an electron equals to removing a hole and vice versa. In further analogy, if an electron could be made equal to a hole, it would be a Majorana fermion.

More rigorously, the starting point is defining standard fermionic creation and annihilation operators $c_i^\dagger$ and c_i, having no spin indeces, with anticommutation relations:

$$\left\{c_i, c_j\right\} = \left\{c_i^\dagger, c_j^\dagger\right\} = 0 \qquad \left\{c_i, c_j^\dagger\right\} = \delta_{ij} \tag{2.1}$$

The operators can be rewritten in terms of new operators γ_1 and γ_2 by splitting c_i and $c_i^\dagger$ into their real and imaginary parts:

$$c_i = \frac{1}{2}\left(\gamma_1 + i\gamma_2\right) \qquad c_i^\dagger = \frac{1}{2}\left(\gamma_1 - i\gamma_2\right) \tag{2.2}$$

Upon inverting the above definition we get

$$\gamma_1 = c_i^\dagger + c_i \qquad \gamma_2 = i\left(c_i^\dagger - c_i\right) \tag{2.3}$$

Clearly, $\gamma_1^\dagger = \gamma_1$ and $\gamma_2^\dagger = \gamma_2$: the creation and annihilation operators are equal to themselves. As a consequence the quasiparticle γ_i is equal to its own anti-particle and therefore a Majorana fermion. It is important to realize that this mathematical identity is the only conjecture between the quasiparticles that are discussed here and Majorana's original prediction. In many aspects the quasiparticle Majorana fermions fundamentally differ from Majorana fermions known in particle physics. The γ_i operators follow the fermionic anticommutation rule via the original $c_i^\dagger$ and c_i operators:

$$\left\{\gamma_i, \gamma_j\right\} = 2\delta_{ij} \tag{2.4}$$

This implies immediately that $\gamma_i^2 = 1$: acting twice with a Majorana operator will result in the initial state, the Pauli exclusion principle does not hold for a Majorana operator. As a consequence, Majorana states are not countable: if a Majorana number operater $n_i^{\text{majorana}} = \gamma_i^\dagger \gamma_i$ would exist it implies that $\gamma_i^\dagger \gamma_i = \gamma_i \gamma_i^\dagger = 1$. The state is empty and filled at the same time which does not have any physical meaning. We will return to this point in section 2.1.5.

Since Majorana operators are constructed by splitting a fermion into its real and imaginary parts, they always have to come in pairs. Two paired Majorana fermions simply form a single fermionic excitation, therefore the transformation to Majorana operators is only sensible to consider when two Majorana fermions are unpaired and isolated from each other.

2.1.3 MAJORANA STATES IN SUPERCONDUCTORS

It has been shown that Majorana operators involve the equal superposition of an electron and a hole. This closely resembles the structure of Bogoliubov quasiparticles in a superconducting system and it is therefore natural to search for Majorana states in such a system. The pairing Hamitonion of a generalized version of standard BCS theory [8, 9] following [10] is given by[1]:

[1] The generalization is to not fix the cooper pair spin degree of freedom to a singlet state as was done in the original BCS theory, thus allowing for unconventional pairing types beyond s-wave superconductivity.

$$H = \sum_{\mathbf{k}\sigma} \epsilon(\mathbf{k})\, n_{\mathbf{k}\sigma} + \sum_{\mathbf{k}\mathbf{l}\sigma_1\sigma_2\sigma_3\sigma_4} V_{\sigma_1\sigma_2\sigma_3\sigma_4}(\mathbf{k},\mathbf{l})\, c^\dagger_{-\mathbf{k}\sigma_1} c^\dagger_{\mathbf{k}\sigma_2} c_{-\mathbf{l}\sigma_3} c_{\mathbf{l}\sigma_4} \tag{2.5}$$

The first term describes the single particle kinetic energy with $\epsilon(\mathbf{k})$ the single particle energy relative to E_F summing over momentum ($\mathbf{k}$) and spin (σ) states. The second term describes superconducting paring of electrons by taking a cooper pair formed of an electron pair with opposite momentum $(-\mathbf{l}\sigma_3, \mathbf{l}\sigma_4)$ and scattering it to the state $(-\mathbf{k}\sigma_1, \mathbf{k}\sigma_2)$ with $V_{\sigma_1\sigma_2\sigma_3\sigma_4}$ the matrix element given by $\langle -\mathbf{k}\sigma_1, \mathbf{k}\sigma_2 | V | -\mathbf{l}\sigma_3, \mathbf{l}\sigma_4 \rangle$. V is an effective electron -electron interaction which gives an attractive force in superconductors [11][2].

The Hamiltonian in (2.5) is analyzed following a mean field approach. To do this the following gap function is defined

$$\begin{aligned} \Delta_{\sigma\sigma'}(\mathbf{k}) &= -\sum_{\mathbf{l}\sigma_3\sigma_4} V_{\sigma'\sigma\sigma_3\sigma_4}(\mathbf{k},\mathbf{l}) \left\langle c_{\mathbf{l}\sigma_3} c_{-\mathbf{l}\sigma_4} \right\rangle \\ \Delta^*_{\sigma\sigma'}(-\mathbf{k}) &= \sum_{\mathbf{l}\sigma_1\sigma_2} V_{\sigma_1\sigma_2\sigma'\sigma}(\mathbf{k},\mathbf{l}) \left\langle c^\dagger_{-\mathbf{l}\sigma_1} c^\dagger_{\mathbf{l}\sigma_2} \right\rangle \end{aligned} \tag{2.6}$$

The pairing Hamiltonian (2.5) can then be approached as [3]:

$$H = \sum_{\mathbf{k}\sigma} \epsilon(\mathbf{k})\, n_{\mathbf{k}\sigma} + \sum_{\mathbf{k}\sigma_1\sigma_2} \left(\Delta_{\sigma_1\sigma_2}(\mathbf{k})\, c^\dagger_{\mathbf{k}\sigma_1} c^\dagger_{-\mathbf{k}\sigma_2} - \Delta^*_{\sigma_1\sigma_2}(-\mathbf{k})\, c_{-\mathbf{k}\sigma_1} c_{\mathbf{k}\sigma_2} \right) \tag{2.7}$$

This Hamiltonian can be diagonalized by a transformation given independently by Bogoliubov [12] and Valentin [13] known as the Bogoliubov or canonical transformation which is given by[4]:

$$c_{\mathbf{k}\sigma} = \sum_{\sigma'} \left(u_{\mathbf{k}\sigma\sigma'} \alpha_{\mathbf{k}\sigma'} + v_{\mathbf{k}\sigma\sigma'} \alpha^\dagger_{-\mathbf{k}\sigma'} \right) \tag{2.8}$$

Because of unitarity of the basis transformation only 4 independent variables remain. It is convenient to introduce a vector notation, with vector $c_{\mathbf{k}}$ (known as the Nambu spinor) defined as

$$c_{\mathbf{k}} = \begin{bmatrix} c_{\mathbf{k}\uparrow} \\ c_{\mathbf{k}\downarrow} \\ c^\dagger_{-\mathbf{k}\downarrow} \\ -c^\dagger_{-\mathbf{k}\uparrow} \end{bmatrix} \tag{2.9}$$

[2] In the original BCS theory a phonon mediated attractive force was proposed in combination with s-wave superconductivity. For unconventional superconducting states the origin of the attractive force is often less understood.

[3] A term containing only the mean field contributions but not any operators is omitted here. This term will only give a contribution to the ground state energy which is not of interest right now, the goal of the present discussion is to get insight in the properties of the excitation spectrum.

[4] Standard notation in literature for the Bogoliubov quasi-particles is $\gamma_{\mathbf{k}\sigma}$, here we use $\alpha_{\mathbf{k}\sigma}$ to avoid confusion with the Majorana operators used throughout the chapter.

The model Hamiltonian (2.7) can then be rewritten in matrix form:

$$H = \begin{bmatrix} H_0 & \Delta(\mathbf{k}) \\ \Delta^*(-\mathbf{k}) & -\mathscr{T} H_0 \mathscr{T}^{-1} \end{bmatrix} \tag{2.10}$$

with $H_0 = \epsilon(\mathbf{k}) \cdot \mathbb{1}$. More generally, H_0 contains all non-superconducting terms. $\Delta(\mathbf{k})$ is the matrix defined by (2.6), $\mathscr{T} = i\sigma_y \mathscr{K}$ is the time reversal operator with $\mathscr{K}$ the complex conjugation operator.

The energy spectrum corresponds to the new quasi-particles defined by (2.8). Combining (2.6) and (2.10), the system can be solved for a particular type of pairing. This quasi-particle excitation spectrum is always calculated with respect to E_F, since superconducting pairing is between electrons close to the Fermi level. Each component of the Nambu spinor (2.9) corresponds to an energy branch in the spectrum, these may be degenerate for all, or certain, $\mathbf{k}$-values.

By explicitly introducing electrons and holes in (2.9), an artificial doubling of the degrees of freedom of the system is introduced. As a consequence, the eigenvector's components are not not independent, neither are the corresponding energies. More explicitly, the system obeys electron hole symmetry, creating a quasi-particle at energy $+E$ is the same as destroying one at energy $-E$:

$$E_{\mathbf{k}} = -E_{-\mathbf{k}} \tag{2.11}$$

This leads to effectively only two independent quasi-particle energy branches in the spectrum, as expressed in (2.11). The doubling of the basis is also visible in the Hamiltonian (2.10): $-\mathscr{T} H_0 \mathscr{T}^{-1}$ is the time reversed of H_0 and thus acts on the hole states.

The most important aspect of the discussion above is that the Bogoliubov transformation is accompanied by a new type of quasi-particle, i.e. the Bogoliubov quasi-particle. Different from the standard excitations of the free electron gas, electrons and holes, Bogoliubov quasi-particles are linear combinations of these electrons and holes. This structure of the Bogoliubov quasi-particle is very similar to the definition of Majorana quasi-particles in (2.2) and (2.3). If one could bring such a Bogoliubov quasi-particle at E_F (this simply means c and $c^\dagger$ having equal weight in the superposition), it necessarily means that its equal to its own anti-particle and it will be a Majorana state. A complication is that in the initial definition of Majorana quasi-particles the spin degree of freedom was completely omitted. As a consequence, we have to seek for superconductors allowing for Bogoliubov quasi-particles that are of same spin species, e.g. of the form $\gamma = \frac{1}{\sqrt{2}}\left(c_{\mathbf{k}\uparrow} + c^\dagger_{-\mathbf{k}\uparrow}\right)$, which implies that a superconductor pairing up equal spin electrons is required.

The gap function as defined by (2.6) may be written as a product of a spin dependent part $\chi(\sigma)$ and a momentum dependent part $\Delta(\mathbf{k})$[5]. Since the gap function has to be fermionic, same spin pairing implies $\chi(\sigma) = \chi(-\sigma)$, and therefore

[5] Strictly speaking this is only possible if spin and momentum are good quantum numbers. In the presence of spin-orbit interaction in the superconductor this simple picture breaks down. Nevertheless, this assumption is widely used to classify superconductors.

the momentum dependent part has to be antisymmetric, $\Delta(\mathbf{k}) = -\Delta(-\mathbf{k})$. The simplest possible case sufficing our purpose is known as a 'chiral p-wave superconductor' [14]. Here the gap function is of the form $\Delta(\mathbf{k}) = \Delta_0 \begin{bmatrix} 0 & p_x \pm i p_y \\ p_x \pm i p_y & 0 \end{bmatrix}$. This type of superconductor is very different from the conventional BCS-type superconductors, which have a scalar Δ as momentum dependent part of the gap function, together with singlet spin paring to ensure a fermionic wave function. In a $p_x + i p_y$ superconductor, a single, isolated Bogoliubov quasi-particle at E_F will be a Majorana fermion.

2.1.4 MAJORANA BOUND STATES IN ONE AND TWO DIMENSIONAL P-WAVE SUPERCONDUCTORS

In the previous discussion we have argued that p-wave superconductors provide an interesting playground to create Majorana states in condensed matter systems. It turns out that the only way of creating an isolated Majorana state has a *topological* origin, they appear at a topological phase transition or at topological defects.

A topological phase transition is a transition between two electronically gapped, topologically different systems. Importantly, no symmetry changes across the phase transition, placing the topological phase transition outside framework of the Landau theory for thermodynamic phase transitions. One gapped system has the same topology as another gapped system when the two systems can be continuously deformed into one another without ever closing the energy gap in the electronic spectrum. In the context of superconducting systems, it turns out that a topological phase transition can be identified depending on the fermion parity of the system. If the fermion parity of the system is even, the system is called topologically trivial and it can be continuously deformed into the vacuum state [6]. If the fermion parity is odd, the system is called topologically non-trivial: only by closing and reopening the energy gap the system can be transformed into a state with even fermion parity.

The crucial aspect now is that a two dimensional (2D) $p_x + i p_y$ superconductor belongs to the topologically non-trivial class [15, 16]. As a consequence, any finite sized 2D $p_x + i p_y$ superconductor *must* undergo a topological phase transition towards the vacuum state around its perimeter. This implies that the superconducting gap has to close continuously crossing the Fermi level and reopen again to form the vacuum state. Because of this, at the edge the system fulfills the Majorana condition, but any possible Majorana state at the edge is delocalized. A single, localized Majorana state can be created by locally closing the superconducting gap at a vortex core [17]. The second Majorana fermion, which has to be present in the system, is now an extended state at the edge of the system.

More important in our present context is the one dimensional (1D) case. In this case the terms 'chiral' p-wave or $p_x + i p_y$ superconductor are not applicable, since

[6] Loosely speaking, the vacuum state can be considered to be a state of absent charge carriers near the Fermi level, e.g. the semiconducting band gap or the physical end of the system

only one propagating momentum direction is present. Hence the system is referred to as a '1D spinless p-wave' superconductor. It has been shown by Kitaev [18] that as a direct consequence of the 1D geometry, at the two ends of a finite sized 1D spinless p-wave superconductor the gap closes and reopens due to the topological phase transition. This creates a single localized Majorana state at each end. Furthermore, the topology of the system depends on the chemical potential (see section 2.2.1). As a consequence, also topological phase transitions with accompanying Majorana states inside a 1D spinless p-wave superconductor may be present, at domain walls between domains of different topology. It is beyond the scope of this thesis to discuss the 2D case into more depth, but the 1D case will be discussed extensively in section 2.2. Since a Majorana state is spatially bound to a topological defect (vortex core, ends of 1D system) or a local topological phase transition, it is known in literature and referred to from here on as a Majorana Bound State (MBS).

It is crucial to realize that such a MBS is *robust* in system parameters: once a superconducting system is driven into a topologically non-trivial phase with an energy gap large compared to energy fluctuations induced by system parameters such as tempearture and chemical potential, a MBS will *always* be present at the spatial point where the topological phase transition happens, regardless of the exact system parameters.

Getting Majorana fermions in condensed matter is reduced to finding a 2D $p_x + ip_y$ or 1D spinless $p_x + ip_y$ superconductor. For over a decade, the material Sr_2RuO_4 is considered to be a candidate system, but experimental evidence for this is ambiguous [14]. As of yet no other viable candidate materials for $p_x + ip_y$ superconductivity are known. A crucial step in the development of candidate systems for finding MBS's is the work by Fu and Kane in 2008[7, 19]. It was shown that MBS's will appear by coupling a topological insulator surface state to an ordinary s-wave superconductor and a magnetic insulator, this because of an equivalent topology of the system to a $p_x + ip_y$ superconductor. Since then more and more theories have been developed to create a system equivalent to a $p_x + ip_y$ superconductor. It was found that both 2D [16] and 1D [20, 21] semiconductors with strong spin-orbit coupling coupled to s-wave superconductors could be driven into a phase equivalent to $p_x + ip_y$ superconductivity in the presence of an external magnetic field. The materials involved in these theories are more common and better understood and therefore the realization of MBS's seems within reach now. The experimental work in this thesis is on the explicit realization of the 1D version, the proposal will be discussed in depth in section 2.2.2.

2.1.5 MAJORANA BOUND STATES AND NON-ABELIAN EXCHANGE STATISTICS

MBS's lead to a profound consequence, both from a fundamental and a more applied viewpoint. The aspect of interest is the so called 'non-abelian' exchange statistics of MBS's, which we elaborate upon now.

In quantum mechanics, the wave function of a system of N indistinguish-

able particles is a function of the coordinates of the individual particles, $\Psi = \Psi(x_1, x_2, .., x_N)$. In 3 or more dimensions, upon particle exchange the wavefunction has to be (anti)symmetric, for example $\Psi(x_1, x_2, .., x_N) = \pm\Psi(x_2, x_1, .., x_N)$. This corresponds to a fermionic (antisymmetric) or bosonic (symmetric) system. In 1D, particle exchange is not a well defined concept in our context, because particles cannot be exchanged without interacting. In the 2D case, interestingly, the possibility exists to go beyond the fermionic or bosonic cases. The wave function may change from Ψ_a to Ψ_b under particle exchange following an operator B_{ab}: $\Psi_b(x_2, x_1, ..x_N) = B_{ab}\Psi_a(x1, x2, ..x_N)$, this exchange process is called *braiding*. If B_{ab} is diagonal, the particles are fermions if the coeficients multiply -1, and bosons if they multiply to +1. If the diagonal entries are of the form $e^{i\phi}$, the particles are called 'anyons' which acquire a phase factor ϕ under braiding. Lastly, when B_{ab} is non-diagonal, the particles follow the so called 'non-abelian' statistics, and MBS's in a 2D system belong to this class of particles. We review part of the properties of a non-abelian state of matter [22] and then show why MBS's have this property.

The most essential property of a non-abelian system is that it has a degenerate ground state manifold, with the degeneracy caused by quasi-particle excitations that appear within the ground state. This degeneracy of the ground state has to be of exponential order in the number of quasi-particles. Moreover, these ground states should be well separated by an energy gap from any other excitations. The ground state degeneracy is robust against local perturbations, because the quasi-particles have a topological origin. When quasi-particles in such a system are being moved around each other or being interchanged in position, the system may transform from one ground state to another. This transformation should only depend on the topology of such a trajectory, or in other words, two trajectories that can be deformed continuously into one another, without the quasi-particles ever coming close enough to interact, must result in the same transformation (up to a phase factor).

Such a system is called non-abelian, in stark contrast to states of matter were quasi-particles acquire only a phase shift upon exchange. The latter does not depend on the order of exchanges and is therefore known as abelian. Contrary, the order of consecutive exchange operations of non-abelian quasi-particles defines what the final groundstate of the system will be, the different braiding operations are non-commuting.

It has been proposed that certain fractional quantum hall states (in particular the $\frac{5}{2}$ state) are non-abelian states, for more information see ([7, 22, 23]. Relevant to our discussion is that a 2D $p_x + ip_y$ superconductor with MBS's constitutes a non-abelian state of matter, which we discuss in more detail now.

To see the ground state degeneracy in the case of MBS's in a 2D $p_x + ip_y$ superconductor, the concept of fermion parity is crucial. In the mean field theory of superconductors there is no particle conservation because of Cooper pair creation/annihilation. The fermion *parity*, however, is a conserved quantity. We have argued at the end of section 2.1.2 that number states are not defined for Majorana

operators. Nevertheless, we can still define a normal fermionic number operator for a given pair of Majorana operators γ_{2i-1} and γ_{2i} via the original fermionic operators c_i and $c_i^\dagger$ by defining $n_i = c_i^\dagger c_i$. n_i can have values of 0, 1 by the Pauli exclusion principle. In other words, a pair of MBS's can either be occupied or non-occupied with a single fermion. As a consequence, the two parity states, which normally have different energy in a superconductor, have become degenerate, each one corresponding to a different ground state of the system. Assuming that the superconductor is isolated, such that no charge transfer can happen from or to it, the parity of the superconductor as a whole is fixed. Now in the presence of a single pair of MBS's it must have the same parity as the superconductor, the system's ground state is non-degenerate. For every new pair of MBS's, however, two new degenerate groundstates are introduced, hence the ground state degeneracy grows as 2^{N-1}, N being the number of pairs of MBS's. The choice of number operators, which corresponds to defining which Majorana operators form a pair, is arbitrary and is a choice of basis. Nevertheless, the number operators n_i are physical observables. These cannot be measured as long as the parity states are truly degenerate, as is the case for well separated MBS's. Contrarily, as soon as overlap between the MBS's is present, a term in the Hamiltonian of the form [24]

$$\frac{i}{2} t \gamma_{2i-1} \gamma_{2i} = t\left(n_i - \frac{1}{2}\right) \tag{2.12}$$

will be present, here t denotes the coupling strength, which is a function of distance between the individual MBS's. Now one parity state of the MBS's corresponds to the ground state energy, but the other parity state leads to an energy gain of the system, making the parity states distinguishable. This process of bringing the non-abelian MBS's together to access their fermionic occupation is formally called *fusion*.

In short, assuming that the MBS's (and the vortices containing them) can be moved, the system fulfils all the necessary conditions to have non-abelian exchange statistics: a groundstate degeneracy is given by the degenerate parity state, this groundstate manifold is separated by the superconducting gap in the $p_x + ip_y$ superconductor from its excitations and the ground state degeneracy is robust as long as the MBS's are well separated.

To see that the exchange statistics is non-abelian, the above concepts are discussed more formally [24]. A particular groundstate of N pairs of MBS's can be represented by $|\psi\rangle$ being a state vector with the n_i's of the pairs of MBS's as entries:

$$|\psi\rangle = |n_1, n_2, ..n_N\rangle \tag{2.13}$$

Once more, the n_i's can have value 0 or 1. These states are eigenstates of the parity operator P_i defined as

$$P_i \equiv 1 - 2n_i = 1 - 2c_i^\dagger c_i = -i\gamma_{2i-1}\gamma_{2i} \tag{2.14}$$

which has values of +1 ($n_i = 0$, even parity) or -1 ($n_i = 1$, odd parity). Since different Majorana operators anticommute, products of the P_i's commute with each other. This is only true if two pairs of MBS's do not share a MBS, as shown in the following example (brackets in initial and final product define different pairs):

$$\begin{aligned}(\gamma_1\gamma_2)(\gamma_3\gamma_4) = -\gamma_1\gamma_3\gamma_2\gamma_4 = \gamma_1\gamma_3\gamma_4\gamma_2 = -\gamma_3\gamma_1\gamma_4\gamma_2 = (\gamma_3\gamma_4)(\gamma_1\gamma_2)\\ (\gamma_1\gamma_2)(\gamma_2\gamma_3) = -\gamma_1\gamma_2\gamma_3\gamma_2 = \gamma_2\gamma_1\gamma_3\gamma_2 = -(\gamma_2\gamma_3)(\gamma_1\gamma_2)\end{aligned} \tag{2.15}$$

Consequently, all P_i's commute with each other since they are defined by pairing up different Majorana operators for every pair. Now the complete Hilbert space of N pairs of MBS's can be given by using the $|\psi\rangle$ states which are the eigenstates of the parity operators

$$|\Psi\rangle = \sum_{n_i=0,1} \alpha_{n_1 n_2 .. n_N} |n_1, n_2, .. n_N\rangle \tag{2.16}$$

The total parity P_{tot} of the system as a whole is obtained by multiplying all P_i's

$$P_{tot} = \prod_{i=1}^{N} P_i = (-i)^N \prod_{i=1}^{2N} \gamma_i \tag{2.17}$$

P_{tot} has eigenvalues ± 1 corresponding to an even or odd number of occupied fermionic modes. As a consequence, only states that are eigenstates of P_{tot} need to be considered, or more precisely, states that obey $P_{tot}|\Psi\rangle = \pm|\Psi\rangle$. Especially linear combinations of even and odd total parity states are not allowed. This is a formal way of demanding that the system is closed, it can only have a single total parity, since no particle transfer from or to the system is allowed to happen. This constraint is only put on the total parity, as mentioned before, the individual pairs can have both parities as long as the total combination of parities results in the required total parity of the state.

Next we consider exchange of MBS's. The exchange process has to be adiabatically to ensure the system stays in the groundstate manifold. Furthermore, the initial and final Hamiltonians of the system are identical, the exchange process is a closed trajectory. This means the exchange process can be described by a unitary operator B acting on $|\Psi\rangle$. Since B describes an adiabatic process, the particle number in the system cannot change, hence B commutes with the total parity operator: $[B, P_{tot}] = 0$. Furthermore, it is required that B only depends on the MBS's involved in the exchange process, not on the other MBS's in the system. Assuming a counter clockwise direction of exchange, it can be derived that B is given by (up to an overal phase factor):

$$B_{i,j} = \frac{1}{\sqrt{2}}\left(1 + \gamma_i\gamma_j\right) \tag{2.18}$$

This operator is called a 'braid' operator, the process of exchanging MBS's is called 'braiding'. The operator has a very non-trivial effect. The simplest exchange

possible is considering a system containing only 2 MBS's, γ_1 and γ_2. The corresponding possible groundstates of the system are the two possible occupations of this single pair, $|0\rangle$ and $|1\rangle$. The effect of the braid operator can now be calculated explicitly

$$\begin{aligned} B_{12}|0\rangle &= \frac{1}{\sqrt{2}}(1+i)|0\rangle \\ B_{12}|1\rangle &= \frac{1}{\sqrt{2}}(1-i)|1\rangle \end{aligned} \tag{2.19}$$

Obviously, the braid operator multiplies the initial state with a phase factor, but nothing more happens. This makes complete sense, since for a single pair of MBS's P_{tot} is the same as P_1. The simplest non trivial case is with 2 pairs of MBS's with associated number states $|n_1 n_2\rangle$. For example, the effect of the braid operators on $|00\rangle$ is given by

$$\begin{aligned} B_{12}|00\rangle &= \frac{1}{\sqrt{2}}(1+i)|00\rangle \\ B_{23}|00\rangle &= \frac{1}{\sqrt{2}}(|00\rangle + i|11\rangle) \\ B_{34}|00\rangle &= \frac{1}{\sqrt{2}}(1+i)|00\rangle \end{aligned} \tag{2.20}$$

Exchanging two MBS's belonging to the same pair only multiplies the state with a phase factor (B_{12} and B_{34}). Exchanging MBS's belonging to different pairs (B_{23}), however, produces a superposition state of the different number states. The total parity of each state in the superposition is the same (both $|00\rangle$ and $|11\rangle$ have even parity). This is a clear demonstration that exchanging MBS's can have a profound effect and is non-abelian. The above example for $|00\rangle$ can be extended to all number states involved. Following (2.16), the state $|\Psi\rangle$ can be written as $|\Psi\rangle = \alpha_{00}|00\rangle + \alpha_{01}|01\rangle + \alpha_{10}|10\rangle + \alpha_{11}|11\rangle$, so the state vector $|\Psi\rangle = (\alpha_{00}, \alpha_{01}, \alpha_{10}, \alpha_{11})$ can be defined. Now the braid operators can be given in matrix representation

$$B_{12} = \begin{bmatrix} e^{-i\frac{\pi}{4}} & 0 & 0 & 0 \\ 0 & e^{i\frac{\pi}{4}} & 0 & 0 \\ 0 & 0 & e^{-i\frac{\pi}{4}} & 0 \\ 0 & 0 & 0 & e^{i\frac{\pi}{4}} \end{bmatrix} \tag{2.21a}$$

$$B_{23} = \begin{bmatrix} 1 & -i & 0 & 0 \\ -i & 1 & 0 & 0 \\ 0 & 0 & 1 & -i \\ 0 & 0 & -i & 1 \end{bmatrix} \quad B_{34} = \begin{bmatrix} e^{-i\frac{\pi}{4}} & 0 & 0 & 0 \\ 0 & e^{i\frac{\pi}{4}} & 0 & 0 \\ 0 & 0 & e^{i\frac{\pi}{4}} & 0 \\ 0 & 0 & 0 & e^{-i\frac{\pi}{4}} \end{bmatrix} \tag{2.21b}$$

Here the non-abelian nature of the exchange statistics of MBS's is explicit: since B_{23} is non-diagonal, the order of exchanges matters, for instance $B_{12}B_{23} \neq B_{23}B_{12}$. Note that two different braid operators are only non-commuting when some of their MBS's are involved in both exchange processes.

As a final point the potential use of MBS's in quantum computing is discussed. In (2.19) it was made explicit that braiding two MBS's involves only a single quantum state. To define a qubit at least two quantum states are needed, which means a single qubit based on MBS's (called a topological qubit or Majorana qubit) consists of at least 4 MBS's. A further constraint is that within a closed system P_{tot} is fixed. This means that a possible qubit is confined to the even or odd parity subspace. A qubit in the even parity subspace can be defined by $|\tilde{0}\rangle \equiv |00\rangle$ and $|\tilde{1}\rangle \equiv |11\rangle$. In the standard Bloch sphere representation with $|\tilde{0}\rangle$ and $|\tilde{1}\rangle$ being the north and south pole respectively, the braid operations shown before correspond to single qubit rotations

$$B_{12} = B_{34} = e^{-i\frac{\pi}{4}\sigma_z} \qquad B_{23} = e^{-i\frac{\pi}{4}\sigma_y} \tag{2.22}$$

This shows that braiding operations can implement single qubit rotations by an angle of $\frac{\pi}{2}$. By using braiding only, no single qubit rotations with arbitrary angle can be made. Furthermore, using braiding operations it is not possible to create a two qubit gate [25] which could create entangled qubits. As a consequence, braiding MBS's is insufficient for universal quantum computing. There is, however, a potential advantage in using MBS's for quantum computing purposes. 'Conventional' qubits use a local degree of freedom to encode information. Such a qubit is inevitably sensitive to decoherence: local perturbations of the system tend to randomize the superposition state of the qubit. Since the Majorana qubit is defined nonlocally on spatially separated MBS's, these decoherence mechanisms are absent if the MBS's are well separated and the energy gap between groundstate manifold and excitations is sufficiently large.

The exception is physical processes that change the parity of the superconductor introduced as P_{tot} earlier. Such an event would randomize the computational basis. Processes involving charge tunneling into a superconductor are known as 'quasi-particle poisoning' and are a well known phenomenon in superconducting qubits, resulting in an undefined parity. The idea is that by engineering the system carefully quasi-particle tunneling timescales can be brought down to a level well surpassing coherence times of existing qubit systems. Another problem is that initialization/readout of MBS based qubits can only be achieved by coupling them as given by (2.12). This is an unprotected operation, local perturbations might result in decoherence of the qubit.

All together this indicates that MBS's are not a full solution to implement robust quantum computing but they may very well provide an important subsystem which together with conventional qubits will enable this in the future.

2.2 MAJORANA BOUND STATES IN 1D NANOWIRES

In this section we discuss MBS's in 1D systems. We start with a discussion of the Kitaev chain model (2.2.1), followed by its physical implementation in 1D semiconducting nanowires with spin-orbit interaction and induced s-wave superconductivity (section 2.2.2). In the last part of this section the focus is on particular aspects of this model: its magnetic field angle dependence (section 2.2.3), and interaction of MBS's in finite sized sytems (section 2.2.4).

2.2.1 1D KITAEV CHAIN

A simple toy model introduced by Kitaev in 2001 [18] expressed the idea of MBS's arising at the end of a 1D p-wave superconductor for the first time. We shall discuss its essence here, since all 1D proposals on engineering MBS's are direct realizations of it. A 1D nanowire can be described effectively by a tight binding chain of N fermionic sites. By attaching a p-wave superconductor to the nanowire, the Hamiltonian is given by

$$H_{\text{chain}} = \sum_{i=1}^{N} \left(-t\left(c_{\text{i}}^{\dagger} c_{\text{i+1}} + c_{\text{i+1}} c_{\text{i}}^{\dagger}\right) - \mu\left(c_{\text{i}}^{\dagger} c_{\text{i}} - \frac{1}{2}\right) + \Delta c_{\text{i}} c_{\text{i+1}} + \Delta^{*} c_{\text{i}}^{\dagger} c_{\text{i+1}}^{\dagger} \right) \tag{2.23}$$

where t is the tunneling amplitude between two sites, μ is the chemical potential and Δ is the effective superconducting gap in the chain. The summation is over all sites i of the chain and the phase of the superconductor is assumed to be 0 such that $\Delta = |\Delta|$. p-wave superconductivity is included by pairing neighboring electrons with the same spin, therefore the spin indices are omitted in the Hamiltonian and electrons are effectively spinless. Because of the Pauli exclusion principle each site in the chain can only be occupied by a single spinless electron.

As discussed in section 2.1.2 Majorana operators can be introduced for each site by defining $c_{\text{i}} = \frac{1}{2}\left(\gamma_{\text{i},1} + i\gamma_{\text{i},2}\right)$ and $c_{\text{i}}^{\dagger} = \frac{1}{2}\left(\gamma_{\text{i},1} - i\gamma_{\text{i},2}\right)$. Inverting this definition gives $\gamma_{\text{i},1} = c_{\text{i}}^{\dagger} + c_{\text{i}}$ and $\gamma_{\text{i},2} = i\left(c_{\text{i}}^{\dagger} - c_{\text{i}}\right)$. The subscripts 1 and 2 represent the two different Majorana operators from the same site i. Plugging these Majorana operators into equation (2.23), the Hamiltonian becomes:

$$H_{\text{chain}} = \frac{i}{2} \sum_{i=1}^{N} \left(-\mu\gamma_{\text{i},1}\gamma_{\text{i},2} + (t + |\Delta|)\gamma_{\text{i},2}\gamma_{\text{i+1},1} + (-t + |\Delta|)\gamma_{\text{i},1}\gamma_{\text{i+1},2} \right) \tag{2.24}$$

Although the behavior of the full Hamiltonian is somewhat complex, there are two special cases that are much simpler and still representative for a certain behavior. Here we will discuss them one by one, a schematic representation is given in Figure 2.1. The first case is when $|\Delta| = t = 0$ and $\mu < 0$. The Hamiltonian is reduced to:

$$H_{\text{chain}} = -\frac{i}{2}\mu \sum_{i=1}^{N} \gamma_{\text{i},1}\gamma_{\text{i},2} \tag{2.25}$$

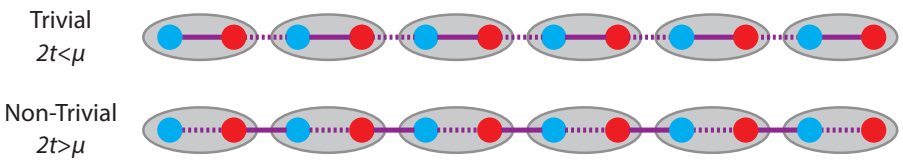

Figure 2.1 |A schematic of the Kitaev chain in topological trivial and topological non-trivial phases. Each fermionic site is indicated by a gray oval. Top chain is the trivial case where two Majorana operators (blue and red circles) from the same site pair up (solid purple line) and Majorana operators from different sites are tunnel coupled (dotted purple line). Bottom chain is the non-trivial case, Majorana operators from different sites are paired together while Majorana operators from the same site are tunnel coupled. In the bottom case there is a unpaired Majorana operator at each end of the chain.

This is a rather trivial case since two Majorana operators from the same site are paired together which is the same as having fermion operators. In other words all sites are still occupied by electrons, see also Figure 2.1, top.

In the second case, $|\Delta| = t > 0, \mu = 0$ and the Hamiltonian has the form:

$$H_{\text{chain}} = i t \sum_{i=1}^{N} \gamma_{\text{i},2} \gamma_{\text{i}+1,1} \tag{2.26}$$

Now the paired Majorana operators $\gamma_{\text{i},2}$ and $\gamma_{\text{i}+1,1}$ are from neighbouring sites. New fermionic operators can be defined by combining these two neighbouring Majorana operators:

$$\tilde{c}_{\text{i}} = \frac{1}{2}\left(\gamma_{\text{i}+1,1} + i\gamma_{\text{i},2}\right) \qquad \tilde{c}_{\text{i}}^{\dagger} = \frac{1}{2}\left(\gamma_{\text{i}+1,1} - i\gamma_{\text{i},2}\right) \tag{2.27}$$

Using these the Hamiltonian becomes:

$$H_{\text{chain}} = 2t \sum_{i=1}^{N-1} \left(\tilde{c}_{\text{i}}^{\dagger}\tilde{c}_{\text{i}} - \frac{1}{2}\right) \tag{2.28}$$

Figure 2.1, bottom illustrates this case. As is visible, there are two unpaired Majorana operators at the ends of the chain, i.e. $\gamma_{1,1}$ and $\gamma_{\text{N},2}$. Notably, these two Majorana operators do not enter the Hamiltonian. This is reasonable because a single Majorana operator does not preserve the fermionic parity. The two Majorana operators can be combined into an operator

$$\tilde{c}_{\text{M}} = \frac{1}{2}\left(\gamma_{1,1} + i\gamma_{\text{N},2}\right) \tag{2.29}$$

Combination of the two non-local Majorana operators thus results in a non-local fermionic operator (the Nth operator missing in the summation of (2.28)).

Since the operator does not show up in the Hamiltonian, energy required to add or to remove one fermion from this state is zero. This is a direct demonstration of the degeneracy of the two parity ground states for a pair of MBS's as discussed in section 2.1.5.

Although the two special cases discussed above are intuitive for understanding the Majorana physics, the arguments are applicable to the Hamiltonian in general as well. To see this, one Fourier transforms the fermionic operators to k-space:

$$c_{\mathrm{i}} = \frac{1}{\sqrt{N}} \sum_{-\infty}^{\infty} e^{-ik\cdot x_i} c_{\mathrm{k}} \qquad c_{\mathrm{i}}^{\dagger} = \frac{1}{\sqrt{N}} \sum_{-\infty}^{\infty} e^{ik\cdot x_i} c_{\mathrm{k}}^{\dagger} \tag{2.30}$$

with k the wavefactor and x_i the position of the site. Now the Kitaev chain Hamiltonian (2.23) can be rewritten in matrix form acting on electron-hole space:

$$H = \frac{1}{2} \sum_{k=0}^{\infty} \begin{bmatrix} c_{\mathrm{k}}^{\dagger} & c_{-\mathrm{k}} \end{bmatrix} H_{\mathrm{BdG}} \begin{bmatrix} c_{\mathrm{k}} \\ c_{-\mathrm{k}}^{\dagger} \end{bmatrix} \tag{2.31}$$

H_{BdG} is the Bogoliubov-de Gennes Hamiltonian which is now contrary to the more general case discussed in section 2.1.3 only acting in electron hole space since the system is effectively spinless. It has the form:

$$H_{\mathrm{BdG}} = \begin{bmatrix} \mu - 2t\cos(k) & -2i\Delta\sin(k) \\ 2i\Delta\sin(k) & -\mu + 2t\cos(k) \end{bmatrix} \tag{2.32}$$

Solving equation (2.31) gives the bulk spectrum:

$$E(k) = \pm\sqrt{\left(2t\cos(k) - \mu\right)^2 + 4|\Delta|^2\sin^2(k)} \tag{2.33}$$

At $k = 0$, the energy gap closes at $2t = \mu$, which is the boundary of the two different phases we encountered before in the the simplified cases (see (2.25) and (2.26)). For $2t > \mu$ the phase is topologically non-trivial, it is topologically trivial for $2t < \mu$. In the case of the topologically non-trivial phase, MBS's appear at the end of the Kitaev chain with zero occupation energy for a non-local fermionic mode as given in (2.29). This shows that a 1D spinless p-wave superconductor allows for the presence of MBS's and a corresponding topologically non-trivial phase.

2.2.2 MAJORANA BOUND STATES IN A 1D NANOWIRE

As mentioned before, no established p-wave superconducting material suitable for detection of Majorana bound states exists, but a p-wave superconductor may be effectively engineered out of known materials. Two theory works from 2010 ([20, 21]) in this spirit are crucial to the experimental work in this thesis. In these works the candidate system is introduced to engineer a 1D p-wave superconductor which is implemented in the experiments of this thesis. The p-wave superconductor is replaced by an ordinary s-wave superconductor, combined with Zeeman and spin orbit interaction in a 1D nanowire. This combination of materials results effectively

in a 1D p-wave superconductor under the right circumstances. In the following we discuss this proposal in more depth.

In the context of the following discussion involving the standard continuum representation of a semiconductor, we switch to the continuum representation of a 1D p-wave superconductor. To this end, we define the fermionic annihilation field operator $\mathbf{\Psi}_x = [\Psi_{x\uparrow}, \Psi_{x\downarrow}]$ acting in spin space, x indicating the one dimensional direction of motion in the system. In the context of 1D p-wave superconductivity the system is effectively spinless, thus the spin index is ommitted and the field operator is defined as Ψ_x as opposed to the spinfull operator $\mathbf{\Psi}_x$. Now the Kitaev Hamiltonian (2.23) becomes

$$H = \int_{-\infty}^{\infty} \left(\Psi_x^\dagger \left(\frac{p_x^2}{2m} - \mu \right) \Psi_x + e^{i\phi} \Delta p_x \Psi_x \Psi_x + \text{H.c.} \right) \mathrm{d}x \tag{2.34}$$

with μ th chemical potential, m the effective electron mass, p_x the momentum in x direction, ϕ the superconducting phase and Δ the superconducting pairing strength.

Next we turn to a general description of a semiconductor in 3D, given by

$$H_0 = \frac{\mathbf{p}^2}{2m} - \mu + V(\mathbf{r}) - \frac{\hbar^2}{4m_0^2 c^2} \left(\nabla V(\mathbf{r}) \times \mathbf{p} \right) \cdot \boldsymbol{\sigma} + \frac{1}{2} g \mu_B \mathbf{B}(\mathbf{r}) \cdot \boldsymbol{\sigma} \tag{2.35}$$

with parameters $\mathbf{p}$ momentum, m effective electron mass, μ chemical potential, V electrostatic potential, $\mathbf{r}$ position, $\hbar$ reduced Planck's constant, m_0 free electron mass, c speed of light, $\boldsymbol{\sigma} = [\sigma_x, \sigma_y, \sigma_z]$ a vector containing the Pauli spin matrices, g Landé g-factor, μ_B Bohr magneton and $\mathbf{B}$ the applied magnetic field. The term proportional to $\left(\nabla V(\mathbf{r}) \times \mathbf{p} \right) \cdot \boldsymbol{\sigma}$ is the spin-orbit interaction (SOI) in the material, which in the presence of spatial inversion assymetry in the structure is approximated by the Rasba SOI Hamiltonian [26]

$$H_R = e\alpha_0 \boldsymbol{\sigma} \cdot \mathbf{k} \times \mathbf{E} \tag{2.36}$$

with e the electron charge, α_0 a material specific prefactor, and $\mathbf{k}$ the wavevector. Dresselhaus SOI can be left out of consideration since no bulk inversion asymmetry is present in the growth direction of our nanowires. In 1D, (2.36) simplifies considerably by assuming $\mathbf{E} = E\hat{\mathbf{z}}$, where $\hat{\mathbf{z}}$ is perpendicular to the direction of motion $\hat{\mathbf{x}}$. This assumption is justified because in reality the nanowire is symmetric in a plane perpendicular to $\hat{\mathbf{x}}$. Incorporating the electric field strength into an effective Rashba spin-orbit strength parameter α_{SO}, we obtain

$$H_R^{1D} = -\alpha_{SO} k_x \sigma_y \tag{2.37}$$

Next we assume that the applied magnetic field is in the $\hat{\mathbf{x}}$ direction, along the axial direction of the 1D wire. The final Hamiltonian now becomes

$$H_0 = \frac{\hbar^2 k_x^2}{2m} - \mu - \alpha_{SO} k_x \sigma_y + E_Z \sigma_z \tag{2.38}$$

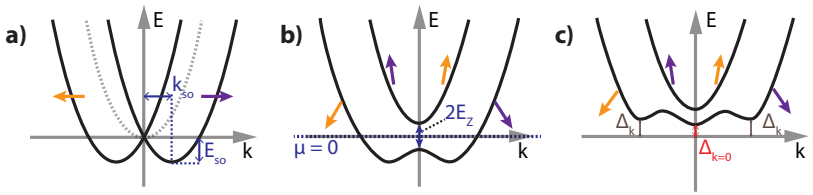

Figure 2.2 |Electronic dispersion of a one dimensional quantum wire with Rashba SOI, Zeemam effect and induced superconductivity. a) $B = 0$ T. The grey dotted parabola corresponds to the case without SOI. Rasbha SOI results in a shift of $\pm k_{SO}$ of each parabola along k_x and and an energy shift of E_{SO}. The parabola's are of opposite spin along an axis orthogonal to k_x, here for illustrating purpose they are drawn along k_x. b) A B along the axial direction ($\hat{\mathbf{x}}$) of the nanowire is applied, resulting in mixture between spin polarization along the σ_y of B_{SO} and along σ_x of the external B. At $k = 0$, a pure Zeeman gap opens up. $\mu = 0$ is defined as the middle of the Zeeman gap. c)$B \neq 0$, μ is fixed in the middle of the Zeeman gap in b) and superconductivity is included. The spectrum of b) is mirrored in the Fermi level and gaps open at finite k.

Here $E_Z = g\mu_B B/2$ is the Zeeman energy. Strong confinement in the $(\hat{\mathbf{y}}, \hat{\mathbf{z}})$-plane is assumed and μ is chosen such that only the lowest 1D nanowire subband is occupied. Without any loss of generality we define $\mu = 0$ to be at the bottom of the band at $k_x = 0$. The corresponding eigenenergy spectrum is given by:

$$E_\pm = \frac{\hbar^2 k_x^2}{2m} - \mu \pm \sqrt{\alpha_{SO}^2 k_x^2 + E_Z^2} \tag{2.39}$$

At $B = 0$, the two initially spin degenerate parabola in the dispersion relation of a system without Rashba SOI are shifted apart along the k_x-axis by an amount $k_{SO} = (m\alpha_{SO})/\hbar^2$, and down by an amount of $2E_{SO}$, $E_{SO} = \left(m\alpha_{SO}^2\right)/\left(2\hbar^2\right)$, leaving the point $k = 0$ spin degenerate and unchanged in energy, as expected for SOI. E_{SO} sets the characteristic energy scale of the SOI. The effect of Rashba SOI at $B = 0$ is illustrated in Figure 2.2a.

At finite B the picture changes considerably. The Rashba SOI in (2.36) may be expressed as $H_R = \frac{\hbar}{2}\mathbf{B}_{SO} \cdot \boldsymbol{\sigma}$, with $\mathbf{B}_{SO} = \frac{2\alpha_{SO}}{\hbar}(\mathbf{k} \times \hat{\mathbf{z}})$. This reduces in 1D to $H = \frac{\hbar}{2} B_{SO}\sigma_y$, with $\mathbf{B}_{SO} = B_{SO}\hat{\mathbf{y}} = \frac{2\alpha_{SO}}{\hbar} k_x \hat{\mathbf{y}}$ a momentum dependent effective B-field. This shows that SOI provides a quantization axis for the spin, causing the spin at opposite k_x values to have opposite sign. Since a B field along $\hat{\mathbf{x}}$ is applied orthogonal to B_{SO}, mixing occurs, tilting spins at all k_x towards a second common quantization axis. This behavior is the key ingredient in obtaining p-wave like superconductivity below: at $B = 0$, a $(k_x, -k_x)$ pair of states forms a singlet along σ_y, but at finite B, an increasing triplet component along σ_x develops whereas the singlet component along σ_y decreases. This behavior is illustrated in Figure 2.2b. At $k = 0$, where the SOI is zero, the spins are purely quantized along the σ_x axis, opening up a gap of

size $2E_Z$ in the spectrum. For all μ within the energy range of this gap, the spectrum is non-degenerate at a given energy and the spin degree of freedom is completely locked to the momentum with only a single possible spin direction for each energy value. This regime is often referred to as 'helical' (a helical state being a state with opposite momentum states having opposite spin), since spins at opposite momentum have nearly opposite sign at low B[7].

We turn to the final ingredient of the proposal, s-wave superconductivity. If the nanowire is put in contact with a conventional s-wave superconductor, Cooper pairs can tunnel into the semiconducting nanowire thus inducing superconductivity in the nanowire. This phenomenon is the so called *proximity effect*. The paring Hamiltonian of a s-wave superconductor is given by

$$H_{\mathrm{SC}} = \int_{-\infty}^{\infty} \left(e^{i\phi} \Delta \Psi_{\uparrow \mathrm{x}} \Psi_{\downarrow \mathrm{x}} + \mathrm{H.c.} \right) \mathrm{d}x \tag{2.40}$$

with Δ the paring strength, ϕ the phase of the superconductor and field operators as defined before (2.34). It is assumed that the pairing as present in a bulk s-wave superconductor is transferred to the semiconducting nanowire and possible effects on the strength of superconductivity are captured by rescaling Δ. Then the total Hamiltonian describing the proximitized semiconducting nanowire becomes:

$$\begin{aligned} H &= H_0 + H_{\mathrm{SC}} \\ &= \int_{-\infty}^{\infty} \left(\mathbf{\Psi}_{\mathrm{x}}^{\dagger} \left(\frac{\hbar^2 k_{\mathrm{x}}^2}{2m} - \mu - \alpha_{\mathrm{SO}} k_{\mathrm{x}} \sigma_{\mathrm{y}} + E_Z \sigma_{\mathrm{x}} \right) \mathbf{\Psi}_{\mathrm{x}} + e^{i\phi} \Delta \Psi_{\uparrow \mathrm{x}} \Psi_{\downarrow \mathrm{x}} + \mathrm{H.c.} \right) \mathrm{d}x \end{aligned} \tag{2.41}$$

In the Bogoliubov-de Gennes matrix formalism as introduced in section 2.1.3 the Hamiltonian is given by

$$H_{\mathrm{BdG}} = \begin{bmatrix} H_0 & \mathbf{\Delta} \\ \mathbf{\Delta}^* & -\mathcal{T} H_0 \mathcal{T}^{-1} \end{bmatrix} \qquad \mathbf{\Delta} = \begin{bmatrix} 0 & e^{i\phi}\Delta \\ -e^{i\phi}\Delta & 0 \end{bmatrix}$$

$$H_0 = \begin{bmatrix} \frac{\hbar^2 k_{\mathrm{x}}^2}{2m} - \mu & E_Z + i\alpha_{\mathrm{SO}} k_{\mathrm{x}} \\ E_Z - i\alpha_{\mathrm{SO}} k_{\mathrm{x}} & \frac{\hbar^2 k_{\mathrm{x}}^2}{2m} - \mu \end{bmatrix} \tag{2.42}$$

$$-\mathcal{T} H_0 \mathcal{T}^{-1} = \begin{bmatrix} -\frac{\hbar^2 k_{\mathrm{x}}^2}{2m} + \mu & -E_Z - i\alpha_{\mathrm{SO}} k_{\mathrm{x}} \\ -E_Z + i\alpha_{\mathrm{SO}} k_{\mathrm{x}} & -\frac{\hbar^2 k_{\mathrm{x}}^2}{2m} + \mu \end{bmatrix}$$

with $\mathcal{T}$ the time reversal operator. The relevant physics arises from the interplay between the s-wave superconducting pairing, SOI and Zeeman effect in

[7] Note that the usage of the term 'helical' is slightly inappropriate here, the whole point is to not have a purely helical state but to create a significant fraction of common spin direction as well resulting in the p-wave character of the superconducting state.

the above Hamiltonian. The role of superconductivity is to pair up states forming $(k_x, -k_x)$ opposite momentum pairs into Cooper pairs, this happens around the Fermi level. Consequentially, a gap opens up in the spectrum and the quasi-particle branches of the spectrum become a mixture of electron like states from above the Fermi level and hole like states from below the Fermi level, completely along the lines of the discussion in section 2.1.3. This behavior is depicted in Figure 2.2. For simplicity, in the following we consider the case of $\mu = 0$.

At $B = 0$, superconducting pairing results in a pure s-wave superconducting system, since the initial electronic states of opposite momentum form a pure spin singlet state. As soon as any B field is applied along $\hat{\mathbf{x}}$, a triplet component will be present as well, resulting in a p-wave like contribution to the superconductivity. This p-wave character increases gradually as the B-field increases. The transition to a topologically non-trivial superconducting state can now be understood as reaching a critical B value above which the superconducting state becomes more p-wave like than s-wave like. Importantly, the system never becomes a pure 1D p-wave superconductor. That would mean that the spins of opposite momentum pairs are fully polarized, thus becoming a pure triplet state with coupling to the s-wave superconductor not possible anymore. One could say that the spin polarizing Zeeman effect is necessary to give the superconducting phase a strong enough triplet, p-wave character, whereas the SOI is necessary to protect it against full spin polarization, thus enabling a strong enough singlet, s-wave like character to still allow for superconducting pairing.

Upon introducing superconductivity in the system, the quasi-particle spectrum consists of two non-degenerate bands, as shown in Figure 2.2c. The lowermost one of these becomes effectively spinless at high B. However, this is only true if μ is placed in the Zeeman induced gap, as present in the spectrum without superconductivity (see Figure 2.2b). For other μ values, due to a second crossing of the Fermi level at lower k_x, another spin species is present preventing from an effectively spinless system. Given that μ is placed within the Zeeman gap (in our definition within a range of $\pm E_Z$ from $\mu = 0$) and B is large such that $E_Z >> (E_{SO}, \Delta)$, only the lowermost band has to be considered, with corresponding spinless fermionic operator Ψ_x. In this limit, the original operators $\Psi_{\uparrow x}$ and $\Psi_{\downarrow x}$ are approximated by $\Psi_{\uparrow x} \approx (\alpha_{SO} k_x) / (2E_Z) \Psi_x$ and $\Psi_{\downarrow x} \approx \Psi_x$ ([27]) and the original Hamiltonian (2.41) may be written for this band as

$$H_{\text{eff}} = \int_{-\infty}^{\infty} \left(\Psi_x^\dagger \left(\frac{\hbar^2 k_x^2}{2m} - \mu - E_Z \right) \Psi_x + e^{i\phi} \frac{\alpha_{SO} \hbar k_x}{2E_Z} \Delta \Psi_x \Psi_x + \text{H.c.} \right) \mathrm{d}x \tag{2.43}$$

Introducing an effective chemical potential $\mu_{\text{eff}} = \mu - E_Z$ and an effective superconducting paring strength $\Delta_{\text{eff}} = (\alpha_{SO} \Delta) / (2E_Z)$ shows that this Hamiltonian is exactly the same as that of an 1D p-wave superconductor as given in (2.34) and the system constructed is a realization of the Kitaev chain introduced before.

For μ inside the Zeeman gap in the spectrum, the system undergoes a topological phase transition with an accompanying gap closure and reopening in the

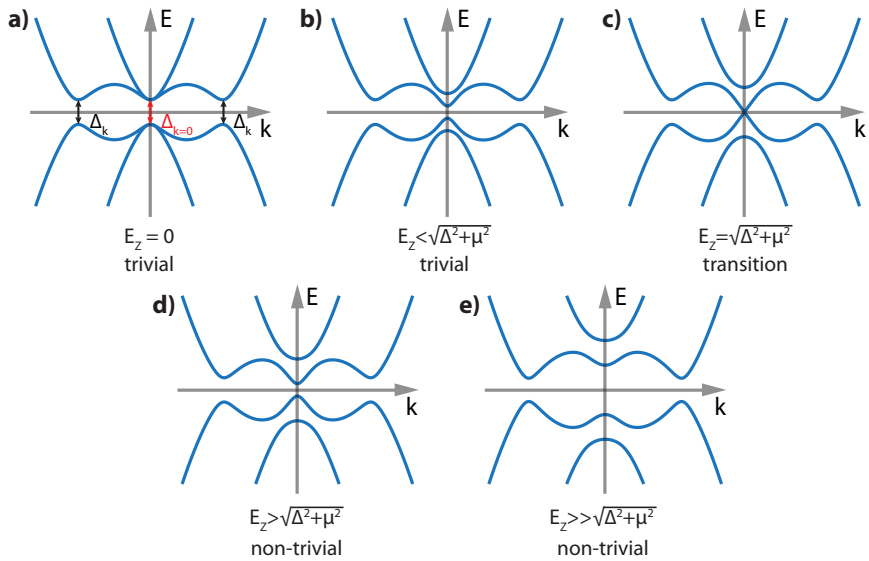

Figure 2.3 |Bogoliubov-de Gennes spectra as a function of magnetic field for a 1D nanowire with Rashba SOI. $\mu = 0$, $\Delta = (0.5\alpha_{\mathrm{SO}})^2$, α_{SO} is kept dimensionless and units are arbitrary. SOI is in the $\hat{\mathbf{y}}$-direction. a) $E_{\mathrm{Z}} = 0$. Gaps at $k = 0$ and finite k have equal size and the spectrum is degenerate at $k = 0$. Both gaps at finite k and k =0 are indicated as in Figure 2.2 b) $E_{\mathrm{Z}} = 0.5\Delta$. Gap at $k = 0$ is closing linearly, gap at finite k closes slowly in B. c) $E_{\mathrm{Z}} = \Delta$, the critical B field at which the topological phase transition happens. The state at $k = 0$ exactly fulfills the Majorana condition. d) $E_{\mathrm{Z}} = 1.5\Delta$, the gap at $k = 0$ has reopened. e) $E_{\mathrm{Z}} = 3\Delta$, now the $k = 0$ has opened further and the gap at finite k has become the effective gap in the system.

spectrum as a function of increasing B and reaches the form of (2.43) at high B. To investigate this gap closure and reopening, we focus on the spectral gap at $k_x = 0$. There the Hamiltonian reduces to

$$H_{\text{BdG}} = \begin{bmatrix} -\mu & E_Z & 0 & e^{i\phi}\Delta \\ E_Z & -\mu & -e^{i\phi}\Delta & 0 \\ 0 & -e^{-i\phi}\Delta & \mu & -E_Z \\ e^{-i\phi}\Delta & 0 & -E_Z & \mu \end{bmatrix} \tag{2.44}$$

The BdG-formalism introduced in (2.8) is used here, note that SOI is absent since $k_x = 0$. By solving this Hamiltonian, the size of the energy gap at $k = 0$ can be found which is

$$E_{\text{gap,k=0}} = \sqrt{\Delta^2 + \mu^2} - E_Z \tag{2.45}$$

This shows when $E_Z = \sqrt{\Delta^2 + \mu^2}$, the gap at $k = 0$ closes, marking the topological phase transition from a topological trivial to non-trivial system. Importantly, at the point of gap closure, the dispersion fulfills the Majorana condition: at the Fermi level, a single, non-degenerate pair of states is present constructed from exactly half a fermionic creation and half a fermionic annihilation operator of equal spin. For larger B, $E_Z > \sqrt{\Delta^2 + \mu^2}$ the gap reopens leaving the bulk of the nanowire without states again but Majorana bound states now emerges at the ends of the system (we elaborate on this below). The sign of the $k_x = 0$ gap marks the topological state of the system, positive corresponding to trivial and negative to non-trivial. This behavior is shown in Figure 2.2d,e,f, where energy spectra before, at and after the topological phase transition are shown.

Next we consider the gap at finite k. This gap has its minimum value around a value of $k = 2k_{\text{SO}}$, we refer to its exact finite k-value as k_f. A general expression for this gap is rather complex and not so insightful, but at $\mu = 0$ the expression is less complex and given by

$$E_{\text{gap,k=k}_f} = \frac{2\Delta E_{\text{SO}}}{\left(E_{\text{SO}}(2E_{\text{SO}} + \sqrt{E_Z^2 + 4E_{\text{SO}}^2})\right)^{1/2}} \tag{2.46}$$

This shows that the gap at k_f decreases as a function of $\sim 1/\sqrt{E_Z}$, while the gap at $k = 0$ linearly depends on E_Z, thus allowing for a gap closure and reopening at $k = 0$ while the system effectively stays superconducting due to the finite k gap. The effective superconducting gap in the system is the minimum of both gaps. At high B field where $E_Z >> E_{\text{SO}}$, the finite k gap becomes negligible in size and the system is no longer superconducting. A large Rashba SOI in the semiconducting nanowire is therefore essential to allow for a long enough B field range in which a topologically non-trivial phase is accompanied by a large enough superconducting gap. The B dependence of the gaps is shown in Figure 2.4. It should be remarked that we up to now assumed a constant s-wave pairing strength Δ, but in a realistic experimental

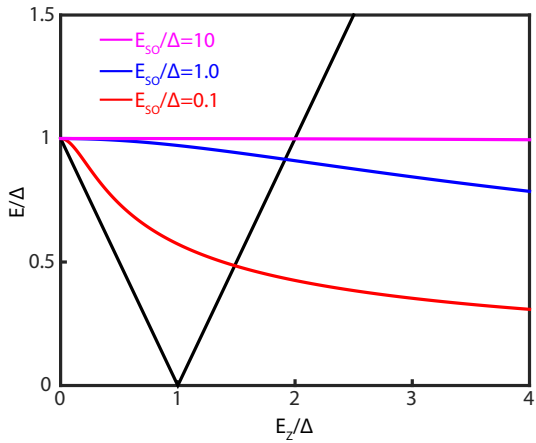

Figure 2.4 |Spectral gaps as a function of magnetic field in a superconducting 1D nanowire with Rashba SOI. Gaps are shown for $\mu = 0$. Black line is the gap at $k = 0$ which is indepent of SOI strength. Colored lines represent the gap at finite k for different SOI strength. The gap at $k = 0$ closes and reopens linearly determining the effective gap at low B. Between $E_Z/\Delta = 1$ and $E_Z/\Delta = 2$, the finite k gap becomes smaller as the $k = 0$ gap, thus determining the effective gap at higher B fields.

setting, Δ will decrease in B as well since the bulk s-wave superconducting material used to achieve the proximity effect will eventually turn normal again at high B. Both a bulk superconducting material sustaining B fields such that $E_Z >> \Delta$ and a large effective g-factor in the semiconducting wire such that E_Z grows fast are essential factors in realizing the topological non-trivial state. We comment on realistic scenario's for material parameters at the end of this chapter.

The emergence of MBS in the system can easily be seen now. Since any realistic system has a finite length, after the topological phase transition, at the wire ends the topologically non-trivial gap has to close before it may reopen to connect to the topologically trivial vacuum gap. This may be viewed as Δ or E_{SO} becoming zero at the wire ends, E_Z becoming small because of the vacuum g-factor or μ going to $-\infty$. At the point of gap closure, the system will reach the Majorana condition and now a single, localized MBS will be present at each wire end, in complete equivalence to the localized MBS's in the Kitaev chain model. This behavior is schematically shown in Figure 2.5. Although the MBS are localized, their wavefunction has a finite extension into the wire which falls off exponentially with $\sim e^{x/\xi}$, ξ being the effective coherence length of the topologically non-trivial phase set by the particular parameter values of Δ, μ, E_Z and E_{SO}. It is important that the nanowire's length L is long compared to ξ.

Rather than ending the nanowire physically to localize a MBS, the same may

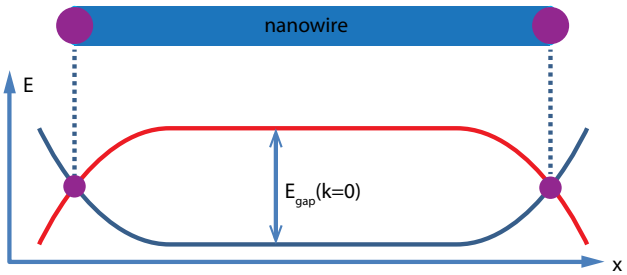

Figure 2.5 |Schematic of MBS arising at the ends of the 1D nanowire. Once the nanowire has undergone the topological phase transition and the gap is inverted, it as to close at the wire ends to connect the system to the topologically trivial vacuum. The case depicted here corresponds to μ diverging to $-\infty$ at the wire ends. The point of gap closure corresponds to a localized, single MBS. This immediately implies that the MBS's come in pairs, at both ends of a topologically non-trivial section a MBS is present.

be achieved by changing μ outside the Zeeman gap in the spectrum. In this way the length of the topologically non-trivial superconductor may be controlled, along with the exact position of the MBS. In general, μ and B are from an experimental viewpoint the primary handles to control the emergence and exact location of MBS's.

2.2.3 ANGLE DEPENDENCE OF THE TOPOLOGICAL PHASE TRANSITION

The combination of the vector nature of SOI with an external magnetic field gives a strong anistropic behavior of the system as a function of the relative angle between SOI and the external B. We discussed so far the specific case of $\mathbf{B} = B\hat{\mathbf{x}}$ and $\mathbf{B}_{\mathrm{SO}} = B_{\mathrm{SO}}\hat{\mathbf{y}}$. The reason for this choice was the orthogonal spin quantization axes provided by those two fields enabling both spin singlet and triplet components of the superconducting pairing in the lowest quasi-particle bands. Assuming that $\mathbf{B}_{\mathrm{SO}}$ indeed has a pure Rashba SOI origin, we may stick to our previous definition of $\mathbf{B}_{\mathrm{SO}} = B_{\mathrm{SO}}\hat{\mathbf{y}}$ without any loss of generality [28, 29] .

To consider arbitrary B field directions, the spherical angles θ and φ are introduced. θ is the angle of rotation in the xz-plane, $\theta = 0$ corresponds to $+z$. φ is the angle of rotation in the xy-plane, $\varphi = 0$ corresponds to $+x$. A schematic of the definitions given here is shown in Figure 2.6a. The Zeeman interaction term is now altered to $E_Z\left(\sin\theta\cos\varphi\sigma_x + \sin\theta\sin\varphi\sigma_y + \cos\theta\sigma_z\right)$ and the full Hamiltonian is given by

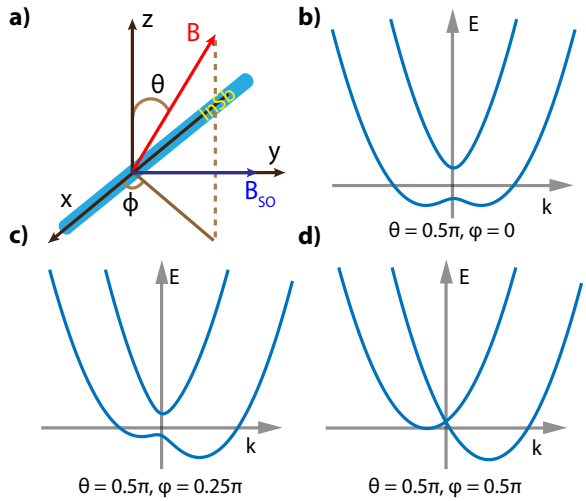

Figure 2.6 |Effect of magnetic field direction on a one dimensional nanowire with Rasba SOI. No superconductivity is included. a) Schematic representation of the set-up showing the definition of the spherical angles, $\theta = 0$ corresponds to $+z$ and $\varphi = 0$ corresponds to $+x$. B_{SO} is in the y-direction. b) $B \neq 0$, $\theta = 0.5\pi$, $\varphi = 0$, the case of orthogonal angles between external B and B_{SO} (same as Figure 2.2b. c) $B \neq 0$, $\theta = 0.5\pi$, $\varphi = 0.25\pi$ representing an intermediate case between mixing of spins along σ_{x} and σ_{y}. The spin parabolas start to shift in energy and the gap at $k = 0$ becomes smaller. d) $B \neq 0$, $\theta = 0.5\pi$, $\varphi = 0.5\pi$, the external B and B_{SO} are aligned. The spins fully polarize along σ_{y}, resulting in a closure of the gap at $k = 0$ and an energy difference of $2E_{\mathrm{Z}}$ between the two bands. Topologically non-trivial superconductivity is only possible in a (narrow) range of angles around $\varphi = 0$.

$$H_{\mathrm{BdG}} = \begin{bmatrix} H_0 & \mathbf{\Delta} \\ \mathbf{\Delta}^* & -\mathcal{T} H_0 \mathcal{T}^{-1} \end{bmatrix} \qquad \mathbf{\Delta} = \begin{bmatrix} 0 & e^{i\phi}\Delta \\ -e^{i\phi}\Delta & 0 \end{bmatrix}$$

$$H_0 = \begin{bmatrix} \frac{\hbar^2 k_{\mathrm{x}}^2}{2m} - \mu + E_{\mathrm{Z}}\cos\theta & E_{\mathrm{Z}}\sin\theta\left(\cos\varphi - i\sin\varphi\right) + i\alpha_{\mathrm{SO}}k_{\mathrm{x}} \\ E_{\mathrm{Z}}\sin\theta\left(\cos\varphi + i\sin\varphi\right) - i\alpha_{\mathrm{SO}}k_{\mathrm{x}} & \frac{\hbar^2 k_{\mathrm{x}}^2}{2m} - \mu - E_{\mathrm{Z}}\cos\theta \end{bmatrix}$$

$$-\mathcal{T} H_0 \mathcal{T}^{-1} = \begin{bmatrix} -\frac{\hbar^2 k_{\mathrm{x}}^2}{2m} + \mu - E_{\mathrm{Z}}\cos\theta & -E_{\mathrm{Z}}\sin\theta\left(\cos\varphi + i\sin\varphi\right) - i\alpha_{\mathrm{SO}}k_{\mathrm{x}} \\ -E_{\mathrm{Z}}\sin\theta\left(\cos\varphi - i\sin\varphi\right) + i\alpha_{\mathrm{SO}}k_{\mathrm{x}} & -\frac{\hbar^2 k_{\mathrm{x}}^2}{2m} + \mu + E_{\mathrm{Z}}\cos\theta \end{bmatrix} \tag{2.47}$$

To see the effect of arbitrary B field direction it is useful to first consider the case $\Delta = 0$. This is shown in Figure 2.6. Two planes of B-rotation showing distinguished behavior can be identified. Rotating B in the xz-plane will not change anything in the spectrum, since for all angles in this plane, $B \perp B_{\mathrm{SO}}$. Only the quantization axis of the Zeeman interaction changes which has no consequences for the other physical properties. The other rotation plane of interest is the xy-plane. Rotating B from $\hat{\mathbf{x}}$ to $\hat{\mathbf{y}}$, a gradual transition of decreasing spin mixing along σ_{x} and σ_{y}, towards full spin polarization along σ_{y}, takes place. This transition is clearly visible in the spectrum, the Zeeman gap gradually closes and the two spin parabola gradually shift apart in energy. Importantly, the case of the xz-plane is unique to the angle $\varphi = 0$, such that no parallel component of B to B_{SO} is present. Contrarily, the case of the xy-plane holds for all angles θ.

The full Bogoliubov-de Gennes spectrum is shown in Figure 2.7 as a function of the relative angle between B and B_{SO}. The relevant aspect visible is that of a topological phase transition as a function of angle of B. This phase transition can easily be understood based on the previous discussion: the more the external B is aligned with B_{SO}, the less the spin singlet component becomes along σ_{y}. In fact, above a critical angle, the superconducting gap in the spectrum simply closes and the superconducting state is destroyed, because the singlet component of opposite k_{x} pairs becomes too weak to allow for sufficient coupling between bulk s-wave superconductor and nanowire. This critical angle φ_{c} at which the gap closes is given by [29]

$$\sin\varphi_{\mathrm{c}} = \frac{E_{\mathrm{gap,k=k_f}}}{E_{\mathrm{Z}}} \tag{2.48}$$

For B applied along B_{SO}, the superconducting gap in the spectrum closes at $E_{\mathrm{Z}} = \Delta$ and the system never becomes topologically non-trivial. For B orthogonal to B_{SO} the discussion of the previous section holds: the system becomes topologically non-trivial above $E_{\mathrm{Z}} = \Delta$ (assuming $\mu = 0$) and stays in this phase until the finite k gap is destroyed. For arbitrary φ, in a range between $E_{\mathrm{Z}} = \Delta$ and $E_{\mathrm{Z}} = E_{\mathrm{gap,k=k_f}} / \sin\varphi$ the system is in the non-trivial state (assuming $\mu = 0$). Note that for non-zero μ, the expression (2.46) no longer holds and a μ-dependent version should be used in (2.48) to obtain φ_{c}.

2.2.4 INTERACTING MAJORANA BOUND STATES

The previous discussions about MBS's, their braiding and potential qubits based on them, are all based on the assumption that the two unpaired MBS's are well isolated and therefore not interacting with each other. In a realistic system, however, the two bound states are always coupled due to a small but finite overlap of the individual MBS wavefunctions. Such coupling leads to a hybridization of the two bound states: they are no longer true MBS's, but one of them becomes slightly electron like and the other one slightly hole like, and as a consequence the MBS's will split in two states with a small energy splitting. This energy splitting depends on the degree of overlap of the individual MBS wavefunctions. The decaying 'tail' of

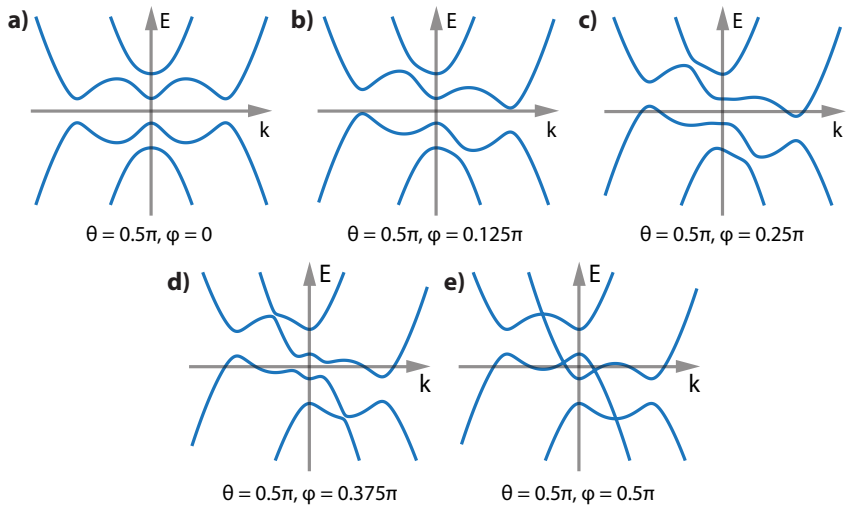

Figure 2.7 |Bogoliubov-de Gennes spectra as a function of relative angle between external magnetic field and Rashba SOI field for a 1D nanowire. $\mu = 0$, $E_Z = 2\Delta$, $\Delta = (0.5\alpha_{SO})^2$, α_{SO} is kept dimensionless and units are arbitrary. a) B is applied along $\hat{\mathbf{x}}$ orthogonal to B_{SO}. This spectrum corresponds to a case in between the cases shown in Figure 2.3d and e, the system is in the topologically non-trivial phase. b), c) d) and e) correspond to a rotation of B in the xy-plane towards B_{SO}. In b) the superconducting finite k gap is almost closed, in c) this gap is visibly closed, the local minima at finite k have crossed the k-axis which corresponds to the level of μ here. d) shows further progression of this effect and some of the anti-crossings in the spectrum are almost gone. completely closure of these gaps is reached in e) where B is in the $\hat{\mathbf{y}}$-direction parallel to B_{SO}. In the spectra shown, $E_Z = 2\Delta$, such that the critical angle $\varphi_c = 0.167\pi$, showing that a) and b) are both topologically non-trivial, although the gap in b) is almost closed.

the MBS wavefunction in the nanowire can be approximated as [30]

$$\Psi \sim e^{-x/\xi} e^{\pm i k_F x} \tag{2.49}$$

with k_F the effective wave vector at the Fermi level and ξ the effective superconducting coherence length. x is the coordinate measuring the distance from the center of the MBS i.e. the point where $|\Psi|^2$ is maximal. The energy splitting ΔE resulting from the coupling of two MBS's separated by a distance L is approximated by [30]:

$$\Delta E \approx \hbar^2 k_F \frac{e^{-2L/\xi}}{m\xi} \cos(k_F L) \tag{2.50}$$

This approximation is valid when (2.49) holds, i.e. when $L >> \xi$ such that only the 'tails' of the wavefunctions overlap. Since the MBS's are localized at the ends of the system, L corresponds to the effective topologically non-trivial nanowire length.

The three parameters L, ξ and k_F all influence this energy splitting. The upper limit of L is set by the physical length of the superconducting nanowire section. Possible local control over μ allows for shortening L. ξ is determined by the effective superconducting gap in the spectrum and k_F. Both these parameters strongly depend on the values of μ, E_Z and E_{SO}. Both μ and E_Z can easily be varied in situ. Because of the $\cos(k_F L)$ dependence of ΔE, this may lead to an oscillatory behavior of the coupling between the two MBS's. For particular parameter values or ranges the coupling may be absent, implying that the coupling between MBS's in the nanowire system may be engineered to a high degree. This tunability of the MBS coupling may be crucial to enable non-abelian exchange statistics, which strictly requires the MBS's to be at zero energy. On the other hand, the fermionic occupation of a pair of MBS's may be probed by deliberately turning on a coupling between the two. More realistic numerical calculations on the effective coupling of MBS's in a finite sized nanowire sytem are discussed in chapter 6.

2.3 DETECTION OF MAJORANA BOUND STATES

The most defining property of a pair of MBS is their single fermionic degree of freedom, which can be occupied at no energy cost and leads to their non-Abelian exchange statistics (see section 2.1.5). It is safe to say that the unambiguous observation of this non-Abelian exchange statistics would leave no room for alternative interpretations besides the existence of MBS's. However, such an observation requires exchange of several (at least 4) MBS's followed by a measurement detecting changes in fermionic occupation of the individual pairs. Performing such an experiment is the first grand goal of the newly emerging research field of topological superconductivity.

A crucial first step in reaching this final goal is to gather evidence of the existence of a localized MBS after assembling the right material combination into a

device which potentially hosts MBS's. Due to the fact that MBS's possess no charge and no effective spin, detection of a MBS is challenging. Nevertheless, a few methods are proposed to observe MBS's in various systems. Here we discuss the two most relevant ones to our experiments: the detection of a MBS caused zero bias conductance peak (ZBP) in a tunneling spectroscopy experiment, and the observation of the 4π-Josephson effect in a Josephson junction containing MBS's. Although not revealing any of the non-Abelian properties of MBS's, such an observation would be extremely important as a first clear indication of the existence of MBS's.

2.3.1 ZERO BIAS CONDUCTANCE PEAK IN TUNNELING SPECTROSCOPY

In the hybrid superconductor-semiconducting nanowire system discussed above, MBS's emerge at the ends of the nanowire. In the density of states, such MBS's appear as a single state in the middle of the superconducting gap. The presence of MBS's at the Fermi level in the middle of the superconducting gap induces so called resonant Andreev reflection: an incident electron will be Andreev reflected into a hole with unitary probability. Due to this effect a zero bias conductance peak (ZBP) with unitary height of $2e^2/h$ will appear in a tunneling spectroscopy measurement [31]. In the following we elaborate on this.

Figure 2.8a shows a schematic set-up for a two terminal device suitable to perform tunneling spectroscopy. A semiconducting nanowire is covered by a normal metal contact at one side and a superconducting contact at the other side. Not shown in the schematic but of crucial importance is that local control over μ is necessary, this could be achieved with local electrostatic gates. The density in the nanowire section uncovered by metal / superconductor may be tuned with a local gate to create a tunneling barrier or a quantum point contact. The section of the nanowire covered by the superconducting contact may be tuned into the topologically non-trivial phase with a local gate, given that all other necessary conditions are met (see previous sections 2.2.2 and 2.2.3). As a consequence a pair of MBS's will appear at the ends of the topologically non-trivial phase as indicated by colored dots in the schematic.

When an electron from the normal contact incidents onto the superconducting contact, it may either get Andreev reflected into a hole and effectively transfer a Cooper pair into the superconductor, or undergo a normal reflection and return as an electron. Such a process can be described by a scattering matrix in the following way:

$$r = \begin{bmatrix} r_{ee} & r_{he} \\ r_{eh} & r_{hh} \end{bmatrix} \tag{2.51}$$

where r_{ee} and r_{hh} are the probabilities of normal reflections of electrons and holes respectively and r_{eh} and r_{he} are the probabilities of Andreev reflection of electrons and holes respectively. The transport through the device in Figure 2.8a can be reduced to a scattering matrix problem. Based on the Landauer equation, the con-

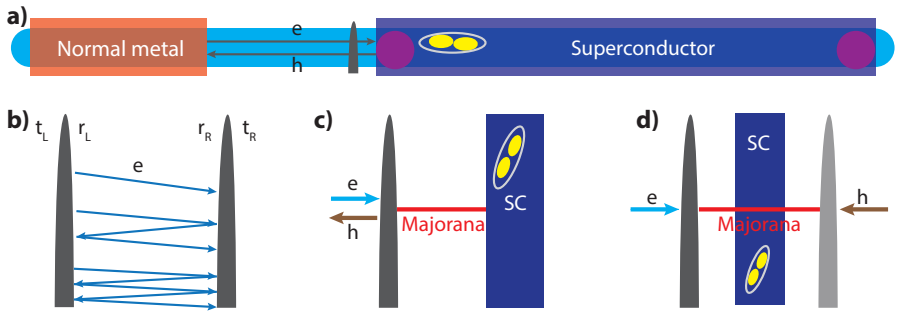

Figure 2.8 |Schematic outline of the tunneling spectroscopy set-up. a) Typical geometry of a device suitable for detecting a MBS via tunneling spectroscopy. Andreev reflection occurs at the superconductor interface where electrons (holes) are reflected back as holes (electrons). b) A double barrier junction. Electrons trapped in the double barrier may tunnel out via different trajectories as illustrated by the light blue lines. When the transmission coefficients of the left and right barriers are equal, tunneling through the junction may be resonant and have unit probability. c) Tunneling event in the presence of Majorana bound states, the normal contact acts as both the electron and hole lead with equal transmission for both tunneling events, effectively resulting in resonant tunneling. d) is the same as c) but with the hole lead mirrored to the right side to emphasize the analogy to b).

ductance caused by tunneling into the superconductor is:

$$G = \frac{2e^2}{h}\mathrm{Tr}\left(r r^\dagger\right) \tag{2.52}$$

Since the scattering matrix is unitary, we have

$$r_{ee} r_{eh}^* + r_{he} r_{hh}^* = 0 \tag{2.53}$$

At the Fermi level, particle-hole symmetry requires $\sigma_x r^* \sigma_x = r$, which implies:

$$\begin{aligned} r_{ee} &= r_{hh}^* & r_{hh} &= r_{ee}^* \\ r_{he} &= r_{eh}^* & r_{eh} &= r_{he}^* \end{aligned} \tag{2.54}$$

Combining particle-hole symmetry and unitarity it follows that

$$r_{ee} r_{he} = r_{hh} r_{eh} = 0 \tag{2.55}$$

This indicates that at the Fermi level Andreev reflection is either perfect with $r_{he} = 1$ or vanishing with $r_{he} = 0$.

As for the case of a topologically non-trivial superconductor, a MBS is present at the Fermi level in the middle of the gap and therefore the Andreev reflection is perfect with $\det(r) = -1$. Then the scattering matrix can be rewritten as:

$$r = \begin{bmatrix} 0 & e^{i\phi} \\ e^{-i\phi} & 0 \end{bmatrix} \tag{2.56}$$

with ϕ the phase an electron obtains during the reflection process. Consequently the conductance as given by (2.52) is $G = 2e^2/h$.

A more intuitive understanding may be obtained by comparing the system to a double tunneling barrier junction (see Figure 2.8b). The transmission amplitudes of the two barriers are t_L, t_L' and t_R, t_R' and the reflection amplitudes are r_L, r_L' and r_R, r_R' for left and right barriers. When an electron enters the double junction via tunneling through the left barrier, the probability amplitude of the electron tunneling out via the right barrier after n times reflecting back from thee right barrier is given by (including the initial tunneling throught the left barrier):

$$A_n = t_L t_R \left(r_L' r_R\right)^{n-1} e^{i(2n-1)\phi} \qquad t = \sum_{n=1}^{\infty} A_n = \frac{t_L t_R e^{i\phi}}{1 - r_L' r_R e^{2i\phi}} \tag{2.57}$$

With ϕ the phase obtained while travelling once the distance between the two barriers. The total probability amplitude for crossing the double barrier is now a summation over all A_n as is shown on the right. The resulting transmission coefficient of the double junction given by:

$$T = |t|^2 = \frac{T_L^2 T_R^2}{1 + R_L R_R - 2\sqrt{R_L R_R}\cos(2\phi)} \qquad T_{max} = \frac{4T_L^2 T_R^2}{\left(1 - \sqrt{R_L R_R}\right)^2} \tag{2.58}$$

with $T_{L,R} = |t_{L,R}|^2$ and $R_{L,R} = 1 - T_{L,R}$. T_{max} corresponds to $\phi = 0$, this expression implies that when the two tunnel barriers have the same transmission coefficients, i.e. $T_L = T_R$, the total transmission $T = 1$ and the tunneling is resonant, resulting in a conductance peak with unitary conductance [8].

Resonant tunneling via a double barrier may serve as an analogy to perfect Andreev reflection via a MBS. In the latter case, an incident electron from the normal lead is reflected back as a hole at the interface of the superconducting contact (Figure 2.8a),c)). In this case the normal contact is used as both the electron lead and the hole lead. This can be considered effectively as two tunnel barriers (Figure 2.8d) for two subsequent tunneling events. The MBS equally couples to 'both' leads, hence resonant tunneling is the result. Because of Andreev reflection, every tunneling process transports a Cooper pair into the superconducting lead which gives the unitary conductance of $2e^2/h$.

It is important to realize that the ZBP resulting from a MBS is expected to be always present once the system is in the topologically non-trivial state. Phrased differently, since the MBS does not disperse in B or μ within the topologically non-trivial phase, also the ZBP is expected to last in the B and μ ranges within the non-trivial phase. Coupled MBS's, however, (see section 2.2.4) are expected to result in a splitting of the ZBP due to the energy splittig of the MBS's.

Using tunneling spectroscopy as a method to probe MBS's may be the simplest available approach. The ZBP induced by MBS's may be obscured, however, by resonances in the normal lead, or other subgap states in the superconducting gap.

Wimmer et. al. [32] show that extending the device transmission from the tunneling limit to the transparant limit still results in an unique signal caused by the presence of a MBS. A schematic of the setup considered is shown in the inset of Figure 2.9. A quantum point contact (QPC) is attached to two leads, of which one may be a (non-trivial) superconductor. This is fully equivalent to the set-up of Figure 2.8a, except that the tunnel barrier of that set-up is replaced here with a QPC. Tuning the electrostatic potential profile inside the nanowire with local gates should in principle allow for in situ creation of either a tunnel barrier or a QPC.

In the presence of a finite B field, if the superconductor would be absent, due to spin splitting the QPC conductance would be quantized in units of e^2/h (black dotted line in Figure 2.9, note that the depicted case relies on the naive assumption of spin splitting equal to nanowire subband spacing for all subbands).

This changes considerably if the superconductor is present. Due to Andreev reflection, the conductance of each transport mode is doubled. Furthermore, particle-hole symmetry requires each transport mode to be twofold degenerate,

[8] Note that (2.58) is derived for $B = 0$ T, whereas tunneling via a MBS happens at $B \neq 0$ T.

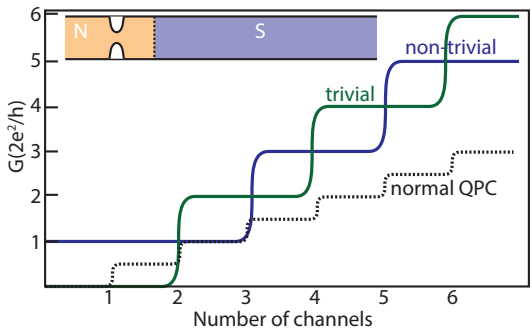

Figure 2.9 |Quantum point contact (QPC) as a probe of a topological superconductor. The schematic set-up is shown in the inset, a normal lead containing a QPC is attached to a superconductor which may (not) be topologically non-trivial. This is equivalent to a simple model of a superconducting 1D nanowire with spin orbit interaction. The curves show the idealized QPC conductance at zero bias. The black dotted curve corresponds to a QPC connected to two normal metallic leads at finite B, resulting in spin splitting of the QPC plateaus and conductance is quantized in unites of e^2/h. When one of the normal leads is replaced with a superconducting lead, the conductance increases in steps of $4e^2/h$ (also at finite B). In the topologically trivial case (green curve) the first plateau is at $4e^2/h$ and subsequent plateaus are at integer multiples of $4e^2/h$. For the topologically non-trivial case (blue curve), due to the presence of a Majorana bound state in the middle of the superconducting gap, the first plateau is quantized at $2e^2/h$ and the other plateaus are quantized at half-integer multiples of $4e^2/h$. Importantly, the first plateau at $2e^2/h$ in the topologically non-trivial case is robust against disorder and is expected to be present even when the higher QPC plateaus are no longer visible. This schematic figure is based on the work of Wimmer et al. [32].

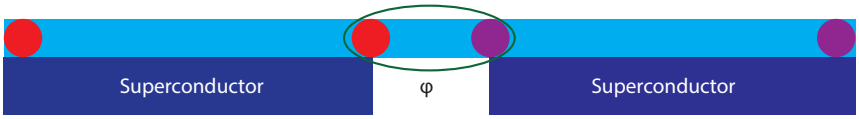

Figure 2.10 |Schematic of a Josephson junction build from two topologically non-trivial superconductors. The two pairs of Majorana fermions are indicated by colored circles. Coupling of the two Majoranas from different pairs close to the junction will give rise to a 4π periodicity of the Josephson current phase relation.

even if time-reversal symmetry is broken in the presence of a B-field. This results in quantization of the QPC conductance in units of $4e^2/h$. Wimmer et al. show that depending on the topology of the superconducting nanowire, the QPC conductance is given by

$$G = \frac{4e^2}{h} \times \begin{cases} n & \text{trivial} \\ n+\frac{1}{2} & \text{non-trivial} \end{cases} \tag{2.59}$$

with $n = 0, 1, 2, \cdots$. In the topologically trivial case without a MBS at the edge of the superconductor, the conductance through the QPC is quantized in units of $n \cdot 4e^2/h$ (green curve in Figure 2.9). Contrarily, in the topologically non-trivial case with a MBS present at the edge of the superconductor, the first plateau is quantized at $2e^2/h$ and the other plateaus are quantized at $n \cdot 4e^2/h + 2e^2/h$.

The QPC probing scheme is a direct generalization of the earlier discussed tunneling spectroscopy of a MBS. In the tunneling regime a narrow peak quantized at $2e^2/h$ is predicted, which broadens into the first QPC plateau at $2e^2/h$ upon increasing the QPC transmission. The specific prediction from Wimmer et al. is that this quantized plateau at $2e^2/h$ reflects the topologically different state of the superconductor and therefore its sensitivity to disorder is much less compared to normal QPC plateaus. Whereas other QPC plateaus are very sensitive to disorder, the topological plateau is expected to last. Observation of such a robust conductance plateau in a parameter range corresponding to the topologically non-trivial phase would be a direct indication of the topological nature of the corresponding zero bias conductance peak in the tunneling limit.

We comment in chapter 6 more extensively on realistic scenarios related to the tunneling spectroscopy and QPC measurements discussed here. Details of tunneling spectroscopy as an experimental method in the context of the nanowire devices proposed here are given in chapter 3.

2.3.2 4π JOSEPHSON EFFECT

Topologically non-trivial superconductors affect the Josephson effect in an unique way which results in a modification of the Josephson current-phase relationship (CPR). This may provide another unique signature of MBS's in the system. A schematic of a Josephson junction made of two topologically non-trivial supercon-

ductors is shown in Figure 2.10. Two pairs of MBS's are present in the system as indicated by the colored dots. The inner two MBS's from the different pairs couple to each other if the distance between the two and the junction transmission are finite. These coupled inner MBS's give a phase dependent contribution to the energy which is given by [18]

$$E_\phi = \sqrt{T}\Delta\cos\left(\phi/2\right) \tag{2.60}$$

with T the transmission of the junction, Δ the superconducting gap and ϕ the gauge invariant phase difference between the two superconducting leads. This ϕ dependent energy spectrum is shown in Figure 2.11a, the MBS's form a single pair of Andreev bound states (ABS's). The associated supercurrent is given by

$$I\left(\phi\right) = -\frac{2e}{\hbar}\frac{\partial E\left(\phi\right)}{\partial\phi} = I_c\sin\left(\phi/2\right) \tag{2.61}$$

where $I_c = e\sqrt{T}\Delta/\hbar$. The supercurrent therefore is 4π periodic in the phase difference between the two superconducting leads and proportional to $\sqrt{T}$.

This is in strong contrast to Josephson junctions built from topologically trivial superconductors. In such 'conventional' Josephson junctions, the CPR may contain harmonic terms depending on integer multiples of ϕ only (see also chapter 4), i.e. on $\sim\sin\left(n\phi\right)$, n integer. However, no term proportional to $\sim\sin\left(\phi/2\right)$ is expected. The presence of a $\sim\sin\left(\phi/2\right)$ term in the CPR makes the CPR as a whole 4π-periodic as opposed to the 2π-periodicity of a conventional Josephson junction.

The physics behind the 4π-periodic Josephson effect can be understood by considering the single fermionic degree of freedom of a pair of MBS's. This fermionic mode may or may not be occupied, corresponding to the two different fermionic parity states of even and odd parity. The pair of ABS's formed by the inner MBS's corresponds to two levels with opposite fermionic parity. This in contrast to a conventional Josephson junction where the ABS's correspond to even parity. The consequence of this is shown in Figure 2.11. In both cases, the ABS dispersion in ϕ may have a sinusoidal form crossing zero energy when $\phi = \pi$. In the trivial case (Figure 2.11b), at the degeneracy point the states are indistinguishable and therefore the system may minimize its energy by staying in the lowest energy branch. This immediately results in a 2π periodicity of the ABS dispersion. In the topologically non-trivial case, however, (Figure 2.11a), at the degeneracy point the levels are still distinguished by their different parity. Since parity is a conserved quantity, it is not possible to relax to the lowest energy state after crossing zero energy, thus the spectrum is 4π periodic in ϕ.

The 4π-effect is more fragile and therefore harder to observe compared to tunneling spectroscopy signatures of MBS's. Firstly, in the topologically trivial case, an anti-crossing will typically open up in the spectrum. In the non-trivial case this is not possible, since the crossing of the two different parity branches is protected by parity conservation. This assumes that the MBS's left and right of the junction are

truly at zero energy. Any finite coupling to the outer MBS's will result in a gap opening up in the non-trivial case as well, but this gap will be exponentially small in the separation distance within each MBS pair. As discussed before (section 2.2.4), in principal the coupling of MBS's at a finite distance may be engineered to a negligible level, and this effect is therefore not expected to be detrimental in obtaining the 4π Josephson effect.

Secondly, a much more detrimental effect is random quasi-particle tunneling into the junction. If this happens, the system flips from one parity state to the other, which resets the periodicity back to 2π (indicated Figure 2.11a). To avoid this, the CPR has to be measured faster than the quasi-particle tunneling rate into the junction.

Thirdly, another complication is the presence of other ABS's in the junction. Only in the ideal case of a very short junction (junction length $L << \xi$ the effective coherence length), a single pair of ABS's is present. Even in that case, the energy maxima of the ABS's will be points close to the gap edge, and thereby close to a continuum of states. The problematic aspect is that escape from the topologically non-trivial ABS into another nearby level again restores the 2π periodicity. Landau-Zener tunneling across small gaps between trivial and non-trivial ABS's may provide a possible mechanism [33].

Finally, provided these previous two problems can be avoided, it may still be that the 4π component is only a fraction of the total supercurrent. Sensitive detection techniques potentially capable of measuring a small 4π spectral contribution to the total CPR signal are therefore required.

The 4π effect is a direct consequence of the degeneracy of different parity states of a pair of MBS's, which in turn provides the necessary ground state degeneracy resulting in non-Abelian exchange statistics of MBS's. Measuring the 4π Josephson effect would constitute an independent alternative signature of MBS's directly probing an intrinsic, defining property of these quasi-particles, namely their correspondence to a single fermionic degree of freedom.

2.4 ESTIMATES OF PARAMETERS IN REALISTIC DEVICE GEOMETRIES

We conclude this theoretical introduction to Majorana fermions, non-Abelian statistics and Majorana bound states in one-dimensional semiconducting wires with a brief survey of the available candidates for nanowires and superconductors. Based on the single subband model introduced before, estimates for some properties of the topological non-trivial phase are given.

Before going into material details, it should be remarked that the whole previous discussion assumed an effective temperature T which is much smaller than the energy gap in the topologically non-trivial state. Such a gap is likely to be in the $10^{-6} - 10^{-5}$ eV range, as argued below. Since $k_B T = 86\ \mu$eV/K, with k_B Boltzmann's constant, typical temperatures required are below 100 mK.

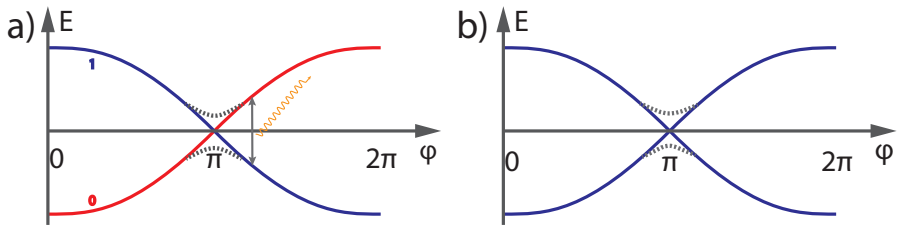

Figure 2.11 |Energy spectrum of a pair of Andreev bound states with and without Majorana bound states. a) The phase dependent energy spectrum of the pair of Andreev bound states arising from two MBS's coupled across a Josephson junction. The blue and red lines indicate the two different parity states of the Andreev level. At $\phi = \pi$ the two levels cross, but due to parity conservation the initial Andreev level will stay occupied instead of relaxing to the Andreev level with opposite parity at lower energy. This directly results in 4π periodicity in ϕ of these particular levels and since this is the only level with this property, the CPR as a whole will be 4π periodic. b) In a conventional Josephson junction, the two Andreev levels also cross at $\phi = \pi$. Since the two levels have the same parity, the system will remain in the lowest energy state, i.e. stay in the lower branch. This results a 2π periodicity in ϕ, and of the CPR as a whole, since all ABS share this 2ϕ periodicity. Importantly, in the case of a), if the parity of the junction is flipped (yellow zigzagged line), the Andreev level will jump to the ground state, restoring the 2π periodicity. Furthermore, in a realistic system, an energy gap exponentially small in each separation distance of the MBS pairs left and right of the junction will be present.

A further relevant consideration is the role of disorder. Effects such as random electrical potential fluctuations lead to a spatially varying topological gap size. As with temperature, the energy scale related to this should be small compared to the energy gap in the topologically non-trivial phase. In practice this implies that the host semiconducting material has to be clean, e.g. its mobility needs to be high. Establishing a more quantitative requirement is difficult, however, due to the complex interplay between device geometry and the different materials involved.

Next we turn to possible material systems. Two viable material candidates for semiconducting nanowires are InAs and InSb. Both materials have a small bandgap, small effective mass, large Landé g-factor and strong spin-orbit interaction. Besides, growing nanowires from these material is relatively well established such that defect free nanowires with diameters $50-100$ nm and lengths of several microns are possible. Due to the strong confinement in nanowires, accurate estimates of the Landé g-factor and Rashba spin-orbit interaction are hard to make and depend on the exact details of the confinement in the nano-structure. Different values for Rashba spin-orbit interaction and Landé g-factor are considered in the following.

Regarding s-wave superconductors several materials are available. The most applied material in nano/micro fabrication is Al. Other often used material are Nb, alloys of Nb and Ti and their nitrides. The advantage of the latter is their compatibility with large magnetic fields. Superconducting gap values representative for these materials are considered.

Table 2.1 gives an overview for relevant parameter ranges of the critical magnetic fields of the topologically non-trivial phase. A g-factor of 10 is typical for InAs, a g-factor of 55 is typical for InSb. A value of $E_{\mathrm{SO}} = 50$ μeV has been observed in quantum dots in InAs and InSb nanowires [34] and serves as a lower limit (since quantum dot confinement is expected to result in smaller E_{SO}). $E_{\mathrm{SO}} = 1$ meV is at the high end of what is realistically possible. The bulk gaps of Al and Nb are 0.19 meV and 1.3 meV respectively. Depending on the details of the proximity effect, any gap size up to the bulk value of the material may be present, hence the variation of Δ in the table. Finally, in the table we have assumed that the superconducting gap in the bulk material is independent of B. This is a rather naive assumption, especially in the case of Al, where the critical B field of the material may be between some tens and ~ 100 mT. Bulk Al seems therefore an unsuitable material, since at best it will result in a very short lived non-trivial phase that only occurs near the critical B field of Al. For an in plane B field and a very thin Al film, however, the critical B field of the film can be as high as 1 T. Nb and related alloys are known to withstand an external B field well in the bulk state and seem particularly suitable choices for the superconducting material.

The table has a clear message: nanowires made of InAs or InSb are very suitable material candidates to realize the topologically non-trivial phase. In particular InSb is very attractive, since its large effective g-factor results in a relatively low onset B field of the non-trivial phase; for any realistic superconducting gap size this is

$\Delta = 0.1$ meV

E_{SO} (meV)	g	B_{c1} (T)	B_{c2} (T)
0.05	10	0.34	2.4
	25	0.14	0.96
	55	**0.06**	**0.43**
0.2	10	0.34	9.6
	25	0.14	3.8
	55	**0.06**	**1.7**
0.5	10	0.34	>10
	25	0.14	9.6
	55	**0.06**	**4.3**
1.0	10	0.34	>10
	25	0.14	>10
	55	**0.06**	**8.7**

$\Delta = 0.2$ meV

E_{SO} (meV)	g	B_{c1} (T)	B_{c2} (T)
0.05	10	0.69	>10
	25	0.28	4.3
	55	**0.13**	**1.9**
0.2	10	0.69	>10
	25	0.28	>10
	55	**0.13**	**7.8**
0.5	10	0.69	
	25	0.28	>10
	55	**0.13**	
1.0	10	0.69	
	25	0.28	>10
	55	**0.13**	

$\Delta = 0.5$ meV

E_{SO} (meV)	g	B_{c1} (T)	B_{c2} (T)
0.05	10	1.7	
	25	0.69	>10
	55	**0.31**	
0.2	10	1.7	
	25	0.69	>10
	55	**0.31**	
0.5	10	1.7	
	25	0.69	>10
	55	**0.31**	
1.0	10	1.7	
	25	0.69	>10
	55	**0.31**	

$\Delta = 1.0$ meV

E_{SO} (meV)	g	B_{c1} (T)	B_{c2} (T)
0.05	10	3.4	
	25	1.4	>10
	55	**0.63**	
0.2	10	3.4	
	25	1.4	>10
	55	**0.63**	
0.5	10	3.4	
	25	1.4	>10
	55	**0.63**	
1.0	10	3.4	
	25	1.4	>10
	55	**0.63**	

Table 2.1 |Overview of system parameters and corresponding critical magnetic fields of the topologically non-trivial phase. B_{c1} corresponds to the magnetic field at which $E_Z = \Delta$, the minimal onset field of the non-trivial phase (corresponding to $\mu = 0$). B_{c2} corresponds to the magnetic field value at which the energy gap at finite k as given by equation (2.46) equals 50 μeV. B_{c2} is therefore an indication of the upper critical field of the non-trivial phase (at $\mu = 0$). In this table, the superconducting gap Δ is assumed to be constant in B, which is not the case in reality, the B_{c2} should therefore be taken as a rough indication. The relevant case for InSb nanowires, as used in the experiments throughout this thesis, is that of g-factor = 55, which is indicated in bold in the table.

expected to be in the range of 0.05 – 0.5 T. This puts less stringent conditions on the superconductor used. Even for the large InSb g-factor an $E_{SO} = 50$ μeV is already strong enough to result in a non-trivial phase lasting for a few hundreds of mT's in magnetic field, a range very well detectable in experiment. InAs is less favorable, since in combination with a larger Δ (which is highly desirable for long term purposes), the onset field easily becomes on the order of 1 T. Nevertheless, also for InAs, non-trivial phases that may be detected in experiment seem within reach.

REFERENCES

[1] P. A. Dirac, "The quantum theory of the electron," in *Proceedings of the Royal Society of London A: Mathematical, Physical and Engineering Sciences*, vol. 117, pp. 610–624, The Royal Society, 1928.

[2] C. D. Anderson, "The positive electron," *Physical Review*, vol. 43, no. 6, p. 491, 1933.

[3] E. Majorana, "Teoria simmetrica dell'elettrone e del positrone," *Engl. transl [translation from Nuovo Cimento 14, 171 (1937)]F*, vol. 63, p. 149, 1981.

[4] F. Wilczek, "Majorana returns," *Nature Physics*, vol. 5, no. 9, pp. 614–618, 2009.

[5] M. Franz, "Viewpoint: Race for majorana fermions," *Physics*, vol. 3, p. 24, 2010.

[6] F. Wilczek, "Majorana and condensed matter physics," *arXiv preprint arXiv:1404.0637*, 2014.

[7] A. Stern, "Anyons and the quantum hall effect—a pedagogical review," *Annals of Physics*, vol. 323, no. 1, pp. 204–249, 2008.

[8] M. Tinkham, *Introduction to superconductivity*. Courier Corporation, 2012.

[9] P. De Gennes, *Superconductivity of Metals and Alloys (Advanced Book Classics)*. Addison-Wesley Publ. Company Inc, 1999.

[10] M. Sigrist and K. Ueda, "Phenomenological theory of unconventional superconductivity," *Reviews of Modern physics*, vol. 63, no. 2, p. 239, 1991.

[11] L. N. Cooper, "Bound electron pairs in a degenerate fermi gas," *Physical Review*, vol. 104, no. 4, p. 1189, 1956.

[12] N. Bogoliubov, "Nuovo cim. 7 (1958) 794; jg valatin," *Nuovo Cim*, vol. 7, no. 813, p. 1000, 1958.

[13] J. Valatin, "Comments on the theory of superconductivity," *Il Nuovo Cimento*, vol. 7, no. 6, pp. 843–857, 1958.

[14] G. Koster, L. Klein, W. Siemons, G. Rijnders, J. S. Dodge, C.-B. Eom, D. H. A. Blank, and M. R. Beasley, "Structure, physical properties, and applications of srruo$_3$ thin films," *Rev. Mod. Phys.*, vol. 84, pp. 253–298, Mar 2012.

[15] N. Read and D. Green, "Paired states of fermions in two dimensions with breaking of parity and time-reversal symmetries and the fractional quantum hall effect," *Physical Review B*, vol. 61, no. 15, p. 10267, 2000.

[16] L. Fu and C. L. Kane, "Superconducting proximity effect and majorana fermions at the surface of a topological insulator," *Physical review letters*, vol. 100, no. 9, p. 096407, 2008.

[17] D. A. Ivanov, "Non-abelian statistics of half-quantum vortices in p-wave superconductors," *Physical review letters*, vol. 86, no. 2, p. 268, 2001.

[18] A. Y. Kitaev, "Unpaired majorana fermions in quantum wires," *Physics-Uspekhi*, vol. 44, no. 10S, p. 131, 2001.

[19] J. D. Sau, S. Tewari, R. M. Lutchyn, T. D. Stanescu, and S. D. Sarma, "Non-abelian quantum order in spin-orbit-coupled semiconductors: Search for topological majorana particles in solid-state systems," *Physical Review B*, vol. 82, no. 21, p. 214509, 2010.

[20] R. M. Lutchyn, J. D. Sau, and S. D. Sarma, "Majorana fermions and a topological phase transition in semiconductor-superconductor heterostructures," *Physical review letters*, vol. 105, no. 7, p. 077001, 2010.

[21] Y. Oreg, G. Refael, and F. von Oppen, "Helical liquids and majorana bound states in quantum wires," *Physical review letters*, vol. 105, no. 17, p. 177002, 2010.

[22] A. Stern, "Non-abelian states of matter," *Nature*, vol. 464, no. 7286, pp. 187–193, 2010.

[23] N. Read and G. Moore, "Fractional quantum hall effect and nonabelian statistics," *Progress of Theoretical Physics Supplement*, vol. 107, pp. 157–166, 1992.

[24] M. Leijnse and K. Flensberg, "Introduction to topological superconductivity and majorana fermions," *Semiconductor Science and Technology*, vol. 27, no. 12, p. 124003, 2012.

[25] L. H. Kauffman and S. J. Lomonaco Jr, "Braiding operators are universal quantum gates," *New Journal of Physics*, vol. 6, no. 1, p. 134, 2004.

[26] R. Winkler, S. Papadakis, E. De Poortere, and M. Shayegan, *Spin-Orbit Coupling in Two-Dimensional Electron and Hole Systems*, vol. 41. Springer, 2003.

[27] J. Alicea, "Majorana fermions in a tunable semiconductor device," *Physical Review B*, vol. 81, no. 12, p. 125318, 2010.

[28] J. Osca, D. Ruiz, and L. Serra, "Effects of tilting the magnetic field in one-dimensional majorana nanowires," *Physical Review B*, vol. 89, no. 24, p. 245405, 2014.

[29] S. Rex and A. Sudbø, "Tilting of the magnetic field in majorana nanowires: critical angle and zero-energy differential conductance," *Physical Review B*, vol. 90, no. 11, p. 115429, 2014.

[30] S. D. Sarma, J. D. Sau, and T. D. Stanescu, "Splitting of the zero-bias conductance peak as smoking gun evidence for the existence of the majorana mode in a superconductor-semiconductor nanowire," *Physical Review B*, vol. 86, no. 22, p. 220506, 2012.

[31] J. Liu, A. C. Potter, K. Law, and P. A. Lee, "Zero-bias peaks in the tunneling conductance of spin-orbit-coupled superconducting wires with and without majorana end-states," *Physical review letters*, vol. 109, no. 26, p. 267002, 2012.

[32] M. Wimmer, A. Akhmerov, J. Dahlhaus, and C. Beenakker, "Quantum point contact as a probe of a topological superconductor," *New Journal of Physics*, vol. 13, no. 5, p. 053016, 2011.

[33] C. Wittig, "The landau-zener formula," *The Journal of Physical Chemistry B*, vol. 109, no. 17, pp. 8428–8430, 2005.

[34] S. Nadj-Perge, V. Pribiag, J. Van den Berg, K. Zuo, S. Plissard, E. Bakkers, S. Frolov, and L. Kouwenhoven, "Spectroscopy of spin-orbit quantum bits in indium antimonide nanowires," *Physical review letters*, vol. 108, no. 16, p. 166801, 2012.

3

EXPERIMENTAL METHODS

The device fabrication and measurement techniques enabling the experiments in this thesis are discussed. The fabrication steps for making the devices used are introduced in section 3.1, the typical measurement setup in which experiments are carried out is described in section 3.2 and the different types of measurement configurations employed are explained in section 3.3.

[1] Both Vincent Mourik and Kun Zuo actively contributed to the underlying scientific discussion, both Vincent Mourik and Kun Zuo took equal shares in writing a first draft, and the final version is the result of joined writing by both Vincent Mourik and Kun Zuo.

3.1 DEVICE FABRICATION

To engineer and detect Majorana fermions in a hybrid superconducting semiconducting nanowire system, two very similar types of devices are fabricated. These are two terminal devices with one normal and one superconducting contact to the nanowire, and three terminal devices with two normal contacts to the nanowire and one superconducting contact in between. After combining with a set of local, individually addressable gates, the full device is obtained in which local control over the chemical potential is possible.

Each step in fabricating these devices is based on electron beam lithography as depicted in Figure 3.1. A substrate is first coated with a thin layer of electron sensitive polymers (resist) which is mostly poly(methylmethacrylate) (PMMA) in our fabrication scheme. Exposure to electrons changes the molecular bonds of the polymers, thereby changing the solubility in a solvent made of methyl isobutyl ketone (MIBK) and isopropanol (IPA). The exposed area (for positive resist, as used in our fabrication scheme) will be removed during development in the MIBK/IPA solution, this results in the so called resist mask. Materials may then be deposited on top of the mask, covering both resist and substrate where resit was removed during development. Deposited materials can be metals or dielectrics. Various thin film deposition techniques are employed during fabrication. In a final lift-off stage, the remaining resist and material on top is removed, by placing the sample in a strong resist solvent, typically acetone.

Most of the processing is based on lift-off processes. In a few occasions chemical wet etching of the underlying substrate through the windows in the PMMA mask has been employed.

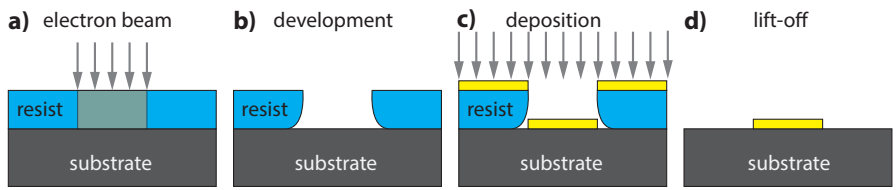

Figure 3.1 |A typical electron beam lithography process using positive resist. a) The substrate is coated with a thin layer of electron sensitive resist. A pattern is written in the resist using a focused electron beam. b) Development of the patterned resist. Areas exposed to the electron beam are dissolved. Due to back scattering of electrons undercuts are commonly obtained in this step. c) Deposition of materials, typically via thermal evaporation or sputtering. d) Lift-off removes the resist mask and materials on top.

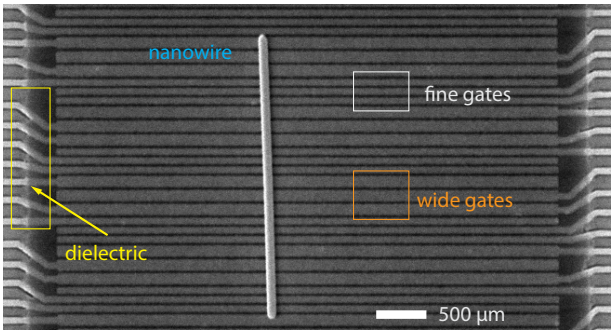

Figure 3.2 |Bottom gates are fabricated for the purpose of locally controlling the chemical potential in the nanowire. An alternating pattern of three narrow and three wide gates is designed. Throughout the thesis, a width of 50 nm is used for the narrow gates, these gates are used to induce the local tunnel barrier necessary in tunneling spectroscopy measurement. The width of the wide gates varies between 150 and 300 nm between different devices. All gates have a spacing of 50 nm to each other and are made of 5/10 nm of thermally evaporated Ti/Au in a lift off process. A 25 nm thick layer of dielectric (HfO_2) is deposited on top of the gates to electrically separate them from the nanowire. A window is etched in the dielectric layer at the edge of the metallic gates (indicated in yellow), enabling individual contacting of the gates. After placing the nanowire on top of the bottom gates, SEM imaging combined with the gate array as alignment grid enables contact deposition with a precision of ~25 nm.

3.1.1 FABRICATION OF LOCAL GATES

Devices used in this thesis are all fabricated on a p-doped Si substrate with 285 nm SiO_x on top. The doped Si substrate can serve as a global backgate to tune the chemical potential in the nanowire. An advantage of a global backgate is its straightforward implementation, however as its name suggests it cannot be used to obtain local control over the chemical potential in the nanowire. To locally control the chemical potential, arrays of small, individually addressable gates are fabricated on top of the silicon oxide, which act as bottom gates to the nanowire on top. Figure 3.2 shows a typical local gate array used in this thesis. It consists of an alternating pattern of three narrow gates and three wider gates. The narrow gates are designed to create a sharp tunnel barrier to perform tunneling spectroscopy measurements, while the wide gates are used to uniformly control the chemical potential underneath the superconducting contacts.

A thin layer of dielectric is deposited on top of the metallic gates to separate them electrically from the nanowire. In order to deliver high enough electric field for control over the chemical potential in the nanowire, high quality dielectrics with high dielectric constant k are required. This is especially relevant to the gates un-

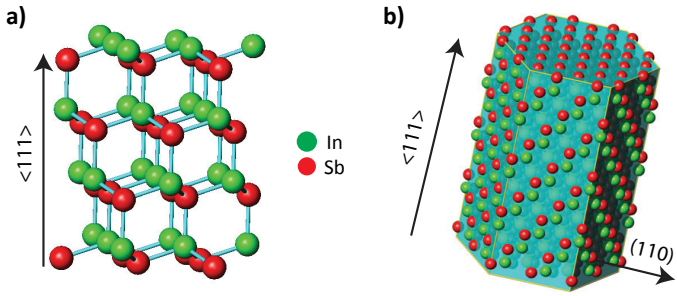

Figure 3.3 |Crystal structure of zinc-blende InSb nanowires. a) Detail of the crystal lattice, the <111> direction is indicated. Bulk inversion asymmetry is absent in this direction. b) Schematic depiction of a nanowire grown in the <111>B Sb-terminated direction. The 6 (110) facets are non-polar due to equal amounts of In and Sb atoms on the surface. Figures adapted from [1].

derneath the superconducting contact since this contact will screen the electric field heavily. In part of the experiments the bottom gates are made in two steps. Here first the wide gates are deposited and covered by ~30 nm of sputtered Si_3N_4, next the fine gates are deposited on top of this first layer of dielectric and again a layer of ~30 nm of sputtered Si_3N_4 is deposited, with a dielectric constant $k = 8$. This method is used in chapters 4 and 5. Alternatively, the gates are deposited in a single step and covered by a single layer of 25 nm HfO_2 deposited via atomic layer deposition (ALD) with a measured dielectric constant $k = 20$ (chapters 7, 8, 9).

3.1.2 INSB NANOWIRE GROWTH AND PROPERTIES

The InSb nanowires used throughout this thesis are grown on an InP substrate from gold catalyst particles, using metal-organic vapor phase epitaxy (MOVPE) via the vapor-liquid-solid (VLS) mechanism. Nanowire growth is performed by S.R Plissard and D. Car in the research group of E.P.A.M. Bakkers at Eindhoven University of Technology. Because the organic precursor (tri-methyl antimony, TMSb) preferentially cracks at the Au catalyst droplet, the crystal growth mainly happens in close vicinity to catalyst particle, thus preventing from relatively fast side growth and corresponding tapering as is typical for similarly grown InAs nanowires. The diameter is mostly determined by the size of the gold catalyst particle and is typically 80-100 nm. Due to the high lattice mismatch between InP and InSb, it is not possible to grow InSb nanowires directly on the InP substrate, but an InP stem needs to be grown to help uniform nucleation of the InSb nanowires. At InSb growth conditions, this stem slowly evaporates, limiting the maximum length of the InSb nanowires to typical 1-4 μm. For an extensive discussion of the nanowire growth, see [2, 3].

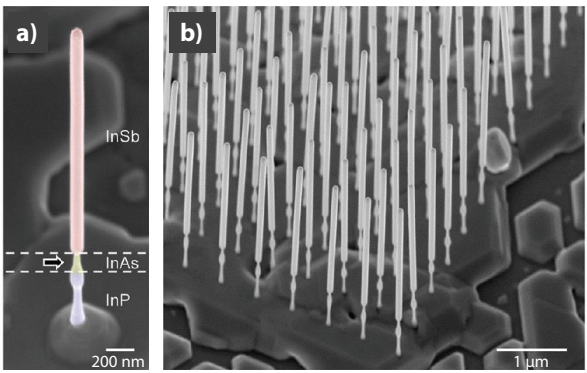

Figure 3.4 |SEM image of a typical InSb nanowire growth chip. a) shows a zoom in on a single nanwire. Important for deterministic nanowire deposition is that the thin growth stem is the point at which the nanowire preferable breaks off the substrate. b) shows an overview of a dense array of nanowires, the longest wires out of such a dense array can be selected to pick up and deposited on the target chip. Figures adapted from [2].

This way, pure, defect free InSb nanowires of zinc-blende crystal structure are grown. The zinc-blende lattice structure consists of two face-centered cubic lattices (one for each element) shifted by $a/4$ (a being the lattice constant) along the body diagonal of the cube. The nanowires grow in the <111>B Sb-terminated direction. In this direction, no bulk inversion asymmetry is present (see Figure 3.3a), and hence Dresselhaus spin-orbit interaction is absent in the nanowires used in this thesis. The nanowires have a hexagonal cross section, and the side facets are the 6 different (110) facets, which contain an equal amount of In and Sb, making the surface non-polar (see Figure 3.3b).

Upon taking the nanowires out of the growth reactor, quickly an oxide layer forms on the (110) side facets. This natural oxidation process, studied in [4], forms at room temperature a ~30 Å thick layer of mixed In_2O_3 and Sb_2O_5. The oxide consists mainly of In_2O_3 and to a less degree of Sb_2O_5. From the time dependence of the natural oxidation process it is concluded that after very fast initial monolayer oxidation, further rearrangement and oxidation is governed by diffusion. The dense In_2O_3 slows this process down considerably and eventually terminates the oxidation process, typically on a timescale of seconds.

3.1.3 NANOWIRE TRANSFER FROM GROWTH CHIP TO DEVICE CHIP

Nanowires have to be transferred from the growth chip to the substrate chip. Initially, a semi-random technique was used for this. Using a little tip cut from clean-room quality tissue (to reduce spurious tissue fibers) handheld with a tweezer, first the growth chip is wiped and then the designated area of the target chip is wiped.

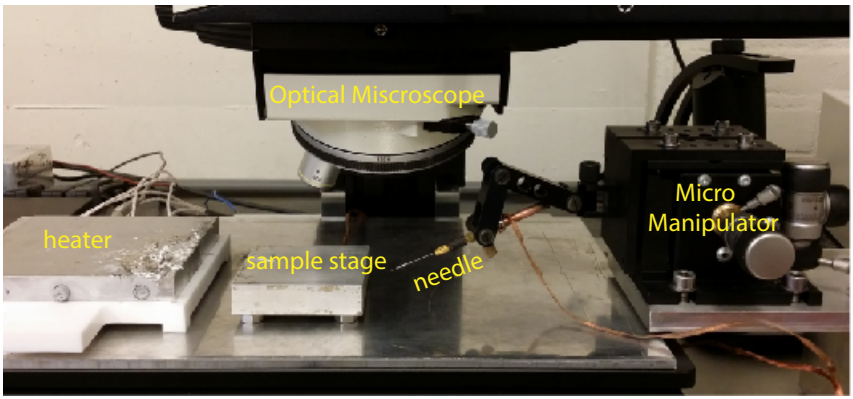

Figure 3.5 |Setup for deterministic nanowire deposition. The setup consists of an optical microscope with long focus length and 1000x magnification, a heater to melt Indium, and a micromanipulator that controls the needle attached to it.

The nanowires transferred in this way land random on the spots touched with the tissue tip. This deposition method is already more controlled to the often used technique of dissolving the nanowires in a solution and putting a drop of this solution on the target chip. Nevertheless, very large arrays of local gates with typical array dimensions of 100 x 100 μm are necessary. After nanowire deposition these have to be searched under SEM for nanowires crossing the gates at a proper angle. Furthermore, the nanowire type leading to the development of this deposition method is InAs. The density of InSb nanowires on a growth chip is much less compared to InAs resulting in a fast wearing out of a InSb nanowire growth chip using the tissue deposition method.

In consideration of all these drawbacks, a deterministic nanowire deposition method has been developed based on the method described by [5]. Using this technique, nanowires can be deposited with sub-micrometer precision. This enables using much smaller bottom gate arrays. Furthermore, a high quality growth batch can be used much more efficiently, such that it will effectively last for years. Finally, it is possible to select the longest wires which creates optimal freedom in device design.

The setup for deterministic nanowire deposition is shown in Figure 3.5, it consists of a long focus microscope, a heater and a micro manipulator. First immersing and then slowly pulling out a needle from a melted Indium droplet forms a sharp Indium tip. This tip, with a diameter of a few hundreds of nm's, is small enough to pick up an individual nanowire from the growth chip by controlling the needle movement via a micro manipulator. The picked up nanowire is then transferred to the target substrate. Due to the larger contact area the nanowire sticks stronger to the substrate than to the needle, and thus the nanowire is deposited. Importantly,

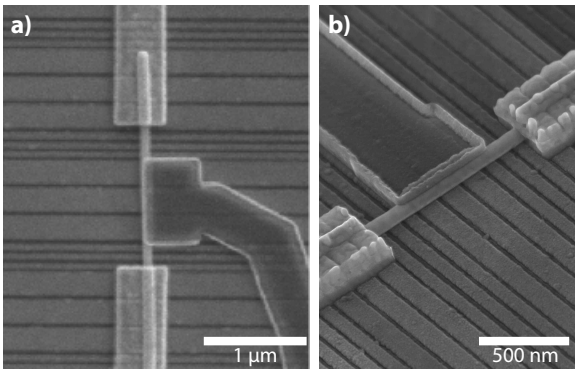

Figure 3.6 |SEM images of a typical device. a) shows a topview and b) an angular view of a typical device, the devices shown in a) and b) are not the same. In both cases, the middle superconducting contact is made of a ~100 nm thick layer of sputtered NbTiN, the contact has a length of 1 μm in a) and 0.6 μm in b). The outer two normal metallic contacts are made of a 125 nm thick layer of Au with a 10 nm thick Ti sticking layer in between substrate/nanowire and Au. The wide gates underneath the superconducting contact have a width of 150 nm, the narrow gates underneath the nanowire junction have a width of 50 nm and all gates are spaced by 40-50 nm. The dielectric in this case is HfO_2 deposited via ALD. Comparing the sputtered NbTiN contact and the thermally evaporated Au contact in b), the more isotropic deposition in the case of sputtering is revealed by the presence of standing sidewalls because of sputtering on the sides of the mask.

by gently pushing the nanowire with the indium tip, a rotational alignment within a precision of $\sim 10^\circ$ is possible. A more detailed description can be found in the original work of D. J. van Woerkom [6].

3.1.4 CONTACT DEPOSITION

Superconductivity is a prerequisite in engineering a topological phase. Experimentally superconductivity is induced in the nanowire by contacting it with a superconducting material. The strength of the superconductivity is determined by the contact quality, the better the contact the stronger the induced superconductivity. At the same time a transparent normal contact that does not introduce unwanted resonant states is crucial in probing the Majorana bound states in a tunneling spectroscopy experiment. Therefore both the normal and the superconducting contacts have to be of superb quality to enable good experiments. However, on the surface of the nanowire a few atomic layers of oxide are formed, as explained earlier. This insulating oxide layer acts as a tunnel barrier if one directly put contacts onto the nanowire. In order to achieve high quality contacts, one first has to remove the oxide layer. There are generally two methods to remove this oxide layer which we will

introduce briefly below, for more details see chapter 8.

The first type approach is an in situ etch with an Ar RF plasma. Ar ions from the plasma bombard the nanowire surface and kick out the atoms of the top layers. In this way the oxide layers are removed efficiently and the nanowire crystal is exposed. The advantage of this method is that the deposition of contacts can be done right after removal of the oxide without breaking the vacuum, thus avoiding re-oxidization. The drawback however in this cleaning procedure is that the nanowire crystal lattice is damaged and often the surface is etched non-uniformly. This is believed to be a source of disorder resulting in a large subgap density of states within the induced superconducting gap [7].

The other way of cleaning off the surface oxide is by using an ex situ chemical wet etch. An attractive approach is to use sulfur passivation [8]. This technique etches the oxide uniformly and leaves a flat surface. Moreover, since it is a selective chemical etching process, the bulk crystal lattice is left intact. These are important advantages over in situ Ar RF plasma etching. Finally, besides etching the oxide, sulfur passivation terminates the etched nanowire surface with a sulfur layer, thus preventing re-oxidization during sample transfer to the deposition chamber. An important disadvantage of this technique is that it is less reproducible compared to Ar etching. Furthermore, the effect of the thin layer of sulfur is unknown, it might act as a tunnel barrier itself, which maybe has to be removed in situ via a short plasma etch, or it may dope the nanowire surface.

A detailed discussion of the effect of contact preparation methods is given in a separated chapter (see chapter 8). The Ar RF plasma etching technique is employed in the experiments described in chapters 4, 5, 7. Sulfur passivation is used in chapter 9.

Figure 3.6 shows a finished device. For the superconducting contact, NbTiN is used as material. This superconductor has a very high critical magnetic field typically between 15 to 20 T. This is an excellent property for the research in this thesis, with the typical B field scale being $B \leq 3$ T, far below the critical field of NbTiN. The material is deposited via DC sputtering in a designated sputtering tool used for superconducting materials only. Sputtering is done from an alloyed NbTi target (70/30 atomic percentage of Nb/Ti) by using an Ar RF plasma in the presence of a small nitrogen flow. Different from thermal evaporation, where vacuum chamber background pressures are typically below 10^{-6} mbar, the typical gas pressure during the sputtering process is $\sim 10^{-2}$ mbar. At such a pressure, atoms kicked from the target by impacting Ar ions from the plasma do not move ballistically towards the sample, but undergo diffusive motion due to collisions with ions in plasma, in contrast to the ballistic movement of thermally evaporated atoms. This results in an isotropic deposition on the sample in the case of sputtering, causing film deposition on the sides of the mask. This film piece physically connects the film pieces deposited on the bare substrate and on top of the resist. As a consequence, removal of the sputtered material on top of the mask via lift off is much harder compared to thermal evaporation. A simple solution to this issue which suffices in our case is the

use of a single layer PMMA mask with a thickness of roughly two times the typical film thickness of 100 nm. This enables small enough feature size for our purposes and collapse of the sidewalls is rare. The effect of sidewall deposition is clearly visible in Figure 3.6b.

Normal contacts are deposited via thermal evaporation atop a double layer PMMA mask designed to create a large undercut easing lift off. Throughout this thesis, Au is used as normal contact material on top of a thin 10 nm thick adhesion layer of either Ti or Cr. Thermal evaporation results in anistropic material deposition, therefore lift off problems and bad contacts may arise because the different film pieces next to and on top of the nanowire are not connected. To avoid this, the film thickness should be more than the nanowire thickness to ensure full coverage of the nanowire. Here film thickness's between 120 and 150 nm are used.

3.2 MEASUREMENT SETUP

The experiments in this thesis are on gathering evidence for the existence of topologically non-trivial phases and on studying the Josephson effect, both in nanowires. These effects are very sensitive to temperature and are expected to be only fully developed at temperatures well below 1 K. For this reason it is absolutely essential to go to the lowest possible temperatures at which conventional electrical measurements are still possible and reduce the environmental noise as much as possible. A zoom in on the low temperature parts of the setup used is shown in Figure 3.7 and discussed in the following.

The first step in this approach is to cool down the sample using a ^{3}He/^{4}He dilution refrigerator. The general operation principle of the apparatus can be found in for example [9]. Here it suffices to say that a closed cycle cooling mechanism is implemented based on a thermodynamic phase transition in a mixture of diluted ^{3}He in ^{4}He. The lowest temperatures are obtained at the so called mixing chamber, this is where the sample is mounted. The lowest possible temperatures in a dilution refrigerator (not considering adiabatic demagnetization) are slightly below 10 mK. This temperature corresponds to the lattice temperature, the temperature of the phonon bath, and is referred to as the system's 'base T'.

To perform electrical measurements on a sample, wiring connecting the sample with a room temperature measurement device is necessary. Inevitably such wiring will always introduce an extra heat load onto the coldest stage of the refrigerator, leading to a higher base T. For DC wires thermally well anchored at the several different temperature stages of the refrigerator, a typical base T around ≤ 15 mK is possible. A much more important concern however is the effective temperature of the electrons. Due to the direct electrical connection to room temperature, electrical noise leads to significantly higher effective electron temperatures. Several important measures are taken to reduce this effect.

A first crucial step is the room temperature electronics. A battery powered, custom made rack containing all voltage/current sources and voltage/current amplifiers is optically decoupled from in going control signals and outgoing measured

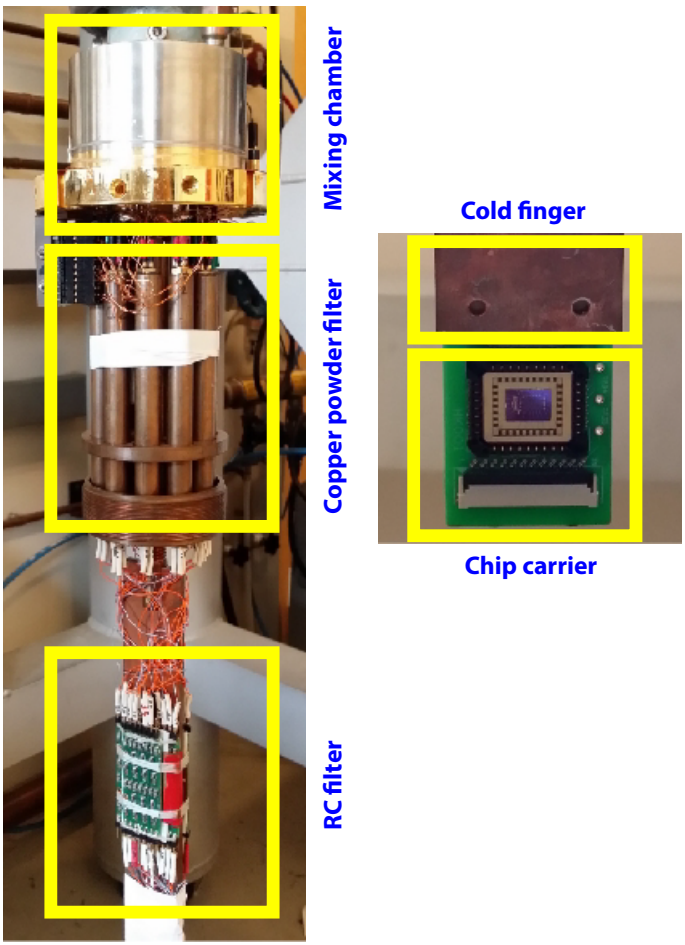

Figure 3.7 |Zoom in on the lowest temperature part of a dilution refrigerator with electrical filters installed. Filters and chip carrier on which the sample is mounted are all installed on a plate which is directly attached to the mixing chamber.

signals. This provides total galvanic isolation from the power grid, an important source of electrical interference. At this room temperature stage, each DC line passes through a π filter, providing noise filtering from about 10 MHz to 100 MHz.

To cover the low and high frequency parts, two further filtering stages are implemented. This is done at low temperature near the sample to filter out thermal noise and to avoid additional noise pick up between sample and room temperature stage. First each DC line passes through a copper powder filter, which efficiently filters the high frequency noise up to several GHz. Next they pass through an RC-filter with a cut-off frequency around 10 kHz. To avoid pick up of high frequency noise, the RC filters and sample are placed in a copper can acting as Faraday cage.

At room temperature, the IVVI rack contains 16 digital to analog converters which are used to provide gate voltages and measurement signals. These are computer controllable via an optical fiber connection. On the measurement side, after amplifying the small voltages and currents coming from the sample to a typical voltage scale of 1mV-1V scale, they are measured with standard equipment such as a Keithley 2000 digital multimeter and a Stanford Research SR380 lockin amplifier.

3.3 MEASUREMENT CONFIGURATION

3.3.1 TUNNELING SPECTROSCOPY WITH A TWO TERMINAL DIFFERENTIAL CONDUCTANCE MEASUREMENT

The main experimental method used in this thesis is tunneling spectroscopy. We assume a metallic lead on one side separated by a sharp tunnel barrier from another region with a density of states (DOS) to be investigated, this is in our case the superconducting nanowire. Up to a proportionality constant, the tunneling current is given by

$$I \sim |T|^2 \int_{-\infty}^{\infty} N_{\mathrm{n1}}(E)\, N_2(E) \left[f(E) - f(E+eV) \right] \mathrm{d}E \tag{3.1}$$

with E the energy with respect to the Fermi level, N_{n1} the normal metallic DOS of the lead, f the Fermi-Dirac distribution and V the bias voltage applied across the tunnel junction. T is the transmission through the tunnel barrier and is assumed to be energy independent. N_2 is the actual DOS of interest. When both leads are metallic, the expression simply reduces to the ohmic relation $I = G_{\mathrm{nn}} V$, with $G_{\mathrm{nn}} \sim |T|^2 N_{\mathrm{n1}}(0)\, N_{\mathrm{n2}}(0)$, the standard temperature independent result. Based on this, differentiating 3.1 results in

$$\begin{aligned} \frac{\mathrm{d}I}{\mathrm{d}V} &= G_{\mathrm{nn}} \int_{-\infty}^{\infty} \frac{N_2(E)}{N_{\mathrm{n2}}(0)} \left[-\frac{\partial f(E+eV)}{\partial eV} \right] \mathrm{d}E \\ \left.\frac{\mathrm{d}I}{\mathrm{d}V}\right|_{T=0} &= G_{\mathrm{nn}} \frac{N_2(eV)}{N_{\mathrm{n2}}(0)} \end{aligned} \tag{3.2}$$

In the second line zero temperature is assumed. This last equation is the essential result: given a tunnel junction with one metallic lead and one lead with a DOS of interest N_2, the differential conductance is directly proportional to the DOS N_2. The two underlying assumptions are 1) the independence of tunnel barrier transmission on bias voltage and 2) being in the low temperature limit.

We have established that the relevant experimental quantity in tunneling spectroscopy experiments is the differential conductance $\mathrm{d}I/\mathrm{d}V_{\mathrm{bias}}$ across a tunnel barrier. In our experiments, the two electrical contacts serve as the current source and drain, and the tunnel barrier is defined by one of the small local gates (50 nm width). Two possible strategies to obtain $\mathrm{d}I/\mathrm{d}V_{\mathrm{bias}}$ are a) to measure the current and take a numerical derivative of the $I(V_{\mathrm{bias}})$ curve and b) to measure $\mathrm{d}I/\mathrm{d}V_{\mathrm{bias}}$ directly via lockin techniques. In the later case, a small alternating $\Delta V_{\mathrm{bias,AC}}$ is added to the stationary V_{bias}. For small $\Delta V_{\mathrm{bias,AC}}$, the corresponding quantity $\Delta I_{\mathrm{measured,AC}}/\Delta V_{\mathrm{bias,AC}}$ is a direct approximation to $\mathrm{d}I/\mathrm{d}V_{\mathrm{bias}}$. The advantage of this technique is that standard lockin amplification can be used to measure the small AC signal. This leads to considerable noise reduction in the signal compared to measuring the current and taking a numerical derivative. A longer integration time on the order of 10 periods of the typical measurement frequency (typically a frequency between 10-100 Hz away from 50 Hz) is however required, this results in a typical measurement time per datapoint of 0.1-1.0 s compared to 0.01-0.1 s for a direct current measurement.

In a two terminal configuration, ideally the applied voltage bias totally drops across the device. However, series resistances are present, which will lead to a reduction of the actual bias voltage across the device. The DC wires have a resistance on the order of 100 Ω, more important, however, is the contribution of the RC filter, which is on the order of several kΩ. Besides, the current amplifiers have non-negligible impedance. Typically, the total series resistance in a two terminal measurement is on the order of 10 kΩ (the actual value is known within 100 Ω precision and depends on the details of the measurement). Although tunneling spectroscopy as a method implies relatively high device resistance (above hundreds of kΩ, in which case the series resistance is negligible), in our experiments the tunnel coupling is still relatively strong, leading to a typical device resistance range of 50-200 kΩ. Due to this, the reduction in actual bias voltage across the sample may be up to ~20 % and cannot be ignored.

To account for series resistances, there are two possibilities. Firstly, if the series resistance in the circuit is known, the actual bias voltage across the sample can be calculated directly from the total applied voltage bias. Also the contribution in the measured differential conductance can be corrected for. More accurately however is to apply a quasi four terminal measurement technique. By splitting the source and drain leads on chip, one pair of leads may be used to inject and retrieve current. This can still be done by voltage biasing the corresponding two lines in the setup, with the current meter placed in this part of the circuit as well. The other pair of lines can be used to measure the actual voltage bias drop across the device. This

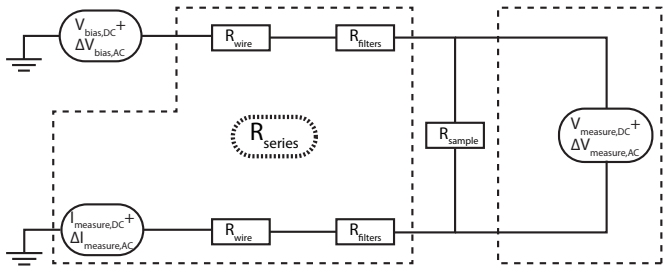

Figure 3.8 |Schematic representation of the measurement circuit. The sample is depicted by a variable resistance R_{sample}. On the left of the sample, the voltage bias and current measurement is depicted. The current amplifier has an impedance adding to the effective R_{series}, which is the total of the resistances in the dashed region. Typically, $R_{\text{series}} = 0.05 - 0.2R_{\text{sample}}$, leading to a significant correction to the voltage bias across R_{sample}. R_{series} is known with a precision of a few percent and may be corrected for afterwards. The other option is depicted on the right of the sample, in the dashed box. An additional voltage measurement in a quasi four terminal geometry (obtained by splitting the source and drain leads on chip and contacting them separately) directly measures the voltage across the sample. Series resistances at this side of the circuit are not shown. Note that neither of the two methods take contact resistances between lead and nanowire into account.

second method is the more accurate one of the two since no assumptions about series resistances have to be made, but it is more demanding in terms of measurement equipment. Since the series resistance are known to a few percent, correcting the bias voltage after the measurement is quite an accurate method. Throughout this thesis in all differential conductance measurements the effect of series resistances in the circuit is accounted for, in most cases by correcting afterwards, in a few cases by measuring the actual voltage bias drop across the sample. Note that neither of the methods can take into account the effect of contact resistances arising at the contact-nanowire interface.

3.3.2 MEASUREMENTS IN THREE TERMINAL DEVICES

Part of the measurements are done in three terminal devices, with three electrical contacts onto a single nanowire of which the middle one is superconducting.

Firstly, by pinching off one of the two N-nanowire-S sections with a local gate, the two terminal geometry is recovered. The advantage of the 3 terminal geometry in this case is that the best of the two junctions may be chosen for an in depth tunneling spectroscopy study. This type of operation covers the majority of measurements presented in this thesis on three terminal devices. For explanation of the measurement technique, see previous section.

A second possibility is to perform tunneling spectroscopy simultaneously from both sides of the S contact. This can be achieved by either biasing the two N terminals simultaneously or by biasing the S terminal, in both cases current meters are placed at the N terminal side. The effects of unequal contact resistances, slightly differing series resistances in the filters/amplifier and the possibility of differing thermo-electric voltages make it challenging however to keep two terminals at exactly the same voltage. An alternative option to perform simultaneous tunneling spectroscopy is to take an $I(V)$ at one side while the other terminal is left floating and then reverse the configuration. The latter technique is used in this thesis in the few instances where tunneling spectroscopy from two sides of the S contact is studied.

Finally, instead of focusing on tunneling spectroscopy at two sides of the superconducting contact, the conductance into S and into the second N terminal may be studied upon biasing the first N terminal. To this end, the second N terminal should be in operated in a transparent regime. Both S and the second N terminal should be connected via a current meter to the ground. This type of measurement has been done in a few instances in the context of non-local gating effects.

REFERENCES

[1] M. Hjort, *III–V Nanowire Surfaces*. PhD thesis, Lund University, 2014.

[2] S. R. Plissard, D. R. Slapak, M. A. Verheijen, M. Hocevar, G. W. Immink, I. van Weperen, S. Nadj-Perge, S. M. Frolov, L. P. Kouwenhoven, and E. P. Bakkers,

"From insb nanowires to nanocubes: looking for the sweet spot," *Nano letters*, vol. 12, no. 4, pp. 1794–1798, 2012.

[3] S. R. Plissard, I. van Weperen, D. Car, M. A. Verheijen, G. W. Immink, J. Kammhuber, L. J. Cornelissen, D. B. Szombati, A. Geresdi, S. M. Frolov, *et al.*, "Formation and electronic properties of insb nanocrosses," *Nature nanotechnology*, vol. 8, no. 11, pp. 859–864, 2013.

[4] X. Tang, R. Van Welzenis, F. Van Setten, and A. Bosch, "Oxidation of the insb surface at room temperature," *Semiconductor science and technology*, vol. 1, no. 6, p. 355, 1986.

[5] K. Flöhr, M. Liebmann, K. Sladek, H. Y. Günel, R. Frielinghaus, F. Haas, C. Meyer, H. Hardtdegen, T. Schäpers, D. Grützmacher, *et al.*, "Manipulating inas nanowires with submicrometer precision," *Review of scientific instruments*, vol. 82, no. 11, p. 113705, 2011.

[6] D. Van Woerkom, *Majorana fermions in well aligned InSb-nanowires with superconducting and normal contacts*. PhD thesis, TU Delft, Delft University of Technology, 2012.

[7] T. Schäpers, *Superconductor/semiconductor junctions*, vol. 174. Springer Science & Business Media, 2001.

[8] D. B. Suyatin, C. Thelander, M. T. Bjork, I. Maximov, and L. Samuelson, "Sulfur passivation for ohmic contact formation to inas nanowires," *Nanotechnology*, vol. 18, no. 10, p. 105307, 2007.

[9] F. Pobell, *Matter and methods at low temperatures*. Springer Science & Business Media, 2007.

4

SUPERCURRENT OSCILLATIONS IN INSB NANOWIRES

Semiconductor nanowires coupled to superconductors form an excellent, versatile platform to develop novel devices based on the Josephson effect. This has already led to breakthroughs such as Josephson transistors, Josephson π-junctions and recently a new type of transmon qubit. Besides, these devices are crucial in proposals for inducing topological superconductivity and Majorana fermion bound states. Here we study supercurrents flowing in quasi-ballistic nanowires with strong spin-orbit interaction and in high magnetic fields, thus combining the essential ingredients required for Majorana fermions. Without taking particular care of the chemical potential in the nanowire, we observe supercurrent oscillations, accompanied by higher order Shapiro steps and zero-bias enhancement of conductance that occurs at finite field. Having ruled out a conventional Fraunhofer effect, we analyze these oscillations in terms of supercurrents modified by Zeeman splitting, orbital effects and spin-orbit interaction. Demonstration of these effects is important for better understanding of the signatures of Majorana fermions in Josephson junctions and it will inform the future construction of topological quantum circuits.

[1] Vincent Mourik and Kun Zuo took equal shares in sample fabrication and measurements. Data analysis and reporting of results were mainly done by Vincent Mourik, with comments and assistance of Kun Zuo.

[2] In collaboration with S. M. Frolov, D.J. van Woerkom, S. R. Plissard, E. P. A. M. Bakkers, L.P. Kouwenhoven

4.1 INTRODUCTION

One of the most promising candidates at this moment to realize Majorana fermions in the solid state is a 1D topological superconductor as envisioned by Kitaev [1]. Such a topological superconductor may be engineered by proximitizing a 1D semiconducting nanowire with strong spin orbit interaction with a s-wave superconductor as proposed by Lutchyn and Oreg in 2010 [2, 3]. Under the right circumstances, Majorana bound states (MBS's) arise at the ends of the superconducting nanowire.

The key ingredient in this proposal is to induce superconductivity in the semiconducting nanowire via the proximity effect. One of the simplest methods to show that superconductivity is induced in the nanowire is by observing the Josephson effect in a nanowire based Josephson junction (JJ). Besides proof of successfully proximitizing the nanowire, a 4π Josephson effect may be revealed in a Josephson junction if the superconducting sections of the device become topological superconductors [1–4]. When observed this would constitute a very important independent signature of MBS's next to existing evidence from tunneling spectroscopy measurements [5]. These two reasons are the main motivation behind this research.

Not directly related to MBS's but in itself very important is the fact that nanowire based JJ's are proven to be extremely versatile devices due to the high degree of local control over the electron density that can be obtained. Among others, this has lead to the demonstration of the first Josephson transistor [6] and a novel type of Josephson π-junction in a S-quantum dot-S device [7]. Importantly, recent works have shown the first demonstration of a superconducting transmon qubit based on a nanowire Josephson junction [8, 9], illustrating the potential of such a junction for quantum computing purposes. The possibility of discovering new device functionality further motivates our research.

Two viable candidates for the semiconducting nanowire are InAs and InSb. Here, we focus on InSb nanowires, mostly because of the much larger Landé g-factor compared to InAs nanowires (~55 vs ~10 respectively). This enables larger Zeeman energies at lower magnetic fields, which is highly relevant to creating MBS's. This study focuses on the Josephson effect in the presence of a moderate (B>100mT) to strong ($B \leq 2$ T) magnetic field. Understanding the system in this largely unexplored regime is essential to the direction of detecting MBS's through observation of the 4π Josephson effect, and may also lead to new behavior of non-topological origin.

4.2 THEORY OF JOSEPHSON JUNCTIONS

The Josephson effect is the flow of a dissipationless supercurrent through a non-superconducting region between two superconductors, a structure which is called a Josephson junction (JJ). The supercurrent is governed by the gauge invariant superconducting phase difference $\phi \equiv \phi_1 - \phi_2$ between the phases ϕ_1 and ϕ_2 of the superconducting condensates at both sides of the non-superconducting region. Fun-

damental to the understanding of the Josephson effect is the Andreev bound state (ABS). An ABS is a bound state in the JJ confined by the two superconducting gaps: at each interface an incoming electron above the Fermi level undergoes Andreev reflection into a hole below the Fermi level, to be reflected again at the second superconducting interface as an electron above the Fermi level, thus forming a standing wave. The bound state condition is a combination of the phase accumulated while traveling the junction andϕ (refer to quantum transport book for a derivation), resulting in a ϕ dependent energy dispersion of the ABS. The ϕ dependent energy contribution E to the junction's total energy is a summation over the ABS's in all N occupied transport channels of the JJ and is given (in the short junction limit[1]) by [10].

$$E(\phi) = \sum_{n}^{N} E_n = \Delta \sum_{n}^{N} \sqrt{1 - T_n \sin^2(\phi/2)} \tag{4.1}$$

Here Δ is the superconducting gap which is assumed to be equal for both superconductors. T_n is the transmission of the n^{th} spin degenerate conduction channel. The ϕ dependence of the ABS's is clearly visible in this expression. The second Josephson equation relates the time evolution of ϕ to voltage V:

$$\frac{d\phi}{dt} = \frac{2eV}{\hbar} \tag{4.2}$$

This in turn enables deriving the related current:

$$I(\phi) = \frac{dE}{dt}\frac{1}{V} = \frac{\partial E}{\partial \phi}\frac{d\phi}{dt}\frac{1}{V} = \frac{2e}{\hbar}\sum_{n}^{N}\frac{\partial E}{\partial \phi} = \frac{e\Delta}{2\hbar}\sum_{n}^{N}\frac{T_n \sin\phi}{\sqrt{1 - T_n \sin^2(\phi/2)}} \tag{4.3}$$

Equations 4.2 and 4.3 show that for a stationary ϕ a current $I_S(\phi)$ may flow without a voltage developing across the junction, this dissipationless current is called *supercurrent*. Equation (4.3) is an expression for the so called current-phase relation (CPR) which describes the dependence of the supercurrent on ϕ. In general, I_S is a periodic function defined on the interval $(-\pi, \pi)$, if time-reversal symmetry is present I_S is an odd function. and has a maximum value which is known as the critical current I_c. Upon applying a larger current than I_c the junction will switch to the normal state and a voltage will develop across the junction. Traditionally the Josephson effect was studied in planar JJ's with an insulating tunnel barrier. Here the limit of many channels is valid, and the tranmission $T_n << 1$ for all channels. In this limit, (4.3) reduces to the so-called first Josephson equation

$$I_S(\phi) = I_c \sin\phi \tag{4.4}$$

More generally however, (4.3) can be expanded into a sine series

[1] Short junction limit implies superconducting coherence length $\xi >> L$, L being junction length. For long junctions the expression becomes more complex, but here for the purpose of introducing the relevant concepts this limit suffices.

$$I_S(\phi) = \sum_{n=1}^{\infty} I_{c,n} \sin(n\phi) \tag{4.5}$$

The coefficients $I_{c,n}$ determine the maximum supercurrent of the n^{th} harmonic and generally depend on all T_n's, thus disabling a simple relation to total supercurrent I_c. A more intuitive understanding of the higher harmonics of the supercurrent is the following: $n = 1$ corresponds to tunneling of a single Cooper pair across the JJ, $n = 2$ corresponds to the simultaneous tunneling of two Cooper pairs etc. As a consequence, higher harmonics correspond to higher order tunneling processes which are suppressed at a much higher rate while lowering T_n. This explains why the sinusoidal CPR applies in many cases. Only under specific circumstances resulting in high enough T_n are the higher harmonics of supercurrent expected to have a significant contribution.

In the context of MBS's the possibility of the 4π Josephson effect is relevant. As discussed in chapter 2, a JJ can be envisioned consisting of two topologically non-trivial superconductors formed in a nanowire section. Both superconducting sections host a pair of MBS's which should be spatially well separated. By connecting both sections via a piece of nanowire a JJ may be formed in which the inner MBS's couple, while the outer MBS's stay unaffected. In such a system, quasiparticles can tunnel from one side to the other via the coupled MBS's without dissipation and can thus contribute to the supercurrent. This component of the supercurrent will be proportional to $\sin(\phi/2)$. Such a 4π-periodic dependence will lead to a 4π-periodic CPR. The 4π Josephson effect is a signature of the presence of MBS's; since it is clear from (4.5) that no conventional CPR can give rise to a term proportional to $\sin(\phi/2)$, only higher harmonics may arise.

Importantly, the experimental system under consideration contains richer physics at finite magnetic field than what is suggested by (4.1). InSb has a large effective g-factor, which gives rise to a strong Zeeman energy dependence, affecting the ABS spectrum considerably, and a strong spin-orbit interaction (SOI) further influencing the ABS spectrum. Finally, the geometric effect of threading a magnetic flux through the junction leads to an additional phase pick up, which enters the ABS resonance condition. However, no theory incorporating all these effects simultaneously has been put forward to date.

4.2.1 JOSEPHSON π-JUNCTIONS

As discussed above, in a conventional Josephson tunnel junction I_c is positive and the CPR is sinusoidal. Under certain conditions, however, I_c may flip its sign and become negative, thus leading to the following CPR:

$$I_S(\phi) = -I_c \sin\phi = I_c \sin(\phi + \pi) \tag{4.6}$$

The sign of the critical current indicates the direction of flow of the supercurrent, while a small but positive phase difference is applied across the JJ. When

$I_c < 0$, it implies that the direction of the supercurrent is opposite to the direction of the phase gradient across the junction. It is evident from (4.6) that in this case the JJ is in the ground state when the phase difference equals to π rather than 0, as would be the case for a conventional JJ. This type of Josephson junction is therefore called a 'π-junction'. Several types of π-junctions have been realized [7, 11, 12] , here a π-junction based on exchange or Zeeman interaction is relevant.

To understand the 0 to π transition in the presence of exchange or Zeeman interaction it is helpful to consider the Ginzburg-Landau superconducting order parameter Ψ in the junction's barrier region. In a diffusive normal metal the order parameter decays exponentially as $\Psi(x) = \Psi(0)\,e^{-x/\xi_N}$, with x the distance to the superconductor and ξ_N the coherence length in the normal metal. This picture changes considerably if Zeeman interaction[2] is present. As illustrated in Figure 4.1a, this will split the electron's energy by $2E_Z$ (with $E_Z = \frac{1}{2} g\mu_B B$, where g is the effective g-factor, μ_B the Bohr magneton, and B the magnetic field). One spin species shifts up by E_Z and one down by E_Z. Superconducting pairing, however, happens at the Fermi level. To pair electrons of equal energy, but opposite spin, the Cooper pair gains a net momentum of $2\Delta k = 2E_Z/(\hbar v_F)$. As a consequence, the superconducting order parameter (which is an average over all Cooper configurations) becomes

$$\Psi(x) = \Psi(0)\,e^{-\frac{x}{\xi_N}} \frac{e^{-i\Delta k x} + e^{i\Delta k x}}{2} = \Psi(0)\,e^{-\frac{x}{\xi_N}} \cos(\Delta k x) \tag{4.7}$$

A spatial oscillation of Ψ, induced by the Zeeman interaction, is now present on top of the exponential decay. Whenever Ψ changes sign due to this oscillation its phase jumps by π. In a nanowire based JJ such oscillatory decay of Ψ is present from both superconductor contacts into the nanowire. The effective Ψ throughout the junction is the sum of the decaying order parameters from both sides. The oscillatory decay of Ψ leads to a competition as a function of Δk between having minimum free energy either at $\phi = 0$ or at $\phi = \pi$, resulting in 0 to π junction transitions. This behavior is schematically shown in Figure 4.1b.

In a diffusive junction model, the relevant energy scales governing the 0 to π transition are the strength of exchange or Zeeman interaction versus the Thouless energy E_T ($E_T = \hbar D/L^2$ in the diffusive limit, with D the diffusion constant and L the system length). The exchange or Zeeman interaction has to overcome E_T for the π state to occur, typically by an amount given by a scaling factor between 5 and 10 (based on numerical diffusive junction models [13]). In a superconductor-ferromagnet-superconductor (S-F-S) junction the typical parameters to vary are F-layer thickness and temperature to change E_T and exchange interaction strength, thus enabling the switch from the 0 to π state [14]. This is by now an established method for the creation of a π-junction [11, 15–17]. In the context of Zeeman interaction however no π-junction has been reported to date. This is primarily due to the challenging nature of acquiring measurable supercurrents at magnetic fields

[2] We focus on Zeeman interaction here, but the same holds for ferromagnetic exchange interaction.

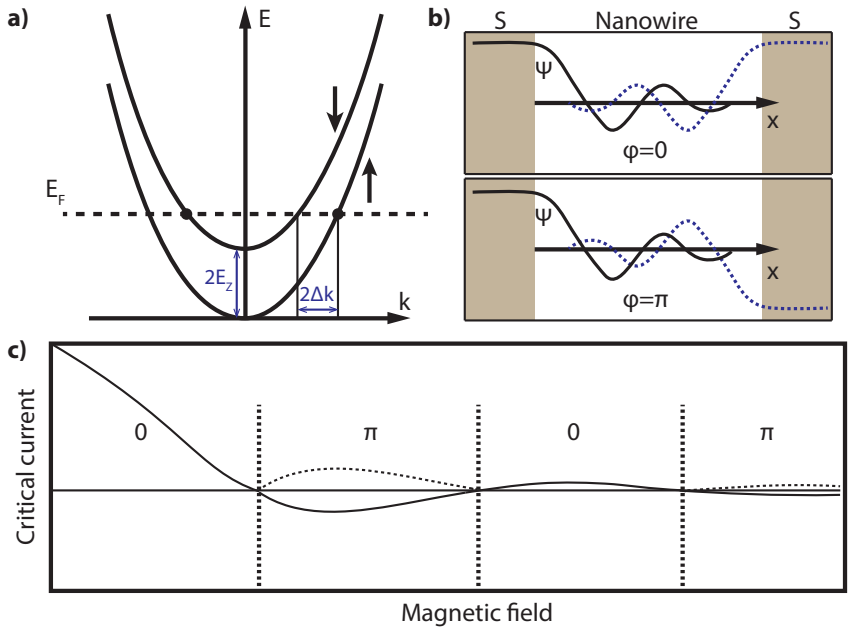

Figure 4.1 |Zeeman π-junction. a) Spin split nanowire dispersion due to Zeeman interaction. Electrons at E_{F} with opposite spin form Cooper pairs, resulting in a net momentum of $2\Delta k$ per Cooper pair. b) The net momentum of Cooper pairs causes the order parameter in the nanowire to start oscillating (solid black and dotted blue lines). For certain degrees of overlap of the oscillations the junction's ground state corresponds to 0 phase difference across the junction (top), in other cases it corresponds to π (bottom). The transition is governed by the details of the oscillatory decay, which directly depend on Δk. c) Qualitative dependence of the critical current through the nanowire on the magnetic field (solid line). The case depicted here corresponds to the π state being reached well before I_{c} vanishes in B. I_{c} changes sign after each 0 to π transition. In reality, whenever the supercurrent becomes negative, only the absolute value of I_{c} is measured (dashed line). Fixing the direction of current flow in the experiment makes the phase difference across the junction jump by π, instead of reversing the direction of the supercurrent.

large enough for the 0 to π transition to happen. InSb nanowires however are excellent candidates due to the high effective g-factor and gate tunable E_T. An order of magnitude estimate of E_T in our system yields $E_T = 10 - 100$ μeV, whereas it is estimated that $E_Z = 1.6$ meV/T (see supplementary information section 4.7.2 for estimates). This results in an expected minimal magnetic field of ~100 mT ($E_Z \sim 150$ μeV) for the 0 to π crossover to happen, which may well allow for observable supercurrents. Consequently, realizing a Zeeman π-junction may be within reach, which in this setting would enable an in situ, magnetic field tunable and gate potential tunable 0 to π transition. This is experimentally often highly preferable to varying a device parameter like F layer thickness or a set-up parameter like temperature. Noticeably, the previous discussion assumed a diffusive, metallic junction. The actual nanowire junction considered here however is a quasi-ballistic junction with only a few occupied nanowire subbands. A more adequate description based on the microscopic details of the ABS's is therefore required and will be discussed in section 4.4.

An expected signature of the occurance of a 0 to π transition in a JJ is illustrated in Figure 4.1c. For increasing strength of exchange or Zeeman interaction, usually a monotonous decay of I_c is expected (which is approximately gaussian shaped for this type of JJ). If a π-junction is achieved before I_c vanishes, on top of the monotonous decay an oscillatory behavior of I_c crossing zero and changing sign is present. Each crossing of zero represents a sign change in I_c, and therefore a 0 to π phase shift in the CPR. In a realistic experiment the JJ is current biased: only the current can be varied in a controllable manner and ϕ adjusts itself to keep the JJ in the groundstate. As a consequence the 0 to π transition will show up as a cusp in I_c, as illustrated in Figure 4.1c.

This picture only holds in the case of a sinusoidal CPR, as in (4.6). If the CPR contains higher harmonics, as in (4.5), the first harmonic's $I_{c,1}$ may undergo a sign change and thus cause a 0 to π transition, whereas the higher harmonic's $I_{c,n}$ will stay positive. In such a case a strong cusp in the (I_c, B) dependence is still expected. However, due to the non-vanishing contribution of the higher harmonics the supercurrent will not go to zero exactly, but will retain a finite value.

Evidence for such a scenario may be found upon irradiating the JJ with microwave radiation and subsequently studying the behavior of Shapiro steps across a supercurrent node [15]. A basic treatment of the origin of Shapiro steps can be found in a standard textbook such as [18]. Here it suffices to say that microwave radiation of frequency f effectively results in a sinusoidal drive of the junction, generating discrete steps on the $V(I)$ characteristic at fixed voltages of

$$V_m = m\frac{hf}{2e} \tag{4.8}$$

with m an integer. This is only true, however, for the first harmonic of the supercurrent. More generally, for the n^{th} harmonic, fractional Shapiro steps are generated at voltages of

$$V_{\mathrm{m,n}} = \frac{m}{n}\frac{hf}{2e} \tag{4.9}$$

The microwave drive power dependence of Shapiro steps for such a non-sinusoidal CPR will generally be a rather complex combination of the power dependence of the individual harmonics. However, the Shapiro step power dependence at zero magnetic field will typically be dominated by the $\sin\phi$ contribution, since that harmonic has a large contribution, whereas around the node of I_c it will be dominated by the higher harmonics and the corresponding fractional Shapiro steps, due to the vanishing $\sin\phi$ term.

A last important remark is the role of orbital effects. The Zeeman effect discussed previously results in an extra, spin dependent phase contribution to the resonance condition of ABS, thus altering the simple form of the spectrum, as given in (4.1). As will be discussed in more detail in section 4.4, this is the microscopic origin of the 0 to π transition. However, passing a magnetic flux through an area enclosed by an ABS has a similar effect, resulting in an additional geometric phase contribution to the ABS resonance condition. This is known as the orbital effect, which may result in similar behavior of supercurrent minima in B in the experiment.

4.3 EXPERIMENTS

4.3.1 METHODS

Superconductor-nanowire-superconductor (S-NW-S) Josephson junctions are fabricated, a typical device is shown in Figure 4.2a). The device consists of an InSb nanowire contacted at both ends with NbTiN contacts. Typically, contacts cover the nanowire for at least 300 nm and are spaced by 500-1000 nm. The device is made on top of a prefabricated array of bottom gates which are separated from the nanowire and contacts by a 30 nm thick dielectric layer of Si_3N_4. The gates enable local control over the chemical potential in the nanowire. For more details on fabrication, see chapter 3. We report measurements on two devices, referred to as device 1 and device 2. Device 1 has a junction length of 625 nm, is controlled by 3 local gates and the nanowire is aligned with the direction of the magnetic field ($\pm 5\,^\circ$). Device 2 has a junction length of 940 nm, is controlled by 5 local gates and the nanowire has an angle of $25 \pm 5\,^\circ$ with the magnetic field direction. Both nanowires have a diameter of 80 ± 10 nm. For device schematics, see supplementary information (section 4.7).

The devices are measured in a dilution refrigerator with a base temperature of 60 mK and equipped with dc lines including noise filtering stages (RC filters and copper powder filters) at low temperature. Superconducting leads are split at the chip enabling a quasi 4-terminal current biased measurement excluding series resistances in the set-up from the measured voltage. All measurements are performed at the base temperature of the refrigerator. Device 1 is cooled down a second time, to add a coaxial line connected to an radiofrequency (RF) antenna

near the sample, enabling Shapiro step measurements. Device and cooldown from which the data originates is specified at the end of each figure caption.

4.3.2 DEVICE CHARACTERIZATION

Figure 4.2 contains the basic device characterization at B = 0 T for device 1. Device 2 behaves similarly. Current versus local gate voltage is measured at V_{bias} = 10 mV showing a complete control over the device transparency (Figure 4.2b). Taking known series resistances into account, a residual resistance of ~6 kΩ is found, corresponding to the sum of the channels and contact resistances. This implies that the contact resistance is in the order of a few kΩ, suggesting transparent contacts, which is further confirmed by the presence of a supercurrent in the device. As shown in Figure 4.2c, by optimizing the gate voltages a maximal supercurrent of 8 nA was found, with a corresponding voltage of 32 μV, which developed upon jumping to the normal state. The junction is highly hysteretic as shown by the low retrapping current, and has a sharp transition to the normal state, indicating that the junction is in the underdamped regime [18]. Self-heating may also contribute to the hysteresis [19].

To further characterize the system, the supercurrent is studied as a function of a local gate voltage in Figure 4.2d. The supercurrent clearly modulates with the gate voltage and vanishes at low gate voltage when the device transparency becomes low. The voltage developed across the junction upon switching to the normal state is constant over a wide gate range, indicating that the size of the supercurrent inversely follows the normal state resistance R_{N}. Such a behavior of gate tunable supercurrent has been reported in several studies on carbon nanotube [20], and InAs [6] and InSb [21] nanowire based JJ's. The switching voltage measured here is much smaller compared to the superconducting gap Δ_{NbTiN} ~ 2 meV of bulk NbTiN. A detailed discussion of this can be found in the supplementary information (section 4.7.3). Note that an extra feature is present in the retrapping branch corresponding to a constant voltage of 15 μV (7 GHz), this may be an effective microwave resonance in the circuit which falls the switching and retrapping current.

In this study we focus on the gate voltage regime where the supercurrent at zero magnetic field is ~1 nA or more, e.g. rather transparent regimes comparable to V_{gate} = 0 to 1.5 V in Figure 4.2d. In our devices, such a regime typically corresponds to a few occupied nanowire subbands [22]. A discussion and estimation of the relevant energy and length scales of the junction is given in the supplementary information (section 4.7.2), here we quote their values: Zeeman energy E_{Z} ~1.6 meV/T, Thouless energy E_{T} = 10-100 μeV, proximity induced superconducting gap Δ = 0.1-0.5 meV, effective superconducting coherence length ξ = 0.3-1.0 μm, mean free path l ~0.1 μm [23], spin orbit length l_{SO} ~0.1 μm [24], superconducting coherence length of NbTiN λ_{NbTiN} ~250 nm. Given the junction length L of device 1 and device 2 of respectively 625 and 940 nm, this implies the junctions are in the long junction limit ($\xi \leq L$) and are close to the ballistic regime.

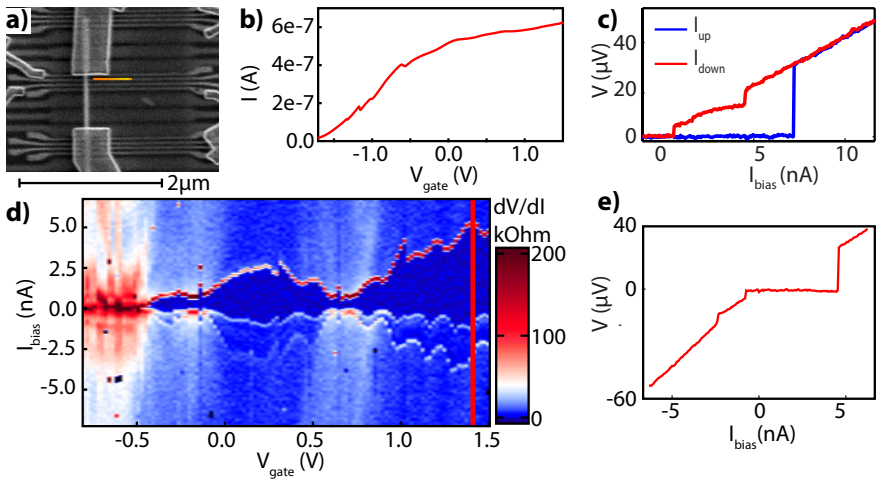

Figure 4.2 |a) Scanning electron microscope (SEM) image of a typical superconductor-nanowire-superconductor (S-NW-S) device. b) Device current as a function of gate voltage, $V_{\text{bias}} = 10$ mV. The varied gate is indicated in a), all other gates are at a high positive voltage, ensuring maximum device conductance. Full control over the device transparency is achieved. c) Voltage-current characteristic for both upwards (blue) and downwards (red) sweeping direction of current bias. The supercurrent of 8 nA is the maximum supercurrent observed in this device and corresponds to all gates at high positive voltage. d) Gate dependence of supercurrent, numerical derivative $\mathrm{d}V/\mathrm{d}I$ of $V(I)$ characteristics is shown. Current bias is swept from negative to positive. Supercurrent is modulated by the gate, following the normal state resistance modulations. Below $V_{\text{gate}} =$ -0.5 V no supercurrent is present. e) Voltage-current characteristic at indicated gate value in d), showing similar behavior to c). Panel c) is at a higher gate voltage, optimized for maximum supercurrent compared to d) and e). Data is from device 1, first cooldown.

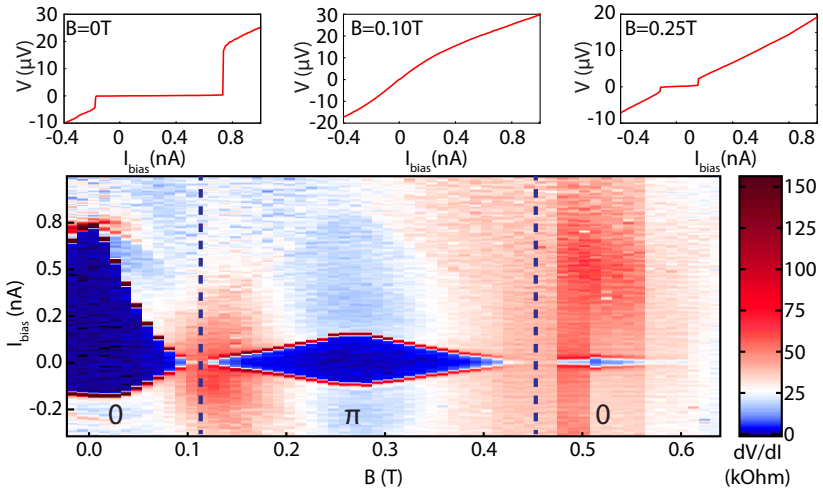

Figure 4.3 |Supercurrent as a function of magnetic field B applied along the nanowire. After an initial rapid decrease with virtually no supercurrent left around 120 mT (middle linetrace), the supercurrent revives to reach a maximum again around 280 mT (right linetrace). A third period starting at around 450 mT is weakly visible. Such an oscillatory behavior of supercurrent is very similiar to the expected behavior for a magnetic field induced 0-π transistion, the possible 0 and π regions are indicated in the figure. Numerical derivative $\mathrm{d}V/\mathrm{d}I$ of the original $V(I)$ curves is shown. Data is from device 1, first cooldown.

4.3.3 MAGNETIC FIELD DEPENDENCE OF SUPERCURRENT

The magnetic field dependent behavior of the supercurrent, as presented in Figure 4.3 and Figure 4.4, constitutes the main result of this work. The gate regime for the measurement in Figure 4.3 is comparable to the the regime around V_{gate} ~0.75 V in Figure 4.2d. A striking pattern is visible in the dependence of the supercurrent on B: after an initial fast decay, I_{S} displays an oscillatory behavior forming 2 subsequent 'lobes' of supercurrent in B field. This pattern is very similiar to the case of a magnetic field induced 0 to π transition as sketched in Figure 4.1c. In such a scenario, from 0 to 120 mT the junction is in the 0 state, in a long B field range between 120 and 450 mT it is in the π state and beyond it is in the 0 state again. As discussed in section 4.2.1 an onset B field for the π phase from 100 mT onwards fits in the diffusive junction model for a Zeeman π-junction [13]. Since the junction is long compared to the superconducting penetration depth in NbTiN (625 nm vs ~250 nm), and the superconducting film thickness is small in comparison (~80 nm vs ~250 nm), flux expulsion from the superconducting leads is not expected to play a role in governing E_{Z}. This justifies the assumption that the actual B field in the nanowire junction is equal to the applied global B field. Note that although

the pattern appears superficially similar to the well known Fraunhofer interference pattern for Josephson junctions the distance in B between first and second minimum is more than twice the distance from $B = 0$ T to the first minimum, whereas an equal spacing of minima is expected in the Fraunhofer case.

Two additional features are visible in the data: the difference between switching and retrapping current, and varying resistance in the normal state. At $B = 0$ T, the difference between switching and retrapping current has the same origin as in Figure 4.2, and is likely caused by the junction being in the underdamped regime. Upon suppressing supercurrent in B, the junction acquires equal switching and retrapping currents at finite B and the transition becomes rounded, indicating an increasing contribution of thermally excited quasi-particles for small critical currents. The broad resistance modulations in the normal state are likely caused by dispersion of nanowire states in B, since relatively small magnetic fields already correspond to considerable spin splitting. The origin of the narrow feature visible between 0.5 and 0.8 nA is unknown, but since it does not correspond to a fixed voltage, a microwave resonance in the junction (e.g. a Fiske step) cannot explain this.

Possible alternative explanations to the Zeeman π-junction scenario for the observed B dependence of the supercurrent should be considered. Firstly, a natural question is whether the observed oscillations in supercurrent simply result from B-field induced conductance fluctuations in the normal state, a scenario which does not necessarily invoke a 0 to π transition. Secondly, it is well known that upon threading a flux through the junction's supercurrent density, interference effects may occur leading to oscillations in the supercurrent (the Fraunhofer patterns observed for planar junctions in perpendicular B field are the most well known example). Essential to this is having supercurrent trajectories enclosing magnetic field lines. Both scenarios will be discussed in the following.

Figure 4.4a,b shows two additional B dependencies of supercurrent. The device is tuned to a more transparent regime, comparable to the gate regime around 1.4 V in Figure 4.2d. As a consequence, compared to the measurement in Figure 4.3, fluctuations in the normal state are less pronounced. Furthermore, it is clear especially in Figure 4.4b that the position of the minima in supercurrent do not coincide with a larger resistance in the normal state. The independence of supercurrent modulations and normal state fluctuations is further illustrated in Figure 4.4c: here the supercurrent clearly varies considerably, whereas the slope in the normal state is almost constant for the different $V(I)$ curves shown. This shows that the $I_c R_N$ product is not constant, but the supercurrent fluctuates irrespective of the normal state conductance, showing its different origin. In fact, the coexistence of higher normal state resistance and vanishing supercurrent in Figure 4.3 is a coincidence which is often absent. Note that, as in Figure 4.3, an additional resonance in the normal state of unknown origin is visible in Figure 4.4a and b. Clearly visible especially in Figure 4.4b around 150 mT is a residual supercurrent at the local minimum. Such a non-vanishing supercurrent at the supercurrent nodes in B is a general observation; it is rare for the supercurrent to (almost) vanish as in Fig-

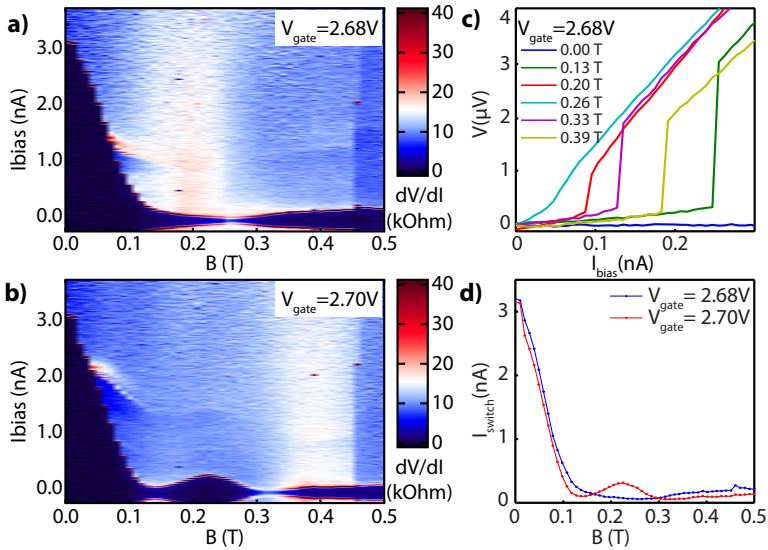

Figure 4.4 |Influence of gate potential on supercurrent at finite B. a), b) correspond to B dependence of supercurrent at two different gate potentials. For a difference in gate potential of 20 mV, a clear difference in position of the first supercurrent node is observed (250 mT in a) vs 150 mT in b)). Furthermore, a second node appears in b) at considerably smaller B field. There is no correlation between supercurrent node position and resistance in the normal state. In both cases small, but finite, supercurrent is visible at the nodes of supercurrent in B. c) $V(I)$ curves from a) at different B. The $B = 0$ T curve is shown for comparison of residual resistance. At finite B, residual resistance in the superconducting state becomes more pronounced, resulting in a smeared out transition at $B = 0.26$ T. All curves show comparable slopes in the normal state indicating the irrelevance of normal state resistance fluctuations to supercurrent oscillations. d) Comparison of switching currents extracted from a) and b) showing the strong dependence of the oscillatory behavior of supercurrent in B on gate potential. Numerical derivative $\mathrm{d}V/\mathrm{d}I$ of the original $V(I)$ curves is shown in a) and b). Data is from device 1, first cooldown.

ure 4.3. Besides, it is often impossible to conclude if supercurrent really vanishes at a node or if it becomes undetectably small. As discussed in section 4.2.1, a feasible explanation for this phenomenon in the Zeeman π-junction scenario is that second and/or higher harmonics of the supercurrent are present which do not vanish at the node, whereas the dominating $\sin\phi$ term undergoes a π phase change. We will discuss this scenario in more depth in section 4.3.4 in the context of Shapiro steps.

A last, very important, observation illustrated in Figure 4.4 is the strong gate dependence of the B induced supercurrent oscillations, which is made explicit in Figure 4.4d. A more extensive version of the dataset is shown in the supplementary information section 4.7.4. Evidently, upon varying gate potential over a small range of 20 meV the oscillations of supercurrent in B change drastically. Typical coupling factors of the local gates in a quantum dot regime are on the order of 0.1 eV/V [25, 26]. As such, we expect the typical change in chemical potential in 4.4 to be ~1 meV. This is small compared to the typical subband spacing of 15 meV [22], which explains why no significant difference of resistance in the normal state is observed between Figures 4.4a and b. Nevertheless, such a change will cause differences in Fermi velocities of the occupied subbands, which translates into a change in E_T. Especially close to the bottom of a nanowire subband strong gate tunability of v_F is expected, leading to significant fluctuations in E_T without a strong variation in normal state resistance. In the Zeeman π-junction scenario this explains a changing onset field of the π phase for different gate potentials. The strong gate tunability of supercurrent nodes presented in Figure 4.4 is an optimal case, in other gate regimes the effect is weaker. This is also in line with the scenario suggested earlier, of strong gate tunability of v_F near a subband bottom, and a weaker effect for E_F higher in the subband. Another aspect to point out, possibly even more relevant, is a gate voltage induced change in the geometrical shape of an ABS trajectory inside the nanowire. For example, the dwell time inside a barrier in the nanowire may change a lot by shifting a local potential, leading to strong modulations of E_T. The combination of these effects explains the absence of a regular pattern in the gate tuning of supercurrent nodes. Overall, the significant gate tunability of the B induced supercurrent oscillations fits well with having the Zeeman π-junction scenario in our system. Similar behavior is found for the other local gates underneath the junction (data not shown), leading to the conclusion that the observed oscillations of supercurrent and their gate dependence are very general phenomena, not sensitive at all to the precise details of the gate configuration. We emphasize once more that only the rather transparent device regime is investigated here. This is done to avoid strong dependence of the normal state resistance on V_{gate} and B which is typically present in regimes $G << G_0$ due to Coulomb blockade related phenomena.

Next we discuss interference of supercurrent caused by magnetic field, as observed in, for instance, the well known Fraunhofer interference pattern. This is a manifestation of a more general effect. The wavefunction of an ABS picks up a geometrically determined phase at finite B, due to a magnetic flux being threaded

through it. This phase enters the resonance condition of the ABS, thereby affecting its ϕ dependence and the supercurrent it carries. The strictly geometrical, orbital effect is opposed to the spin related phenomena of the Zeeman effect and spin-orbit coupling at finite B (note, however, that the latter effects effectively also introduce a phase into the ABS resonance condition). The so called orbital interference effect described here has to be considered as one of the possible causes of strong supercurrent oscillations in B and V_G, as presented in Figures 4.3 and 4.4.

In the planar junction case assuming a sinusoidal CPR and a spatially homogeneous supercurrent density, upon applying a B orthogonal to the supercurrent flow direction, the familiar Fraunhofer type interference pattern is obtained. Clearly, a Fraunhofer type interference pattern cannot explain our data: B is applied along the direction of supercurrent flow, and moreover the supercurrent minima are higly non-equidistant and strongly gate tunable. These aspects are directly contradictory to such a scenario. Furthermore, a more general analysis along these lines, assuming a spatially inhomogeneous supercurrent density, is irrelevant here, since this relies (amongst others) on a significant orthogonal B component, which is not present here.

An important and relevant nuance should be made however. Although the nanowire junction under consideration is to a good approximation a 1D object, it still has a finite diameter of ~100 nm. As a consequence the transverse part of the nanowire subband wavefunction will always pick up a phase, even if a B field is applied along the nanowire's axial direction. This causes an orbital interference effect to be present, which has been discussed in a nanowire context recently [27]. In this theory oscillations of supercurrent as a function of axial flux are found, and under certain conditions supercurrent nodes with vanishing supercurrent are shown. This is superficially similar to the behavior presented in Figures 4.3 and 4.4. However, that particular model is not so relevant to the InSb nanowire case of this work, since a cylindrical conducting shell was assumed as may be relevant to InAs nanowires, due to their presumed surface conductance. Furthermore, no spin related effects are considered in the work, whereas Zeeman spin splitting is one of the principal dominating effects in our system due to the large effective g-factor, further invalidating the applicability of the model from ref [27]. It is not clear, however, whether our observations cannot be explained in any possible scenario based on the orbital interference effect. To get a better understanding of the interplay between the spin splitting of ABS due to the Zeeman effect and the orbital interference effect, realistic simulation of our system considering the number of subbands, length of the junction and disorder is necessary. It is, at this moment, impossible to conclusively determine if a certain minimum of supercurrent is caused by a Zeeman induced 0 to π transition or by the orbital interference effect. Nevertheless, the Zeeman π-junction effect fits the observations very well and is expected to be the dominant effect at low B fields.

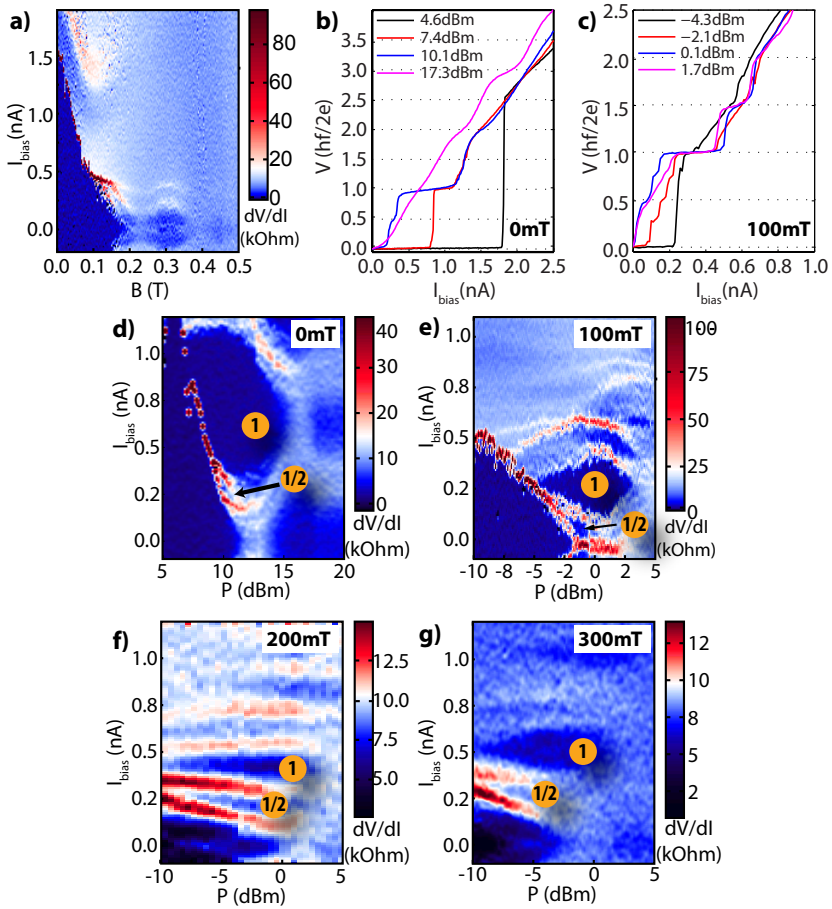
a)
b)
c)
d)
e)
f)
g)
B (T)
V (hf/2e)
dV/dI (kOhm)
4.6dBm
7.4dBm
10.1dBm
17.3dBm
0mT
−4.3dBm
−2.1dBm
0.1dBm
1.7dBm
100mT
200mT
300mT
P (dBm)
1
1/2

4.3.4 SHAPIRO STEPS AT FINITE MAGNETIC FIELD

To investigate the possible contribution of higher harmonics to the supercurrent, the sample has been cooled down a second time with a radiofrequency (RF) antenna near the sample. This enables the studying of Shapiro steps in the junction as a function of microwave power and frequency. Here, we focus on power dependence of Shapiro steps for different B fields. Thermally cycling the device did not change the qualitative behavior of the device, although exact gate tunings are different. The device is again operated in a transparant regime, comparable to V_{gate} = 0.5 V or higher in Figure 4.2d. As a consequence of adding the RF antenna the noise level in the vicinity of the device increased, which in turn led to lower overall supercurrent (25 μV typical switching voltage vs 32 μV before) and a lower sensitivity to small supercurrents. Figure 4.5 summarizes the main findings of these measurements.

Figure 4.5a is a B dependence of supercurrent in the absence of microwave drive. After an initial rapid decay of supercurrent up to ~100 mT, oscillations of supercurrent are observed. At the supercurrent minimum around 250 mT a small supercurrent is present. This type of pattern is very similar to the ones shown in Figures 4.3 and 4.4. The negative impact of adding an antenna on the visibility of supercurrent above 100 mT is clear compared to the other datasets. This supercurrent vs B characteristic is the basis for the Shapiro step study presented here. As discussed in section 4.2.1, a possible explanation for the small, but finite, supercur-

Figure 4.5 ***(preceding page)*** |Shapiro steps in magnetic field. a) B dependence of supercurrent without microwave radiation applied. Numerical derivative $\mathrm{d}V/\mathrm{d}I$ of the original $V(I)$ curves is shown. b) Shapiro steps at $B = 0$ T for different microwave powers. At the lowest RF power (black line) no Shapiro steps are present. A small half integer step is visible at 0.1 dBm (blue line). c) Shapiro steps at $B = 100$ mT for different microwave powers. Half and quarter integer steps are visible, in particular at -2.1 dBm (red curve) and 0.1 dBm (blue curve). d)-g) Microwave power dependence of Shapiro steps for different B. Numerical derivative $\mathrm{d}V/\mathrm{d}I$ of the original $V(I)$ curves is shown, in this representation the Shapiro step plateau corresponds to low differential resistance (blue color). At $B = 0$ T (panel d)), the power dependence is dominated by integer Shapiro steps and only a small contribution of half integer steps is visible. At $B = 0.1$ T (panel e)) most fractional steps are visible. Here not only half integer steps, but also quarter steps are weakly present. $B = 0.2$T (panel f)) is closest to the minimum supercurrent at 0.25 T. Here the half integer and integer steps are almost equal in width. Finally, beyond the minimum of supercurrent, at $B = 0.3$ T (panel g)), the integer steps increase again in width compared to the half integer step. Curves in b) and c) correspond to the same datasets as shown in respectively d) and e). Values given for the RF power in panels b)-g) is the ouput power of microwave source, 60 dB attenuation, of which 20 dB at low T, is applied. Data is from device 1, second cooldown.

B (T)	I_{switch} (nA)	$w_{1/2}$ (nA)	w_1 (nA)	$w_{1/2}/w_1$
0.0	2.41	0.12	0.87	0.14
0.1	0.63	0.12	0.34	0.35
0.2	0.34	0.15	0.23	0.65
0.3	0.35	0.16	0.30	0.53

Table 4.1 |Summary of switching current and maximum plateau widths of the 1/2th and 1st Shapiro steps for different magnetic field strenghts. Data extracted from Figure 4.5b,d,e,f, except switching current at $B = 0$ T, which is taken from the larger dataset of which part is shown in Figure 4.5d.

rent at the node around 250 mT is the presence of higher harmonics in the CPR. Such higher harmonics do not vanish at the point in B where the first harmonic goes through zero undergoing a π phase shift. This behavior should manifest itself by the presence of fractional Shapiro steps, due the to higher harmonics which become more prominent at the node.

To study this, we focus on power dependence of Shapiro steps at different B strengths of 0, 100, 200 and 300 mT corresponding to Figure 4.5d,b,e,f respectively. The microwave frequency is kept fixed at 2.0 GHz. Shapiro steps show up at voltages corresponding to $V = n \cdot \frac{hf}{2e}$, where n may be a fraction. At B = 0 mT (Figure 4.5d), half integer steps are only weakly present. B = 100 mT (Figure 4.5b) corresponds to a sweet spot where most fractional steps are observed: here not only n = 1/2 steps but also weak n = 1/4 steps are visible. This more clearly visible in Figure 4.5c where the same data is plotted in a voltage histogram. High voltage counts correspond to the plateau's of the Shapiro steps, here the n = 1/4 steps are better visible. The B = 200 mT and B = 300 mT cases (Figure 4.5e,f) correspond to barely visible initial supercurrent. As a consequence, the Shapiro step power spectra are of lower quality compared to the 0 and 100 mT cases. Nevertheless, weak Shapiro steps can still be resolved. At 200 mT, which is closest to the minimum of supercurrent, the width of the 1/2 step is more than half the width of the 1st step, here the maximum step ratio is found. At 300 mT the 1/2 step is still large compared to the 1st step, but slightly less pronounced compared to 200 mT. This behavior is summarized in Table 4.1.

Observing fractional Shapiro steps is, in itself, not conclusive evidence for having a non-sinusoidal CPR, as a higher order driving of junction may also have this result. However, the observed behavior of fractional Shapiro steps having a larger contribution around the supercurrent minimum fits well into a model of having a non-sinusoidal CPR, of which the $\sin\phi$ term undergoes a π phase shift while higher harmonics do not vanish (see section 4.2.1). Since the junction is in the long junction limit and in the quasi-ballistic regime, several ABS's with rather high transmission are expected to be present. This will result in a non-sinusoidal CPR. Indeed the fractional steps observed are quite robust in microwave frequency (data not shown) and power, suggesting that they are an intrinsic property of the junction. The Shapiro step data presented here supports the hypothesis of having a B in-

duced Zeeman π junction combined with a non-sinusoidal CPR. At the same time, however, it does not allow for further discrimination of the π-junction effect versus the orbital inteference effect. In the latter case the first harmonic of the CPR may be suppressed as well around a supercurrent minimum, resulting in similar behavior.

4.3.5 POSSIBLE OBSERVATION OF ANOMALOUS SUPERCURRENT

The remaining data discussed in this work is taken from device 2. The device behaves highly similar to device 1, the main difference is the device being slightly more resistive. This can be explained by both a factor 1.4 larger junction length (940 vs 625 nm) and slightly worse contact quality. A consequence is the presence of more pronounced conductance fluctuations compared to device 1. Another significant difference between device 1 and device 2 is the angle with respect to the external B field: device 1 is aligned along the B field, whereas device 2 has an angle of 25° with respect to the B field.

Here we focus on a different type of behavior not investigated in device 1. Figure 4.6 shows a B dependence of supercurrent. Firstly, in this device the same type of supercurrent oscillations in B are observed as in device 1. In Figure 4.6a the result is shown when the current bias across the device is swept from negative to positive, whereas in Figure 4.6b the result is shown when the current bias is swept from positive to negative. Hysteresis of supercurrent is observed around $B = 0$ T: in Figure 4.6a, the negative retrapping current is small compared to the positive switching current, in Figure 4.6b, the positive retrapping current is small compared to the negative switching current. This is expected if the junction is in the underdamped regime, or if self-heating effects play a role. However, there is an important difference between the two sweep directions: the switching current differs upon starting from zero current bias and going negative or going positive. To explicitly show this behavior the switching currents for both sweep directions are extracted and shown in Figure 4.6c. There is a clear difference visible (Figure 4.6d) above ~50 mT and around 0 mT. Aside from this, differences in the resistance of the normal state are observed, suggesting hysteresis in the normal state: upon sweeping from 0 to $\pm I_{\mathrm{max}}$ one branch is followed and upon returning to 0 another is followed. The sweep direction dependent behavior shown in Figure 4.6 is tunable by gate potential, for some gate values it is clearly visible, while for others it is almost absent.

So far, we have found this behavior in only a single device, though we have not checked for this in the other device. In this particular case, it has been established that this is not a simple measurement artifact. The effect does not show up because of some time dependence between the two panels in Figure 4.6; in fact, the two voltage-current characteristics were both taken in a single current bias sweep from negative to positive back to negative current bias, only then was B stepped. This way, a possible time dependence between both panels is eliminated. Furthermore, the difference in switching current for both sweep directions at $B = 0$ T is a true effect that has been observed on multiple occasions.

A possible partial explanation of this phenomenon is given in ref[28]. Here the

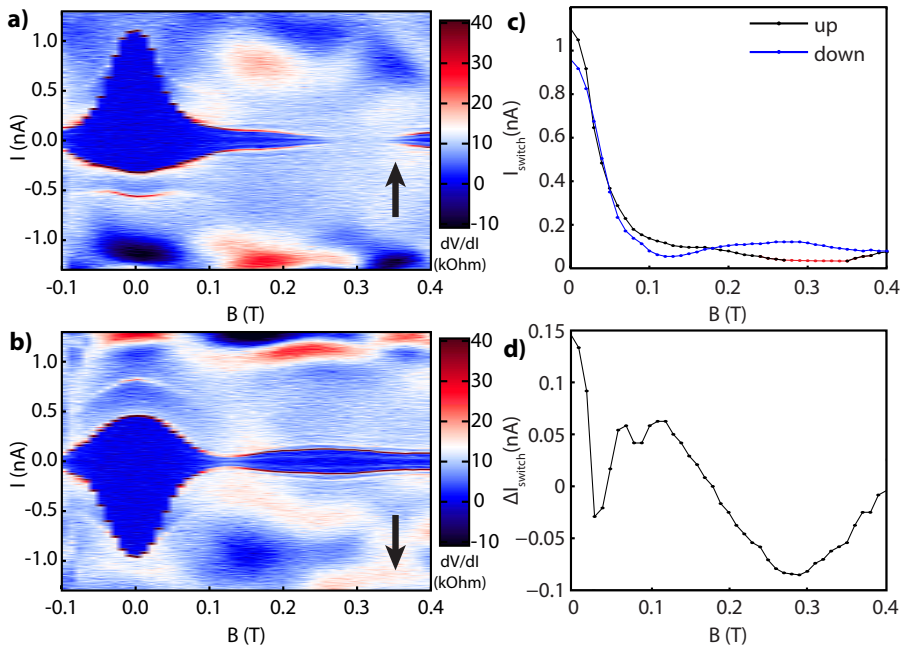

Figure 4.6 |Current bias sweep direction dependence of supercurrent. a), b): B dependence of supercurrent sweeping the current bias upward from -1.2 to +1.2 nA (a)) and downward from +1.2 to -1.2 nA (b)). Clear differences in supercurrent are visible: the first supercurrent node shifts by almost 200 mT upon reversing the sweep direction. In the normal state a clear difference is also visible, suggesting hysteretic behavior above the switching current. Note that these effects are not only present at finite B but also at $B = 0$ T. c) Direct comparison of the switching currents (extracted from a) and b)) for upward (black) and downward (blue) sweeping direction. The red points for the upward sweep direction curve correspond to the noise level; here the supercurrent cannot be detected reliably. d) Difference of switching current for upward and downward sweeping direction. Numerical derivative of the original $V(I)$ curves is shown in a) and b). Data is from device 2.

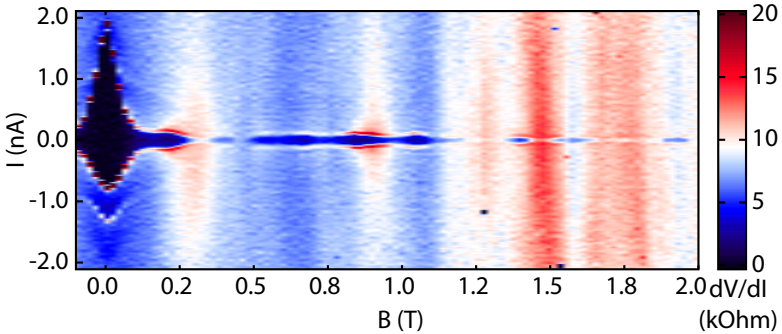

Figure 4.7 |Long lasting supercurrent in magnetic field. A weak but finite supercurrent is visible up to B fields of 2T, the maximum B field range investigated in this experiment. Numerical derivative of original V(I) curves is shown. Data is from device 2.

interplay of Zeeman effect and SOI is considered, which at finite B gives rise to a ϕ_0 junction: a Josephson junction which is in its groundstate for a phase difference ϕ_0 not equal to 0 or π. Under certain circumstances this may give rise to a the difference in switching current between different current bias sweep directions. However, it is essential for this to happen that time reversal symmetry is broken, which in our system only happens at finite B field. As a result, our observations at $B = 0$ T contradict this scenario. Furthermore, the normal state has not been investigated. An interpretation of this data in a ϕ_0 junction context is, as such, not justified due to incompleteness in explaining all observations, but does presents an intriguing possible scenario.

4.3.6 LONG LASTING SUPERCURRENTS IN MAGNETIC FIELD

A final observation on supercurrent we report here is the presence of a small, but finite, long lasting supercurrent in B field. A typical example is shown in Figure 4.6. Up to B fields as high as 2 T a small supercurrent with a typical size between 50 and 100 pA is found. This is quite remarkable given the junction length of 940 nm. As we argued before, with such a junction length it is reasonable to expect the actual B field in the nanowire to be the same as the applied B field. Given the effective g-factor of InSb which is ~55, it implies that the Zeeman energy at 2 T is 3.2 meV. This is a large energyscale compared to Δ_{NbTiN}, which is 2 meV at most, let alone compared to the effective Δ in the nanowire, which is between 0.1-0.5 meV. A reason why the supercurrent lasts so long may be the presence of spin orbit interaction. The characteristic length scale for SOI is the spin orbit length l_{SO} over which the electron spin flips sign. Based on quantum dot and weak anti-localization measurements [24, 25] it is expected that l_{SO} = ~100 nm, which is small compared to the junction length L = 940 nm. SOI therefore may avoid total spin polarization,

and thereby breaking of the Cooper pairs transported across the junction.

4.4 MODEL OF A NANOWIRE JOSEPHSON JUNCTION WITH LARGE ZEEMAN AND SPIN-ORBIT INTERACTION

In section 4.2 ABS's have been discussed in the absence of Zeeman interaction and spin-orbit interaction (SOI). Furthermore, the Zeeman π-junction was introduced based on a diffusive, metallic junction model. Since our nanowire has only a few occupied transport channels and is close to the ballistic transport regime, a more adequate model is required. Based on the experimental findings presented in section 4.3, a microscopic theory of the ABS's for a nanowire like geometry has been developed by Yokoyama et al. in [28, 29]. Here we discuss the main insights of these works and their relevancy to the experiment.

In the model, it turns out that the Zeeman interaction can be conveniently characterized by a phase shift in the ABS resonance condition. This parameter is given by

$$\theta_B = \frac{g\mu_B BL}{\hbar v_F} = \frac{2E_Z}{E_T} \tag{4.10}$$

with E_T the ballistic expression for the Thouless energy. From each initially spin degenerate ABS's pair one gets a phase shift of $+\theta_B$ and the other one a phase shift of $-\theta_B$. This in turn leads to an energy splitting of the two initially spin degenerate ABS's. This simple form of θ_B is only valid in the short junction limit, $L << \xi$. Importantly, it is shown that if only Zeeman interaction or spin orbit interaction is present, the ABS's are always symmetric in ϕ: $E(\phi) = E(-\phi)$ and consequently $I_S(\phi) = -I_S(-\phi)$. As a consequence, only $\phi = 0$ or $\phi = \pi$ are possible groundstates of the junction. If both interactions are present, however, this symmetry relation is broken and the junction's groundstate may correspond to an arbitrary value of ϕ. For more details on calculations of the ABS's spectra see [28], here we focus on their graphical representation from ref [28] as shown in Figures 4.8, 4.9 and 4.10.

The ABS spectra shown in these figures are obtained in [29] by using a 2D tight binding approach. A 2D nanowire of length $L = 1000$ nm and width $W = 60$ nm is placed between superconducting contacts with ideal interfaces between S and nanowire. A random disorder potential on each site is included such that the mean free path $l = L$. Rashba SOI is included and B is applied along the direction of the Rashba SOI and orthogonal to the propagation direction. Finally, continuum contributions to the supercurrent arising from ABS states outside the gap are neglected (the short junction limit $L << \xi$ is applied).

Figure 4.8 shows the result obtained for a single nanowire subband without SOI. At $B = 0$ T, a spin degenerate pair of ABS's is present. As a function of increasing B, these initially degenerate levels split due to the Zeeman effect, as shown in Figure 4.8a. Whenever a level reaches the gap edge $E = \Delta$ and disappears into the continuum, a new level enters at $E = \Delta$ going down in energy. The symmetry

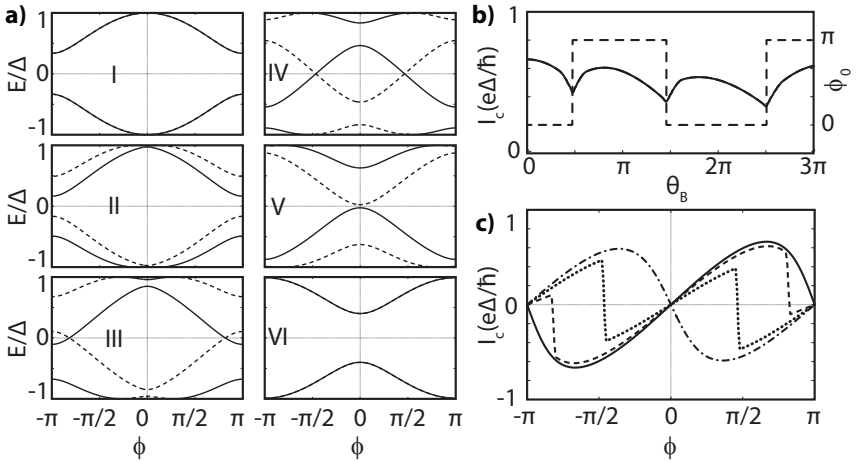

Figure 4.8 |Andreev bound states in an InSb nanowire, single subband, no SOI. a) Andreev levels vs ϕ for different strengths of $\theta_{\mathrm{B}} = \frac{g\mu_{\mathrm{B}}BL}{\hbar v_{\mathrm{F}}}$. Solid and broken lines indicate the two initially degenerate levels. In I), $\theta_{\mathrm{B}} = 0$ and levels are degenerate. In II), $\theta_{\mathrm{B}} = 0.1\pi$ and levels spin split. In III), $\theta_{\mathrm{B}} = 0.27\pi$ and levels cross $E = 0$ close to $\pm\pi$. In IV), $\theta_{\mathrm{B}} = 0.53\pi$ corresponds to a value just after the 0 to π transition, the lowest energy state is now acquired at $\phi = \pi$. In V), $\theta_{\mathrm{B}} = 0.79\pi$ and in VI), $\theta_{\mathrm{B}} = \pi$, showing the further evolution of the levels resulting in degenerate states with a minimum at $\phi = \pi$. b) Critical current I_{c} (solid) and groundstate phase difference ϕ_0 (dashed) as a function of θ_{B}, showing the 0 to π transition in ϕ_0 and the corresponding cusps in I_{c}. c) Nanowire CPR for different values of θ_{B}: 0 (solid), 0.27π (dashed), 0.53π (dotted), and π (dashed dotted), showing the 0 to π transition and the strong anharmonicity of the CPR around the transition point. Figures adapted from [28].

relation $E(\phi) = E(-\phi)$ holds in all cases since SOI is absent. Furthermore, each level is mirrored in the Fermi level as required by particle hole symmetry in the superconductor. Importantly, for large enough spin splitting, the level initially being above E_F crosses the Fermi level and is eventually completely below the Fermi level. Since this level originally had its maximum energy at $\phi = 0$ and its minimum at $\phi = \pi$ this implies that the groundstate phase ϕ_0 of the junction at a certain point in the process of crossing E_F jumps from 0 to π, and the junction undergoes a π transition. This behavior is further illustrated in Figure 4.8b,c. I_c shows clear cusps at the points where the 0 to π transition happens. Aside from this, the CPR obtained around the transition point is strongly anharmonic, giving rise to pronounced higher harmonics in the CPR. The microscopic picture provided here and the behavior illustrated in Figure 4.8 are fully complementary to the diffusive junction theory discussed before in section 4.2.1.

Next we consider the result for a single nanowire subband upon inclusion of SOI. Figure 4.9a shows the evolution of the ABS's as a function of B. At $B = 0$ T a pair of two spin degenerate ABS's is present as in the case without SOI. Upon increasing the B field, these levels spin split. However, besides merely spin splitting, in the presence of both Zeeman interaction and SOI, $E(\phi) \neq E(-\phi)$. This is clearly visible in the figure, as the minima and maxima of the ABS's are no longer fixed to 0 or π, but shift along the ϕ axis. As a consequence, the junction's groundstate no longer corresponds to $\phi_0 = 0$ or π, but instead corresponds to an arbitrary ϕ_0, which shifts continuously with increasing B. On top of this continuous shift, discrete jumps are present which originate from the ABS's minima shifting from close to 0 to close to π. Therefore, on top of a continuous shift in ϕ_0, discrete 'π-like' transitions are present. This behavior is illustrated in Figure 4.9b,c. The 'π-like' transition still results in strong cusps in the I_c vs B curve. Such a junction is called a ϕ_0 junction, as opposed to a 0 or π junction. Clearly visible in the CPR's shown in the figure is the appearance at finite B of anomalous supercurrent, a finite supercurrent at $\phi = 0$, which is a direct consequence of having a ϕ_0 junction. In the single subband case, no difference was found between I_{c+} (the I_c obtained going from $I = 0$ to positive I) and I_{c-} (the I_c obtained going from 0 to negative I).

Finally, we consider the results obtained for multiple subbands in the presence of SOI. Figure 4.10 shows the result for 4 subbands. At $B = 0$ T, 4 spin degenerate pairs of ABS's are present. Upon increasing B, effects very similar to the single subband case are observed. The levels split, but also lose there symmetry in the $\phi = 0$ axis. Again, this combination results in a continuous shift of ϕ_0 with jumps that are 'π-like' on top. Since more levels are present, at higher B fields the dispersion of the ABS's in ϕ is lower compared to the single subband case. This may result in smoother transitions for the large 'π-like' jumps in ϕ_0 as shown in Figure 4.10b. Similar to the single subband case, the CPR's at finite B reveal the presence of anomalous current. For more than one occupied subband, a difference in I_{c+} and I_{c-} is found. This is illustrated in Figure 4.11. Here the corresponding I_{c+} and I_{c-} to Figure 4.10 are shown. The overall dependence on B is similar to the sin-

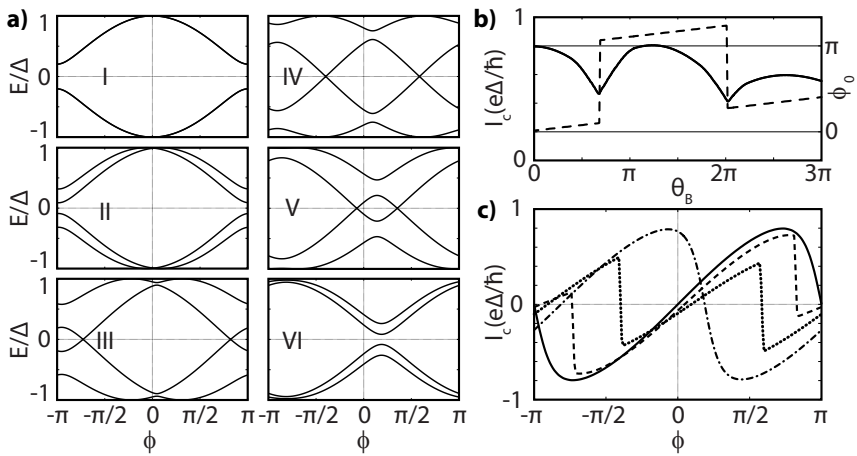

Figure 4.9 |Andreev bound states in an InSb nanowire, single subband, SOI included. a) Andreev levels vs ϕ for different strengths of $\theta_B = \frac{g\mu_B BL}{\hbar v_F}$. In I), $\theta_B = 0$, levels are degenerate and $E(\phi) = E(-\phi)$. In II), $\theta_B = 0.1\pi$ and levels spin split. In III), $\theta_B = 0.35\pi$, levels cross $E = 0$ close to $\pm\pi$. From here on, visibly $E(\phi) \neq E(-\phi)$. In IV), $\theta_B = 0.7\pi$ corresponds to a value close to a 0 to π like transition resulting in a minimum energy reached unequal but close to $\phi = \pi$. In V), $\theta_B = 1.05\pi$ and in VI), $\theta_B = 1.4\pi$, showing the further evolution of the levels resulting in a minimum in energy reached close to $\phi = \pi$. b) Critical current I_c (solid line) and ground-state phase difference ϕ_0 (dashed line) as a function of θ_B. Here, on top of a 0 to π like transition in ϕ_0, a continuous slope in ϕ_0 caused by SOI is present, resulting in a ϕ_0 junction. I_c still exhibits strong cusps and does not show a difference in positive and negative I_c. c) Nanowire CPR for different values of θ_B: 0 (solid line), 0.35π (dashed line), 0.7π (dotted), and 1.4π (dashed dotted), showing the ϕ_0 junction behavior. Figures adapted from [28].

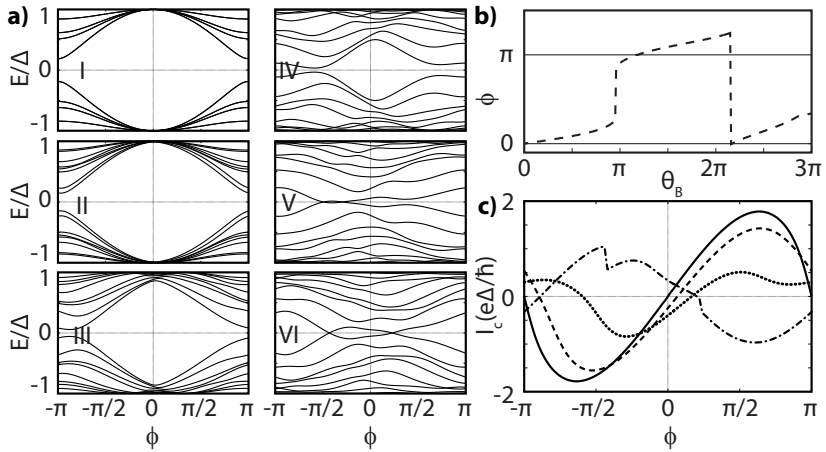

Figure 4.10 |Andreev bound states in an InSb nanowire, 4 subbands, SOI included. a) Andreev levels vs ϕ for different strengths of $\theta_B = \frac{g\mu_B BL}{\hbar v_F}$, similar to the single subband case. In I), $\theta_B = 0$, levels are degenerate and $E(\phi) = E(-\phi)$. In II), $\theta_B = 0.1\pi$, and in III), $\theta_B = 0.4\pi$, the levels spin split. From here on, visibly $E(\phi) \neq E(-\phi)$. In IV), $\theta_B = 0.8\pi$ is just before a 0 to π like transition and in V), $\theta_B = 1.2\pi$ is just after this transition, resulting in a minimum energy reached unequal but close to $\phi = \pi$. In VI), $\theta_B = 1.6\pi$, showing the minimum in energy reached close to $\phi = \pi$ more clearly. b) Groundstate phase difference ϕ_0 as a function of θ_B. Similar to the single channel case, on top of a 0 to π like transition in ϕ_0, a continuous slope in ϕ_0 caused by SOI is present resulting in a ϕ_0 junction. The transition may be smooth and the difference in ϕ_0 is generally not equal to π, different to the single band case. c) Nanowire CPR for different values of θ_B: 0 (solid line), 0.4π (dashed line), 0.8π (dotted line), and 1.6π (dashed dotted line), showing the ϕ_0 junction behavior also in the multiple band case. Figures adapted from [28].

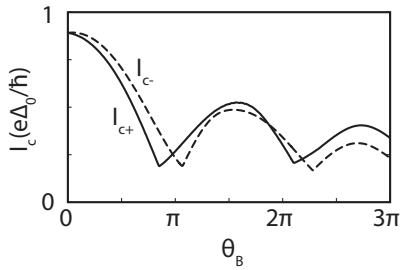

Figure 4.11 |Critical current vs $\theta_B = \frac{g\mu_B BL}{\hbar v_F}$, 4 subbands, SOI present. Critical current in positive direction I_{c+} (solid) and in negative direction I_{c-} (dashed) is shown. Clear cusps because of 0 to π like transitions are visible. Furthemore, a difference between I_{c+} and I_{c-} is present, which results in different positions of the minima in I_c for the different directions. Figure adapted from [28].

gle subband case, again pronounced cusps are visible corresponding to the 'π-like' transitions. A clear difference is visible between I_{c+} and I_{c-} at finite B which results different positions of the cusps in B.

Since the model in [28] was developed to explain our experimental findings, we will now discuss its relevancy. The cusps in I_c as a function of B found in the experiment are explained in the model as resulting from Zeeman interaction and SOI. This is reasonable, and in line with older diffusive junction theory. Furthermore, the presence of a ϕ_0-junction is suggested, which in the case of multiple subbands results in different I_{c+} and I_{c-}, which, to some extend, was observed experimentally. As we pointed out before, the experimental evidence found for the ϕ_0-junction scenario is inconclusive and should rather be viewed as an interesting and stimulating find to pursue further in future experiments.

Aside from these overall remarks, there are also a number of relevant features not included in the model. Firstly, the short junction limit is assumed. However, our junctions are in the long limit ($L \geq \xi$). This means that some contribution can be expected from continuum levels with $E > \Delta$, and, furthermore, that analytic expressions found will not fully apply. On the other hand, the effects induced by Zeeman interaction and Rashba SOI will still be present, though the quantitative picture may change. Secondly, in the model perfect interfaces and a mean free path 5 to 10 times larger than the actual experimental value are assumed. Again, we expect this to lead to quantitative changes, but not to a completely altered picture of the ongoing physics. Thirdly, the orbital interference effect is not included. As discussed in section 4.3.3, this effect is expected to result in additional cusps in the B dependence of I_c. Not including this effect further complicates quantitative comparison between model and experiment.

To summarize, the results obtained by [28] provide a highly relevant and interesting framework to our experimental findings. To allow for quantitative compari-

son, however, more realistic simulations are required, which include non-ideal interfaces, stronger disorder, the long junction limit and most importantly, the orbital interference effect.

4.5 REMARKS ON DETECTION OF MAJORANA BOUND STATES IN INSB BASED JOSEPHSON JUNCTIONS

Finally, we discuss the relevance of our experiment and device geometry to a number of experiments which may possible detect the existence of Majorana bound states in the device. We discuss oscillations or re-entrant supercurrent in B due to overlapping MBS's, disappearing odd Shapiro steps due to the 4π-effect and tunneling spectroscopy into a MBS's in an S-NW-S geometry.

4.5.1 OSCILLATIONS OF SUPERCURRENT CAUSED BY MAJORANA BOUND STATES

In a recent theory work by San-Jose et al. [30], a possible detection scheme for the presence of MBS's in the junction was proposed, relying on supercurrent measurement as a function of magnetic field. The main point is straightforward to understand: Imagine both superconducting nanowire sections undergoing a topological phase transition such that two topological superconductors form a Josephson junction. Assuming the outermost MBS's to be far away, the two innermost MBS's will form zero energy bound states at both sides of the junction. These inner MBS's not only give rise to the 4π Josephson effect, as discussed earlier, but they also add a contribution to the supercurrent of a single JJ. This means that upon entering the topologically non-trivial phase, an increase in supercurrent is expected, which is suggested by the authors as an additional signature of Majorana fermions.

Generally, such an increase will happen on top of supercurrent carried by the other, trivial ABS's. Our measurements clearly show that already several trivial causes may result in a revival of supercurrent as a function of magnetic field. In the transparent device regime studied here it is therefore impossible to discriminate an increase in supercurrent caused by the occurrence of MBS's in the device. This was already realized by San-Jose et al. [30], who suggest, therefore, to operate the device in the tunneling regime (unexplored here). The amount of supercurrent via the MBS's is supposed to scale with junction transmission $\sqrt{T}$ whereas normal supercurrent should scale with T. Therefore, by operating the device in a regime where at $B = 0$ T Cooper pair transport is fully suppressed, a supercurrent occurring at finite B carried by MBS's would mark the onset of the topologically non-trivial phase.

Although the nanowires used in this research are very clean and of high quality, they never reach zero conductance in a completely smooth, monotonous manner as is clearly visible in Figure 4.2d. Instead, rather significant conductance fluctuations are present near pinch off which will translate into significant conductance fluctuations as a function of B due to the rapid growth of the spin splitting. Finally, in Figure 4.12 clear evidence is shown of tiny supercurrents of trivial origin

surviving deep in the tunneling regime. These two considerations of B dependent conductance fluctuations and trivial supercurrent at low T, together with the Zeeman interaction and orbital interference caused oscillations of supercurrent in B, will very likely result in similar features, as proposed by San-Jose et al. [30], that will be indistinguishable in its cause. This unfortunately implies that the MBS detection method put forward by San-Jose et al. [30] will likely not work out in a realistic experiment.

4.5.2 DISAPPEARANCE OF ODD SHAPIRO STEPS DUE TO MAJORANA BOUND STATES

We comment on observing the 4π Josephson effect in a Shapiro step measurement. In the case of MBS's at both sides of the junction, disappearance of the odd integer Shapiro steps is expected. It is not completely unreasonable to expect this to happen, since the superconducting nanowire sections of the device are in no aspect different from those studied in our tunneling spectroscopy work, as reported in [5], where a promising signature of a Majorana bound state has been observed. However, no disappearance of odd integer Shapiro steps has been found in the experiment.

By now several theory works [31, 32] have shown that the signature of the 4π Josephson effect in Shapiro steps is sensitive to the used microwave drive frequency and power. This complicates experimental observation of this effect significantly. Furthermore, from a more practical viewpoint, in a supercondcutor-nanowire-super-conductor device there is no possible way to independently verify whether both superconducting sections have undergone a topological phase transition. As a consequence, getting the 4π Josephson effect depends merely on a lucky coincidence of tuning gates and B field to the right regime. Because of this, we did not attempt to tune into the topologically non-trivial state in this experiment. Finally, given the fact that we already observe complex behavior of integer and fractional Shapiro steps as a function of B in several devices, we are skeptical about the feasibility of this experiment in our nanowire based JJ's. Certainly, the absence of this effect in the measurements presented here does not have any implication for the validity and interpretation of our tunneling spectroscopy work.

As a more general note it should be realized that observing the 4π Josephson effect is more nuanced than may have been suggested earlier. Under certain circumstances, Landau-Zener transitions may occur between nearby ABS's and/or the continuum outside the gap, thus creating an apparent 4π behavior which is not related to topological superconductivity. Such behavior has indeed been observed in single Cooper pair transistors [33]. The take home message is that even upon observing a 4π signature, possibly in Shapiro steps, a careful study of its behavior in parameter space is required to conclude that it supports an MBS hypothesis. In that sense, the role of the 4π Josephson effect in establishing MBS's in no way differs from the tunneling spectroscopy measurements discussed elsewhere in this thesis.

4.5.3 SUPERCURRENTS AND ZERO BIAS PEAKS AT FINITE MAGNETIC FIELD

A final point we address here is the usability of S-NW-S devices in tunneling spectroscopy experiments with the objective to find signatures of MBS's. A few studies [34–36] report on data in an MBS context in such devices.

The results presented in Figure 4.12 show our main point. By putting a negative voltage on one of the local gates controlling the superconcutor-nanowire-superconductor junction of device 2 and varying a gate next to it, a tunneling regime is created with quantum dot like features. This corresponds to a regime comparable to V_{gate} < -0.5 V shown in Figure 4.2d for device 1. The result of a current biased measurement in this regime is shown in Figure 4.12a, showing a couple of conductance resonances crossing the Fermi level. A very small (sometimes 1 pA) supercurrent is visible in parts of this gate range. Interestingly, for gate regimes with lower resistance the supercurrent initially grows, as expected, but then completely loses its contrast. It is unclear if it disappears, or if the signal becomes too small to measure. We focus here on the B dependent behavior as shown in Figure 4.12b,c,d. Picking a gate position with no initially visible supercurrent, in a current biased measurement, at around 200 mT a small supercurrent shows up in a slightly more resistive regime. Such a small supercurrent may show up in a differential conductance measurement as a small zero bias peak (ZBP). Indeed, upon switching to a voltage biased differential conductance measurement, a small ZBP with height $\sim 0.01\frac{2e^2}{h}$ is found. The ranges in which the supercurrent is visible in a current biased measurement and in which the ZBP is visible in a voltage biased measurement partially overlap.

The survival of small supercurrents into the tunneling regime and up to high B fields of 2 T (Figure 4.7) make it not unlikely to have supercurrent induced ZBP's in a differential conductance measurement at finite B. Because of this, any ZBP found in an S-NW-S device fitting the MBS hypothesis should be carefully assessed on its possible origin in supercurrent. The devices in [34–36] are typically operated away from the tunneling regime, with a conductance typically in the order of 1-2 $\frac{2e^2}{h}$. Such relatively transparent regimes may very well allow for small supercurrents up to the highest B fields investigated in [34–36]. Furthermore, these studies involve clear quantum dot features, which may easily provide the necessary conductance fluctuations to have supercurrents repeatedly onsetting and disappearing at finite B. We believe that discriminating between these two is very often impossible, implying that finding convincing evidence for the presence of MBS's by measuring ZBP's in an S-NW-S geometry is impossible and should not be pursued.

4.6 CONCLUSIONS

In this work we have focused on the behavior of InSb Josephson junctions at finite magnetic field. Development of transparent superconducting contacts using a high critical magnetic field superconductor (NbTiN) combined with local gates, enabled

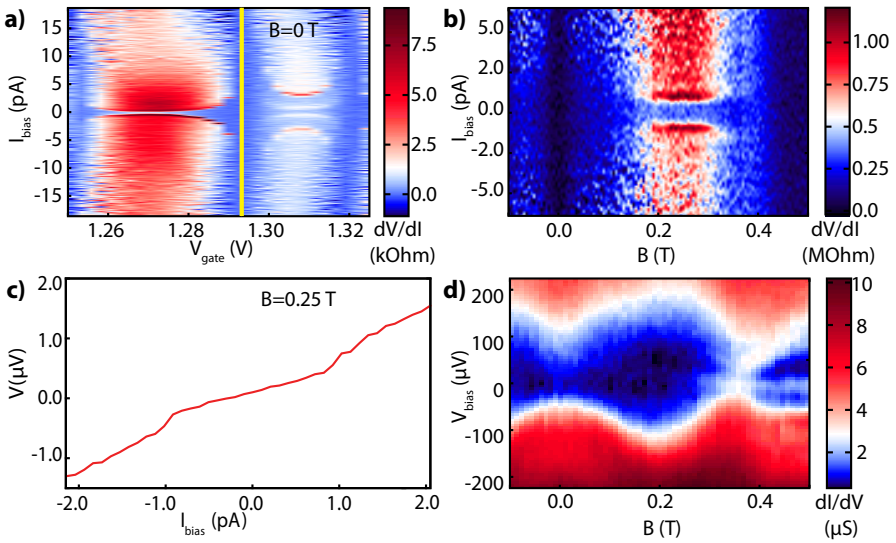

Figure 4.12 |Supercurrents and zero bias peaks at finite B. a) Differential resistance vs gate. All gates are highly positive (+1.5 V) except one local gate, which is at -0.445 V. This creates a quantum dot like regime, with conductance below $0.1 * 2e^2/h$, comparable to the low gate voltage regime in Figure 4.2d. In the panel shown here one of the positive gate voltages is varied to move through a couple of conductance resonances in the device. Importantly, a very small, but finite, supercurrent is still present in the more resistive regimes. Around 1.29 V no supercurrent is visible, although the resistance in the normal state is lower. b) Differential resistance vs B at the indicated gate position in a). Beteween 0.2 and 0.3 T, a small supercurrent is visible. c) Linecut from b) at B = 0.25 T, explicitly showing the supercurrent. A large residual slope is present in the superconducting regime. d) Differential conductance vs B corresponding to b). Importantly, a weak zero bias peak is present above 0.25 T, partially coinciding with the supercurrent visible in b). Numerical derivative of original $V(I)$ curves is shown in a) and b). Data is from device 2.

observing a gate controllable supercurrent at finite magnetic field. This makes the system an excellent candidate to create a topological Josephson junction for observing and studying the 4π Josephson effect.

A novel type of behavior is observed upon applying a magnetic field to the Josephson junction: strong cusps in the supercurrent which fit well in the model of a Zeeman interaction induced 0 to π transition in a junction with non-sinusoidal CPR. This hypothesis is further enhanced by the observation of fractional Shapiro steps being most prominent around such a cusp. However, a conclusive discrimination of the Zeeman induced 0 to π transition from the orbital interference effect is not possible. An additional observation is the dependence of the critical current on the sweep direction of current bias. Recent theory work links this behavior to the possibility of having a ϕ_0-junction, but the data presented does not allow for conclusions on this suggestion. Furthermore, we have observed small but finite supercurrents up to 2 T in a 940 nm long junction, a record among group III-V nanowire based Josephson junctions. Altogether these results show how the combination of one dimensionality, strong Zeeman interaction, strong SOI and large critical B field provide a rich playground to study new phenomena in the Josephson effect.

Two possible directions of future research can be identified. Firstly, from a theoretical perspective, to understand our data quantitatively more realistic numerical simulations are needed. These should include a realistic three dimensional device geometry, realistic interface transparency and disorder strengths. Most importantly, the orbital interference effect should be taken into account since it may give rise to features qualitatively similar to our observations. Secondly, from an experimental viewpoint, although the current dataset is highly supportive of the Zeeman π-junction hypothesis, CPR measurements should be decisive here. Besides, CPR measurements may reveal the presence of a ϕ_0-junction in the devices of which the groundstate phase ϕ_0 may be tuned by gates and/or the magnetic field. This would be an exciting new phenomenon, not observed in any Josephson junction to date. Finally, understanding trivial effects on the CPR is of uttermost importance to the direction of detecting the 4π Josephson effect.

Our work has two clear implications to the direction of detecting MBS's. Firstly, it has been predicted that the occurrence of MBS's may give rise to a revival of supercurrent at finite magnetic field [30]. Our work in the transparent device regime clearly shows such features, which are attributed here to non-topological causes. Understanding and controlling such oscillations is absolutely necessary to assess whether they may be discriminated from possible oscillations in supercurrent resulting from the presence of MBS's. Given the complex behavior observed here this seems impossible in this regime. Secondly, supercurrents may give rise to a zero bias conductance peak unrelated to MBS's, potentially up to high fields of ~ 2 T. We believe that this is a detrimental possibility, inherent to using S-NW-S devices as tunnel spectroscopy tools for detecting MBS's. Such an approach should therefore not be pursued and arguments based on its usage towards detection of MBS's are disputable [34–36].

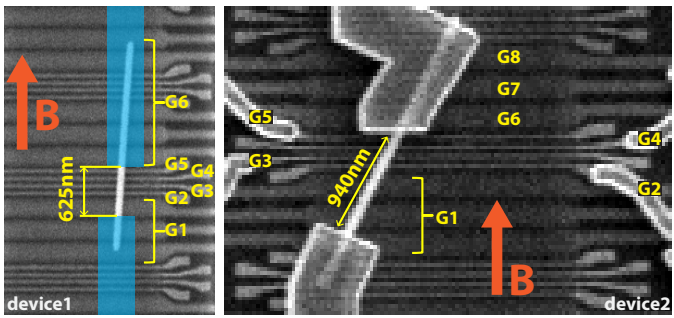

Figure 4.13 |Outline of device 1 (left) and device 2 (right). No SEM image of device 1 after finishing fabrication is available, geometry of the NbTiN contacts is indicated here in blue. Importantly, device 1 is aligned with the magnetic field within the chip mounting precision of ±5°. In contrast, device 2 has an angle of SS25°±5° with the magnetic field. In both devices, not all local gates are operated independently: as indicated in the figures, larger gates are formed by shorting some of the local gates together.

4.7 SUPPLEMENTARY INFORMATION

4.7.1 DEVICE DETAILS

Schematics based on SEM pictures of the two devices discussed in the main text are shown in Figure 4.13. In situ argon plasma etching in the deposition chamber right before deposition of NbTiN is employed as the contact preparation technique. For more extensive details on fabrication see chapters 3 and 8.

The most important differences between device 1 and device 2 are the different junction length (625 vs 940 nm respectively) and the angle of the nanowire with respect to the magnetic field (0° ± 5° vs 25° ± 5° respectively). In the measurements on device 1, gate G4 is varied in Figure 4.2d and gate G1 is varied in Figures 4.4 and 4.14.

4.7.2 OVERVIEW OF RELEVANT ENERGY AND LENGTH SCALES

ZEEMAN ENERGY E_Z

The Zeeman energy $E_Z = 1/2 g\mu_B B$ is estimated to be 1.6 meV/T, based on effective g-factor $g = 55$. This value for g is extracted from magnetic field dependent spin splitting observed in several quantum point contacts (for an example see [22]).

MEAN FREE PATH l

The mean free path l is estimated to be $l \sim 100$ nm. This is based on a field effect mobility study [37] in the same type of InSb nanowires used here.

THOULESS ENERGY E_T

The Thouless energy E_T is defined as $E_T = \frac{\hbar D}{L^2}$, we use the 3D diffusion constant $D = \frac{1}{3} v_F l$ with Fermi velocity $v_F = \sqrt{\frac{2E_F}{m_0}}$ where $m_0 = 0.014 m_e$ is the effective mass in InSb and m_e is the electron mass. The estimate in section 4.3.2 is based on E_F = 20 meV, l = 100 nm, and L = 625 nm, resulting in E_T = 40 μeV. Given the accuracy of the numbers any E_T in the 10^{-5} range is reasonable.

SUPERCONDUCTING GAP Δ

The effective superconducting gap in the nanowire sections underneath the superconducting contacts is estimated to be 0.1-0.5 meV. This is based on gate dependent voltage biased measurements in device 1 and in other devices fabricated with the same contact preparation method.

4

SUPERCONDUCTING COHERENCE LENGTH ξ

The effective superconducting coherence length in the nanowire ξ is estimated to be between 0.3 and 1.0 μm in the ballistic limit, $\xi_{\text{ballistic}} = \frac{\hbar v_F}{\pi \Delta}$. In the diffusive limit, $\xi_{\text{diffusive}} = \sqrt{\xi_{\text{ballistic}} l}$, a similar order of magnitude is expected.

SPIN ORBIT LENGTH l_{SO}

The spin orbit length l_{SO} is estimated to be $l_{SO} \sim 200$ nm based on earlier quantum dot experiments in InSb nanowires. In more recent weak anti localization measurements values up to a factor 2 smaller are found [24] such that $l_{SO} \sim 100$ nm.

SUPERCONDUCTING PENETRATION DEPTH OF NBTIN λ_{NbTiN}

Based on the effective area of nanowire SQUIDS made out of NbTiN measured in our group, the superconducting penetration depth of the NbTiN film is estimated to be $\lambda_{\text{NbTiN}} \sim 250$ nm.

4.7.3 DISCUSSION OF $I_c R_N$

The observed switching voltage of 32 μV is small compared to the superconducting gap Δ_{NbTiN} of bulk NbTiN, which is 1.5-2.0 meV. Contrary to this, in the short junction limit the $I_c R_n$ product is expected to be close to Δ. This discrepancy can be understood based on the following considerations.

Firstly, it is difficult to estimate what the relevant energy scale is for the effective gap Δ, since the system under consideration is not a simple superconduct-insulator- superconductor junction. Instead it is a rather complex cascade of bulk NbTiN S, proximitized nanowire S', normal nanowire N, proximitized nanowire S' and bulk NbTiN S, effectively leading to an S-S'-N-S'-S type junction. The properties of the interface between nanowire and superconductor play a particularly crucial role in determining Δ in the nanowire, see chapter 8. Based on tunneling spectroscopy measurements the relevant energy scale is expected to be in the hundreds of μeV range, lowering the discrepancy between switching voltage and Δ to a factor of ~10.

Secondly, only in the short junction limit $L << \xi$, with L the junction length and ξ the effective superconducting coherence length, the I_cR_n product is expected to be of the order of the superconducting gap. Since we expect ξ to be between 0.1 and 1.0 μm, with $L = 0.625$ μm, $L >\sim \xi$. This implies that the simple quantitative correspondence between I_cR_n and Δ does not hold. The qualitative behavior, however, namely that $I_cR_n = constant$, should still hold, which is reflected in the switching voltage being constant over a wide gate range.

Thirdly, the number quoted as I_cR_n in the main text is actually only the switching voltage. This is an important difference, since upon switching to the normal state the junction is still deep inside the superconducting gap. Hence we can expect a significant contribution of Andreev reflection to the transport. This results in a lower resistance, up to a factor 2 in the ideal interface case, compared to the actual R_N.

Finally, the measured switching current, at which the junction switches from superconducting to normal state, is an effective switching current determined, not only by the junction's intrinsic critical current I_c, but also by the electromagnetic environment. This may lead to a considerably smaller observed switching current compared to the intrinsic I_c of the junction. Since we operate the junction in the transparent regime, the junction's normal state resistance will be of the same order throughout the measurements and no strong fluctuations in the junction's electromagnetic environment are expected. The junction's effective switching current is therefore expected to be a constant downscaling of the intrinsic I_c. This is consistent with the observation of a constant switching voltage over a wide gate range.

In summery, the above arguments make the observation of the switching voltage being roughly an order of magnitude smaller compared to Δ reasonable. The fact that the switching voltage is constant (within $\sim$ 20%) over wide gate ranges still indicates however that this quantity is qualitatively representative of the actual I_cR_n product.

4.7.4 ADDITIONAL DATA ON OSCILLATING SUPERCURRENTS

In Figure 4.14 additional B dependencies are shown for device 1, for gate values close to the gate values of Figure 4.4. This further illustrates the behavior discussed in the main text. Such behavior is found upon varying the gate potential of several gates, while remaining in the transparent device regime. Obtaining supercurrent oscillations in B is, in all these measurements, a very general observation highly insensitive to the actual gate configuration. Gate tunability of these oscillations is also observed very generally, but the data shown in Figures 4.4 and 4.14 does correspond to a gate range with particularly strong tunability of the oscillations. Very similar behavior is observed in device 2.

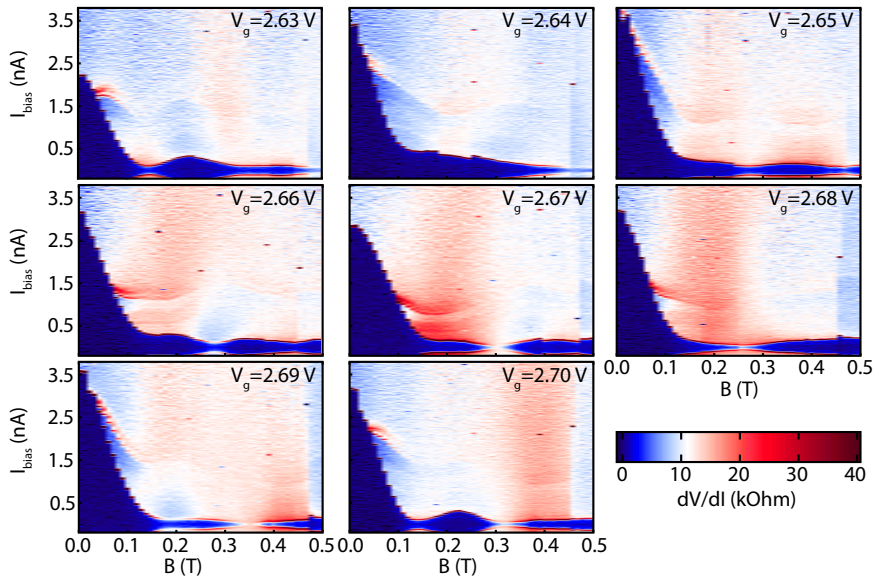

Figure 4.14 |Additional B dependencies of supercurrent for the gate range discussed in Figure 4.4. $V_g = 2.68$ V and $V_g = 2.70$ V are the same data as in Figures 4.4a,b. Numerical derivative of original $V(I)$ curves is shown in all panels. Data is taken from device 1, first cooldown.

REFERENCES

[1] A. Y. Kitaev, "Unpaired majorana fermions in quantum wires," *Physics-Uspekhi*, vol. 44, no. 10S, p. 131, 2001.

[2] R. M. Lutchyn, J. D. Sau, and S. D. Sarma, "Majorana fermions and a topological phase transition in semiconductor-superconductor heterostructures," *Physical review letters*, vol. 105, no. 7, p. 077001, 2010.

[3] Y. Oreg, G. Refael, and F. von Oppen, "Helical liquids and majorana bound states in quantum wires," *Physical review letters*, vol. 105, no. 17, p. 177002, 2010.

[4] L. Fu and C. L. Kane, "Josephson current and noise at a superconductor/quantum-spin-hall-insulator / superconductor junction," *Physical Review B*, vol. 79, no. 16, p. 161408, 2009.

[5] V. Mourik, K. Zuo, S. Frolov, S. Plissard, E. Bakkers, and L. Kouwenhoven, "Signatures of majorana fermions in hybrid superconductor-semiconductor nanowire devices," *Science*, vol. 336, no. 6084, pp. 1003–1007, 2012.

[6] Y.-J. Doh, J. A. van Dam, A. L. Roest, E. P. Bakkers, L. P. Kouwenhoven, and S. De Franceschi, "Tunable supercurrent through semiconductor nanowires," *science*, vol. 309, no. 5732, pp. 272–275, 2005.

[7] J. A. Van Dam, Y. V. Nazarov, E. P. Bakkers, S. De Franceschi, and L. P. Kouwenhoven, "Supercurrent reversal in quantum dots," *Nature*, vol. 442, no. 7103, pp. 667–670, 2006.

[8] G. de Lange, B. van Heck, A. Bruno, D. van Woerkom, A. Geresdi, S. Plissard, E. Bakkers, A. Akhmerov, and L. DiCarlo, "Realization of microwave quantum circuits using hybrid superconducting-semiconducting nanowire josephson elements," *arXiv preprint arXiv:1503.08483*, 2015.

[9] T. Larsen, K. Petersson, F. Kuemmeth, T. Jespersen, P. Krogstrup, J. Nygard, and C. Marcus, "A semiconductor nanowire-based superconducting qubit," *arXiv preprint arXiv:1503.08339*, 2015.

[10] Y. V. Nazarov and Y. M. Blanter, *Quantum transport: introduction to nanoscience*. Cambridge University Press, 2009.

[11] V. Ryazanov, V. Oboznov, A. Y. Rusanov, A. Veretennikov, A. Golubov, and J. Aarts, "Coupling of two superconductors through a ferromagnet: evidence for a π junction," *Physical review letters*, vol. 86, no. 11, p. 2427, 2001.

[12] J. Baselmans, A. Morpurgo, B. Van Wees, and T. Klapwijk, "Reversing the direction of the supercurrent in a controllable josephson junction," *Nature*, vol. 397, no. 6714, pp. 43–45, 1999.

[13] T. Heikkilä, F. K. Wilhelm, and G. Schön, "Non-equilibrium supercurrent through mesoscopic ferromagnetic weak links," *EPL (Europhysics Letters)*, vol. 51, no. 4, p. 434, 2000.

[14] E. Demler, G. Arnold, and M. Beasley, "Superconducting proximity effects in magnetic metals," *Physical Review B*, vol. 55, no. 22, p. 15174, 1997.

[15] S. Frolov, D. Van Harlingen, V. Oboznov, V. Bolginov, and V. Ryazanov, "Measurement of the current-phase relation of sfs pi-josephson junctions," *arXiv preprint cond-mat/0402434*, 2004.

[16] S. M. Frolov, M. J. Stoutimore, T. A. Crane, D. J. Van Harlingen, V. A. Oboznov, V. V. Ryazanov, A. Ruosi, C. Granata, and M. Russo, "Imaging spontaneous currents in superconducting arrays of π-junctions," *Nature Physics*, vol. 4, no. 1, pp. 32–36, 2008.

[17] M. Weides, M. Kemmler, H. Kohlstedt, A. Buzdin, E. Goldobin, D. Koelle, and R. Kleiner, "High quality ferromagnetic 0 and pi josephson tunnel junctions," *arXiv preprint cond-mat/0604097*, 2006.

[18] M. Tinkham, *Introduction to superconductivity*. Courier Corporation, 2012.

[19] H. Courtois, M. Meschke, J. Peltonen, and J. P. Pekola, "Origin of hysteresis in a proximity josephson junction," *Physical review letters*, vol. 101, no. 6, p. 067002, 2008.

[20] P. Jarillo-Herrero, J. A. Van Dam, and L. P. Kouwenhoven, "Quantum supercurrent transistors in carbon nanotubes," *Nature*, vol. 439, no. 7079, pp. 953–956, 2006.

[21] H. Nilsson, P. Samuelsson, P. Caroff, and H. Xu, "Supercurrent and multiple andreev reflections in an insb nanowire josephson junction," *Nano letters*, vol. 12, no. 1, pp. 228–233, 2011.

[22] I. van Weperen, S. R. Plissard, E. P. Bakkers, S. M. Frolov, and L. P. Kouwenhoven, "Quantized conductance in an insb nanowire," *Nano letters*, vol. 13, no. 2, pp. 387–391, 2012.

[23] S. R. Plissard, D. R. Slapak, M. A. Verheijen, M. Hocevar, G. W. Immink, I. van Weperen, S. Nadj-Perge, S. M. Frolov, L. P. Kouwenhoven, and E. P. Bakkers, "From insb nanowires to nanocubes: looking for the sweet spot," *Nano letters*, vol. 12, no. 4, pp. 1794–1798, 2012.

[24] I. van Weperen, B. Tarasinski, D. Eeltink, V. Pribiag, S. Plissard, E. Bakkers, L. Kouwenhoven, and M. Wimmer, "Spin-orbit interaction in insb nanowires," *Physical Review B*, vol. 91, no. 20, p. 201413, 2015.

[25] S. Nadj-Perge, V. Pribiag, J. Van den Berg, K. Zuo, S. Plissard, E. Bakkers, S. Frolov, and L. Kouwenhoven, "Spectroscopy of spin-orbit quantum bits in indium antimonide nanowires," *Physical review letters*, vol. 108, no. 16, p. 166801, 2012.

[26] J. Van den Berg, S. Nadj-Perge, V. Pribiag, S. Plissard, E. Bakkers, S. Frolov, and L. Kouwenhoven, "Fast spin-orbit qubit in an indium antimonide nanowire," *Physical review letters*, vol. 110, no. 6, p. 066806, 2013.

[27] K. Gharavi, G. W. Holloway, C. M. Haapamaki, M. H. Ansari, M. Muhammad, R. R. LaPierre, and J. Baugh, "Josephson interference due to orbital states in a nanowire proximity effect junction," *arXiv preprint arXiv:1405.7455*, 2014.

[28] T. Yokoyama, M. Eto, and Y. V. Nazarov, "Anomalous josephson effect induced by spin-orbit interaction and zeeman effect in semiconductor nanowires," *Physical Review B*, vol. 89, no. 19, p. 195407, 2014.

[29] T. Yokoyama, M. Eto, and Y. V. Nazarov, "Josephson current through semiconductor nanowire with spin–orbit interaction in magnetic field," *Journal of the Physical Society of Japan*, vol. 82, no. 5, p. 054703, 2013.

[30] P. San-Jose, E. Prada, and R. Aguado, "ac josephson effect in finite-length nanowire junctions with majorana modes," *Physical review letters*, vol. 108, no. 25, p. 257001, 2012.

[31] F. Domínguez, F. Hassler, and G. Platero, "Dynamical detection of majorana fermions in current-biased nanowires," *Phys. Rev. B*, vol. 86, p. 140503, Oct 2012.

[32] D. M. Badiane, L. I. Glazman, M. Houzet, and J. S. Meyer, "Ac josephson effect in topological josephson junctions," *Comptes Rendus Physique*, vol. 14, no. 9, pp. 840–856, 2013.

[33] P.-M. Billangeon, F. Pierre, H. Bouchiat, and R. Deblock, "Ac josephson effect and resonant cooper pair tunneling emission of a single cooper pair transistor," *Physical review letters*, vol. 98, no. 21, p. 216802, 2007.

[34] M. Deng, C. Yu, G. Huang, M. Larsson, P. Caroff, and H. Xu, "Anomalous zero-bias conductance peak in a nb–insb nanowire–nb hybrid device," *Nano letters*, vol. 12, no. 12, pp. 6414–6419, 2012.

[35] M. Deng, C. Yu, G. Huang, M. Larsson, P. Caroff, and H. Xu, "Parity independence of the zero-bias conductance peak in a nanowire based topological superconductor-quantum dot hybrid device," *Scientific reports*, vol. 4, 2014.

[36] A. Finck, D. Van Harlingen, P. Mohseni, K. Jung, and X. Li, "Anomalous modulation of a zero-bias peak in a hybrid nanowire-superconductor device," *Physical review letters*, vol. 110, no. 12, p. 126406, 2013.

[37] Ö. Gül, D. J. van Woerkom, I. van Weperen, D. Car, S. R. Plissard, E. P. Bakkers, and L. P. Kouwenhoven, "Towards high mobility insb nanowire devices," *Nanotechnology*, vol. 26, no. 21, p. 215202, 2015.

5

SIGNATURES OF MAJORANA FERMIONS IN HYBRID SUPERCONDUCTOR-SEMICONDUCTOR NANOWIRE DEVICES

Majorana fermions are particles identical to their own antiparticles. They have been theoretically predicted to exist in topological superconductors. Here, we report electrical measurements on indium antimonide nanowires contacted with one normal (gold) and one superconducting (niobium titanium nitride) electrode. Gate voltages vary electron density and define a tunnel barrier between normal and superconducting contacts. In the presence of magnetic fields on the order of 100 millitesla, we observe bound, midgap states at zero bias voltage. These bound states remain fixed to zero bias, even when magnetic fields and gate voltages are changed over considerable ranges. Our observations support the hypothesis of Majorana fermions in nanowires coupled to superconductors.

[1] Vincent Mourik and Kun Zuo took equal shares in all aspects of this research (sample fabrication, measurements, data analysis and reporting results).
[2] In collaboration with S. M. Frolov, S. R. Plissard, E. P. A. M. Bakkers, L.P. Kouwenhoven. This chapter is published in *Science*

5.1 INTRODUCTION

All elementary particles have an antiparticle of opposite charge (for example, an electron and a positron); the meeting of a particle with its antiparticle results in the annihilation of both. A special class of particles, called Majorana fermions, are predicted to exist that are identical to their own antiparticle ([1]). They may appear naturally as elementary particles or emerge as charge-neutral and zero-energy quasi-particles in a superconductor ([2], [3]). Particularly interesting for the realization of qubits in quantum computing are pairs of localized Majoranas separated from each other by a superconducting region in a topological phase ([4–11]).

On the basis of earlier and later semiconductor-based proposals ([6], [7]), Lutchyn et al. ([8]) and Oreg et al. ([9]) have outlined the necessary ingredients for engineering a nanowire device that should accommodate pairs of Majoranas. The starting point is a one-dimensional (1D) nanowire made of semiconducting material with strong spin-orbit interaction (Fig. 5.1 A). In the presence of a magnetic field B along the axis of the nanowire (i.e., a Zeeman field), a gap is opened at the crossing between the two spin-orbit bands. If the Fermi energy μ is inside this gap, the degeneracy is twofold, whereas outside the gap it is fourfold. The next ingredient is to connect the semiconducting nanowire to an ordinary s-wave superconductor (Fig. 5.1A). The proximity of the superconductor induces pairing in the nanowire between electron states of opposite momentum and opposite spins and induces a gap, Δ. Combining this twofold degeneracy with an induced gap creates a topological superconductor ([2], [3]). Particularly interesting for the realization of qubits in quantum computing are pairs of localized Majoranas separated from each other by a superconducting region in a topological phase ([4–11]). The condition for a topological phase is $E_Z > \sqrt{\Delta^2 + \mu^2}$, with the Zeeman energy $E_Z = g\mu_B B/2$ (g is the Landé g factor, μ_B is the Bohr magneton). Near the ends of the wire, the electron density is reduced to zero, and subsequently, μ will drop below the subband energies such that μ^2 becomes large. At the points in space where $E_Z > \sqrt{\Delta^2 + \mu^2}$, Majoranas arise as zero-energy (i.e., midgap) bound states one at each end of the wire ([2], [3]). Particularly interesting for the realization of qubits in quantum computing are pairs of localized Majoranas separated from each other by a superconducting region in a topological phase ([4], [8–11]).

Despite their zero charge and energy, Majoranas can be detected in electrical measurements. Tunneling spectroscopy from a normal conductor into the end of the wire should reveal a state at zero energy ([12–14]). Here, we report the observation of such zero-energy peaks and show that they rigidly stick to zero energy while changing B and gate voltages over large ranges. Furthermore, we show that this zero-bias peak (ZBP) is absent if we take out any of the necessary ingredients of the Majorana proposals; that is, the rigid ZBP disappears for zero magnetic field, for a magnetic field parallel to the spin-orbit field, or when we take out the superconductivity.

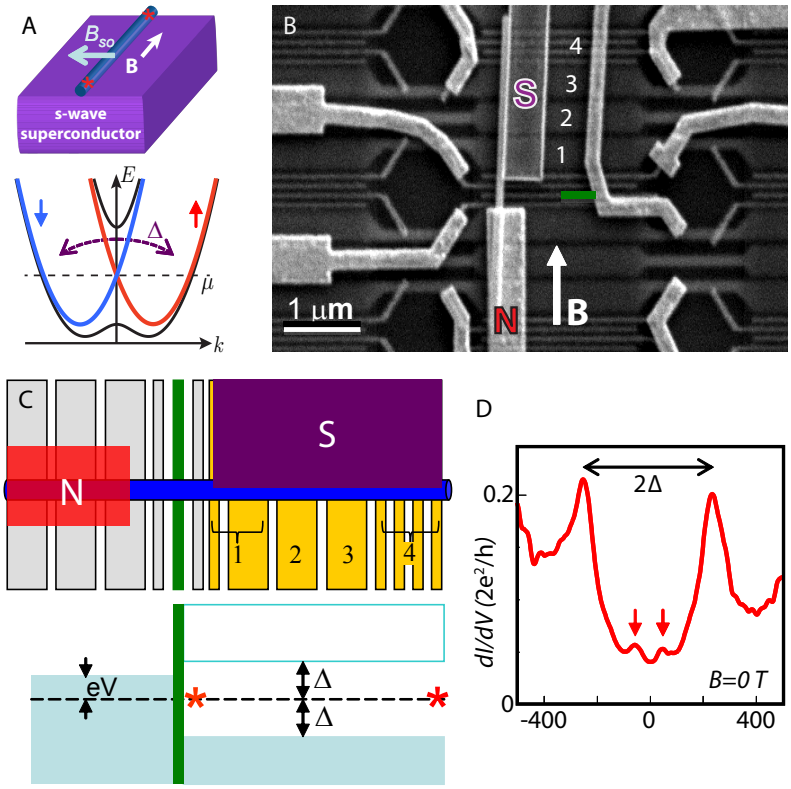
A
B_{so}
B
s-wave
superconductor
E
Δ
μ
k
B
S
4
3
2
1
1 μm
N
B
C
S
N
1
2
3
4
eV
Δ
Δ
D
2Δ
0.2
0
dI/dV (2e²/h)
B=0 T
-400
0
400

5.2 EXPERIMENTS

We use InSb nanowires ([15]), which are known to have strong spin-orbit interaction and a large g factor ([16]). From our earlier quantum-dot experiments, we extract a spin-orbit length $l_{SO} \approx 200$ nm corresponding to a Rashba parameter $\alpha \approx 0.2$ eV·Å ([17]). This translates to a spin-orbit energy scale $\alpha^2 m^*/2\hbar^2 \approx 50$ μeV (m^* = 0.015 me is the effective electron mass in InSb, me is the bare electron mass, and $\hbar$ is Planck's constant h divided by 2π). Importantly, the g factor in bulk InSb is very large (g ≈ 50), yielding $E_Z/B \approx 1.5$ meV/T. As shown below, we find an induced superconducting gap $\Delta \approx 250$ μeV. Thus, for $\mu = 0$, we expect to enter the topological phase for $B \sim 0.15$ T where E_Z starts to exceed Δ. The energy gap of the topolog-

Figure 5.1 ***(preceding page)*** |(A) Outline of theoretical proposals. (Top) Conceptual device layout with a semiconducting nanowire in proximity to an s-wave superconductor. An external B field is aligned parallel to the wire. The Rashba spin-orbit interaction is indicated as an effective magnetic field, B_{SO}, pointing perpendicular to the nanowire. The red stars indicate the expected locations of a Majorana pair. (Bottom) Energy, E, versus momentum, k, for a 1D wire with Rashba spin-orbit interaction, which shifts the spin-down band (blue) to the left and the spin-up band (red) to the right. Blue and red parabolas are for B = 0; black curves are for B ≠ 0, illustrating the formation of a gap near k = 0 of size E_Z (μ is the Fermi energy with μ= 0 defined at the crossing of parabolas at k = 0). The superconductor induces pairing between states of opposite momentum and opposite spin, creating a gap of size Δ. (B) Implemented version of theoretical proposals. Scanning electron microscope image of the device with normal (N) and superconducting (S) contacts. The S contact only covers the right part of the nanowire. The underlying gates, numbered 1 to 4, are covered with a dielectric. [Note that gate 1 connects two gates, and gate 4 connects four narrow gates; see (C).] (C) (Top) Schematic of our device. (Bottom) illustration of energy states. The green rectangle indicates the tunnel barrier separating the normal part of the nanowire on the left from the wire section with induced superconducting gap, Δ. [In (B), the barrier gate is also shown in green.] An external voltage, V, applied between N and S drops across the tunnel barrier. Red stars again indicate the idealized locations of the Majorana pair. Only the left Majorana is probed in this experiment. (D) Example of differential conductance, dI/dV, versus V at B = 0 and 65 mK, serving as a spectroscopic measurement on the density of states in the nanowire region below the superconductor. Data are from device 1. The two large peaks, separated by 2Δ, correspond to the quasi-particle singularities above the induced gap. Two smaller subgap peaks, indicated by arrows, likely correspond to Andreev bound states located symmetrically around zero energy. Measurements are performed in dilution refrigerators with the use of the standard low-frequency lock-in technique (frequency = 77 Hz, excitation = 3 μV) in the four-terminal (devices 1 and 3) or two-terminal (device 2) current-voltage geometry.

ical superconductor is estimated to be a few kelvin ([17]), if we assume a ballistic nanowire. The topological gap is substantially reduced in a disordered wire ([18], [19]). We have measured mean free paths of ~300 nm in our wires ([15]), implying a quasi-ballistic regime in micrometer-long wires. With these numbers, we expect Majorana zero-energy states to become observable below 1 K and around 0.15 T.

A typical sample is shown in Figure 5.1B. We first fabricate a pattern of narrow (50nm) and wider (300nm) gates on a silicon substrate ([20]). The gates are covered by a thin Si_3N_4 dielectric before we randomly deposit InSb nanowires. Next, we electrically contact those nanowires that have landed properly relative to the gates. The lower contact in Figure 5.1B fully covers the bottom part of the nanowire. We have designed the upper contact to only cover half of the top part of the nanowire, avoiding complete screening of the underlying gates. This allows us to change the Fermi energy in the section of the nanowire (NW) with induced superconductivity. We have used either a normal (N) or superconducting (S) material for the lower and upper contacts, resulting in three sample variations: (i) N-NW-S, (ii) N-NW-N, and (iii) S-NW-S. Here, we discuss our main results on the N-NW-S devices, whereas the other two types, serving as control devices, are described in ([20]).

To perform spectroscopy on the induced superconductor, we created a tunnel barrier in the nanowire by applying a negative voltage to a narrow gate (dark green area in Figure 5.1, B and C). A bias voltage applied externally between the N and S contacts drops almost completely across the tunnel barrier. In this setup, the differential conductance dI/dV at voltage V and current I is proportional to the density of states at energy E = eV (where e is the charge on the electron) relative to the zero-energy dashed line in Figure 5.1C. Figure 5.1D shows an example taken at B = 0. The two peaks at ± 250 μeV correspond to the peaks in the quasi-particle density of states of the induced superconductor, providing a value for the induced gap, $\Delta \approx 250$ μeV. We generally find a finite dI/dV in between these gap edges. We observe pairs of resonances with energies symmetric around zero bias superimposed on nonresonant currents throughout the gap region. Symmetric resonances likely originate from Andreev bound states ([21], [22]), whereas nonresonant current indicates that the proximity gap has not fully developed ([23]).

Figure 5.2 summarizes our main result. Figure 5.2A shows a set of dI/dV versus V traces taken at increasing B fields in 10 mT steps from 0 (bottom trace) to 490 mT (top trace), offset for clarity. We again observe the gap edges at ± 250 μeV. When we apply a B field between ± 100 and ± 400 mT along the nanowire axis, we observe a peak at V = 0. The peak has an amplitude up to $0.05 \cdot 2e^2/h$ and is clearly discernible from the background conductance. Above ± 400 mT, we observe a pair of peaks. The color panel in Figure 5.2B provides an overview of states and gaps in the plane of energy and B field from -0.5 to 1 T. The observed symmetry around B = 0 is typical for all of our data sets, demonstrating reproducibility and the absence of hysteresis. We indicate the gap edges with horizontal green dashed lines (highlighted only for B < 0). A pair of resonances crosses zero energy at ~0.65 T with a slope on the order of E_Z (highlighted by orange dotted lines). We have followed these resonances up

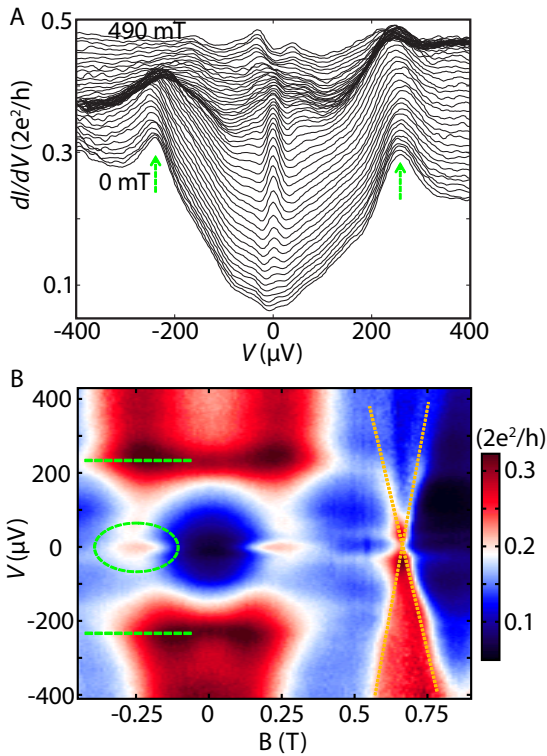

Figure 5.2 |Magnetic field-dependent spectroscopy. (A) dI/dV versus V at 70 mK taken at different B fields (from 0 to 490 mT in 10 mT steps; traces are offset for clarity, except for the lowest trace at B = 0). Data are from device 1. Arrows indicate the induced gap peaks. (B) Color-scale plot of dI/dV versus V and B. The ZBP is highlighted by a dashed oval; green dashed lines indicate the gap edges. At ~ 0.6 T, a non-Majorana state is crossing zero bias with a slope equal to ~ 3 meV/T (indicated by sloped yellow dotted lines). Traces in (A) are extracted from (B).

to high bias voltages in ([20]) and identified them as Andreev states bound within the gap of the bulk NbTiN superconducting electrodes (~ 2 meV). In contrast, the ZBP sticks to zero energy over a range of $\Delta B \sim 300$ mT centered around ~ 250 mT. Again at ~ 400 mT, we observe two peaks located at symmetric, finite biases.

To identify the origin of these ZBPs, we need to consider various options including the Kondo effect, Andreev bound states, weak antilocalization, and reflectionless tunneling versus a conjecture of Majorana bound states. ZBPs due to the Kondo effect ([24]) or Andreev states bound to s-wave superconductors ([25]) can occur at finite B; however, with changing B, these peaks then split and move to finite energy. A Kondo resonance moves with $2E_Z$ ([24]), which is easy to dismiss as the origin for our ZBP because of the large g factor in InSb. (Note that even a Kondo effect from an impurity with g = 2 would be discernible.) Reflectionless tunneling is an enhancement of Andreev reflection by time-reversed paths in a diffusive normal region ([26]). As in the case of weak antilocalization, the resulting ZBP is maximal at B = 0 and disappears when B is increased; see also ([20]). We thus conclude that the above options for a ZBP do not provide natural explanations for our observations. We are not aware of any mechanism that could explain our observations, besides the conjecture of a Majorana.

To further investigate the zero-biasness of our peak, we measured gate voltage dependences. Figure 5.3A shows a color panel with voltage sweeps on gate 2. The main observation is the occurrence of two opposite types of behavior. First, we observe peaks in the density of states that change with energy when changing gate voltage (highlighted with yellow dotted lines); these are the same resonances as shown in Figure 5.2B and analyzed in ([20]). The second observation is that the ZBP from Figure 5.2, which we take at 175 mT, remains stuck to zero bias while changing the gate voltage over a range of several volts. Clearly, our gates work because they change the Andreev bound states by ~ 0.2 meV per volt on the gate. Panels (B) and (C) in Figure 5.3 underscore this observation with voltage sweeps on a different gate, number 4. Figure 5.3B shows that, at zero magnetic field, no ZBP is observed. At 200 mT, the ZBP becomes again visible in Figure 5.3C. Comparing the effect of gates 2 and 4, we observe that neither moves the ZBP away from zero.

Initially, Majorana fermions were predicted in single-subband, 1D wires ([8], [9]), but further work extended these predictions to multisubband wires ([27–30]). In the nanowire section that is uncovered, we can gate tune the number of occupied subbands from 0 to ~ 4 with subband separations of several millielectron volts. Gate tuning in the nanowire section covered with superconductor is much less effective due to efficient screening. The number of occupied subbands in this part is unknown, but it is most likely multiple subbands. As shown in figs. S9 and S11 of ([20]), we do have to tune gate 1 and the tunnel barrier to the right regime to observe the ZBP.

We have measured in total several hundred panels sweeping various gates on different devices. Our main observations are (i) a ZBP exists over a substantial voltage range for every gate starting from the barrier gate until gate 4, (ii) we can oc-

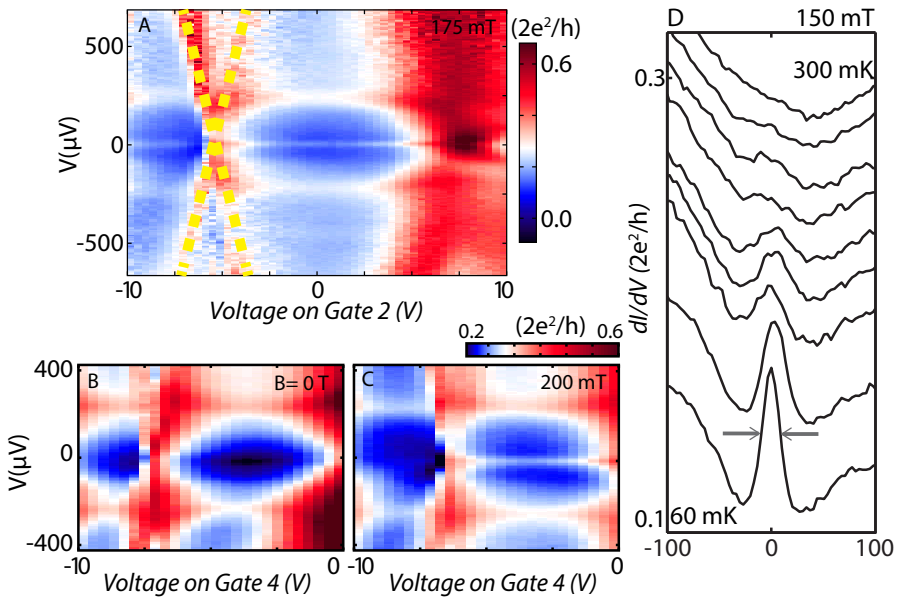

Figure 5.3 |Gate-voltage dependence. (A) A 2D color plot of dI/dV versus V and voltage on gate 2 at 175 mT and 60 mK. Andreev bound states cross through zero bias, for example, near -5 V (yellow dotted lines). The ZBP is visible from -10 to ~ 5 V (although in this color setting, it is not equally visible everywhere). Split peaks are observed in the range of 7.5 to 10 V (20). In (B) and (C), we compare voltage sweeps on gate 4 for 0 and 200 mT with the ZBP absent and present, respectively. Temperature is 50 mK. [Note that in (C) the peak extends all the way to -10 V (19).] (D) Temperature dependence. dI/dV versus V at 150 mT. Traces have an offset for clarity (except for the lowest trace) and are taken at different temperatures (from bottom to top: 60, 100, 125, 150, 175, 200, 225, 250, and 300 mK). dI/dV outside the ZBP at V = 100 μeV is 0.12 ± 0.01·2e2/h for all temperatures. A FWHM of 20 μeV is measured between the arrows. All data in this figure are from device 1.

casionally split the ZBP in two peaks located symmetrically around zero, and (iii) we can never move the peak away from zero to finite bias ([20]). Data sets such as those in Figs. 5.2 and 5.3 demonstrate that the ZBP remains stuck to zero energy over considerable changes in B and gate voltage V_g.

Figure 3D shows the temperature dependence of the ZBP. We find that the peak disappears at ~ 300 mK, providing a thermal-energy scale of kBT sim 30 μeV (where kB is Boltzmann constant and T is temperature). The full width at half maximum (FWHM) at the lowest temperature is sim 20 μeV, which we believe is a consequence of thermal broadening as 3.5·kBT(60 mK) = 18 μeV.

Next, we verify explicitly that all the required ingredients in the theoretical Majorana proposals (Figure 5.1A) are indeed essential for observing the ZBP. We have already verified that a nonzero B field is needed. We then test to see whether spin-orbit interaction is crucial for the absence or presence of the ZBP. Theory requires that the external B has a component perpendicular to B_{SO} (the spin-orbit magnetic field). We have measured a second device in a different setup containing a 3D vector magnet such that we can sweep the B field in arbitrary directions. In Figure 5.4, we show dI/dV versus V while varying the angle for a constant field magnitude. In Figure 5.4A, the plane of rotation is approximately equal to the plane of the substrate. We clearly observe that the ZBP comes and goes, depending on the angle. The ZBP is completely absent around $\pi/2$, which we thus deduce as the direction of B_{SO}. In Figure 5.4B, the plane of rotation is perpendicular to B_{SO}. Indeed, we observe that the ZBP is now present for all angles, because B is now always perpendicular to B_{SO}. These observations are in full agreement with expectations for the spin-orbit direction in our samples ([17], [31]). We have further verified that this angle dependence is not a result of the specific magnitude of B or a variation in g factor ([20]).

As a last check, we have fabricated and measured a device of identical design but with the superconductor replaced by a normal Au contact (that is, a N-NW-N geometry). In this sample, we have not found any signature of a peak that sticks to zero bias while changing both B and V_g ([20]). This test experiment shows that superconductivity is also an essential ingredient for our ZBP.

5.3 CONCLUSION

To summarize, we have reproduced our observation of a rigid ZBP in three different devices and in two different setups. Our general observations are: (i) a ZBP appears at finite B and sticks to zero bias over a range from 0.07 to 1 T; (ii) the ZBP remains at zero bias while changing the voltage on any of our gates over large ranges; (iii) the ZBP comes and goes with the angle of the B field with respect to the wire axis, which is in agreement with the expected spin-orbit interaction; and (iv) the rigid ZBP is absent when the superconductor is replaced by a normal conductor. Based on these observations, we conclude that our spectroscopy experiment provides evidence for the existence of Majorana fermions.

Improving the electron mobility and optimizing the gate coupling will enable

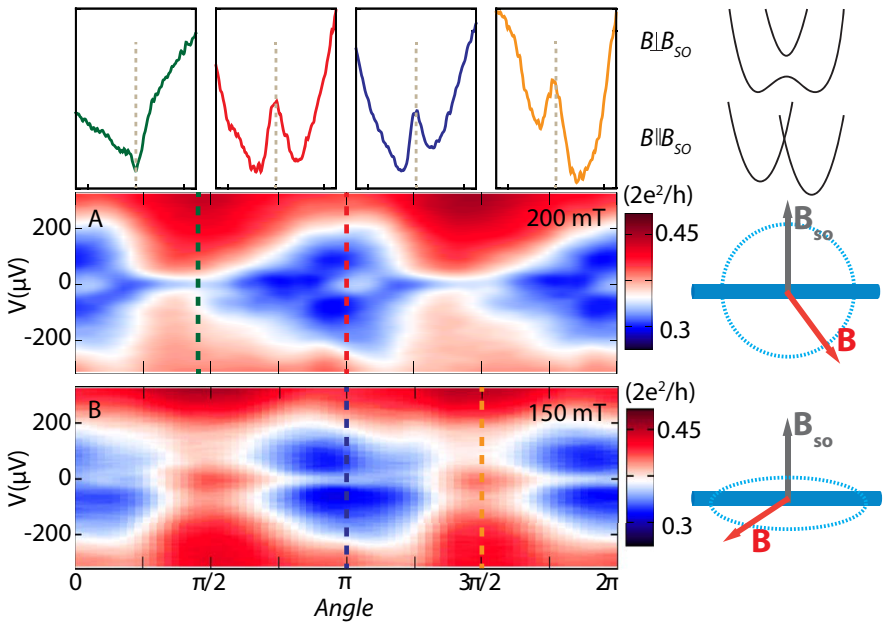

Figure 5.4 |Magnetic-field orientation dependence. dI/dV versus V and varying the angle of B at fixed magnitude. Data from device 2 are measured in a different setup at ~ 150 mK; zero angle is along the nanowire for both panels. (A) Rotation of |B| = 200 mT in the plane of the substrate. The ZBP is at a maximum when B is parallel and is absent when B is perpendicular to the wire. (B) Rotation of |B| = 150 mT in the plane perpendicular to B_{SO}. The ZBP is now present for all angles. The panels on top show linecuts at angles with corresponding colors in (A) and (B). Panels on the right side illustrate, from top to bottom: (i) For B perpendicular to B_{SO} a gap opens lifting fermion doubling, as is required for Majoranas. (ii) For B parallel to B_{SO}, the two spin bands from Figure 1A shift vertically by $2E_Z$. In this configuration, a zero-energy Majorana is not expected. (iii) Panel of rotation of B for data in (A) is shown. (iv) Panel of rotation of B for data in (B) is shown.

us to map out the phase diagram of the topological superconductor in the plane of E_Z and μ ([27–30]). It will be interesting to control the subband occupation underneath the superconductor down to a single subband to make direct comparisons to theoretical models. Currently, we probe induced gaps and states from all occupied subbands, each with a different coupling to the tunnel barrier. The topological state in the topmost subband likely has the weakest coupling to the tunnel barrier. Single-subband models ([8], [9]) predict that one should observe a closing of the topological gap; however, in multisubband systems, this gap closing may not be visible. The constant gap in Figure 5.2 may come from lower subbands. The presence of multiple subbands together with our finite temperature may also be the reason that our ZBP is currently only ~ 5% of the theoretical zero-temperature limit of $2e^2/h$ ([12], [14]).

Finally, we note that this work does not address the topological properties of Majorana fermions. The first step toward demonstrating topological protection would be the observation of conductance quantization ([12], [32]). Second, in a Josephson tunnel junction with phase difference ϕ and a pair of Majoranas on either side, the current-phase relation becomes proportional to $\sin(\phi/2)$. The factor 2 is another distinct Majorana signature, which should be observable as an h/e flux periodicity in a superconducting quantum interference device measurement ([8], [9]). The last type of experiment involves the exchange of Majoranas around each other. Such braiding experiments can reveal their non-Abelian statistics, which are the ultimate proof of topologically protected Majorana fermions ([33–35]).

5.4 SUPPLEMENTARY INFORMATION

Below we provide details of nanowire sample fabrication as well as supporting measurements from multiple devices. The main observations of the paper, i.e. zero-bias peak (ZBP) that appears at finite magnetic field and persists over a significant range of field and gate voltages, are reproduced in three N-NW-S devices measured in two setups (Figures S1, S3, S6,S7, S10). Furthermore we demonstrate S-NW-S devices and N-NW-N devices (Figures S11,S12, S13). In S-NW-S devices persistent zero-bias peaks are also observed, however they cannot be distinguished from Josephson supercurrents. In N-NW-N devices zero-bias peaks are also observed for a small range of gate voltages (Figures S12, S13), however only when gate- and field-tunable states pass through zero bias. This indicates that superconductivity is a required ingredient for the observation of a persistent zero-bias peaks.

Specifically, we present more examples of magnetic field dependences of the zero bias peak in N-NW-S devices (Figures S1, S3, S6,S7, S10). These data establish the magnetic field range of the zero bias peak from 70 mT and up to 1.0 T (varying for different gate settings). Additional gate dependences investigate the splitting of the zero-bias peak (Figures S4, S5). Examples of tunnel barrier gate dependences are provided in Fig. S9. Finally, other features that occur at zero bias are studied in Figures S2 and S8. In Figures S2 we identify Andreev bound states confined in the nanowire segment covered by the superconductor. In Figures S8 we investigate

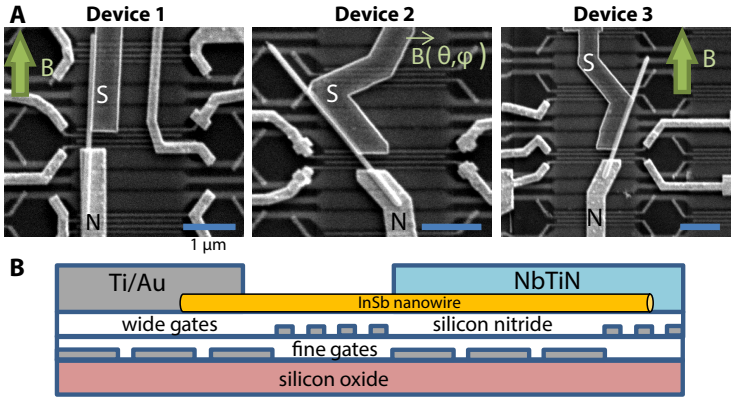

Figure S1 |N-NW-S device fabrication. A) SEM images of three N-NW-S (Normal-Nanowire-Superconductor) devices in which the main findings of this paper are reproduced. Field directions are indicated with arrows. Device 2 was measured in a 3-axis vector magnet. Devices are fabricated simultaneously. Nanowire diameters are 110±10 nm (devices 1 and 3) and 100±10 nm (device 2). B) Schematic of a device cross-section.

zero-bias peaks observed at zero magnetic field. Motivated by B-field dependence for two orthogonal orientations of field, we propose that zero-field ZBP has a different origin than the zero-bias peak at finite field which is the main topic of the investigation.

NANOWIRE GROWTH DETAILS

InSb nanowires are grown by metalorganic vapor phase epitaxy from gold catalysts, as described in Plissard et. al. Nano Lett. 2012 (DOI: 10.1021/nl203846g). The wires in this work are grown on Si substrates. First, stems that consists of InP and InAs segments are grown. Then a stacking-fault and dislocation-free zincblende InSb segment of high mobility (104-5·104cm^2/(Vs) is grown in the 111 crystal direction. A single batch of wires is used for all N-NW-S devices in this paper.

NANOWIRE GROWTH DETAILS

1. p-doped silicon substrates are covered by 285 nm of thermal oxide. Due to screening from local gates substrates are ineffective as back gates.

2. A periodic pattern of 15 micron long and 300 nm wide Ti/Au gates (5 nm/10nm) is defined by 100 kV electron beam lithography and electron beam evaporation.

3. Bottom gate layer is covered by 40 nm of lithographically defined and d.c. sputtered Si3N4 dielectric. Areas for contacts to gates are left free of dielectric.

4. A second layer of finer gates (50 nm wide, 50 nm spacing) is defined using the same method. Fine gates are fabricated in a separate step to reduce proximity exposure.

5. A second layer of Si_3N_4 covers both fine and wide gates. Thus, wide gates are covered by 80 nm of dielectric, fine gates are covered by 40 nm of dielectric.

6. InSb nanowires of 80-120 nm diameter are transferred onto the substrate containing gate patterns. Nanowires land randomly, some are selected for contacting.

7. Superconducting contacts are defined by sputtering NbTiN (75 nm) from a Nb/Ti target (70/30 at. %) with thin film critical temperature TC ~ 7 K. Sputtering done in the group of T.M. Klapwijk with assistance of D.J. Thoen. A window in the 200 nm thick PMMA 950k resist has a boundary along the center of the nanowire with alignment accuracy of 20-30 nm. Prior to sputtering nanowires are etched in Argon plasma.

8. Normal Ti/Au contacts (20 nm Ti/125 nm Au) are made to the nanowires and to the gates. Prior to the deposition of Ti/Au the nanowires are passivated in ammonium sulfide.

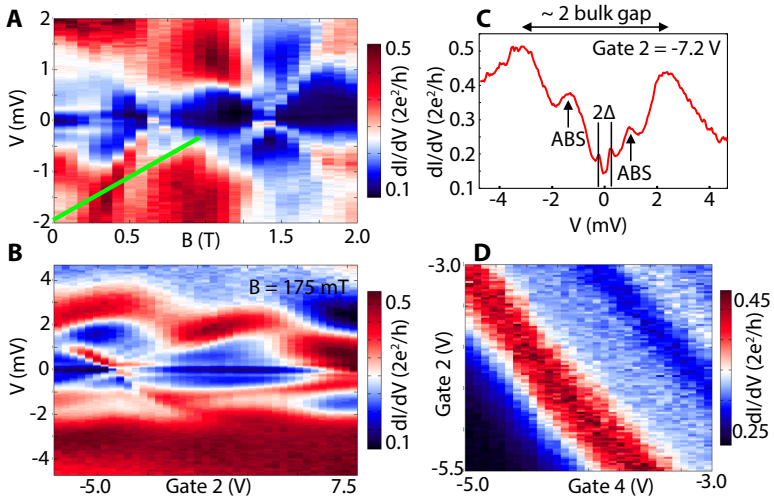

Figure S2 |Large bias scans to identify Andreev bound states. Here we investigate the states that cross zero bias and appear in Figure 5.2 and 5.3 of the main paper. A) Magnetic field dependence of dI/dV extended to higher source-drain voltages. Despite low resolution the induced (soft) gap is observed at ~0.25 mV, and the zero-bias peak is visible between 200 and 700 mT. Two pairs of states exhibit a strong magnetic field dependence, and cross zero at ~0.7 T and ~1.4 T. **Notably, these states extend above the induced gap, but are also present within this gap**. Dashed line indicates the Zeeman energy $1/2g\mu_B B$ for g=50 (the bulk value in InSb). The larger slope of the observed states can be due to field expulsion from the superconductor. B) States that cross zero bias are also tunable with gates 2,3,4 (gate 2 dependence shown). In this scan over a larger range of V they are traceable to the source-drain voltage of ~3 mV, which is on the scale of the bulk gap in the NbTiN electrode. These plots are reminiscent of numerical data by C. Bena ([36]). **We interpret these states as Andreev Bound States (ABS) confined between the bulk superconductor and the gate-defined tunnel barrier**. As expected for ABS, these states come in pairs, one at positive and one at negative bias. C) Linecut from B showing the induced gap at 0.25 mV, a pair of ABS resonances near 1.5 mV and an enhanced conductance on the scale of the gap of NbTiN above 2 mV. D) A plot of dI/dV at V = 640 mV, B = 175 mT showing that the same ABS resonance (red) can be tuned by two gates underneath the superconductor that are 400 nm apart. Apparently the ABS are extended over the entire segment of the nanowire that is underneath the superconductor, suggesting a finite density of states within the apparent gap even deep underneath the superconductor. ABS increase conductance much stronger than ZBP. This may come about if ABS belong to lower subbands and/or have a stronger penetration into the tunnel barrier. (Data from N-NW-S Device 1, T = 60 mK)

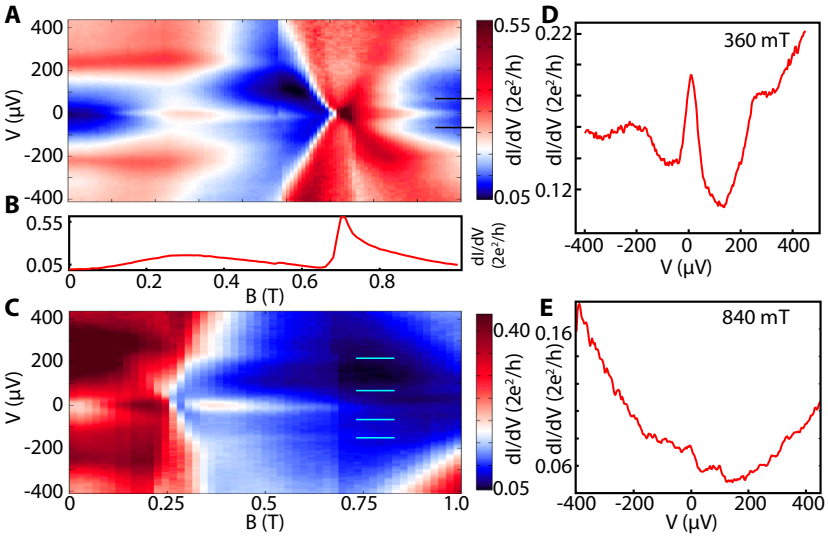

Figure S3 |Additional Magnetic Field Dependences. Here we show more examples of magnetic field dependences from device 1, to complement data in Figure 5.2 of the main text. A) Magnetic field dependence of dI/dV. Zero-bias peak is shown extending up to ~0.9 T. In the vicinity of B = 0.6 T a pair of ABS cross zero bias (Gate 1 = -0.325 V, Gate 2 = 0.2 V, Gate 3 = -1.6 V, Gate 4 = -4.0 V). B) Conductance at zero bias is suppressed at fields immediately below the ABS crossing point and enhanced at the crossing. The same behavior is observed at finite bias. The asymmetric shape of the dI/dV trace is reminiscent of a Fano resonance. We speculate that a Fano resonance results from interference between an ABS and a continuum of states within the bulk gap. We observe that the height of the ZBP is strongly influenced when an ABS crosses zero. The ZBP itself seems to persist throughout an ABS crossing. C) After re-tuning Gate 2 the ABS crossing point is shifted to lower magnetic field B ~ 0.2 T (Gate 1 = -0.325 V, Gate 2 = -3.7 V, Gate 3 = -1.6 V, Gate 4 = -4.0 V). The zero-bias peak is observed starting from B = 0.1 T. The ZBP is traceable to B = 1.0 T in color scale. However the amplitude of the ZBP drops for B > 0.7 T. A number of resonances that run parallel to ZBP, i.e. that do not have a magnetic field dependence, are visible within the induced gap (dashed lines in panels A) and C). D) and E), Linecuts from panel C. (Data from N-NW-S Device 1, T = 60 mK)

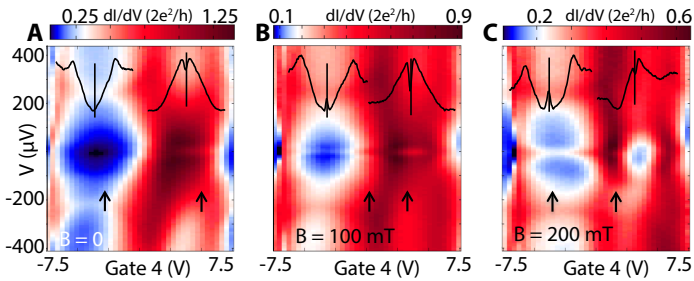

Figure S4 |Gate 4 scans at different magnetic fields. A-C, Gate 4 voltage dependences of dI/dV at three values of magnetic field. These data are an extension of a set displayed in Figure 5.3B,C of the main paper. Zero-bias peaks appear at finite magnetic field where they are best visible in the low conductance regions (blue regions), which are not obscured by ABS resonances (ABS appear as red regions in the color scale). In all panels, including at B = 0, we observe two peaks in the region of high conductance (see line cuts on the right in each panel). Taken at face value, the data in this figure does not suggest a connection between the ZBP and the split peak. However, currently we do not have a precise understanding of the various split peaks and their relation to the rigid ZBP. In each panel two linecuts illustrate dI/dV behavior at gate settings marked by arrows. Dashed lines indicate zero bias. (Data from N-NW-S Device 1, Gate 1 = -0.325 V, Gate 2 = 0.2 V, Gate 3 = -1.6 V, T = 60 mK)

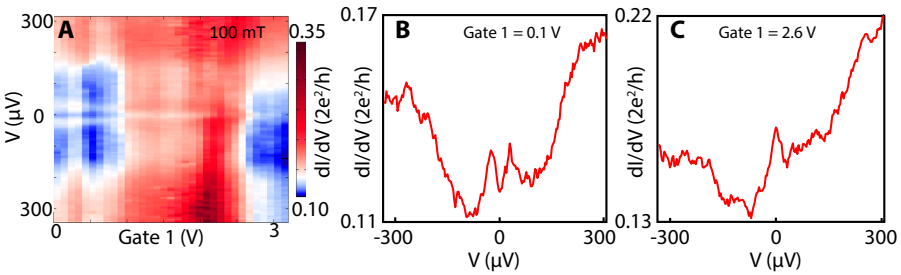

Figure S5 |Apparent Splitting of Zero-Bias Peak. A) In this figure we show that conductance near zero bias can be tuned from a single peak at zero bias to a pair of narrow split peaks also in the regime of low conductance, away from ABS resonances. Black arrows indicate traces displayed in panels B and C. In the context of Majorana fermions split zero-bias peaks can be understood as coupling of two nearby Majorana's. However, split peaks in the low conductance regime (below 0.3·2e2/h) and at low magnetic fields (100-300 mT) are a relatively rare observation in our current experiment. They are not observed frequently enough to draw conclusions in the context of overlapping Majorana's. A detailed investigation of split peaks is beyond the scope of the present manuscript. This will be part of a future study based on devices with optimized gate geometry. (Data from N-NW-S Device 3.)

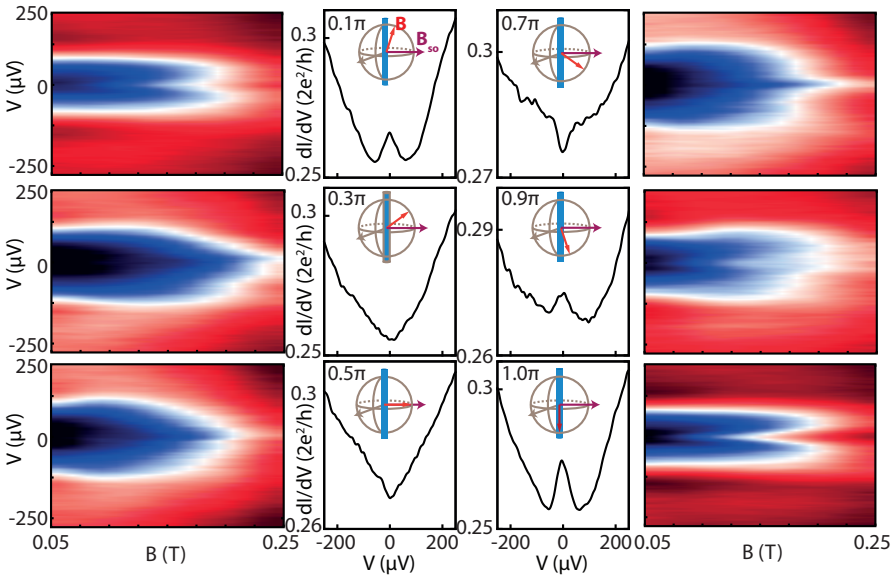

Figure S6 |In-plane field rotation data complementary to Figure 5.4 of the main paper. It also demonstrates that field dependences of the ZBP obtained from N-NW-S device 2 are in qualitative agreement with those from device 1. A-F, Magnetic field vs. bias maps of dI/dV. For each panel magnetic field is applied at a different angle in the plane of the substrate (accuracy 10 degrees). Inner panels show traces at B = 143 mT. Insets to the inner panels illustrate the orientation of the magnetic field for each panel (red arrow), blue is the nanowire axis, purple is the spin-orbit field direction. **The zero-bias peak disappears when the magnetic field is perpendicular to the nanowire. This was determined as the direction of the spin-orbit field in previous work on the same nanowires (17)**. The modulation of ZBP amplitude is observed in the range 0.1T - 0.3T. This demonstrates that the disappearance of the peak is not due to a variation in the onset field of the ZBP induced by g-factor anisotropy. (Data from N-NW-S Device 2, T ~ 150 mK)

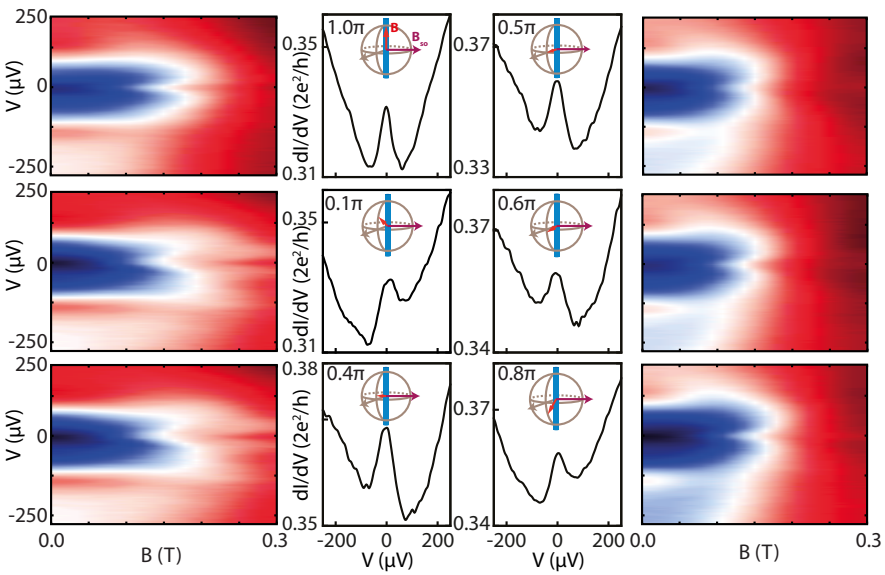

Figure S7 |Out-of-plane field rotation data complementary to Figure 5.4 of the main paper. A-F, Magnetic field vs. bias maps of dI/dV. For each panel magnetic field is applied at a different angle in the plane perpendicular to the spin-orbit field BSO. Inner panels show traces at B = 150 mT. Insets to the inner panels illustrate the orientation of the magnetic field for each panel (red arrow), blue is the nanowire axis, purple is the spin-orbit field direction. **Zero bias peaks of similar amplitude are observed for all orientations perpendicular to spin-orbit field**. (Data from N-NW-S Device 2, T ~ 150mK.) Note that panel S7A is identical to panel S6F.

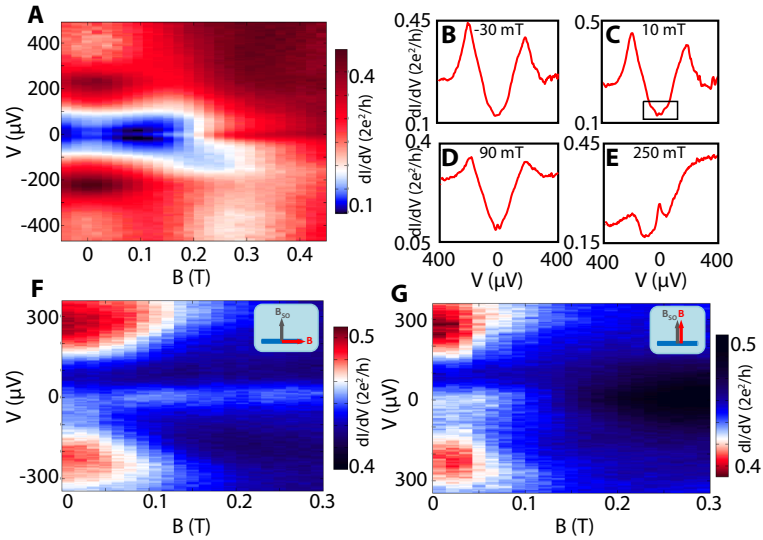

Figure S8 |Zero-bias peak at zero magnetic field. A) A small, but discernible zero bias peak is sometimes observed also for B ≈ 0. This peak is observed for unique gate settings (gate F3 = -0.14 V, gate F2 = -0.1875 V, gate 1 = 0.54 V, gate 2 = 4.665 V, gate 3 = -1.6 V, gate 4 = -4 V). The ZBP at zero field is observed much less often than the robust ZBP at finite magnetic field. (Data in A-E are from N-NW-S Device 1). B-E, Linecuts from panel A at different magnetic fields. The zero-bias feature in the vicinity of B = 0 has a height of 0.005·2e2/h (dashed box, panel C). F and G, The zero-bias peak at zero magnetic field is reproduced in N-NW-S device 2 for certain gates voltage settings combination. However, when the magnetic field is aligned with the spin-orbit field the zero-bias peak is suppressed starting at ~ 100 mT, the typical onset for the finite-field ZBP. (F: field along the wire, G: field along the spin-orbit field, perpendicular to the wire). While not a definite proof, this observation suggests that ZBP near zero magnetic field and ZBP at finite fields have different origins.

Possible origins of ZBP at zero field include weak antilocalization, reflectionless tunneling and Josephson effect. Supercurrent flow is unlikely in our N-NW-S devices, since the critical field of Ti (part of Ti/Au normal contact) does not exceed 30 mT, and superconductivity in Ti is further weakened by the inverse proximity effect from a thick gold layer. The field scale for both weak antilocalization and reflectionless tunneling is determined by $B_0 \sim (h/e)/(A)$, where A is a characteristic area of an electron trajectory perpendicular to the field direction. While field expulsion from the superconductor complicates the prediction of B_0 , it can be estimated in the 100's of milliTesla range.

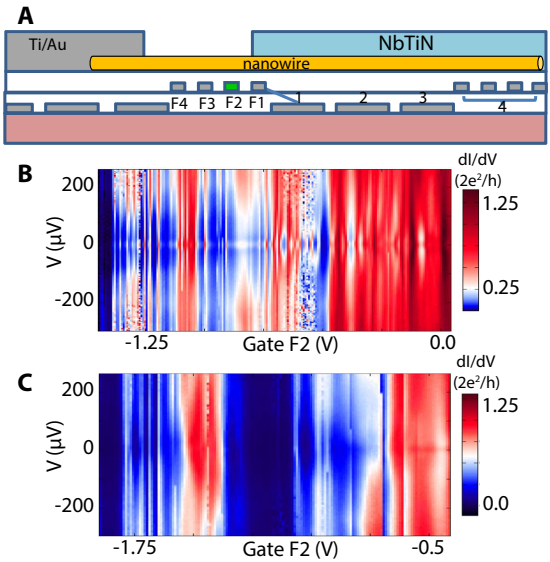

Figure S9 |Pinch-off gate traces of barrier gate. Figure 5.3 in the main paper shows the effect of the gates underneath the superconductor. Here we present the effect of a tunnel barrier gate, the so-called pinch-off traces. In Figure S9, A) Device 1 schematic with bottom gates labelled. Wide gate 1 is connected to an adjacent fine gate. Gate 4 consists of four narrow gates. Details of gate layout in the other two N-NW-S devices differ. B) Conductance map obtained by sweeping the barrier gate F2 from open regime (near 0 V) towards pinch-off at negative voltages. A zero-bias peak is observed for a wide range of barrier gate settings, where it is not obscured by frequent transmission resonances (red in the color plot). Gate 1 = -1.165 V. Similar traces are obtained when F2 is positive and F3 is used to pinch-off, as well as when Gate 1 is swept. C) A pinch-off trace for a different setting of Gate 1 = 4.0 V. The details of conductance are altered. Zero-bias peak is observed only in the high conductance region near F2 = -0.5 V, but not in the lower conductance regions. (Data from N-NW-S Device 1, B = 150 mT, T = 60 mK)

These traces are typical among other hundreds of barrier gate scans measured in devices 1 and 3: for some gate settings ZBPs are observed, and for other settings ZBP disappears. However, in the present devices it is difficult to separate the effect of tuning the chemical potential from the effect of tuning the barrier transmission. Devices with optimized gate geometries will be used to investigate the Zeeman energy-chemical potential phase diagram of ZBP in the future.

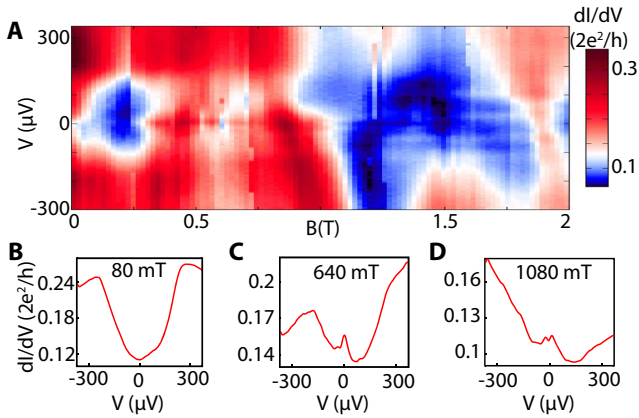

Figure S10 |Field dependences of device 3. **Field dependences of ZBP for N-NW-S device 3 are in qualitative agreement with those from devices 1 and 2**. Figure S10 A) Magnetic field map of conductance shows a zero-bias peak that onsets at finite field (0.2 T) and extends to 1 Tesla. Beyond B = 1 T several field-independent resonances are visible. In addition, resonances that are field tunable cross zero bias at several magnetic fields. Local charge rearrangement results in abrupt conductance switches seen in the data. Such "charge noise" is more dramatic in device 3 compared to devices 1 and 2. B-D, Linecuts from panel A.

All key findings illustrated by data from device 1 throughout the paper and supplementary material are reproduced in device 3. Specifically, we find that ZBP persists in a significant gate range for all gates from the tunnel barrier to gate 3 (the farthest gate from the tunnel barrier for this device). The peak height and width are found to be the same as in device 1 at the lowest temperature (60 mK), temperature dependence was not studied for device 3. The induced gap is of the same magnitude (250 mV). Bound states crossing zero bias are also observed in device 3. Devices 1 and 3 are measured in magnetic field of fixed orientation, therefore comparison of the ZBP height with the spin-orbit field direction is only carried out for device 2.

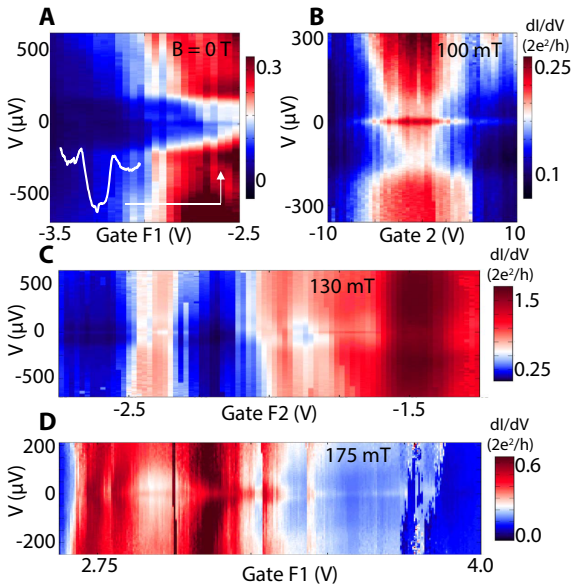

Figure S11 |Gate dependences from device 3. **Gate dependences of the ZBP for N-NW-S device 3 are in qualitative agreement with those from device 1**. A) Zero-field scan of gate F1. A linecut shows the induced gap at a gate setting marked by an arrow. B) A scan of gate 2 at finite magnetic field. ZBP is observed in the entire range, an ABS resonance passes through zero bias near zero gate voltage. C) Gate F2 scan at finite magnetic field. Regions of ZBP, split peak and absent peak are observed. D) Gate F1 scan at finite magnetic field.

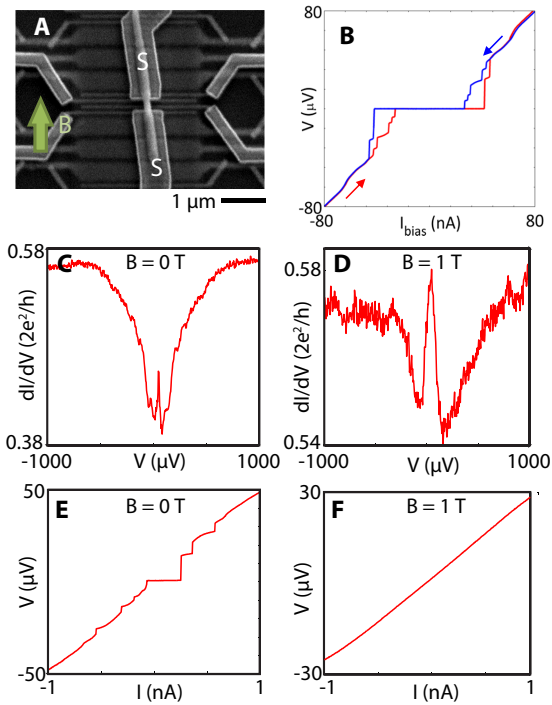

Figure S12 |Superconductor-Nanowire-Superconductor devices. A) Indium antimonide nanowires are contacted by two superconducting NbTiN electrodes. B) In S-NW-S devices supercurrents are observed (see also Nilsson et al. (35)). We found supercurrents exhibiting gate voltage dependence, indicating that superconductivity is induced in the nanowire and confirming proximity effect. C) and D) Zero bias conductance peaks are also observed in S-NW-S devices in voltage-bias experiments. E) and F) Current-biased measurement for the same settings as in panels C and D. The ZBP in panel C is clearly attributed to supercurrent, while a peak at B = 1 T in panel D may have the same origin as ZBP in N-NW-S devices. However, in other S-NW-S devices we observe supercurrents extending to B = 1 T. We also observe supercurrents extending to 100's of mT when the superconductor contact spacing is increased to 600 nm. Small supercurrents do not show up as steps in the I-V curves but could still result in enhancement of dI/dV near zero voltage bias in voltage-biased experiments. **This underscores the importance of using a normal metal contact as a tunnel probe in order to exclude supercurrent as an explanation for the zero-bias peak**.

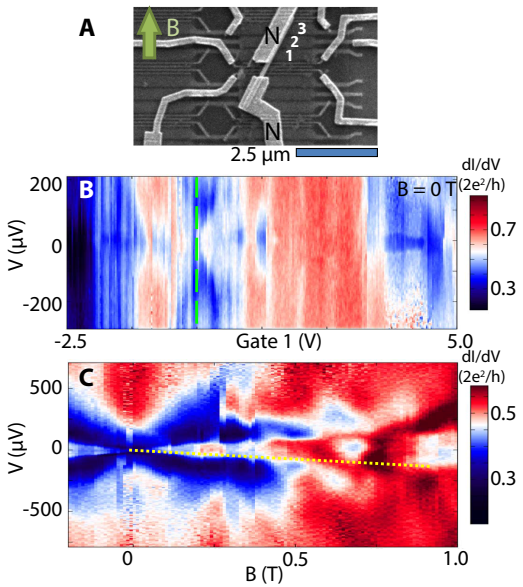

Figure S13 |Normal Metal-Nanowire-Normal Metal device. In order to test superconductivity as a necessary ingredient for the rigid ZBP, we have fabricated an N-NW-N device with two Ti/Au contacts to the InSb nanowire (SEM photo in Figure §13A)). Wide gates underneath the upper normal contact are tuned, the arrow indicates the direction of the applied magnetic field. Figure S13B is a typical scan of Gate 1 near the edge of the half-covering (upper) normal contact. At zero magnetic field no induced gap is observed. A suppressed conductance near zero bias for some gate ranges is not accompanied by quasi-particle peaks characteristic of superconducting gaps. At the green dashed line we observe a zero bias peak (although difficult to see on this scale). In Figure S13C we investigate the B-field dependence of this zero bias peak and observe that the peak splits. Dashed line is a guide to the eye for the splitting. T = 20 mK for these data.

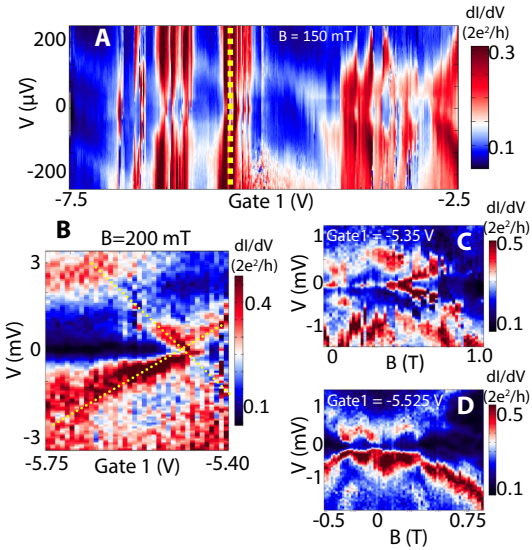

Figure S14 |Normal Metal-Nanowire-Normal Metal device. A) Data from the same N-NW-N device as in S12: Gate 1 scan at finite magnetic field. The gate range is virtually always clear of zero-bias peaks. However in a small range in gate space of order 100 mV (dotted line) we observe a zero bias peak. (Charge switches in this scan result in the apparent doubling, and sometimes quadrupling, of red resonances that pass through zero.) In B we zoom in on this peak in gate range. We observe that the zero bias peak is a near crossing of two gate-tunable resonances (dotted lines). C) and D) Magnetic field dependences obtained for gate settings just left and right of the crossing in panel B. When Gate 1 is set just right of the crossing, a zero-bias peak is observed starting at zero magnetic field and splitting at higher field. When Gate 1 is set left of the crossing, a pair of split resonances is observed at higher bias. These resonances continue to split as the field is increased. We conclude that the zero-bias peak that we observe here only occurs in a narrow gate range and is connected to the crossing of two resonant levels. The crossing shifts its position in gate space by a small amount when magnetic field is increased. This produces a zero-bias peak that persists in magnetic field for a few hundred milliTesla. This effect is distinctly different from the rigid ZBP observed in N-NW-S devices, where the peaks persist in BOTH magnetic field and gate voltages for all gates.

REFERENCES

[1] E. Majorana. Teoria simmetrica dell'elettrone e del positrone. *Engl. transl [translation from Nuovo Cimento 14, 171 (1937)]F* **63**, 149 (1981).

[2] F. Wilczek. Majorana returns. *Nature Physics* **5**, 614 (2009).

[3] M. Franz. Viewpoint: Race for majorana fermions. *Physics* **3**, 24 (2010).

[4] A. Y. Kitaev. Unpaired majorana fermions in quantum wires. *Physics-Uspekhi* **44**, 131 (2001).

[5] L. Fu and C. L. Kane. Superconducting proximity effect and majorana fermions at the surface of a topological insulator. *Physical review letters* **100**, 096407 (2008).

[6] J. D. Sau, R. M. Lutchyn, S. Tewari and S. D. Sarma. Generic new platform for topological quantum computation using semiconductor heterostructures. *Physical review letters* **104**, 040502 (2010).

[7] J. Alicea. Majorana fermions in a tunable semiconductor device. *Physical Review B* **81**, 125318 (2010).

[8] R. M. Lutchyn, J. D. Sau and S. D. Sarma. Majorana fermions and a topological phase transition in semiconductor-superconductor heterostructures. *Physical review letters* **105**, 077001 (2010).

[9] Y. Oreg, G. Refael and F. von Oppen. Helical liquids and majorana bound states in quantum wires. *Physical review letters* **105**, 177002 (2010).

[10] C. Beenakker. Search for majorana fermions in superconductors. *arXiv:1112.1950* (2011).

[11] J. Alicea. New directions in the pursuit of majorana fermions in solid state systems. *Reports on Progress in Physics* **75**, 076501 (2012).

[12] K. Law, P. A. Lee and T. Ng. Majorana fermion induced resonant andreev reflection. *Physical review letters* **103**, 237001 (2009).

[13] K. Flensberg. Tunneling characteristics of a chain of majorana bound states. *Physical Review B* **82**, 180516 (2010).

[14] J. D. Sau, S. Tewari, R. M. Lutchyn, T. D. Stanescu and S. D. Sarma. Non-abelian quantum order in spin-orbit-coupled semiconductors: Search for topological majorana particles in solid-state systems. *Physical Review B* **82**, 214509 (2010).

[15] S. R. Plissard *et al.* From insb nanowires to nanocubes: looking for the sweet spot. *Nano letters* **12**, 1794 (2012).

[16] H. A. Nilsson *et al.* Giant, level-dependent g factors in insb nanowire quantum dots. *Nano letters* **9**, 3151 (2009).

[17] S. Nadj-Perge *et al.* Spectroscopy of spin-orbit quantum bits in indium antimonide nanowires. *Physical review letters* **108**, 166801 (2012).

[18] P. W. Brouwer, M. Duckheim, A. Romito and F. von Oppen. Probability distribution of majorana end-state energies in disordered wires. *Physical review letters* **107**, 196804 (2011).

[19] J. D. Sau, S. Tewari and S. D. Sarma. Experimental and materials considerations for the topological superconducting state in electron-and hole-doped semiconductors: Searching for non-abelian majorana modes in 1d nanowires and 2d heterostructures. *Physical Review B* **85**, 064512 (2012).

[20] See the supplementary .

[21] J. D. Pillet *et al.* Andreev bound states in supercurrent-carrying carbon nanotubes revealed. *Nature Physics* **6**, 965 (2010).

[22] T. Dirks *et al.* Transport through andreev bound states in a graphene quantum dot. *Nature Physics* **7**, 386 (2011).

[23] H. Le Sueur, P. Joyez, H. Pothier, C. Urbina and D. Esteve. Phase controlled superconducting proximity effect probed by tunneling spectroscopy. *Physical review letters* **100**, 197002 (2008).

[24] S. Sasaki *et al.* Kondo effect in an integer-spin quantum dot. *Nature* **405**, 764 (2000).

[25] M. Zareyan, W. Belzig and Y. V. Nazarov. Superconducting proximity effect in clean ferromagnetic layers. *Physical Review B* **65**, 184505 (2002).

[26] B. Van Wees, P. de Vries, P. Magnée and T. Klapwijk. Excess conductance of superconductor-semiconductor interfaces due to phase conjugation between electrons and holes. *Physical review letters* **69**, 510 (1992).

[27] M. Wimmer, A. Akhmerov, M. Medvedyeva, J. Tworzydło and C. Beenakker. Majorana bound states without vortices in topological superconductors with electrostatic defects. *Physical review letters* **105**, 046803 (2010).

[28] A. C. Potter and P. A. Lee. Multichannel generalization of kitaev's majorana end states and a practical route to realize them in thin films. *Physical review letters* **105**, 227003 (2010).

[29] R. M. Lutchyn, T. D. Stanescu and S. D. Sarma. Search for majorana fermions in multiband semiconducting nanowires. *Physical review letters* **106**, 127001 (2011).

[30] T. D. Stanescu, R. M. Lutchyn and S. D. Sarma. Majorana fermions in semiconductor nanowires. *Physical Review B* **84**, 144522 (2011).

[31] P. Středa and P. Šeba. Antisymmetric spin filtering in one-dimensional electron systems with uniform spin-orbit coupling. *Physical review letters* **90**, 256601 (2003).

[32] M. Wimmer, A. Akhmerov, J. Dahlhaus and C. Beenakker. Quantum point contact as a probe of a topological superconductor. *New Journal of Physics* **13**, 053016 (2011).

[33] N. Read and D. Green. Paired states of fermions in two dimensions with breaking of parity and time-reversal symmetries and the fractional quantum hall effect. *Physical Review B* **61**, 10267 (2000).

[34] D. A. Ivanov. Non-abelian statistics of half-quantum vortices in p-wave superconductors. *Physical review letters* **86**, 268 (2001).

[35] C. Nayak, S. H. Simon, A. Stern, M. Freedman and S. D. Sarma. Non-abelian anyons and topological quantum computation. *Reviews of Modern Physics* **80**, 1083 (2008).

[36] C. Bena. Metamorphosis and taxonomy of andreev bound states. *The European Physical Journal B-Condensed Matter and Complex Systems* **85**, 1 (2012).

6

RECENT DEVELOPMENTS ON MAJORANA BOUND STATES IN SEMICONDUCTING NANOWIRES

The experiments on signatures of Majorana fermions led to an intense discussion about its interpretation within the scientific community. Many valuable insights were put forward, of which we discuss the most relevant ones in this chapter. After an introduction (section 6.1, in the first half of the chapter, section 6.2, we discuss adaptions to our specific set-up of the general model for Majorana bounds states in semiconducting nanowires. In the second half, section 6.3, we discuss a number of alternative causes of zero bias peaks put forward based on recent experimental or theoretical work.

[1] Both Vincent Mourik and Kun Zuo actively contributed to the underlying scientific discussion, both Vincent Mourik and Kun Zuo took equal shares in writing a first draft, and the final version is the result of joined writing by both Vincent Mourik and Kun Zuo.

6.1 INTRODUCTION

Our first work on signatures of Majorana fermions in a hybrid superconductor-semiconductor nanowire system garnered wide attention within the scientific community. Much of this interest in our work revolves around the same question: to what extent do the observed signatures constitute an unambiguous prove for Majorana bound states (MBS's). Since our work constitutes the very first experimental data in this context, several of the original models were too idealized to describe the details of a real experiment. In the time span between publication of our work (spring 2012) and the current date, many improved models attempted either to explain more aspects of our observations in the context of Majoranas or attempted to provide an alternative explanation. Furthermore, in this period relevant new experimental observations were done. In this chapter we discuss the state of the art understanding of theory and experiments.

To begin with, we list the most important observations in our work which were initially not anticipated:

- The zero bias peak (ZBP) observed in the measurements has a small height of $0.05G_0$, much lower than the predicted height of $G_0 = 2e^2/h$[1] at zero temperature.
- While undergoing a phase transition from topologically trivial to non-trivial, the excitation gap in the spectrum is expected to close and reopen [2, 3]. Upon reopening a ZBP should appear. Instead, as a function of magnetic field B and gate voltage, appearance of a ZBP is observed, without the accompanying gap closure and reopening.
- Since the superconducting section of the nanowire has a finite length, interaction of MBS's is expected, especially with the spin orbit interaction strength of 50 μeV quoted as a best guess in the experimental paper. This should manifest itself by an oscillatory behavior from single ZBP to split peaks as a function of B and gate [4, 5]. Instead, the ZBP mostly just disappears above a certain B.
- The superconducting gap observed has broadened coherence peaks. Inside the coherence peaks, the gap is rounded and does not go to zero conductance in the middle. This suggests a large residual density of states to be present inside the gap, whereas a BCS like density of states is predicted in idealized models.

As it turns out, the rather realistic assumptions of having a 1) non-ideal, smooth tunnel barrier 2) multiple occupied nanowire subbands 3) stronger spin-orbit interaction strength than anticipated and 4) non-ideal superconductor-semiconductor interface are enough to reconcile most of the deviations from the initial simple picture as sketched in chapter 2. These aspects are discussed in the first part of this chapter, section 6.2.

Since our experimental observations do not follow all aspects of the idealized predictions for MBS's, alternative explanations have to be considered as well. At the time of writing in 2012, we knew of 4 possible mechanisms resulting in ZBP's in semiconducting nanostructures. These are: Andreev bound states crossing each other at the Fermi level, the Kondo effect, reflectionless tunneling and weak anti-localization. All of these were discussed and could be falsified as possible origins of the observed ZBP, see for the details chapter 5.

Although already excluded in our original work, some recent experimental observations are very relevant to MBS related research and deserve discussion here. These observations are:

- Non-topological Andreev bound states (ABS's) in a quantum dot have been observed, which form prolonged level crossings at finite B resulting in ZBP's[6].
- It has been observed experimentally that, under certain conditions, Kondo effect and superconductivity may coexist at finite B, resulting in a ZBP[7].

More importantly, however, a new scenario of a ZBP which onsets at finite magnet field has been put forward shortly after our initial work:

- Disorder in the superconducting nanowire section may generate ZBP's, which under certain conditions seem to follow the predictions for a MBS induced ZBP[8, 9].

These three alternative causes of ZBP's are discussed in depth in the second part of this chapter, section 6.3.

6.2 MAJORANA MODEL IN THE SPECIFIC NANOWIRE SET-UP

In chapter 2 we have strictly confined ourselves to the simplest possible model, based on a semiconducting nanowire, which results in an effective one dimensional p-wave superconductor with MBS's at its ends. Several very relevant and realistic aspects in an actual experimental set-up are neglected in such an idealized model. In particular, the assumptions of a single occupied nanowire subband, a delta-function tunnel barrier, and a perfectly proximitized nanowire, are not necessarily true. Several theory works have investigated more realistic scenario's, considering more realistic geometries. It is the goal of this section to give an overview of these works and their connection to the experiment.

Section 6.2.1 is on the expected influence of multiple occupied nanowire subbands on the topologically non-trivial phase. Section 6.2.2 discusses the role of a non-ideal (i.e. delta-function) tunnel barrier and multiple occupied nanowire subbands in connection to the observed small height of the ZBP. Section 6.2.3 is on the possible cause of the absent gap closure in the experiment. Section 6.2.4 discusses

possible explanations for the absence of peak splitting in the experiment. Finally, in section 6.2.5, possible causes for the non-ideal gap observed in the experiment are discussed. We summarize and conclude in section 6.2.6.

6.2.1 MAJORANA BOUND STATES IN MULTIBAND NANOWIRES

The theory discussion of MBS's in semiconducting nanowires in chapter 2 considered strictly one dimensional nanowires: i. e. only a single orbital subband[1] is occupied. Here we introduce the concept of a quasi one-dimensional, multiband nanowire with several occupied orbital subbands, and discuss the implications for MBS's.

The single orbital subband picture in principal applies to all orbital subbands present in the wire. In other words, every individual orbital subband N undergoes a topological phase transition if the condition $E_Z = \sqrt{\Delta^2 + \mu_N^2}$ is met, with $E_Z = 1/2 g \mu_B B$, Δ the induced superconducting gap and μ_N the chemical potential in the N^{th} subband counted from its crossing point [2]. By changing μ, the subband occupation may be altered, and another subband may enter the topologically non-trivial phase. This behavior is illustrated in Figure 6.1.

In anticipating magnetic field dependent behavior, it is crucial to compare the different relevant energy scales of the non-trivial phase to the subband spacing ΔE_{band} of the different orbital bands in the nanowire.

QPC measurements in InSb nanowires have shown that the first few orbital subbands in the nanowire have a minimal spacing ΔE_{band} of at least 10-15 meV, and occasionally up to ~30 meV [11]. These observations are done in a bare nanowire segment, which is not covered by a metallic contact. The amount of occupied subbands underneath the superconducting contact cannot be determined by the tunneling spectroscopy measurements employed in this thesis. However, when a larger amount of occupied subbands is present, it is unlikely that ΔE_{band} will decrease to the few meV's range.

The B field range of interest in the experiment is order of 1 T. Given InSb g-factors $g = 50$, $E_Z = 1.6$ meV/T. In order to overcome the typical $\Delta E_{\text{band}} = 15$ meV, a B field of ~5 T is necessary. Furthermore, the two other relevant energy scales, spin orbit strength E_{SO} and superconducting gap Δ, are expected to be of order of 1 meV [12]. Hence, the typical energy scale for ΔE_{band} is one order of magnitude larger compared to E_Z, E_{SO} and Δ in experimentally relevant parameter ranges.

Consequentially, for the B field ranges relevant to the experiment, we expect at most a single orbital subband to be in the topologically non-trivial phase even with

[1] We refer to a (orbital) subband as the spin degenerate subband in the absence of SOI and Zeeman effect. Note that at finite B, the twofold degeneracy of these orbital subbands is lifted, resulting in a doubling of the bands in the spectrum, each band consisting of a single spin species. However, the relevant quantity in the context of MBS's is the number of quasi-helical gaps present in the full spectrum, which corresponds directly to the number of spin-degenerate orbital subbands being occupied.

[2] We apply the definition given in chapter 2 of $\mu = 0$ being the bottom of a spin-degenerate orbital subband. In the presence of Rashba spin orbit interaction the spin bands shift apart along the k-axis and shift down in energy, such that $\mu = 0$ exactly corresponds to the $k = 0$ crossing point of both spin bands.

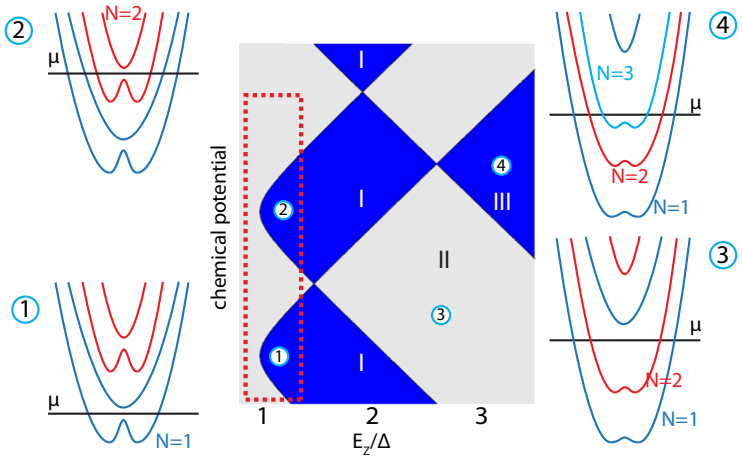

Figure 6.1 |Topological phase diagram of a multiband superconducting nanowire with strong spin orbit interaction. Blue corresponds to the topologically non-trivial state with MBS's. This particular phase diagram, adapted from Stanescu et al. [10] , considers the first 3 orbital subbands. Furthermore, interacting orbital subbands are assumed (see footnote 3), leading to locally interacting MBS's. As a consequence, at higher E_Z, only for an odd number of orbital subbands the system may host a single pair of unpaired MBS's. This causes the alternating pattern between topologically trivial and non-trivial. I indicates a single topologically non-trivial orbital subband and hence a single pair of non-interacting MBS's. II indicates two non-trivial orbital subbands, hence no single pair of non-interacting MBS's, the system as a whole is effectively trivial. III indicates three non-trivial orbital subbands, there are two interacting pairs and one non-interacting pair of MBS's, the system is non-trivial again. The corresponding electronic energy dispersions of the different regions are schematically shown next to the phase diagram. Importantly, the regime most relevant to the experimental situation is when only a single orbital subband is in the non-trivial phase, $E_Z << \Delta E_{\text{band}}$, but $\mu > \Delta E_{\text{band}}$ may be the case, such that multiple orbital subbands are occupied. This regime is indicated with a red dashed box in the phase diagram. $E_Z << \Delta E_{\text{band}}$ is most likely still valid in case more than three orbital subbands are present, although the exact shape of the phase diagram will be altered.

multiple subbands occupied[3].

6.2.2 SMALL HEIGHT OF THE ZERO BIAS PEAK

We first discuss the observed small height of the ZBP. The initial theory work discussing tunneling into the MBS[1], predicted the ZBP to be quantized at $G_0 = 2e^2/h$, assuming a single subband model at zero temperature. In a later work[13], it was shown that this quantization of the ZBP actually is a topological property, that evolves away from the tunneling regime into a quantized plateau of a quantum point contact. How to reconcile these predictions with the observed ZBP height of only $0.05G_0$?

First we consider broadening mechanisms possibly affecting the height of the ZBP. These are the tunnel coupling strength Γ between lead and MBS, and the finite temperature T. The effect of finite temperature on the ZBP is, in the limit of weak tunnel coupling ($\Gamma << T$), given by

$$G(V_{\text{bias}}, T, \Gamma) = \frac{2e^2}{h} \cdot \frac{\pi\Gamma}{4k_B T} \frac{1}{\cosh^2(eV_{\text{bias}}/2k_B T)} \qquad \Gamma << T \tag{6.1}$$

For a fixed Γ, this results in a fixed area underneath the peak, with corresponding full width at half maximum (FWHM) of $3.5k_B T$, and peak height of $G_0 \cdot \pi\Gamma/(4k_B T)$, see Figure 6.2c. Increasing Γ, however, will increase the peak height, at a fixed width of $3.5k_B T$, see Figure 6.2b. To reach a unity peak height, the limit of $T << \Gamma$ has to be reached, in which case the shape of the peak is given by

$$G(V_{\text{bias}}, \Gamma) = \frac{\Gamma^2}{(eV_{\text{bias}})^2 + \Gamma^2} \qquad T << \Gamma \tag{6.2}$$

This shows that increasing Γ will preserve the height of the ZBP, but increase its width, see Figure 6.2a.

In the original experiment, a small ($0.05G_0$) and narrow ($\sim 20\ \mu$V) peak is observed. In fact, the FWHM of the peak corresponds to a temperature of 70 mK, which matches very well with the refrigerator temperature of 60 mK. Furthermore, upon increasing the refrigerator temperature, the ZBP immediately broadens and

[3] Multiple different orbital subbands may simultaneously fulfill the Majorana condition, such as regions 3 and 4 in Figure 6.1. In such a scenario, two different cases are relevant. Firstly, the strength of spin orbit interaction (SOI) E_{SO} may be small compared to ΔE_{band} (nanowire width $W << l_{\text{SO}}$, l_{SO} spin orbit length). This will lead to very weak interband coupling, a regime formally known as the topological BDI class. As a consequence, MBS's in different subbands will not couple, and may coexist in the system (this case is *not* illustrated in Figure 6.1, region 3). Secondly, however, for large E_{SO} ($W >> l_{\text{SO}}$), interband coupling becomes strong, this regime is formally known as the topological D class. Besides, also disorder and orthogonal B components may increase interband coupling. All these mechanisms will result in coupling of MBS's originating from multiple orbital subbands in the topologically non-trivial phase. Only if an odd amount of orbital subbands meets the criterion for undergoing a topological phase transition, a single, unpaired MBS's will be present at each wire end, while the others form pairs of finite energy states (this case is illustrated in Figure 6.1, regions 3 and 4). This is opposed to the case of weak interband coupling, where as soon as an individual orbital subband undergoes the topological phase transition, for all larger E_Z the system will be topologically non-trivial.

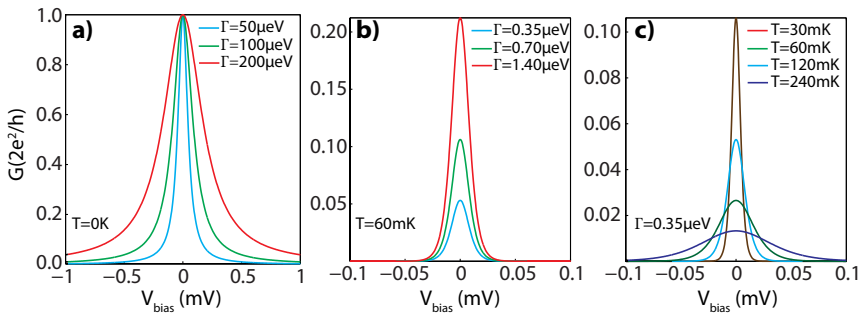

Figure 6.2 |Broadening of the zero bias peak via tunnel coupling Γ and temperature T. At $T=0$, the MBS is a δ-function shaped state at $E=0$ in the density of states. a) A finite tunnel coupling Γ allows for measurement of the MBS as a ZBP in the differential conductance. In the $T=0$ limit, as shown in the left panel, the peak height is quantized at G_0 and has an increasing width for increasing Γ. b) In the more realistic limit of $\Gamma << T$, the ZBP has a reduced height given by $\pi\Gamma/(4k_{\mathrm{B}}T)\,G_0$ and a width of $\mathrm{FWHM}=3.5k_{\mathrm{B}}T$. The middle panel shows that increasing Γ result in an increasing peak height, while the width is fixed by T. The blue curve corresponds to a choice of T and Γ resulting in a ZBP similar to the experimentally observed ZBP. c) Again in the limit of $\Gamma << T$, upon fixing Γ and increasing T, the ZBP broadens with a fixed peak area, such that its height decreases. This is what is observed experimentally upon increasing T. The green curve is similar to the experimentally observed ZBP and has the same parameters as the blue curve in b).

shrinks in height. This indicates that the observed ZBP is already fully thermally broadened and no significant broadening due to tunnel coupling is present. Since the typical conductance in the regime where the ZBP is measured is rather high, of the order of $0.1-0.3G_0$, a significant broadening of the peak due to tunnel coupling is expected and naively the peak height should be closer to its quantized value of G_0. What mechanism could cause such a weak tunnel coupling to the MBS, but maintain a rather high overall tunnel coupling?

This question has been addressed theoretically, most relevantly in the works by Pientka et al., Rainis et al. and Prada et al[5, 14, 15]. In these works, a numerical tight binding calculation of a realistic two dimensional nanowire geometry was performed. The crucial ingredients to explain the small ZBP observed in the experiment are: 1) a spatially extended tunnel barrier with finite height instead of a delta function shaped potential barrier and 2) the presence of multiple subbands in the superconducting device region. Such a model is schematically illustrated in Figure 6.3.

If the tunnel barrier has finite width and height and multiple bands are present, then inevitably this will lead to unequal transmission for the different subbands. More specifically, the lowermost band will have the strongest tunnel coupling, whereas the topmost occupied band will have the weakest tunnel coupling. Since the MBS is carried by the topmost occupied subband, it will have the weakest tunnel coupling of all states. As a consequence, the ZBP originating from the MBS is probed quite deep in the tunneling regime, while states from lower occupied subbands may actually have a considerable transmission leading to a high background conductance, see Figure 6.3.

This effect is shown clearly in the theory works mentioned. An example of a typical outcome is shown in Figure 6.4. Including 4 nanowire subbands and a square shaped tunnel barrier (see Figure 6.3a), Pientka et al. found a conductance outside the superconducting gap comparable to the experimentally observed value, whereas the ZBP is very small. For very smooth tunnel barriers, the signal of tunneling via the MBS may be even suppressed completely (see Rainis et al.[5]).

Next we discuss the two assumptions necessary for this explanation of the small ZBP height. Having a smooth tunnel barrier with finite height and width is not even an assumption, but simple experimental reality. The local gate defining the tunnel barrier has a finite width of 50 nm and is separated from the nanowire by a dielectric layer of 30 nm. This inevitably leads to a non δ-function shaped tunnel barrier with finite height and width. Quantifying the exact shape of the tunnel barrier requires a realistic 3D electrostatic simulation involving the effect of the nanowire subbands on the potential (due to screening). The other necessary ingredient is having multiple nanowire subbands in the superconducting device section. As mentioned before, the amount of occupied subbands in the superconducting section is unknown and the assumption of 4 occupied subbands in the theory works discussed here is simply based on the characteristics of an uncovered piece of nanowire. However, already from more than 1 occupied subband on, qualitatively similar behavior is

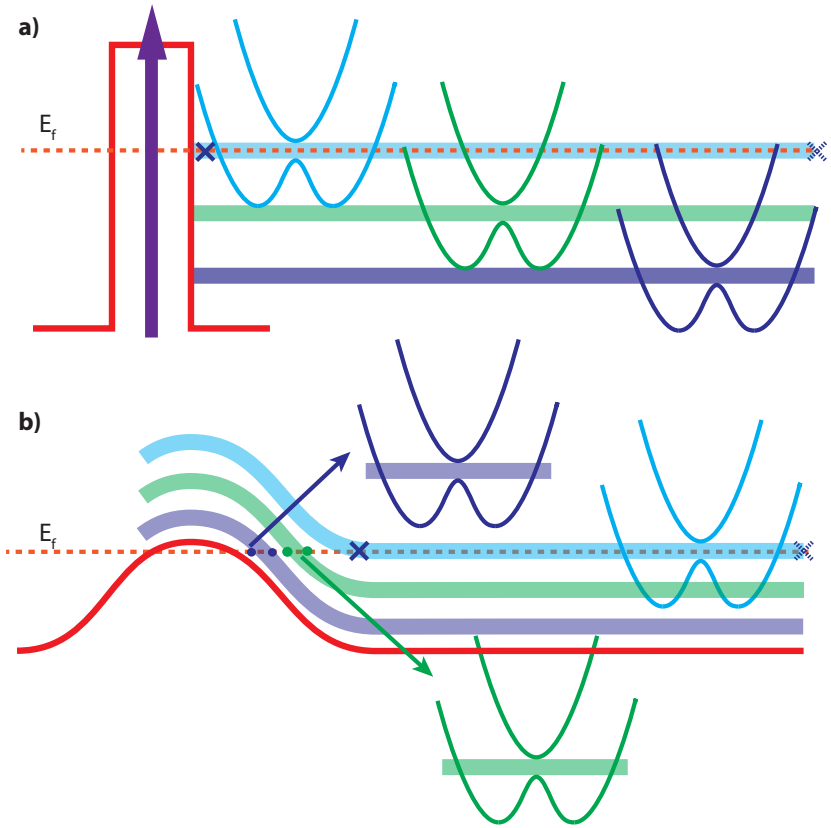

Figure 6.3 |Non-ideal tunnel barrier and multiple orbital subbands. In both panels, on the right side, 3 nanowire orbital subbands are occupied and their quasi-helical gaps are indicated. a) An ideal tunnel barrier corresponds to a delta shaped potential (purple arrow) and results in equal tunneling strength for all nanowire subbands. Any non-ideal tunnel barrier of finite width and height, such as the rectangular potential barrier shown here, results in lower transmission of the higher index orbital subbands, due to their larger energy difference from the Fermi level in the barrier region. b) The more realistic case of a spatially smoothly varying potential barrier. Because of the smoothly varying potential, the lower index subbands, with state occupation far above their bottom in the area away from the barrier region, will be slowly pushed above the Fermi level. This results in small spatial regions near the tunnel barrier in which the Fermi level is in the quasi-helical gap of such a lower index orbital subband. As a consequence, short, additional topologically non-trivial phases may be present near the tunnel barrier, with pairs of additional MBS's, which strongly hybridize and split to finite energy. These may show up as additional, finite energy resonances on occasion crossing the Fermi level in tunneling spectroscopy measurements [16].

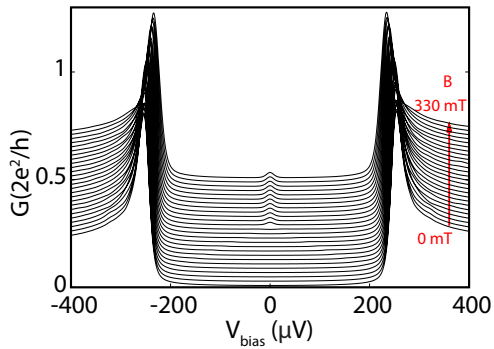

Figure 6.4 |Simulated magnetic field dependent tunneling spectroscopy of a MBS in the presence of a finite width and height tunnel barrier and multiple subbands. 4 subbands are occupied with transmission values T_N for the different modes $T_1 = 0.2$, $T_2 = 0.1$, $T_3 = 0.04$ and $T_4 = 0.01$, from lowermost to uppermost occupied subband respectively. The stronger coupling of the lower subbands leads to a relatively high conductance of $\sim 0.3G_0$ outside the superconducting gap, whereas the weakly coupled topmost subband results in a small, sharp ZBP cause by tunneling into the MBS. Figure adapted from [15].

6

observed ([5]), making the exact amount of occupied subbands not so important, as long as it is more than one.

Due to the experimental uncertainty in both actual tunnel barrier shape and actual number of subbands involved, a quantitative comparison between the simulations and experimental observations is not possible.

Measuring a quantized conductance peak which evolves into the first plateau of a quantum point contact would be a very important observation directly hinting at the topological nature of this phenomenon ([17]). As pointed out by Pientka et al., upon introducing subband mixing close to the tunnel barrier, the MBS should couple stronger to the lead. It does not seem very realistic to expect unity transmission into the MBS resulting from this. However, experimentally if one could manage to reach the single occupied subband regime in the S section, by improving gate coupling, such a problem could be resolved. Or by incorporating a short heterojunction in the nanowire as a sharp tunnel barrier, results in strong coupling to the MBS's, quantized conductance could also be restored.

6.2.3 ABSENCE OF A GAP CLOSURE IN MAGNETIC FIELD

The next question we discuss is the absence of a gap closure at the onset field of the ZBP. From a theoretical perspective, appearance of MBS's should always be accompanied by a closure and reopening of the bulk gap in the system. Therefore, in a tunneling spectroscopy measurement, a ZBP was expected to be accompanied by a closure of the superconducting gap, which was not observed in our experiment.

This apparent discrepancy between basic theory and experiment created concern whether the observed ZBP has a topological origin. Several theory works after our initial findings resolve this matter.

An important consideration is provided by Stanescu et al.[18]. This work studies the behavior of the lowest energy modes in the nanowire, associated with the gap closure and reopening. For chemical potentials near the bottom of the subband, these modes form extended states in the superconducting wire region, with the highest probability density in the middle of the wire. A low probability density of the wave function is present at the wire ends. Contrary to this, after the topological phase transition, MBS's localize at the wire ends. As a consequence, the local density of states (LDOS) at the wire ends does not contain the gap closure, but only the emergence of a MBS, whereas the LDOS in the middle of the wire only contains the gap closure, but no MBS. This behavior is illustrated in Figure 6.5. These findings are independently confirmed by $\mathrm{d}I/\mathrm{d}V$ simulations in several other theory works[4][5, 14, 15].

To observe a gap closure upon entering a topological non-trivial phase, it would be interesting to do a tunneling spectroscopy measurement in the middle of the superconducting wire section as well. In case a gap closure is absent at the wire end, it may still be observable in the middle. Furthermore, the ZBP caused by a MBS is expected to be highly localized and will not be visible in the middle the superconducting wire section. Such a correlated set of observations would further strengthen the case of MBS's.

In conclusion, taking into account a more realistic setting, the absence of a gap closure and emergence of an isolated ZBP in the experiment is, in fact, expected, matching our observations.

6.2.4 ABSENCE OF ZERO BIAS PEAK SPLITTING

Interacting MBS's were discussed in chapter 2. Based on the material parameters estimated in our experiment and the length of the superconducting wire section, the work by Rainis et al.[5] suggests that, in the observed B-field range of the ZBP, already peak splittings due to interacting MBS's should be present, which contradicts the experimental findings.

More specifically, based on the superconducting gap observed in the experiment ($\Delta = 250\ \mu$eV), the quoted SOI strength ($E_{SO} = 50\ \mu$eV) and the device length ($L = 2.2\ \mu$m), Rainis et al. conclude that these parameters are incompatible with the observed ZBP which sometimes extends over a range of 1 T in B. Instead, several oscillations from ZBP to split peak and back should be present. This point is clearly illustrated in Figure 6.6a. Besides observing peak splitting, also a closure of

[4] Another consideration, important again here, is the finite width and height of the tunnel barrier. As pointed out by Prada et al.[14], such a tunnel barrier will lead to 'momentum filtering': transmission for large k-values is higher compared to small k-values. Consequentially, the superconducting gap at finite k will have a better contrast in a tunneling spectroscopy measurement compared to the gap closure at $k = 0$.

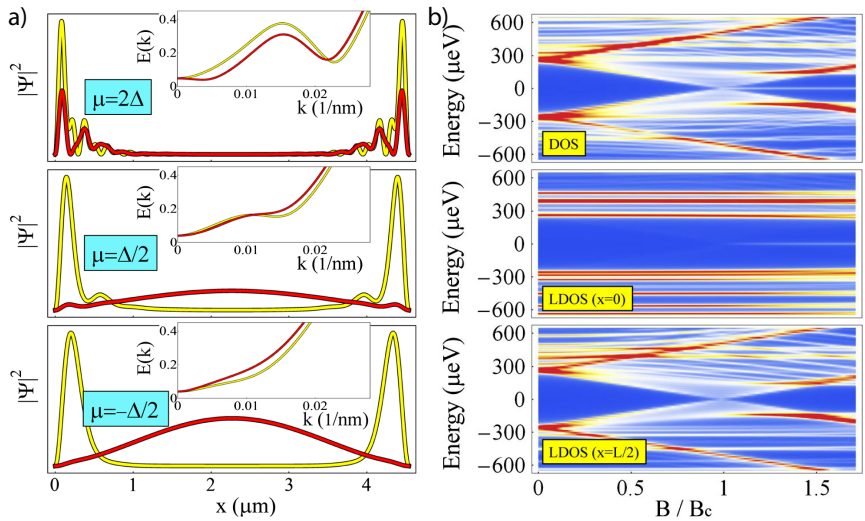

Figure 6.5 |Spatial distribution of the low energy states in a Majorana wire (4 subbands). a) Wavefunction in of the lowest energy, ($k = 0$) state of the nanowire spectrum for different chemical potential μ, the nanowire has a finite size and discrete spectrum. μ is measured from the bottom of the topmost occupied subband at $B = 0$ T. The red curves correspond to a B field just before the critical field B_c associated with the topological phase transition, $B = 0.9B_c$. The yellow curves corresponds to B just after the topological phase transition, $B = 1.1B_c$. In the insets, the lowest branch of the dispersion relation is shown for a continuous nanowire of infinite length, with similar color coding (red: $B = 0.9B_c$, yellow: $B = 1.1B_c$). Importantly, for μ close to the bottom of the subband (middle and bottom panel), the lowest energy states (red) are extended states with highest probability density in the middle of the wire before B_c. These states turn into a pair of highly localized MBS's at the wire ends upon passing B_c (yellow). b) DOS and LDOS as a function of B for $\mu = \Delta/2$ (middle panel a). The top panel shows the complete DOS integrated over the whole superconducting wire region, featuring both gap closure and emergence of MBS's at $B = B_c$. The middle panel shows the LDOS at the wire end, only showing emergence of a MBS at $B = B_c$. The bottom panel shows the LDOS in the middle of the wire, only showing gap closure at $B = B_c$. Figures adapted from [18].

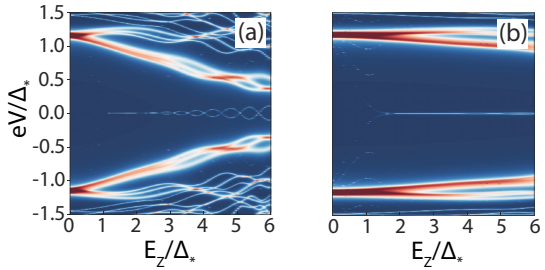

Figure 6.6 |Interacting MBS's inducing ZBP splitting for different strength of SOI. Calculations for InSb, $\Delta = 250$ μeV and $L = 2.2$ μm, corresponding to the experimental situation. To show the peak splitting more clearly, T is set to zero. In the experiment, $E_Z/\Delta = 1$ corresponds to ~150 mT. a) $E_{SO} = 40$ μeV. This SOI strength corresponds to the value quoted in the experiment and is based on quantum dot measurements. Several oscillations from single peak to split peaks are visible and the excitation gap in the spectrum closes fast. b) $E_{SO} = 640$ μeV. As a consequence of the stronger SOI, no peak splitting is visible and the superconducting gap does not disperse much. A very weak gap closure feature is visible here, which is not present at finite T. Figure adapted from [5]

the superconducting gap on a ~1 T scale is expected, based on the experimental parameters, which is not observed experimentally either. Upon assuming a larger SOI strength ($E_{SO} = 640$ μeV), as illustrated in Figure 6.6b, no visible peak splitting is present and the superconducting gap barely disperses on a 1 T B-field scale. This is rather intuitive: SOI sets the effective superconducting gap in the spectrum at finite k (see chapter 4) and stronger SOI will preserve this gap better at finite B. Besides, the coherence length ξ of the MBS's depends on the finite k gap, and therefore on the strength of SOI. Stronger SOI will therefore result in a shorter ξ, which in turn gives smaller energy splitting and less frequent oscillations from ZBP to split peak (see chapter 7). Similar behavior is reported by Prada et al[14].

The suggestion by Rainis et al. is that, to explain the data in chapter 5 in a picture of a topological non-trivial superconductor with MBS's, the effective E_{SO} needs to be roughly an order of magnitude larger compared to the quoted value of ~50 μeV. At the time of the experiment, the only known experimental value for SOI strength in InSb nanowires was measured in a spin-orbit qubit based on a double quantum dot[19]. This yielded a value of $E_{SO} = 50$ μeV. Due to the strong confinement in a quantum dot setting, this value is expected to represent a lower limit compared to a situation closer to a quantum wire. Recent weak anti-localization measurements, performed in an open system, are closer to the relevant scenario for the MBS case. These experiments suggest that E_{SO} indeed may be several hundreds of μeV[12], making the suggestion by Rainis et al. quite reasonable. The exact relevant value of E_{SO} is still uncertain, however, since the electrostatic potential profile underneath

the superconducting contact could influence this quantity significantly.

Assuming a larger SOI strength, splitting of the ZBP should be observed in a device with a shorter superconducting contact. In chapter 7, results obtained in devices with shorter contacts indeed show evidence of such splitting of the ZBP, both in gate space and in magnetic field, being consistent with this scenario.

A crucial aspect has to be discussed here. As initially put forward by Das Sarma et al. [4], most theory works commenting on ZBP splitting ignore the importance of electrostatic self-consistency in the model. The oscillatory behavior from peak to split peaks is based on the assumption of constant chemical potential μ as a function of B (see footnote for comments on definition of μ[5]). Due to the shifting electronic dispersion, this means that the electron density in the system is changing by varying B, see Figure 6.7a,b. However, it is rather unclear to what extent this premise of constant μ holds. Since the system already has a certain electron density, the Coulomb repulsion will counteract changes in electron density by B. In its most extreme form, the electron density is the actual constant value and μ adjusts itself upon varying B to achieve this. Figure 6.7 illustrates these two different scenarios. If the latter scenario holds, Das Sarma et al. [4] point out that barely any oscillations may be present in B. The experimental reality is likely that both effects play a role and an intermediate case between both extremes of constant μ and constant density is happening. This is confirmed by self-consistent electrostatic simulations for realistic nanowire geometries [20]. These simulations suggest that a rather subtle interplay between geometry, number of occupied subbands and SOI strength determines if peak splitting as a function of B will be present and what its periodicity will be[6].

Summarizing, the suggestion that observing periodic peak splitting in B constitutes strong evidence for the presence of MBS's in the system may be true, but represents a special case of constant μ, which unlikely corresponds to experimental reality. The complex interplay between μ and density may on its own very well explain the absence of periodic peak splitting in B in our initial experiment, next to the previous discussion on strength of SOI. Based on the arguments discussed

[5] The chemical potential μ, as used throughout this thesis, is defined as the difference in energy between the Fermi level E_F and a particular reference point in the nanowire spectrum ($\mu \equiv 0$ is the bottom of the first spin degenerate, orbital subband, see footnote 2). This should not be confused with the electrochemical potential μ_e as known from statistical mechanics. In condensed matter, in equilibrium (no bias voltage applied), the latter corresponds to E_F and is constant throughout the nanostructure. Together with the electrostatic potential V, this implies that $\mu = E_F - V$. E_F can be considered an arbitrary constant for all practical purposes. Defining a fixed reference point for μ is therefore useful, since then μ reflects the relative position of the nanowire subband with respect to E_F. Calling this quantity μ, as is common practice in the community, is unfortunately confusing, since the same symbol is reserved for the more fundamental quantity of electrochemical potential as defined in statistical mechanics.

[6] The work of Rainis et al. [5] discussed before presents a calculation of the spacing δ of two consecutive ZBP's in B once the system starts to show a quasi-periodic energy splitting as in Figure 6.6a. It is found that $\delta(B) \sim \sqrt{B}$ for increasing peak index (see also Churchill et al.). Considering the previous discussion on constant density vs constant μ, however, the assumption of constant μ by Rainis et al. is too simplistic and the $\sqrt{B}$ dependence of δ should not at all be considered as a universal property of interacting MBS's.

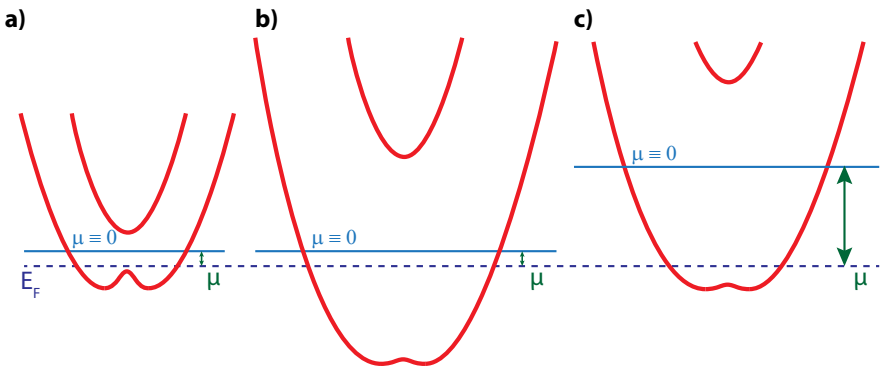

Figure 6.7 |Constant electron density versus constant chemical potential upon varying magnetic field. A schematic band structure (red) with a corresponding Fermi level E_F (black dashed lined) is shown. The reference point of chemical potential $\mu \equiv 0$ (see footnote 2) is shown in blue, and the corresponding μ (the difference between $\mu \equiv 0$ and E_F, see footnote 5) is indicated with a green vertical arrow. For simplicity, no superconductivity is included in the spectrum. The case shown in a) corresponds to a certain non-zero magnetic field B_1. In b) and c), the case of a magnetic field B_2, with $B_2 > B_1 > 0$, is shown, depicting the effect of changing nanowire spectrum as a function of B. b) illustrates the extreme case of constant μ, which leads to a change in electron density, with more occupied states below E_F. In c), the extreme case of constant electron density, with the same amount of occupied states below E_F, and varying μ, is shown. In reality, likely an intermediate case between both extremes occurs, resulting in both varying μ and varying electron density upon varying B.

here, we believe that the absence of periodic peak splitting of the ZBP in B is not a concern at all in a MBS context, but rather represents experimental reality, also in a MBS based scenario.

6.2.5 ORIGIN OF THE SOFT GAP

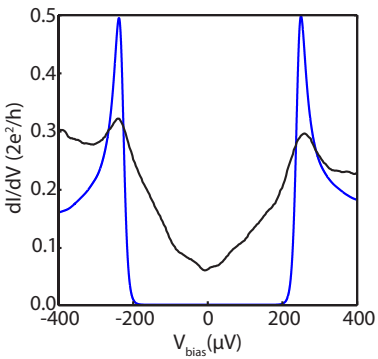

Figure 6.8 |Soft versus hard gap. The black curve corresponds to a $B = 0$ T curve from the initial tunneling spectroscopy experiment (chapter 5). In blue, an ideal BCS density of states including some thermal smearing is superimposed. The smooth, V-shaped gap with small coherence peaks from the experiment, is referred to as a 'soft' gap, whereas the ideal, BCS density of states, with no quasi-particle states in the middle of the gap, is referred to as a 'hard' gap.

The last main issue in the experiments we discuss here is the observation of a 'soft' superconducting gap: in differential conductance measurements, a very rounded, superconducting gap like shape is observed, typically showing low, broadened coherence peaks, a V shaped conductance profile inside the coherence peaks and non-vanishing conductance at zero bias. As illustrated in Figure 6.8, this is opposed to a 'hard' gap: a standard BCS type gap profile. This experimental observation presents a serious difficulty in this research: firstly, in a tunneling spectroscopy experiment, the different subgap states on top of a soft gap become less clear. Secondly, if the soft gap corresponds to the actual DOS underneath the superconductor, the interesting, non-abelian anyonic properties of MBS's are likely inaccessible.

As discussed in the footnote, broadening due to strong tunnel coupling cannot explain the soft gap observed in the experiment[7]. This implies that the actual LDOS

[7]It is well known from standard BTK theory that upon varying the transmission T of an NS junction,

contains many subgap states, resulting in a soft gap.

Recent results from Chang et al.[21], measured in devices based on nanowires with epitaxially grown superconductors on the surface, sheds light on the origin of such subgap states. Figure 6.9a, b shows the structure of such a device. An InAs nanowire is covered by an epitaxially grown Al layer, resulting in an atomically flat interface between the two materials. The Al layer is contacted by a superconducting electrode; by partially etching away the Al and contacting the bare nanowire with a normal metal, a second normal metallic electrode is made. In the resulting NS-junction, a side gate 100 nm away from the bare nanowire channel is used to induced a tunnel barrier (see Figure 6.9b). Such a gate induced tunnel barrier is very similar to our set-up, resulting in a finite width and height as well. However, despite such a non-ideal tunnel barrier, a hard gap is measured, as shown in Figure 6.9c,d. Based on these findings, we conclude that the origin of the soft superconducting gap in our experiments is very likely resulting from a non-ideal, disordered superconductor-nanowire interface, but that realistic solutions to solve this problem are at hand.

This conclusion is supported by Takei et al.[22], which aimed at a theoretical explanation of the experimentally observed soft gap. It was found that an inhomogeneous coupling between superconductor and nanowire along the interface between the two indeed could lead to a soft gap. Combining this effect together with the phenomenological Dynes model (see equation (6.3)), results in a good match

only in the limit of $T << 1$ the differential conductance is proportional to the superconducting density of states (DOS). Upon increasing T, gradually the superconducting gap in the differential conductance measurement becomes smooth and fills up, eventually turning into a twofold enhancement of conductance for $T = 1$ due to Andreev reflection. As discussed before (section 6.2.2, Figure 6.4), our tunnel barrier likely has a finite width and finite height, which may lead to an effective transmission through the system already too high to be in the proper tunneling regime thus preventing observation of a proper BCS type gap.

Several theory studies are (partially) devoted to this topic. The most relevant ones are likely the previously discussed works by Pientka et al., Prada et al. and Rainis et al.[5, 14, 15] and another work by Stanescu et al.[18]. The first three works consider both a finite width/height of the tunnel barrier (rectangular shape in the case of Pientka et al., Gaussian shape in the cases of Prada et al. and Rainis et al.) and a few (~4) occupied nanowire subbands. Regarding the soft gap, the three works lead to the same conclusion: given the conductance $G \leq 0.3G_0$, the superconducting gap should be rather hard (see Figure 6.4). The lowermost occupied subband, which is coupled most strongly, already has a relatively low T in the order of 0.1-0.2, which cannot explain the observed soft gap.

Contrary to this, Stanescu et al. claim that the softness of the gap to a large extent may be caused by this effect (which they call 'inverse proximity effect'). Such a scenario can be tested by changing the tunnel barrier strength, no evidence is found for a hard gap at small tunnel couplings. Furthermore, their claims are largely based on LDOS calculations as a function of tunnel barrier width and height. The regime in which a rounded LDOS is obtained seems to correspond to a rather high ($G > G_0$) device transparency, but the accompanying transport calculations are less complete compared to the other 3 works.

Based on the studies discussed here, we argue therefore that, although our tunnel barrier is non-ideal, its finite width and height cannot explain the soft gap observed in the experiment. This implies that the soft gap observed in the differential conductance corresponds to a large extent to the LDOS behind the tunnel barrier, and hence we actually do have a soft superconducting gap in our system.

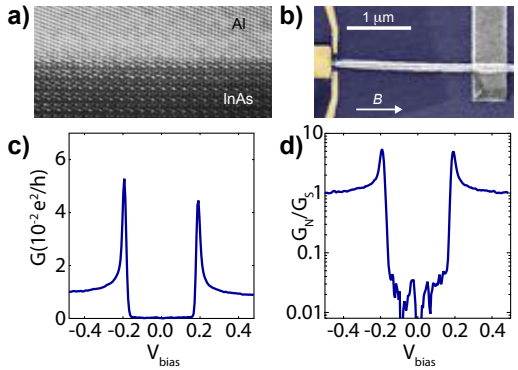

Figure 6.9 |Epitaxial full-shell device and hard induced gap. a) Transmission electron micrograph of the epitaxial N-S interface between InAs nanowire and Al. b) Scanning electron micrograph of a typical device (false color), with on the left the normal contact (yellow) and side gates (yellow), in the middle the nanowire with Al shell (white) and on the right the superconducting electrode (grey). c) Differential conductance as a function of bias voltage of an epitaxial full-shell device at B = 0. d) Normalized differential conductance. The epitaxial full-shell nanowires exhibit a subgap conductance suppression by a factor of ~ 100. Figures adapted from [21]

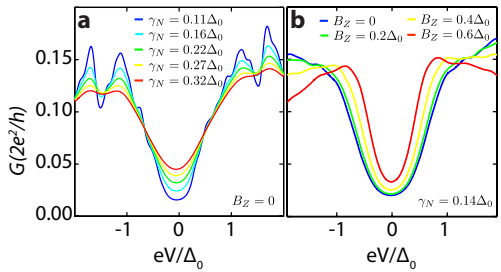

Figure 6.10 |Differential conductance in the presence of inhomogeneous coupling between nanowire and superconductor and quasi-particle broadening. a) For a fixed, realistic strength of spatially randomly changing coupling between superconductor and nanowire, strength of quasi-particle broadening is varied by changing the Dynes parameter γ. Importantly, this results in a profile close to the experimental observations. $B = 0$ T. b) Both inhomogeneous coupling and quasi-particle broadening are fixed, but B is varied. This again resembles the experimental observations quite well. Figure adapted from [22]

between experiment and numerics for realistic strengths of disorder in the model. The numerical results at $B = 0$ T are shown in Figure 6.10a, whereas in Figure 6.10b

the B dependent results are shown, which also closely resemble the experimental observations.

Importantly, both mechanisms are quite realistic in the proximitized nanowire. Although its microscopic origin is poorly understand, the Dynes model is a phenomenological necessity already in bulk superconductors such as Al and Nb.

$$n_S(E) = \left| \mathrm{Re} \frac{E/\Delta_0 + i\gamma}{\sqrt{(E/\Delta_0 + i\gamma)^2 - 1}} \right| \tag{6.3}$$

where n_S the superconducting DOS, E the energy and Δ_0 the original BCS superconducting gap. γ is the so-called Dynes parameter, modeling the presence of quasi-particles in the gap. For small Dynes parameter strength, a rounding inside the superconducting gap is found. Quasi-particle states with comparable phenomenology may very well be present in the proximitized nanowire. Most crucial however, the inhomogeneous coupling strength along the superconductor-nanowire interface is a very realistic assumption: in all cases where a very soft gap was observed, the nanowire surface was cleansed from a native oxide before deposition of the superconductor. Typically these processes involve ex situ wet etches, or in situ physical plasma etching with noble ions. It is not expected that such processing will result in a truly homogeneous coupling between superconductor and nanowire at the microscopic level.

These findings of Takei et al. and Chang et al. point into a clear direction to obtain a hard(er) gap in the nanowire: improve the S-NW interface. Our results on such optimization as presented in chapter 8 confirm this suggestion.

6.2.6 SUMMARY

In summary, we conclude that most of the deviations from the simplest model can easily be reconciled considering a more specific experimental set-up closer to reality. Importantly, this leaves the MBS interpretation completely intact.

At the same time, caution is needed in comparing models and experiment. The models discussed here are all based on a two dimensional tight binding approach for relevant parameter ranges, a geometry which is still quite far from reality. More in particular, the actual shape of the nanowire, possible non-homogeneous gating effects, and interface effects at the microscopic scale, are not considered, but are expected to be influential. Furthermore, most theory works do not consider electrostatic self-consistency, which is, however, very relevant. Finally, the same holds for the magnetostatics, also here a self-consistent approach, as governed by the Ginzburg-Landau theory, considering the presence of a superconducting film, is required. This has not been done so far, resulting in uncertainty in the actual B-profile inside the nanowire. Therefore, any true quantitative comparison between the more complex models discussed above and experimental data seems impossible as of yet and demands more complete and complex numerical models.

Several important experimental research directions can be identified based on the previous discussion. Firstly, by introducing a heterojunction in the nanowire, acting as a tunnel barrier, a sharp enough tunnel barrier may be created to reach the theoretical limit of the ZBP height. Secondly, by also probing the LDOS in the middle of the device, the gap closure accompanying the topological phase transition may be visible. Besides, this may reveal the local, bound state character of the MBS by not observing it. Especially in combination with simultaneous tunneling spectroscopy at the wire end, this would constitute new evidence for the MBS hypothesis. Thirdly, focusing on shorter superconducting wire sections may reveal interaction of MBS's. Finally, improving the superconductor-nanowire interface will result in a better quality induced gap, which in turn should allow for better distinction of subgap states and ZBP's.

6.3 ALTERNATIVE MECHANISMS RESULTING IN ZERO BIAS CONDUCTANCE PEAKS AT FINITE MAGNETIC FIELD

At the time of publication of our initial tunneling spectroscopy work on MBS's, we knew of 4 possible mechanisms resulting in ZBP's in semiconducting nanostructures. These are: Andreev bound states crossing each other at the Fermi level, the Kondo effect, reflectionless tunneling and weak anti-localization. All of these were discussed and falsified as a possible origin of the observed ZBP, see chapter 5.

Nevertheless, recent experimental works by Lee et al. on crossing ABS's and the Kondo effect, both in proximitized nanowires, are very relevant to MBS related research. For this reason, we discuss both scenario's here again, section 6.3.1 is on crossing Andreev bound states and section 6.3.2 on the Kondo effect.

More important, however, a new scenario of a ZBP which onsets at finite magnet field has been put forward shortly after our initial work. This ZBP is induced by disorder in the superconducting nanowire section and is the topic of section 6.3.3.

Section 6.3.4 summarizes this review of alternative explanations for ZBP's.

6.3.1 ZERO BIAS CONDUCTANCE PEAKS CAUSED BY CROSSING ANDREEV BOUND STATES

Upon applying a magnetic field, conventional ABS's gain Zeeman energy. As a consequence, an ABS initially at finite energy at $B = 0$ T may move down in energy and cross zero energy. Because of the equivalence of ABS's above and below the Fermi energy, this will result in a crossing of states in the spectrum. This behavior is illustrated in Figure 6.11.

Such a crossing of ABS's will result in a ZBP lasting for a range in E_Z of order of the life-time broadening of the original states. As pointed out by Lee et al., under the special condition of a superconducting gap closure shortly after this crossing point, the corresponding ZBP may be prolonged, since level repulsion between the

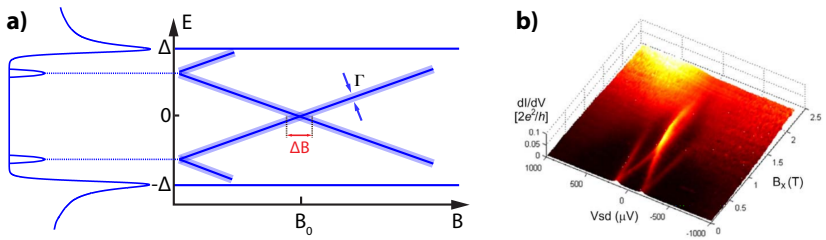

Figure 6.11 |Zero bias peaks caused by crossing Andreev bound states. a) Left: schematic density of states, showing a superconducting gap with a pair of subgap Andreev bound states (ABS's). Right: schematic dispersion of the ABS's as a function of magnetic field. The superconducting gap edge is assumed to be constant in B (horizontal blue lines). The ABS's, which are typically spin degenerate, split in energy upon applying finite B, one pair of levels moves down and eventually crosses the Fermi level, resulting in a ZBP. This zero bias peak extends over a B field range ΔB corresponding to the life-time broadening Γ of the levels. b) An example of an experimental observation where the crossing of a pair of ABS's is accompanied by a superconducting gap closure, resulting in a prolonged ZBP, due to level repulsion between the continuum of states and the ABS's. Such a ZBP, however, is sensitive to the exact values of μ and B and does not robustly occur in (μ, B)-parameter space. This allows for distinction from a possible MBS caused ZBP. Figure b) adapted from Lee et al.[7]

continuum and the ABS's prevents the ABS's moving away from zero energy. This behavior is illustrated in Figure 6.11[8]

The behavior of this type of ZBP is to some extent very similar to the expectations for a MBS induced ZBP. However, since this is essentially a crossing of two ABS's, no truly robust ZBP in (B,μ)-space is expected. Those aspects provide the means to distinguish this from a potential MBS induced ZBP. Firstly, a clearly distinguishable pair of levels, symmetrically positioned around the Fermi level, is expected. Secondly, these levels move down in energy as a function of B with the g-factor of the nanowire material. Thirdly, upon crossing the Fermi level, these levels may stick a bit to zero bias voltage, but only for a B field range corresponding in energy of order of the ZBP peakwidth. Finally, anisotropic behavior in B field angle is expected to be accompanied by a corresponding anisotropic g-factor.

In all these aspects, the experimental data shown in [23] paper and chapter 5 differs. No pair of states moving down in energy with the material's g-factor before the ZBP onset B field is observed. Based on the different B-field ranges of the ZBP observed, a maximum possible g-factor in the range of $g = 0.5 - 1$ is obtained[9] for a pair of crossing states, which is much smaller than the expected g-factor of the nanowire material InSb $\left(g \sim 55\right)$, making this a highly unlikely scenario. Furthermore, the observed ZBP extends over large gate ranges, as expected in a topologically non-trivial phase. Contrarily, crossing ABS's in a quantum dot, such as observed by Lee et al., are strictly single electron related effects, implying a ZBP at most extending over a gate range corresponding to the single electron addition energy. Finally, possible g-factor anisotropy as a cause for the observed B field angle dependence is explicitly excluded by measuring full B-dependencies over a wide range of angles (see supplementary information of chapter 5). All these observations directly contradict a scenario of crossing ABS's and this scenario is therefore irrelevant in explaining the ZBP reported in chapter 5.

Concluding, we believe that a robust, long lived ZBP in both B and gate voltage as observed in our experimental work cannot be explained by such a mechanism.

6.3.2 ZERO BIAS CONDUCTANCE PEAKS CAUSED BY THE KONDO EFFECT

The Kondo effect in quantum dots manifests itself as a conductance peak at zero bias. If only visible at finite B, such a ZBP would be similar to a MBS caused ZBP. In the Kondo effect, if a single magnetic impurity having a degenerate electronic quantum state couples to reservoirs, a many body ground state may form between reservoirs and the impurity, effectively 'screening' its free quantum number. In this

[8] Some of the experimental data obtained in other research groups in similar set-ups, may be explained by this scenario, in particular, the ZBP reported by Das et al. Because of the small B field range of the ZBP in the work by Das et al. and the fact that superconductivity in that experiment is destroyed above 100 mT, it is hard to distinguish the data conclusively from the scenario presented by Lee et al.[7]

[9] Taking $E_Z = 1/2\text{FWHM}$ as the maximum, experimentally unresolvable peak splitting ΔW, given the B field range ΔB in which the ZBP is visible, a maximum possible g-factor of $g = 2\Delta W / \left(1/2\mu_B \Delta B\right)$ can be defined for a pair of crossing states of spin 1/2.

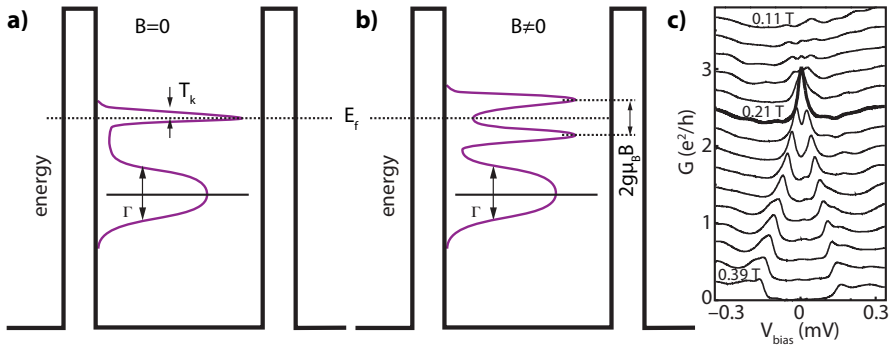

Figure 6.12 |Zero bias peaks caused by the Kondo effect. a) In a quantum dot, at $B = 0$ T, a level (indicated by a black line, life-time broadening shown in purple and denoted by Γ) may not be accessible for direct transport. If this level corresponds to odd dot occupation, a Kondo resonance (indicated by top purple peak, characteristic width set Kondo temperature T_K) may form at the Fermi level E_F between the leads and the oddly occupied, spin $1/2$ quantum dot acting as impurity. b) Upon applying a magnetic field, this Kondo resonance splits, with a total splitting of $2E_Z$. c) Under certain conditions, a Kondo effect may arise at finite magnetic field, such as at the degeneracy point of a spin singlet and triplet state. Such a ZBP, however, will split upon varying the magnetic field away from the degeneracy point. In general, a ZBP caused by the Kondo effect corresponds to a specific parameter setting, but not to a robust phase in (μ, B)-parameter space, as is expected for a MBS caused ZBP. Figure c) adapted from Sasaki et al. [25]

case, even if direct tunneling is not allowed in the electronic transport, higher order tunneling processes through the impurity via the many body ground state are possible. This leads to a conductance enhancement at the Fermi level, resulting in a ZBP, known as the Kondo effect. For in an depth review of its relevancy to nanostructures, see [24, 25].

The simplest possibility for the Kondo effect is a spin $1/2$ state for odd dot occupation. This results in the typical Kondo resonance running through odd Coulomb diamonds at zero bias voltage [24]. However, upon removing the spin degeneracy by applying a magnetic field, the Kondo resonance splits and moves to finite energy, each remaining resonance gaining an energy of $2E_Z = g\mu_B B$. Consequently, such a type of Kondo effect is not at all a candidate to consider as a cause for the observed ZBP, since it happens at zero magnetic field.

A more intricate form of the Kondo effect is the spin singlet-triplet Kondo effect[25], which happens at finite magnetic field, giving rise to a ZBP occurring at finite B. However, as with the spin $1/2$ Kondo effect, also here the degeneracy only exist for a short while in B, since the relevant levels move in energy due to the

Zeeman effect. This therefore may give rise to a crossing of two Kondo states, which form a true Kondo peak at the Fermi level while crossing each other.

More generally, the Kondo effect is only expected to result in a ZBP when a degeneracy is present in the quantum dot. Any system parameter tuning through this degeneracy will make the ZBP disappear or split in two conductance resonances at finite energy. Especially at finite magnetic field, no degeneracies possibly resulting in a Kondo effect are known which exist robustly in magnetic field, therefore no robust ZBP in magnetic field caused by the Kondo effect is expected. Furthermore, since the Kondo effect is directly originating from single electron states being degenerate in a quantum dot, any ZBP caused by the Kondo effect is only stable in gate space for at most the electron addition energy. This is opposed to the expected behavior for a MBS caused ZBP, which is stable in the whole (μ, B)-parameter space of the topologically non-trivial phase.

These characteristics of the Kondo effect allow for relatively easy distinction from a possible MBS induced ZBP. Only for a B-range corresponding to a change in E_Z similar to T_K (the characteristic linewidth of the Kondo peak), the splitting of the Kondo peak cannot be resolved. By applying a larger magnetic field, the ZBP will split. No such behavior has been observed in the experiment reported in chapter 5. In fact, based on the upper B field B_{max} at which that ZBP disappears in that work, an upper limit can be set to the possible g-factor of a spin 1/2 Kondo effect, which is in the range of 0.2 - 0.5 for the different disappearance fields observed[10]. This is highly unlikely in the system, since the InSb g-factor is measured to be ~ 55. For a Kondo effect occurring at finite B as a cause of the ZBP observed in chapter 5, the same arguments used in the previous section on crossing ABS's apply and this scenario is therefore highly unlikely to explain the experimental observations.

In summary, the above considerations rule out the Kondo effect as a cause of the observed ZBP presented throughout this thesis[11].

6.3.3 ZERO BIAS CONDUCTANCE PEAKS CAUSED BY DISORDER

As a last possible alternative cause that we are aware of, we discuss disorder induced ZBP's. Disorder in a superconducting system may create subgap states with an Andreev character, forming symmetric pairs around the Fermi level. These states may move down in energy as a function of system parameters, but in the absence of Coulomb interaction and if time reversal symmetry is preserved, avoided

[10] Again taking $E_Z = 1/2\text{FWHM}$ as the maximum, experimentally unresolvable peak splitting ΔW, given the disappearance field B_{max} of the ZBP, a maximum possible g-factor of $g = \Delta W / (\mu_B B_{max})$ can be defined for a splitting spin 1/2 Kondo resonance. For a crossing of Kondo resonances at finite B, this condition alters to $g = 2\Delta W / (\mu_B \Delta B_{max})$ with ΔB the ZBP B field range, resulting in a factor 2 larger possible g-factors.

[11] A further consideration of relevance is the competition of superconducting transport via Andreev reflection and/or direct Cooper tunneling vs single electron transport via an impurity as in the Kondo effect. Superconductivity suppresses the latter. However, upon decreasing the strength of superconductivity by applying a magnetic field, the Kondo effect may become visible again, as was shown in a recent experiment carried out by Lee et al.[7] in a related nanowire set-up. Nevertheless, in such a case, the same argument of splitting of the Kondo peak applies.

crossings form around the Fermi level. However, upon applying finite B, time reversal symmetry is broken and the spin degeneracy of such states is lifted. In this case, a single spin state that moves down in energy as a function of system parameters, such as μ and B, can cross the Fermi level instead of forming an avoided crossing. This results in the formation of a ZBP. Considering level repulsion between other disorder induced states at finite energy, together with both thermal and tunnel broadening, a ZBP may occur for considerable magnetic field ranges. Such a disorder induced ZBP mimics to some extent the expected behavior for a MBS. Several theory studies (e.g. Liu et al.[26], Bagrets and Atland[27], Pikulin et al.[9], Rainis et al.[5], Mi et al.[28]) performing tight binding calculations have shown how disorder induced ZBP may arise at finite magnetic field[12].

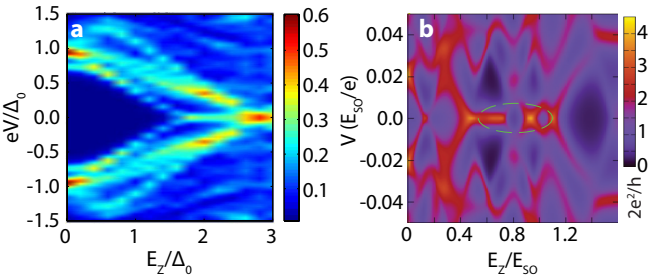

Figure 6.13 |Numerical simulations of disorder induced zero bias peaks at finite magnetic field. a) Differential conductance in the tunneling regime, shown as a colorscale representation, figure adapted from Liu et al. Finite energy states induced by disorder at $B = 0$ T move gradually down in energy and cluster around zero energy, thus mimicking the expected signal for a MBS[13]. b) Differential conductance in the transparent device regime for a particular disorder realization, figure adapted from [9]. Differential conductance shown in colorscale as a function of bias voltage and parallel magnetic field. The magnetic field range is in the topologically trivial phase, but still exhibits a conductance peak pinned to zero voltage (green circle), as in the tunneling limit shown in a).

Two features of a disorder induced ZBP distinguish it from a MBS induced ZBP. Firstly, a disorder induced ZBP is always originating from states originally at finite

[12] All theoretical evidence found so far for disorder induced ZBP's relies on rather simplistic geometries, typically involving a 2D tight binding lattice. It is, as of yet, theoretically not known if in more realistic numerical models, accounting for the actual 3D device geometry, a similar behavior will be found.

[13] In the work of Liu et al., the topological state of the system has not been checked explicitly. As pointed out Adagideli et al., upon introducing disorder in the system, the total size of the topologically non-trivial phase in parameter space is conserved (for long wires). The phase diagram, however, gets a more fragmented shape. Importantly, regions being topologically trivial in the clean case may turn non-trivial upon adding disorder to the system. Contrary to this, the work by Liu et al. assumes that the phase space of the topologically non-trivial phase does not extent beyond the clean limit case. It is therefore unclear if the simulations presented in that work actually correspond to topologically trivial cases or not.

energy which move down in energy as a function of B to form the ZBP. Secondly, a disorder induced ZBP is accompanied by discrete states at finite energy; disorder resulting in only a single pair of discrete states forming a robust ZBP at finite B is highly unlikely. These main features of a disorder induced ZBP are clearly demonstrated in the numerical simulations, as shown in Figure 6.13.

Consequentially, the strongest evidence against the scenario of a disorder induced ZBP is the absence of both a gap closure and discrete states at finite energy. Instead, a single, isolated ZBP is observed at finite B, arising without precursory finite energy states, which can be understood in a MBS framework (see section 6.2). The considerable conductance background inside the superconducting gap may be viewed as a counter argument to this, since it may reduce the contrast of the gap closure and discrete states at finite energy. However, this makes the observation of a clearly distinguishable ZBP even more puzzling, since there is no simple reason why finite energy states may loose their contrast, but the ZBP stays well visible. On the other hand, the MBS explanation, together with a soft superconducting gap due to a non-ideal superconductor-nanowire interface, offers a natural explanation to these observations.

A last important aspect is that ZBP's caused by disorder have a random origin, and are not expected to be very robust against significant changes in model parameters. This is opposed to a MBS induced ZBP, which is robust throughout the whole topologically non-trivial phase.

In stark contrast to this, the ZBP observed in our work has a robust character in both gate voltage and magnetic field. Interestingly, all working devices show this feature of a robust ZBP. Furthermore, in other chapters of this thesis, we show comparable ZBP's observed in improved devices. Although the device quality clearly improves, see chapter 7 and chapter 9, still the same robust ZBP can be observed. This is rather counter-intuitive if the ZBP is caused by disorder, in such a scenario improved device quality would correspond to a less disordered scenario, thus suppressing the crucial ingredient for this type of ZBP.

To conclusively rule out the disorder induced ZBP scenario, a number of measurements could be conducted in future tunneling spectroscopy experiments.

Firstly, the disorder induced ZBP does not have a universal height. Depending on the specific limit considered, it may either be much smaller (tunneling regime) or larger (transparent limit) than $G_0 = 2e^2/h$. The simplest way of ruling out this scenario, and confirm a MBS interpretation, is by demonstrating a robust, quantized ZBP. In a realistic setting this may be hard to achieve, however, as discussed in section 6.2.2.

Secondly, observing a systematic, controllable peak splitting and recombination would be strong evidence for a scenario of a pair of interacting MBS's. Such systematic behavior is not expected in the more random case of a disorder induced ZBP.

Thirdly, observing a topological phase diagram along the lines of Figure 6.1 would present compelling evidence against a disorder induced ZBP. This demands,

however, a careful study of the occurrence of the ZBP in (B, μ)-space over considerable parameter ranges, which is challenging in a realistic experimental setting.

Finally, increasing device complexity by adding a third, normal metallic contact at the other side of the superconducting device section could be an important step. Such a device would allow for the simultaneous observation of a ZBP at both sides of the superconducting section, showing that the LDOS at both sides contains a zero bias state. This directly disfavors a disorder induced ZBP because of its dependence on the local disorder configuration.

In summary, the observation of a robust, isolated ZBP, present in all working devices, even if their quality improved, cannot be explained by the theoretical predictions for a disorder induced ZBP. Contrarily, a realistic model invoking MBS's captures the observations well.

6.3.4 SUMMARY

Three alternative mechanisms for a ZBP have been discussed. The possibility of a ZBP caused by crossing ABS's and the Kondo effect show the importance of observing a robust ZBP, particularly in magnetic field. The observation of a narrow, long lasting ZBP which onsets at finite magnetic field in our experiments cannot be explained by these scenario's.

Possibly more relevant to our previous work, theoretically, a disorder induced ZBP at finite magnetic field is found in a wide range of different transport limits, ranging from the tunneling limit to the transparent regime of several G_0 conductance. Due to the fact that this phenomenon involves similar parameters as a MBS induced ZBP, it mimics to some extent the behavior of a MBS induced ZBP. However, at a qualitative level, some clear differences between these predictions and the experimental observations can be identified: no states at finite energy evolving into a ZBP are observed, and the ZBP is not accompanied by discrete states at higher energy, while both are expected in the disorder scenario. This leaves our observations of a robust, isolated ZBP unexplained in this scenario. By improving device quality in future experiments, further discrimination between both scenarios in tunneling spectroscopy experiments should be possible.

More generally, up to date, no alternative mechanism has been put forward capable of explaining the observed ZBP in our experiments, leaving the MBS hypothesis as the most plausible interpretation of the observations.

REFERENCES

[1] K. Law, P. A. Lee and T. Ng. Majorana fermion induced resonant andreev reflection. *Physical review letters* **103**, 237001 (2009).

[2] R. M. Lutchyn, J. D. Sau and S. D. Sarma. Majorana fermions and a topological phase transition in semiconductor-superconductor heterostructures. *Physical review letters* **105**, 077001 (2010).

[3] Y. Oreg, G. Refael and F. von Oppen. Helical liquids and majorana bound states in quantum wires. *Physical review letters* **105**, 177002 (2010).

[4] S. D. Sarma, J. D. Sau and T. D. Stanescu. Splitting of the zero-bias conductance peak as smoking gun evidence for the existence of the majorana mode in a superconductor-semiconductor nanowire. *Physical Review B* **86**, 220506 (2012).

[5] D. Rainis, L. Trifunovic, J. Klinovaja and D. Loss. Towards a realistic transport modeling in a superconducting nanowire with majorana fermions. *Physical Review B* **87**, 024515 (2013).

[6] E. J. Lee *et al.* Spin-resolved andreev levels and parity crossings in hybrid superconductor-semiconductor nanostructures. *Nature nanotechnology* **9**, 79 (2014).

[7] E. J. Lee *et al.* Zero-bias anomaly in a nanowire quantum dot coupled to superconductors. *Physical review letters* **109**, 186802 (2012).

[8] J. Liu, A. C. Potter, K. Law and P. A. Lee. Zero-bias peaks in the tunneling conductance of spin-orbit-coupled superconducting wires with and without majorana end-states. *Physical review letters* **109**, 267002 (2012).

[9] D. Pikulin, J. Dahlhaus, M. Wimmer, H. Schomerus and C. Beenakker. A zero-voltage conductance peak from weak antilocalization in a majorana nanowire. *New Journal of Physics* **14**, 125011 (2012).

[10] T. D. Stanescu, R. M. Lutchyn, and S. D. Sarma, "Majorana fermions in semiconductor nanowires," *Physical Review B*, vol. 84, no. 14, p. 144522, 2011.

[11] I. van Weperen, S. R. Plissard, E. P. Bakkers, S. M. Frolov and L. P. Kouwenhoven. Quantized conductance in an insb nanowire. *Nano letters* **13**, 387 (2012).

[12] I. van Weperen *et al.* Spin-orbit interaction in insb nanowires. *Physical Review B* **91**, 201413 (2015).

[13] İ. Adagideli, M. Wimmer and A. Teker. Effects of electron scattering on the topological properties of nanowires: Majorana fermions from disorder and superlattices. *Physical Review B* **89**, 144506 (2014).

[14] E. Prada, P. San-Jose and R. Aguado. Transport spectroscopy of n s nanowire junctions with majorana fermions. *Physical Review B* **86**, 180503 (2012).

[15] F. Pientka, G. Kells, A. Romito, P. W. Brouwer and F. von Oppen. Enhanced zero-bias majorana peak in the differential tunneling conductance of disordered multisubband quantum-wire/superconductor junctions. *Physical review letters* **109**, 227006 (2012).

[16] G. Kells, D. Meidan and P. W. Brouwer. Near-zero-energy end states in topologically trivial spin-orbit coupled superconducting nanowires with a smooth confinement. *Phys. Rev. B* **86**, 100503 (2012).

[17] M. Wimmer, A. Akhmerov, J. Dahlhaus and C. Beenakker. Quantum point contact as a probe of a topological superconductor. *New Journal of Physics* **13**, 053016 (2011).

[18] T. D. Stanescu, S. Tewari, J. D. Sau and S. D. Sarma. To close or not to close: the fate of the superconducting gap across the topological quantum phase transition in majorana-carrying semiconductor nanowires. *Physical review letters* **109**, 266402 (2012).

[19] S. Nadj-Perge *et al.* Spectroscopy of spin-orbit quantum bits in indium antimonide nanowires. *Physical review letters* **108**, 166801 (2012).

[20] A. Vuik, D. Eeltink, A. Akhmerov and M. Wimmer. Effects of the electrostatic environment on the majorana nanowire devices. *arXiv preprint arXiv:1511.08044* (2015).

[21] W. Chang, V. Manucharyan, T. S. Jespersen, J. Nygård and C. M. Marcus. Tunneling spectroscopy of quasiparticle bound states in a spinful josephson junction. *Physical review letters* **110**, 217005 (2013).

[22] S. Takei, B. M. Fregoso, H.-Y. Hui, A. M. Lobos and S. D. Sarma. Soft superconducting gap in semiconductor majorana nanowires. *Physical review letters* **110**, 186803 (2013).

[23] V. Mourik *et al.* Signatures of majorana fermions in hybrid superconductor-semiconductor nanowire devices. *Science* **336**, 1003 (2012).

[24] S. M. Cronenwett, T. H. Oosterkamp and L. P. Kouwenhoven. A tunable kondo effect in quantum dots. *Science* **281**, 540 (1998).

[25] S. Sasaki *et al.* Kondo effect in an integer-spin quantum dot. *Nature* **405**, 764 (2000).

[26] K. Law and P. A. Lee. Robustness of majorana fermion induced fractional josephson effect in multichannel superconducting wires. *Physical Review B* **84**, 081304 (2011).

[27] D. Bagrets and A. Altland. Class d spectral peak in majorana quantum wires. *Physical review letters* **109**, 227005 publisher=APS.

[28] S. Mi, D. Pikulin, M. Marciani and C. Beenakker. X-shaped and y-shaped andreev resonance profiles in a superconducting quantum dot. *Journal of Experimental and Theoretical Physics* **119**, 1018.

7

TUNNELING SPECTROSCOPY IN HYBRID SUPERCONDUCTOR-INSB SEMICONDUCTING NANOWIRE DEVICES

We report on tunneling spectroscopy measurements, focusing on a zero bias conductance peak, in improved hybrid superconductor-InSb nanowire devices. As a consequence of optimizing the contact preparation method of both superconducting and normal contact, much less spurious resonances are present compared to our initial work. We again observe a robust zero bias conductance peak, behaving very similar to the one observed before. New observations are that the zero bias peak is exclusively affected by gates underneath the superconducting region, and that the zero bias peak occasionally splits and recombines. Both new observations fit in a framework of weakly coupled Majorana bound states, and are hard to explain otherwise. Lastly, although the device quality clearly improved, the results show the necessity of a better solution to obtain a high quality superconductor-semiconductor nanowire interface.

[1] Vincent Mourik and Kun Zuo took equal shares in sample fabrication and measurements. Data analysis and reporting of results were mainly done by Vincent Mourik, with comments and assistance of Kun Zuo.

[2] In collaboration with D.J. van Woerkom, D. Car, S. R. Plissard, E. P. A. M. Bakkers, L.P. Kouwenhoven

7.1 INTRODUCTION

Majorana fermions in condensed matter are predicted to obey non-abelian exchange statistics, which may lead to topologically protected fault tolerant quantum computing [1, 2]. A very promising candidate system to establish Majorana fermions is a one dimensional nanowire with strong spin-orbit coupling that is proximitized with a standard s-wave superconductor [3, 4]. Here, Majorana bound states (MBS's) emerge at both ends of the nanowire when a topological superconducting state is reached at finite magnetic field. By incorporating such one dimensional nanowires into a two dimensional network, the non-abelian exchange statistics of MBS's can be studied [5].

These ideas are becoming increasingly relevant after our previous work on InSb nanowires proximitized with NbTiN [6]. In that work, we have established a strikingly robust conductance peak at zero voltage bias (ZBP) in a tunneling spectroscopy experiment, which resembles the expected signal if a MBS is present in the device. As pointed out in the previous chapter 6, important questions were raised by these results. Some of these can be addressed from a theoretical perspective (see chapter 6), whereas others require more thorough experimental investigations. This stimulated us to continue to improve our tunneling spectroscopy experiment.

The focus of this work is on the behavior of ZBP's in a magnetic field B parallel to the nanowire and its dependence on the different gates. Our results provide clear evidence for a robust ZBP in magnetic field, which occasionally splits and recombines, and only depends on gates underneath the superconducting contact. These observations all support the MBS hypothesis, but are impossible to explain in alternative scenario's.

This chapter is organized as follows: in section 7.2, the experimental methods are described, in section 7.3, device characterization at zero magnetic field is discussed, in section 7.4, magnetic field dependent tunneling spectroscopy data is presented, section 7.5 focuses on gate dependent tunneling spectroscopy at finite magnetic field, and in section 7.6 we discuss and summarize the work.

7.2 DEVICE FABRICATION AND MEASUREMENT SETUP

Devices are fabricated following the techniques discussed in chapter 3. Contrary to our previous work, a third normal contact is added at the other side of the superconducting contact. Such a three terminal device is shown in Figure 7.1. The nanowire is contacted at both ends with normal metallic (N) leads made from Au, and in the middle with a superconducting (S) NbTiN lead. First of all, similar to the previous work [6], the S contact only covers one half of the nanowire diameter. This is done in order to reduce the electrostatic screening of the local gate potential by the S contact, thus enabling a larger degree of control over the electron density underneath the S contact. Secondly, several optimizations on interface, dielectric and gates are implemented. Among these optimizations, the most decisive one is the improvement of the interface between nanowire and the contacts. By optimiz-

ing the Ar etch recipe parameters used for S contact preparation, and by switching the N contact preparation before thermal evaporation from sulphur passivation to physical Ar RF plasma etch, the amount of spurious resonances present in the device is much decreased.

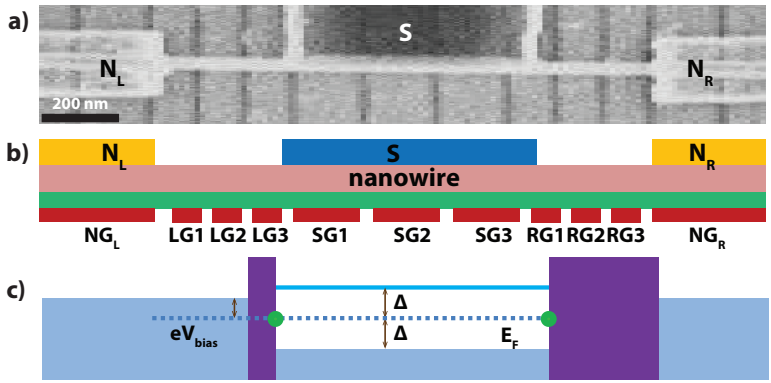

Figure 7.1 |Device layout and experimental set-up. a) Scanning electron microscope image of an Indium Antimonide (InSb) nanowire device with a left and right normal metallic contact (Au) and a superconducting (S) contact (NbTiN) in the middle. Gates underneath are isolated by a 30 nm thick layer of dielectric (HfO_2), enabling control over the local electrostatic potential. The gates underneath the S contact have a width of 150 nm, the gates underneath the bare nanowire have a width of 50 nm, gates underneath the N contacts are connected to form a single gate; all gates are spaced by 50 nm. b) Schematic device layout. c) The device is operated in an effective two terminal geometry, by applying negative voltages to the right junction gate. A sharp tunnel barrier is induced by appling a negative voltage to a single gate in front of the S contact, enabling tunneling spectroscopy measurements. Supposed position of MBS's is indicated with a green dot. The SEM image of a) corresponds to the device discussed in the text, the actual NS junction investigated is the left one.

Three terminal NSN devices are very versatile and can be operated in many different schemes for different purposes. From a practical viewpoint, a very important advantage is the freedom to choose the best NS junction in a single device, given that the S contact quality is good. Experiments involving both NS junctions, however, are very demanding, since all 3 contacts and both NS junctions in the device have to be of high quality. We therefore focus on a single NS junction, representing the best quality device obtained with contact preparation based on Ar RF plasma etching. All data discussed originates from this single NS junction, while the other NS junction was made non-conducting by applying a negative voltage to its local gates. This means that the device is effectively reduced to a two terminal NS device, as depicted in Figure 7.1c.

The device discussed here has a superconducting contact length of 600 nm and an NS contact separation of 250 nm. An SEM image of the device is shown in Figure 7.1a, the NS junction discussed in the main text corresponds to the left one of the two. All measurements are performed in a dilution refrigerator with a base temperature of 15 mK equipped with noise filtering at low temperature; standard AC lockin techniques are used to measure differential conductance.

7.3 DEVICE CHARACTERIZATION AT ZERO MAGNETIC FIELD

First we discuss device performance at $B = 0$ T. The device is characterized by measuring differential conductance $\mathrm{d}I/\mathrm{d}V$ as a function of both bias voltage V_{bias} and tunnel barrier gate voltage. Figure 7.2 shows such characterization measurements of tunnel barrier gate LG3 in a conductance regime ranging from 0 to a few conductance quanta (units of $G_0 = 2e^2/h$).

Figure 7.2a shows a $\mathrm{d}I/\mathrm{d}V$ measurement versus LG3 for a bias range of ±7.5 mV. Around $V_{\mathrm{bias}} = \pm 0.75$ mV, conductance peaks that are reminiscent of BSC type quasi-particle peaks are visible (yellow arrows) for the full gate range. Some weak and broad conductance resonances modulated by the tunnel barrier gate are visible, leading to a conductance variation of the order of $0.1G_0$. No Coulomb blockade related phenomena are observed, showing that no additional tunnel barriers are present in the device.

A zoom in on the low conductance region is shown in Figure 7.2c. In the relevant conductance range for the tunneling spectroscopy experiment, no strongly resonant states crossing zero energy are observed. This is a significant improvement compared to the devices shown in our previous work [6] as can be seen easily by comparing to Figure S9 of that work.

An accompanying differential conductance trace is shown in Figure 7.2d. Such a trace represents the typical choice for the tunnel barrier conductance in the experiment. The horizontal feature at $V_{\mathrm{bias}} = \pm 0.75$ mV in Figure 7.2a and 7.2c is visible here as a pair of broadened coherence peaks. The pairing strength $\Delta = 0.75$ mV does not correspond to the typical bulk superconducting gap of 1.5-2.0 mV in the NbTiN lead. However, since the nanowire is only half covered by the superconductor, a possible smaller gap towards the edge of the superconducting contact is plausible. Inside the superconducting gap, on top of a rounded, slightly V shaped background density of states, a pair of shoulders at $V_{\mathrm{bias}} \pm 0.1$ mV is visible. This feature is robust in gate voltage, and therefore likely corresponds to the effective induced gap in the nanowire.

Despite the clear improvements compared to our previous work, the superconducting gap observed is still rather 'soft', especially compared to the shape of the superconducting gap measured in devices with an epitaxially grown S contact [7]. Optimizing the S-nanowire interface further is therefore an ongoing effort, see also chapter 8.

7.4 MAGNETIC FIELD DEPENDENT TUNNELING SPECTROSCOPY

Next we focus on tunneling spectroscopy measurements as a function of B. The main results on this topic are presented in Figure 7.3. Two different datasets are shown, dataset I (Figure7.3 a, c, e) and dataset II (Figure7.3 b, d, f).

Dataset I shows a B dependent $\mathrm{d}I/\mathrm{d}V$ measurement for a particular combination of gate voltages underneath S and tunnel barrier gate. In 7.3a, the dataset is represented as a colormap, in 7.3e $\mathrm{d}I/\mathrm{d}V$ vs V_{bias} traces from 7.3a are plot above each other. In both 7.3a and 7.3e a feature around ± 100 μV reminiscent of a superconducting gap is visible up to 1.2 T. A ZBP emerging around B = 160 mT is

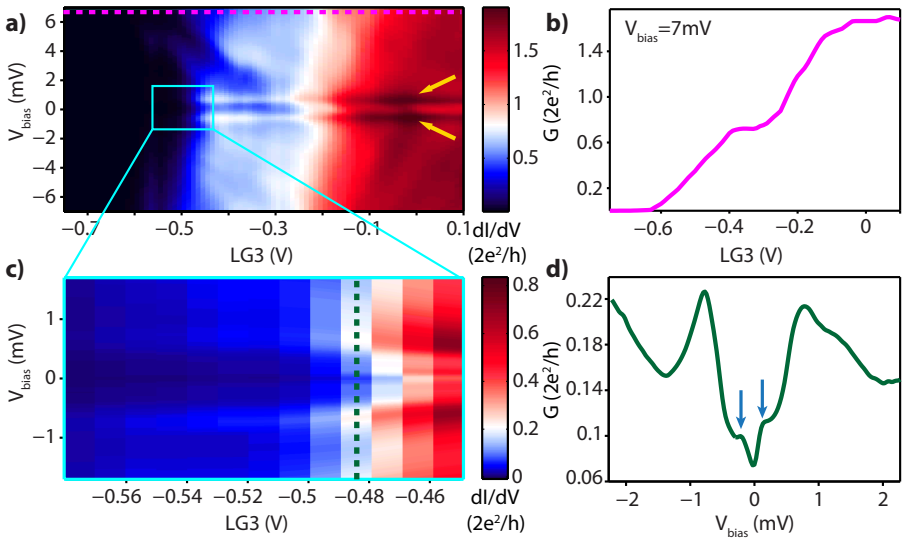

Figure 7.2 |Device characterization at $B = 0$ T. a) $\mathrm{d}I/\mathrm{d}V$ measurement versus tunnel barrier gate LG3. Gates NGL, LG1,2 are put at positive gate voltages of $+1.25$ V, maximizing the junction transparency. Peaks reminiscent of a superconducting density of states, likely corresponding to the bulk gap, are visible (yellow arrows). b) Differential conductance as a function of LG3 at Vbias = 7 mV (pink dotted line in a)), showing a typical pinch off curve. c) Zoom in on a) (yellow box in a)), the relevant conductance range for the tunnel spectroscopy experiment. d) Differential conductance as a function of bias voltage at LG3 = -0.49 V (green dotted line in c)), representing a typical choice for the tunneling barrier conductance in the experiment. Again, a superconducting density of states with coherence peak around $V_{\mathrm{bias}} = \pm 0.75$ mV is visible. Inside the superconducting gap, a pair of shoulders at $V_{\mathrm{bias}} = \pm 0.1$ mV, stable in the whole gate range of c), is present, likely corresponding to a smaller effective induced superconducting gap in the nanowire.

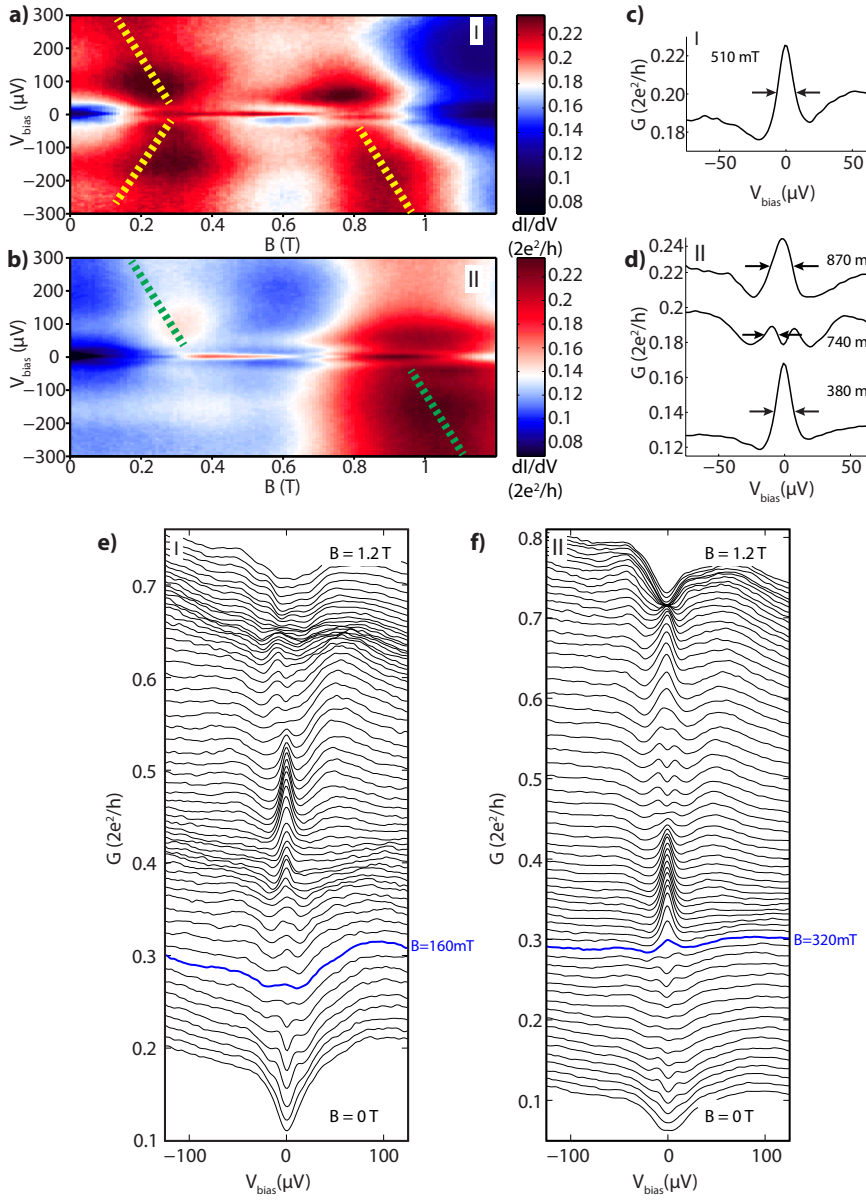
a)
b)
c)
d)
e)
f)
I
II
B (T)
V_bias (μV)
dI/dV (2e²/h)
G (2e²/h)
510 mT
870 mT
740 mT
380 mT
B = 1.2 T
B = 0 T
B=160mT
B=320mT

observed, which corresponds to a Zeeman energy E_Z of 230 μV ($E_Z = 1/2 g\mu_B B$, $g = 50$). This matches well the criterion for reaching a topologically non-trivial state, $E_Z > \sqrt{\Delta^2 + \mu^2}$, assuming $\Delta = 100$ μV and a small non-zero μ. Above 710 mT,

Figure 7.3 ***(preceding page)*** |Magnetic field dependent tunneling spectroscopy. The magnetic field B is applied along the nanowire within a precision of $\sim 5°$. Two different datasets, indicated by I and II, are shown. a) Dataset I: B dependent $\mathrm{d}I/\mathrm{d}V$ measurement for a particular combination of gate voltages underneath S and tunnel barrier gate. A ZBP emerging around 160 mT is visible, preceded by a pair of symmetrically positioned states around zero energy that come together at the ZBP onset field. Above 710 mT, the ZBP splits into a pair of peaks symmetrically positioned around zero bias voltage which run parallel for about 200 mT. Resonances with a ~2 meV/T slope are indicated with yellow dotted lines, which, upon crossing zero energy, affect the contrast of the low energy features, as is visible around 200 and 900 mT. b) Dataset II: B dependent $\mathrm{d}I/\mathrm{d}V$ measurement for a different combination of gate voltages underneath S and tunnel barrier. Now a ZBP emerges at $B = 320$ mT. At lower fields, again a pair of states symmetric around zero bias voltage is visible, which merge into the ZBP at ~ 300 mT. At ~ 650 mT, the ZBP splits into a pair of states symmetric around zero bias voltage, becoming a single ZBP again at ~ 810 mT. Finally, the ZBP disappears around ~ 1.1 T. As in a), resonances with a high slope in B are present, indicated by green dotted lines. c) Zoom in on part of a $\mathrm{d}I/\mathrm{d}V$ trace from dataset I, taken at 510 mT. The peak height and full width at half maximum (FWHM) are $0.05G_0$ (G_0 in units of $2e^2/h$) and 16 μV respectively, position of FWHM is indicated with arrows, background conductance level is taken as peak base. d) Zoom in on parts of $\mathrm{d}I/\mathrm{d}V$ traces from dataset II, taken at 380 mT, 740 mT and 870 mT. The 740 mT trace is offset for clarity by $0.035G_0$, the 870 mT by $0.015G_0$. The ZBP peak at 380 mT has a FWHM value of 15 μV and a height of $0.05G_0$. At 740 mT, both peaks have a FWHM value of 12 μV , a height of $\sim 0.01G_0$ and are separated by 20 μV. The ZBP at 870 mT has a FWHM value of 22 μV and a height of $\sim 0.035G_0$ and is slightly broadened by the zero energy crossing of a fast dispersing resonance (see b)). In all cases, the FWHM is indicated by arrows, and the background conductance level is taken as the peak base. e) $\mathrm{d}I/\mathrm{d}V$ vs V_{bias} traces from dataset I, shown in a,) plot above each other, and f) $\mathrm{d}I/\mathrm{d}V$ traces from dataset II, shown in b), plot above each other. In both cases, the lowermost trace corresponds to $B = 0$ T and the uppermost trace to $B = 1.2$ T, and each subsequent trace corresponds to an increase in B of 20 mT. In both panels, individual curves are offset for clarity by $0.01G_0$, except the lowermost trace taken at $B = 0$ mT. The ZBP onset magnetic fields are highlighted in c) and d) with blue lines. Difference in gate values of dataset I vs dataset II: LG3 (tunnel barrier) = -0.54 V vs -0.56 V, SG1 = 1.5 V vs 1.55 V, SG2 = 1.25 V vs 1.26 V and SG3 = 1.0 V vs 1.26 V. All other gates have the same potential. Colorscales in a) and b) are different.

the ZBP splits into a pair of peaks which run parallel for about 200 mT. At higher B fields, the poor contrast of low energy features does not allow for further distinction of the different states, but no clear ZBP is present any more. In Figure 7.3a, resonances with a ~2 meV/T slope in the $\mathrm{d}I/\mathrm{d}V$ measurement are indicated with yellow dotted lines. Such states clearly have a non-Majorana character, but upon crossing the Fermi level, they affect the contrast of the low energy features, as is visible around 200 and 900 mT. In Figure 7.3c, a single linecut of the ZBP at $B = 510$ mT is shown, the peak height and full width at half maximum (FWHM) are $0.05G_0$ and 16 μV respectively, comparable to the value measured in our previous work.

Dataset II is similar to dateset I, but with a sligtly different combination of gate voltages of gates underneath S (see caption Figure 7.3). In this second dataset, a ZBP onsets at $B = 320$ mT, corresponding to $E_Z = 450$ μV. At ~650 mT, the ZBP splits into a pair of symmetric states around zero energy, which recombine into a single ZBP at ~810 mT. Finally, the ZBP disappears at around 1.1 T. Similar to dataset I, resonances with a high slope (~2 meV/T) in B are visible (green dotted lines). In Figure 7.3d shows several $\mathrm{d}I/\mathrm{d}V$ traces taken at different B strengths, illustrating that the ZBP in dataset II has a similar width and height as in dataset I.

A few important differences can be identified between datasets I and II. Firstly, the ZBP onset field is 160 mT in dataset I vs. 320 mT in dataset II. Secondly, the ZBP splits into two peaks from 710 mT on in dataset I vs. the ZBP splits at 650 mT and recombines into a single ZBP at 810 mT in dataset II. This different ZBP onset field and the different behavior of the ZBP at higher B fields are strong indications that the ZBP and its appearance are highly dependent on the gates underneath the superconducting section. This is expected if a topological superconductor is created [3, 4].

The ZBP observed here is very robust in magnetic field, sticking to zero voltage bias for more than 500 mT. Considering the resolution of our measurement, split peaks with a rather small splitting of the order of 20 μV can easily be distinguished from a single ZBP. Taking the typical peak width W of the ZBP (15 μV) as an experimentally unresolvable peak splitting, a pair of states linearly crossing through zero bias would result in a maximum possible g-factor of $g = 2E_Z/\left(\mu_B B\right)$ with $E_Z = W/2$. In the case of dataset I, where the ZBP extends over 550 mT, this corresponds to a maximal possible g-factor of ~ 0.5. Such small effective g-factors are to our knowledge impossible to occur in our system, given the large measured InSb g-factor of ~50. Furthermore, the fact that the ZBP splits and recombines is impossible to explain by a level crossing of states with a small effective g-factor. Therefore, explanations in terms of a crossing of topologically trivial, spinfull states, for example the singlet-triplet Kondo effect or non-topological Andreev bound states [8, 9], cannot explain our observations.

In conclusion, the data presented in Figure 7.3, reproduces the data shown in Figure 2 of our previous work (chapter 5). This type of long lived ZBP appearing at finite magnetic field has been observed in 5 independently fabricated and measured devices (data on 4 other devices not shown). Moreover, an oscillatory behav-

ior from single peak to split peaks is sometimes observed. This new feature does remind of the expected pattern in magnetic field for a pair of interacting MBS's [10–12]. However, as pointed out before (chapter 6), it is unknown whether the system locally favors a constant charge density or a constant chemical potential (or a combination of these) upon varying the magnetic field, hindering a more quantitative analysis [13].

7.5 INFLUENCE OF GATES ON ZERO BIAS PEAK

The emergence of MBS's not only depends on B, but also depends on μ, which is controlled locally by changing gate voltages. Studying the gate voltage dependence of the observed ZBP is therefore a very important complementary to the B dependent observations. Ideally one would completely map out the phase diagram of the ZBP in (B, μ) space. However, in practice, this turned out to be impossible due to limited charge stability of our devices. Nevertheless, demonstrating a particular type of behavior as a function of gate voltage is possible and will be discussed here.

As different gates in the device have different roles, the discussion on gate dependent tunneling spectroscopy will be split into three parts. We first discuss the effects of gates at the N side of the tunnel barrier, next we discuss the influence of the tunnel barrier gate itself and finally the gates underneath the S contact are discussed.

7.5.1 EFFECT OF GATES AT THE N SIDE OF THE TUNNEL BARRIER

The discussion on gates at the N side of the tunnel barrier focuses on gate LG2, the gate next to tunnel barrier gate LG3. Figure 7.4 and Figure 7.5 show a single dataset of 3 different B dependent tunneling spectroscopy measurements, represented as colormaps in Figure 7.4 and as line traces plot above each other in Figure 7.5. The 3 measurements are taken for slightly different values of gate LG2 (see caption).

Varying the LG2 gate potential varies the background conductance in the different scans. This is visible in particular for the broad resonance crossing through zero bias around 800 mT, which is shifted downwards to a lower magnetic field. Importantly, however, the low energy features are not affected at all by such conductance modulations. The onset magnetic field of the ZBP and the magnetic field where it splits, recombines and disappears are the same in all 3 scans, as indicated in the figure by the dotted vertical lines. The behavior of LG1 and NLG is very similar to the effect of LG2 (data not shown). More generally, except affecting its contrast, in none of the devices evidence has been found of tuning effects on the ZBP by gates at the N side of the tunnel barrier.

7.5.2 EFFECT OF THE TUNNEL BARRIER GATE

Next we focus on the effect of the tunnel barrier gate. An important experimental limitation is that the tunnel barrier is never defined by a single gate only. Especially the neighboring gates, both at the N and S side of the tunnel barrier, affect its

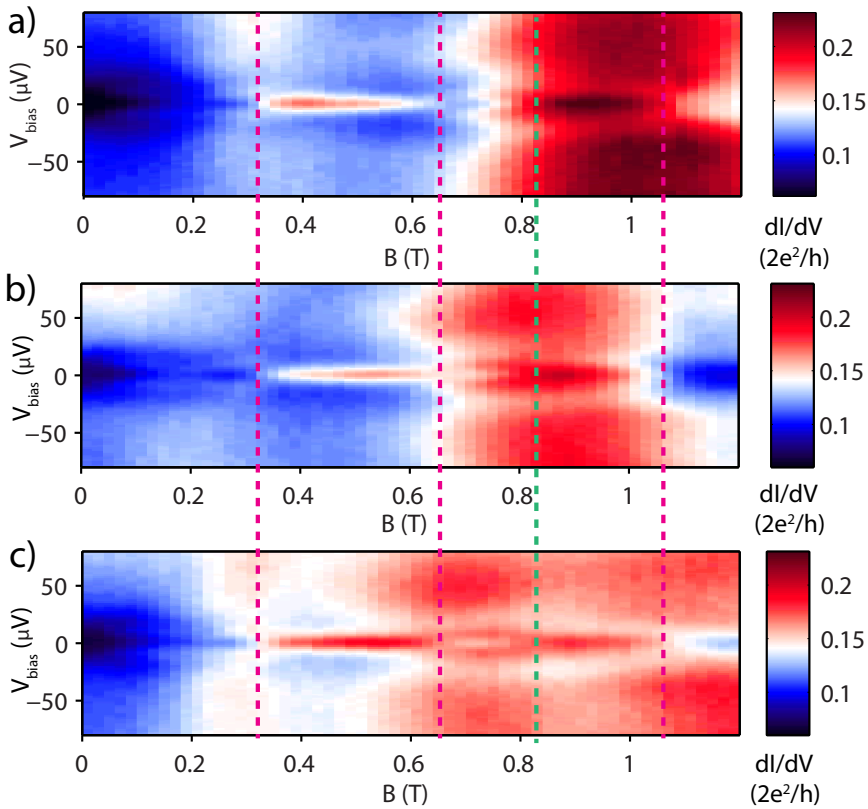

Figure 7.4 |Robustness of low energy features against background conductance fluctuations induced by N gates. a), b), c): B dependent $\mathrm{d}I/\mathrm{d}V$ measurements for different values of gate LG2. a) corresponds to the exact same gate tuning of Figure 7.3b), here LG2 = 1.25 V. In b), LG2 = 1.3 V, in c) LG2 = 1.4 V. The most important B values for the low energy features are indicated with dotted lines: the ZBP onset field at 310 mT, the ZBP splitting field at 650 mT, the second ZBP onset field at 810 mT and the field at which the ZBP disappears at 1050 mT. These B field values are constant in all measurements, although the background conductance is changing. In particular the resonance crossing zero bias around 800 mT is shifting down in B in b) and c) without affecting the low energy features. Colorscales are identical in all panels.

strength upon varying their potential. Importantly, the gate SG1, which is next to the tunnel barrier gate LG3, is a crucial gate in observing a ZBP. This particular gate is located at the edge of the S contact, next to the nanowire segment in which the tunnel barrier is formed, and therefore couples capacitively to the tunnel barrier

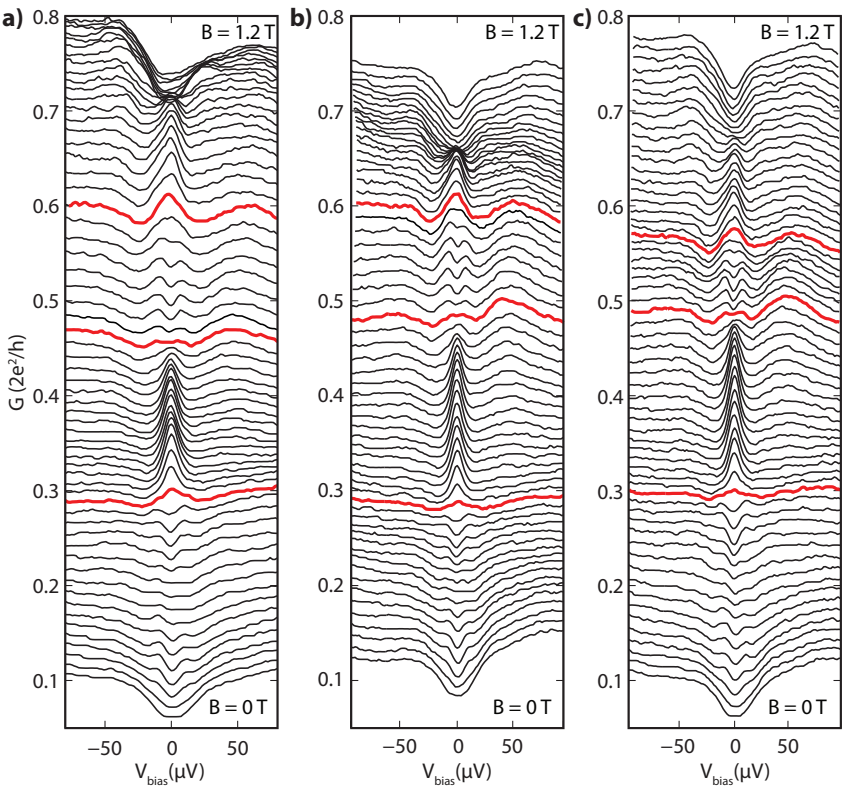

Figure 7.5 |Robustness of low energy features against background conductance fluctuations induced by N gates. Line traces in a), b), c) are from the same data as shown in Figure 7.4a), b), c) respectively. In all panels, the lowermost curve corresponds to $B = 0$ T and the uppermost curve to $B = 1.2$ T, and curves are plot above each other with a $0.01G_0$ offset for clarity, except for the 0 T curves. B fields where the ZBP onsets, splits and recombines, are colored in red.

rather efficiently.

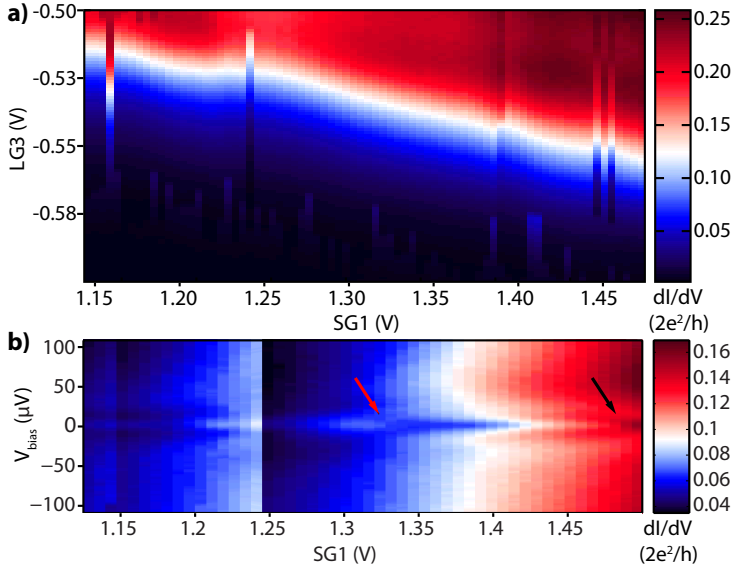

Figure 7.6 |Dependence of tunnel barrier strength on gates near S contact edge. a) $\mathrm{d}I/\mathrm{d}V$ measurement as a function of both tunnel barrier gate LG3 and the first gate under S, SG1. This is done at a fixed $V_{\mathrm{bias}} = 0$ μV. Decreasing conductance is visible in the diagonal direction from upper right to lower left corner, a consequence of both LG3 and SG1 coupling to the tunnel barrier. Several discrete jumps are present in the data, likely caused by moving charges near the device. Such jumps complicate and often disable a large scale systematic investigation of the gate parameter space. Device settings: $B = 800$ mT, SG2 = 0.735 V, SG3 = 0.5 V. b) Gate dependent $\mathrm{d}I/\mathrm{d}V$ measurement for SG1 at $B = 0.6$ T. The other relevant gate potentials are LG3 = -0.54 V, SG2 = 0.735 V, SG3 = 0.5 V. Starting from a ZBP at 1.5 V, a pair of split peaks appears around 1.48 V and a ZBP appears again at 1.33 V (see black and red arrows), showing that SG1 changes low energy features considerably.

Figure 7.6a shows this coupling effect. Here a $\mathrm{d}I/\mathrm{d}V$ measurement as a function of both LG3 and SG1 at $V_{\mathrm{bias}} = 0$ μV is shown. The data reveals a clear trend of decreasing conductance in the diagonal direction from upper right to lower left corner, explicitly showing that both gates tune the transparency of the tunnel barrier. The cross coupling shown here is very typical for most of the devices, typically changing the potential on LG3 results in a factor 5 to 10 times stronger effect in device conductance compared to the same potential change on SG1.

This cross coupling complicates the experimental situation considerably, because ideally one would like to tune the chemical potential underneath S and the

tunnel barrier strength independently by individual gates. By aligning the tunnel barrier gate exactly at the edge of the S contact or by extending it slightly (10-20 nm) underneath the S contact, the coupling of SG1 to the tunnel barrier could be largely minimized. However, in all devices investigated, a complete separation of the roles of these two gates has never been achieved. Therefore, performing a true systematic tunnel barrier strength dependence of the ZBP has been not been possible in our experiments up to now.

7.5.3 EFFECT OF GATES UNDERNEATH THE S CONTACT

Finally we discuss the effect of gates underneath the superconducting contact. In Figure 7.6b, a dI/dV measurement at 600 mT is shown as a function of SG1. Going from right to left, firstly, a significant overall conductance dropping is visible, mainly caused by coupling of gate SG1 to the tunnel barrier, as discussed before. Secondly and more importantly, the ZBP is strongly tuned by this gate. At the right end of the gate range a ZBP is present, which becomes a pair of split peaks around 1.48 V. Upon decreasing the gate voltage further, around 1.33 V, a ZBP emerges again, which extends till the left end of the gate range. This behavior is very typical for SG1, it changes the ZBP and its splitting considerably. In fact, the general observation from all devices is that the first gate underneath the S contact plays a crucial role in determining the ZBP onset field, at what B field the ZBP will split and if it will recombine into a ZBP again.

In Figure 7.7 the effects of gates SG2 and SG3 are shown. Figure 7.7a and Figure 7.7c shows gate dependent dI/dV measurements for SG2 and SG3 at $B = 0.4$ T respectively; Figure 7.7b and Figure 7.7d are the same measurements at $B = 0.6$ T. Since these gates are deep underneath the S contact, different from SG1, the background conductance only slowly varies due to the inefficient coupling to the tunnel barrier. For both gates, at 0.4 T a ZBP is present in the full gate ranges. Contrary to this, at 0.6 T, a strong tuning effect of the ZBP is observed for both gates. It is likely that the pattern of a periodically disappearing ZBP at 600 mT is directly connected to the oscillatory behavior between ZBP and split peaks observed in B (see Figure 7.3), which is expected in the case of interacting MBS's. However, experimentally this could not be established explicitly.

In conclusion, the data shows that the appearance of the ZBP, its onset B field and its splitting are strongly tuned exclusively by the gates underneath S. This observed tunability of the ZBP by all gates underneath the S contact, and the absence of such tuning by gates at the N side, is expected in the presence of a MBS at the edge of the S contact [3, 4].

7.6 CONCLUSION

A few important conclusions based on the research presented here can be reached. To start, the observed ZBP presented here is a direct reproduction of the feature that was presented in our previous work, except its magnetic field angle dependence, which was not investigated here. Based on both works no distinction can be made

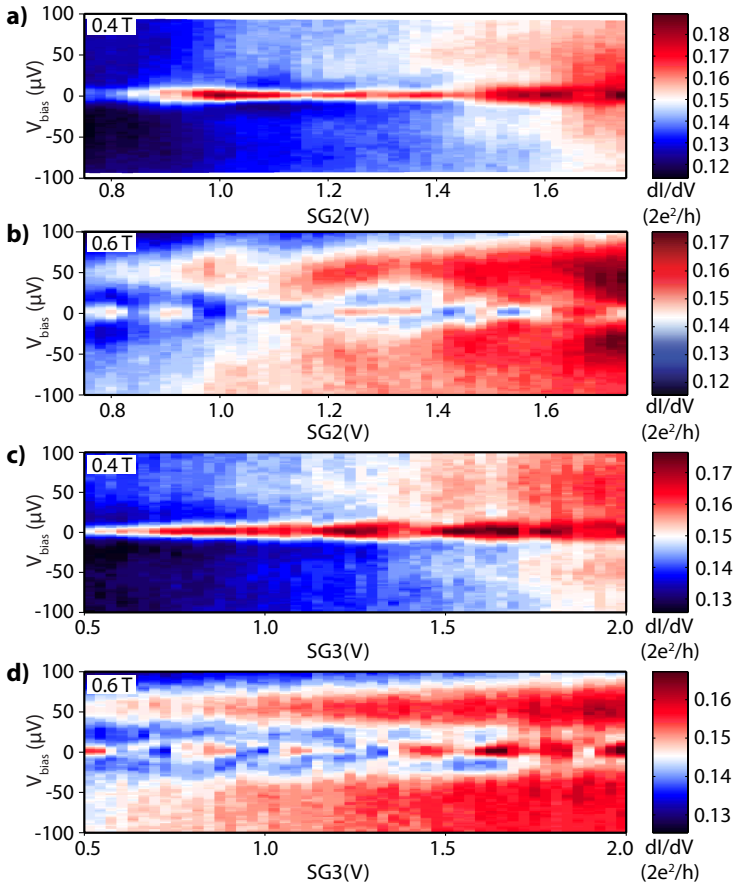

Figure 7.7 |Tunability of ZBP by gates deep under S. a) and b) are gate dependent $\mathrm{d}I/\mathrm{d}V$ measurements for SG2 at different B fields. a) $B = 0.4$ T. On top of a slowly varying background, a ZBP is visible. At this B field the ZBP is not tuned by changing SG2. b) $B = 0.6$ T. Now on top of a slowly varying background, a strong tuning effect of the ZBP is observed. It is not clear if the ZBP splits or simply disappear as a function of gate. Gate tuning: LG3 = -0.575 V, SG1 = 1.575 V, SG3 = 1.0 V. c) and d) are gate dependent $\mathrm{d}I/\mathrm{d}V$ measurements for SG3 at different B fields. In c) $B = 0.4$ T. As for SG2, on top of a slowly varying background, a ZBP is visible which is not tuned by SG3. d) $B = 0.6$ T. As in b), on top of a slowly varying background conductance, the ZBP is strongly modulated. Sometimes it may split, but the data quality does not allow for strong conclusions on this. Gate tuning: LG3 = -0.575 V, SG1 = 1.575 V, SG2 = 1.31 V.

in terms of physical origin of the feature. Such a ZBP has now been reproduced in at least 5 different devices.

Besides mere reproduction, the work presented here evidently adds important new observations to the previous work. Firstly, it is clear now that the ZBP couples to gates underneath the superconducting contact exclusively, which strongly indicates that it originates from a physical process in the nanowire section underneath the S contact. Secondly, splitting and recombination of ZBP's in magnetic field is shown, a possible direct consequence of interacting MBS's. Together, all these observations further support the hypothesis of having MBS's in our device, especially since alternative models based on crossing ABS's or the Kondo effect are ruled out.

Furthermore, our current work shows a very important aspect of this specific research. Regardless of the initially rather easily observed promising signatures of MBS's, it is a complicated task to fully control and understand the possibly emerging topologically non-trivial superconducting state. We strongly believe that this can only be achieved by controlling and understanding the devices better from a material and fabrication viewpoint first. In particular, the improved data quality shown here was achieved by optimizing the Ar plasma etch used in S contact preparation. This indicates that the interface between superconducting contact and InSb nanowire is the most crucial factor in this research. Therefore, this interface is further optimized, as discussed in the next chapter 8. Also, recent experiments carried out with epitaxial growth of superconductors on nanowires are important and are a promising research direction [7]. Either way, obtaining high quality devices, in which a full, systematic investigation of the ZBP dependence in (gate,B)-parameter space is possible, should result in further understanding of the observed ZBP and its likely cause, a MBS.

REFERENCES

[1] C. Nayak, S. H. Simon, A. Stern, M. Freedman, and S. D. Sarma, "Non-abelian anyons and topological quantum computation," *Reviews of Modern Physics*, vol. 80, no. 3, p. 1083, 2008.

[2] A. Kitaev, "Fault-tolerant quantum computation by anyons," *Annals of Physics*, vol. 303, no. 1, pp. 2 – 30, 2003.

[3] R. M. Lutchyn, J. D. Sau, and S. D. Sarma, "Majorana fermions and a topological phase transition in semiconductor-superconductor heterostructures," *Physical review letters*, vol. 105, no. 7, p. 077001, 2010.

[4] Y. Oreg, G. Refael, and F. von Oppen, "Helical liquids and majorana bound states in quantum wires," *Physical review letters*, vol. 105, no. 17, p. 177002, 2010.

[5] J. Alicea, "Majorana fermions in a tunable semiconductor device," *Physical Review B*, vol. 81, no. 12, p. 125318, 2010.

[6] V. Mourik, K. Zuo, S. Frolov, S. Plissard, E. Bakkers, and L. Kouwenhoven, "Signatures of majorana fermions in hybrid superconductor-semiconductor nanowire devices," *Science*, vol. 336, no. 6084, pp. 1003–1007, 2012.

[7] W. Chang, S. Albrecht, T. Jespersen, F. Kuemmeth, P. Krogstrup, J. Nygård, and C. Marcus, "Hard gap in epitaxial semiconductor–superconductor nanowires," *Nature nanotechnology*, vol. 10, no. 3, pp. 232–236, 2015.

[8] E. J. Lee, X. Jiang, R. Aguado, G. Katsaros, C. M. Lieber, and S. De Franceschi, "Zero-bias anomaly in a nanowire quantum dot coupled to superconductors," *Physical review letters*, vol. 109, no. 18, p. 186802, 2012.

[9] E. J. Lee, X. Jiang, M. Houzet, R. Aguado, C. M. Lieber, and S. De Franceschi, "Spin-resolved andreev levels and parity crossings in hybrid superconductor-semiconductor nanostructures," *Nature nanotechnology*, vol. 9, no. 1, pp. 79–84, 2014.

[10] S. D. Sarma, J. D. Sau, and T. D. Stanescu, "Splitting of the zero-bias conductance peak as smoking gun evidence for the existence of the majorana mode in a superconductor-semiconductor nanowire," *Physical Review B*, vol. 86, no. 22, p. 220506, 2012.

[11] D. Rainis, L. Trifunovic, J. Klinovaja, and D. Loss, "Towards a realistic transport modeling in a superconducting nanowire with majorana fermions," *Physical Review B*, vol. 87, no. 2, p. 024515, 2013.

[12] E. Prada, P. San-Jose, and R. Aguado, "Transport spectroscopy of n s nanowire junctions with majorana fermions," *Physical Review B*, vol. 86, no. 18, p. 180503, 2012.

[13] A. Vuik, D. Eeltink, A. Akhmerov, and M. Wimmer, "Effects of the electrostatic environment on the majorana nanowire devices," *arXiv preprint arXiv:1511.08044*, 2015.

8

OPTIMIZATION OF SUPERCONDUCTOR-INSB NANOWIRE INTERFACE

Forming Majorana bound states in semiconducting nanowires directly implies inducing superconductivity in the nanowire via the proximity effect. Two different consequences of the proximity effect can be measured experimentally in a straightforward manner. Firstly, a Josephson junction can be formed, which can be verified by measuring a supercurrent in the device. Secondly, by operating such a device in the tunneling regime, an induced superconducting gap should be visible in a voltage-biased measurement. In order to determine the quality of induced superconductivity in semiconducting nanowires, one can use different benchmarks, here we focus on the size and shape of the induced superconducting gap. This is the most relevant aspect in the current tunneling spectroscopy measurements on Majorana bound states, furthermore, in view of future experiments which rely on parity conservation, no quasi-particle states are allowed within the superconducting gap near the Fermi level. Therefore, this chapter reports on the results of our optimization strategy for the induced superconducting gap in semiconducting InSb nanowires.

[1] Kun Zuo contributed to sample fabrication and measurements. Vincent Mourik assisted with measurements. Vincent Mourik and Kun Zuo contributed to data analysis. Kun Zuo was mainly responsible for reporting of the results, with comments and assistance of Vincent Mourik.
[2] In collaboration with O. Gul, F.K. de Vries, D.J. van Woerkom, D.B. Szombati, D. Car, S. R. Plissard, E. P. A. M. Bakkers, L.P. Kouwenhoven

8.1 INTRODUCTION

In a hybrid superconductor-semiconductor nanowire device, signatures of a Majorana bound state (MBS) were observed (chapter 5). This is the first step towards exploring topological superconducting states and non-abelian exchange statistics. Unfortunately, the non-ideal induced superconducting gap observed in these experiments results in a considerable background of electronic states, as discussed in chapter 6. The crucial next step therefore is to improve the quality of the induced superconducting gap and thus enable furthering this research.

Both on theoretical and experimental grounds (chapter 6), the non-ideal induced superconducting gap originates to a large extend from a poor quality, inhomogeneous interface between superconductor and semiconducting nanowire. Such an interface is likely caused by the etching required to remove the nanowire's native surface oxide prior to superconductor deposition. To improve this interface, the removal of the nanowire surface oxide can be optimized.

Alternatively, the formation of a surface oxide can be avoided altogether by in situ epitaxial growth of a superconducting film onto the nanowire. The epitaxial growth technique has already shown a very promising superconducting gap quality in the case of superconducting Al and InAs semiconducting nanowires1 [1]. However, up to date, this technique is not applied to InSb nanowires. Furthermore, superconducting Al has a low critical magnetic field, hindering the formation of a topologically non-trivial state. Therefore we focus on optimizing the oxide removal technique for InSb nanowires prior to deposition of the high critical magnetic field superconductor NbTiN.

Here we compare Ar plasma based oxide etching to chemical wet etching and develop an optimized etching recipe, resulting in a better quality induced superconducting gap surviving up to magnetic field strengths of order 1 T.

8.2 METHODS

After growth, when the nanowires are taken out of the growth reactor, almost instantly a thin, self-terminating oxide layer forms on the nanowire surface as a consequence of exposure to air [2]. This surface oxide, with a typical thickness of less than 5 nm, forms an insulating layer and has to be removed before any electrical contacts can be made. To achieve the superconducting proximity effect and have a high quality induced gap in the nanowire, a very homogeneous, high transparency interface is demanded, making careful etching of the surface oxide a crucial process.

8.2.1 ETCHING OF NATIVE OXIDE ON INSB NANOWIRE SURFACE

To remove oxide prior to superconductor deposition, a few simple strategies can be applied. Firstly, an ex situ chemical wet etch may be applied, which either only etches the oxide away (e.g. etching with HF) or which etches the oxide and at the same time passivates the nanowire surface against re-oxidation (e.g. sulfur passi-

vation). Another attractive method is in situ etching right before deposition of the superconducting material. Typically, this is done via Ar RF plasma etching or by using Ar ion milling.

The benefit of a chemical wet etch is that it leaves the underlying nanowire crystal intact (although it might create surface roughness at the atomic level), whereas bombardment of the nanowire surface with Ar ions likely damages the nanowire crystal, both at the surface and below. On the other hand, the physical Ar etching is an in situ process and thus prevents formation of a new oxide layer in the timespan between etch and superconducting contact deposition, something that may happen in the case of chemical wet etching.

8.2.2 SUPERCONDUCTING CONTACT MATERIALS

Although a true microscopic understanding of what happens at the nanowire- superconductor interface is lacking, the specific superconducting material used to contact the nanowire surface plays an important role in obtaining a good contact. Several factors may be important to this. Firstly, the workfunction of the superconducting material may determine the dopant level near the nanowire surface. Secondly, if the superconductor is reactive, it may chemically bond to the surface, forming a transition layer between semiconductor and metal. Thirdly, diffusion of the material over the surface may lead to a more homogeneous coverage of the nanowire. Lastly, the type of deposition method of the material, which is typically thermal evaporation or DC magnetron sputtering, may influence the contact details at the nanowire surface.

Among available superconducting contact materials, the combination of a Ti sticking layer with an Al top layer is commonly used in contacting semiconducting nanowires [3–6]. This results in a decent quality induced superconducting gap, but is not compatible with typical magnetic fields required to create MBS's. Contacts based on Nb, Pb or V give a larger critical magnetic field [7–11], but due to their susceptibility to oxidation and/or strain, these materials are hard to combine with standard lithographic processing for Majorana devices. For this reason, we previously developed the NbTiN contact combined with in situ Ar etching, resulting in a large enough critical magnetic field, but a low-quality induced gap. In this work, we aim at optimizing the induced gap quality by combining the advantages of the Ti/Al and NbTiN contact. Therefore we focus on Ti, Al, NbTi and NbTiN as possible contact materials.

8.2.3 EXPERIMENTAL SET-UP

To optimize the quality of the induced superconducting gap, a simple device geometry, allowing for easy characterization measurements showing the quality of the proximity effect, is necessary. The simplest possible geometry is a nanowire (NW) contacted with two superconducting (S) contacts (S-NW-S), combined with a gate controlling the nanowire electron density.

Using the S-NW-S geometry, instead of the more realistic N-NW-S geometry

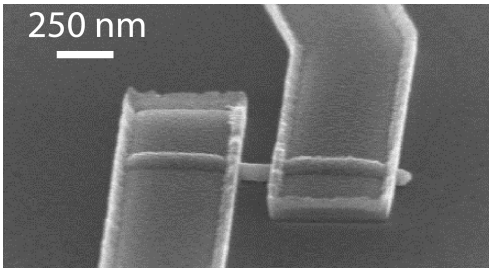

Figure 8.1 |Typical superconductor-InSb nanowire-superconductor device on a Si/SiO_2 substrate. The distance between the two contacts is 200 nm, and the width of the contacts is 500 nm. The Si substrate is doped and can be used as global gate. This particular device has NbTiN contacts.

involving one normal (N) and one superconducting contact as used in tunneling spectroscopy experiments, has the important advantage of simpler device fabrication: only a single contact deposition step is needed. The disadvantage, however, is that measuring the induced superconducting gap in this geometry does not simply correspond to the same type of measurement in the N-NW-S geometry. Different from the N-NW-S geometry, where a BSC type curve is expected in tunneling spectroscopy, a convolution of two superconducting density of states in the S-NW-S geometry will lead to a differential conductance curve having a) coherence peaks at $\pm 2\Delta$ (Δ superconducting gap), instead of at $\pm\Delta$, b) enhanced coherence peaks, and c) a stronger suppression inside the coherence peaks. Accordingly, results on induced gap measurements obtained in S-NW-S devices are not a quantitative measure for the induced gap quality in a comparable N-NW-S device measurement. However, the measurement can still be used to compare different types of S-NW-S devices, thus allowing to perform an optimization cycle in which the relative simplicity of the S-NW-S geometry compared to the N-NW-S geometry is an important advantage.

A device image of a typical S-NW-S device is shown in Figure 8.1. The substrate can be used as a global gate, enabling complete control over the electronic transparency of the device. To enable direct comparison between different contact preparation methods, a constant contact separation distance (200 nm) and contact length (500 nm) is used in all devices. Measurements are performed in a dilution refrigerator with a base temperature of ~ 100 mK or in a Helium-3 cryostat with a base temperature of ~ 250 mK, as will be specified for the individual measurements. A single chip corresponding to a specific fabrication run typically contains ~10 devices. Devices suited for cooldown are selected at room temperature by measuring the two terminal resistance at a bias voltage of 10 mV without a gate voltage applied. Typical resistance values for potentially good devices are in the 10-100 kΩ's range. To get insight in the spread between individual devices, typically ~ 5 devices are characterized at low temperature, in the results section, we show a representa-

tive dataset for each type of contact preparation.

8.3 RESULTS

We first show the best results obtained with Ar based etching, applied right before superconducting NbTiN contact deposition in the same vacuum chamber. In the next section, results on sulfur passivation combined with Ti/Al contact deposition are shown. In the final section, we discuss a 'hybrid' recipe, in which we combine sulfur passivation, followed by a short, in situ, Ar etch, with NbTiN contact deposition. This is the final, optimized superconducting contact preparation method arrived at. Intermediate steps are discussed in the appendix and referred to in the main text.

8.3.1 NBTIN CONTACTS BASED ON AR ETCH

To etch the native oxide, Ar RF plasma etching in the same vacuum chamber right before NbTiN deposition is used. The two point resistance of a S-NW-S device, measured at low temperature and high device transparency (high gate voltage), is a simple method to estimate the contact quality. By minimizing this resistance, as a function of Ar pressure, RF power, and etch time, a good contact quality may be achieved. This way, one can reproducibly achieve a total device resistance as low as 2 kΩ, indicating that each individual contact to the nanowire has a resistance less than 1 kΩ. Such type of contact results in good quality Josephson junctions with large critical currents, withstanding high magnetic fields, as reported in chapter 4. However, a poor quality induced gap is observed in tunneling spectroscopy measurements, as pointed out before.

To optimize the induced gap quality, the change of nanowire surface morphology after Ar etching has been investigated by SEM imaging. Figure 8.2a shows a typical InSb nanowire surface exposed to the Ar rf plasma etch. Many small pillars are clearly visible on top of the etched InSb nanowire surface. For these particular etching settings, about 1/3 of the nanowire diameter has been etched; the pillars can be as tall as 25 nm, corresponding to the etch depth. It is not entirely clear what the origins of these pillars are: it may be partially caused by inhomogeneous etching; furthermore, the RF plasma etching is a sputtering process, during which material may deposit back onto the nanowire, thus causing formation of pillars during etching. Not visible under SEM imaging, but likely relevant as well, is penetration of the high-energy Ar ions into the crystal, leading to defects below the surface of the nanowire.

By varying the Ar etch parameters, most importantly, by reducing the RF power from 100 W to 25 W (see appendix for details), a much smoother nanowire surface can be obtained, as visible in Figure 8.2b. Here no roughness is observed under SEM imaging. Likely, however, at the microscopic level roughness is still present. Furthermore, Ar ions likely still penetrate and damage the crystal lattice deeper underneath the surface.

A typical dI/dV measurement as a function of gate voltage, taken from a device

based on the improved, lower power Ar etch, is shown in Figure 8.3. The induced gap is indicated with yellow dotted lines symmetric around zero bias. At more positive gate voltages, a zero bias conductance peak due to supercurrent appears. Inside the gap, small peaks at half the gap value are visible (see also linetrace), corresponding to the n = 2 multiple Andreev reflection (MAR) process, indicative of a high device tranmission[1]. Generally, no MAR is observed with the higher power Ar etch. Furthermore, devices based on the more gentle Ar etch show much less spurious resonances in gate voltage compared to devices based on the higher power Ar etch. This demonstrates that the more gentle Ar etching does improve the contact quality.

However, the fact that still only a single MAR is visible within the superconducting gap, is already indicative that the S-NW interface is decent, but not excellent (several orders of MAR have been observed in [5]). Furthermore, suppression of conductance inside the gap is far from ideal, a ratio of $G_{\text{inside}}/G_{\text{outside}} \sim 0.5$ comparing inside (G_{inside}) and outside (G_{outside}) gap conductance is found. This shows that even devices based on an optimized Ar etch will not result in a good quality induced gap.

Concluding, NbTiN contacts based on Ar etching did not results in a good induced gap quality, even after optimizing the etching recipe. This method of contact preparation is therefore unsuitable for future tunneling spectroscopy experiments aimed at detecting MBS[2].

8.3.2 SULFUR PASSIVATION

As an alternative to the Ar etching based contact preparation, we investigate sulfur passivation[3] In this process, after development of the lithographic mask, the sample is placed in a diluted ammoniumsulfide solution (see appendix for details)[13]. At a low concentration, this solution selectively etches the oxide present on the InSb surface. At high concentrations, however, also the InSb is etched significantly after oxide etching. Due to the oxide etching, possibly roughness at the microscopic level

8

[1] Multiple Andreev reflection (MAR) is a transport process in which quasi-particles are transferred at sub-gap energies from one S lead to another S lead via a weak link. This process happens when the bias voltage across the weak link equals an integer fraction $2\Delta/n$, n integer, of the sum of the superconducting gaps Δ in each S leads [12]. The index n indicates the number of Andreev reflections the quasi-particle undergoes before reaching the gap edge. $n = 1$ corresponds to normal quasi-particle transport, if $n = 2$, the quasi-particle undergoes a single Andreev reflection, for $n = 3$, it undergoes two Andreev reflections etc. All MAR processes with $n > 1$ are higher order processes, and are suppressed by $\sim T^n$, given some junction transparency T. Observing several MAR's is therefore an indication of a highly transparent junction, which in turn implies having highly transparent S-NW interfaces.

[2] Ar etching is reliable and efficient in generating large supercurrents (~100 nA at zero magnetic field) up to high magnetic fields (~100 pA at several tesla's magnetic field strength) when combined with NbTiN contacts. This statement holds for both the high and low power rf plasma etch. To study Josephson effect in the nanowire junction, this approach therefore suffices.

[3] Another popular chemical wet etching technique, HF etching, has been investigated, but we never found good results based on this. Also normal metallic contacts to InSb based on this method show poor conductance. This is different from InAs nanowires, were HF etching typically results in good quality contacts.

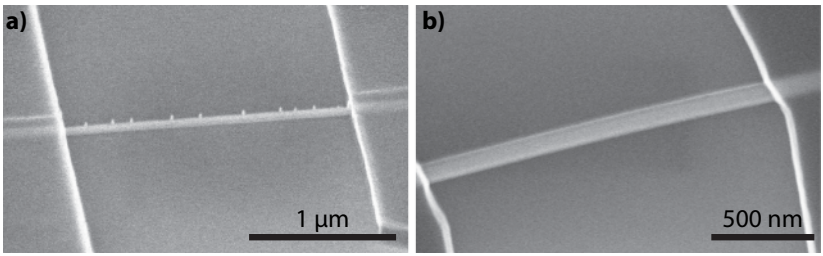

Figure 8.2 |InSb nanowire surface after Ar etch. SEM images are taken right after the etching, the window in the lithographic mask is visible. Etch depth is the same in both cases and around 1/3 of the nanowire diameter. a) 100 W RF power is applied, the nanowire surface contains pillars with a height of 25 nm corresponding to the etch depth. b) 25 W RF power is applied, resulting in no visible surface roughness using SEM imaging.

will be present. Upon taking the sample out of the sulfur passivation solution, a sulfur layer, bound to the InSb surface, is present, preventing the nanowire facet from reoxidation. This passivation of the surface has a limited stability and the sample should be put in vacuum as soon as possible after the sulfur passivation has finished. Since sulfur passivation has not been successfully combined with NbTiN as of yet, we first investigate a more conventional contact made of Ti/Al, to see the quality of the induced superconducting properties.

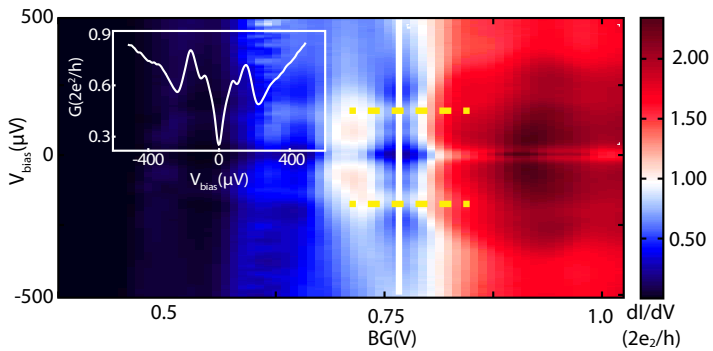

Figure 8.3 |NbTiN contacts based on Ar etching. A $\mathrm{d}I/\mathrm{d}V$ measurement as a function of backgate voltage BG is shown. At high conductance, a zero bias peak due to supercurrent is visible. At lower conductance, the coherence peaks of the induced gap are visible, indicated by yellow dotted lines. Inset is the linecut indicated by the white line, showing two small peaks inside the induced gap corresponding to the $n=2$ MAR. A ratio $G_{\mathrm{inside}}/G_{\mathrm{outside}} \sim 0.5$ is found. $T \sim 250$ mK, $B = 0$ T.

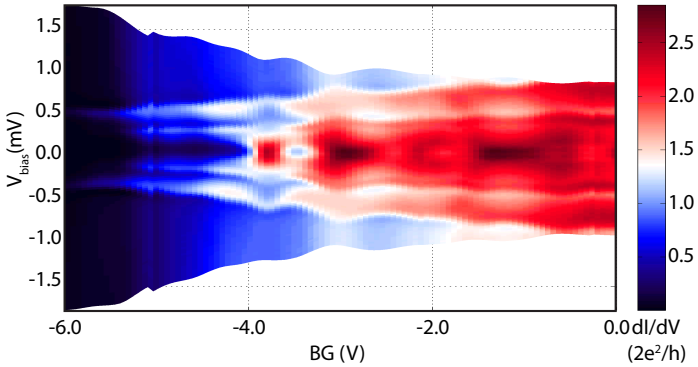

Figure 8.4 |Ti/Al contacts based on sulfur passivation. A $\mathrm{d}I/\mathrm{d}V$ measurement as a function of gate voltage is shown, covering the regime from pinch off to several G_0 conductance. At high device transmission (around 0 V on the gate), several MAR events are visible, see also Figure 8.5. At low device transmission (below ~ -5 V), all MAR's are suppressed, and only peaks from the induced gap remain, see Figure 8.6. $T \sim 100$ mK, $B = 0$ T.

8.3.3 TI/AL CONTACTS BASED ON SULFUR PASSIVATION

A typical device, having Ti/Al 5/125 nm contacts deposited after sulfur passivation, and with the same geometry as the device shown in Figure 8.1, is discussed here. Figure 8.4 shows a $\mathrm{d}I/\mathrm{d}V$ measurement as a function of global gate voltage. In contrast to the characteristics shown in Figure 8.3 of the Ar etched NbTiN contacts, several order of MAR's are visible instead of only one. This shows a better transparency of the device as a whole, indicating better contact quality. The MAR's are better visible in Figure 8.5, up to $n = 6$, at high device transparency.

Figure 8.6 focuses on the quantity of interest, the superconducting gap. Here, in the tunneling regime, the gap looks much clearer compared to the Ar etch NbTiN based devices. More quantitatively, a conductance ratio $G_{\mathrm{inside}}/G_{\mathrm{outside}} = 0.1$ is observed ($G_{\mathrm{inside}}/G_{\mathrm{outside}} \sim 0.5$ in the Ar etching case). The data clearly shows that this contact recipe results in better quality induced superconductivity compared to the Ar etch based contacts.

Figure 8.6b shows a $\mathrm{d}I/\mathrm{d}V$ measurement as a function of magnetic field (B applied in plane with the superconducting film). The critical field B_{c} of this superconducting film is very low, of the order of 40 mT. This makes the contact not suitable for research focusing on establishing a topological superconductor in InSb nanowires.

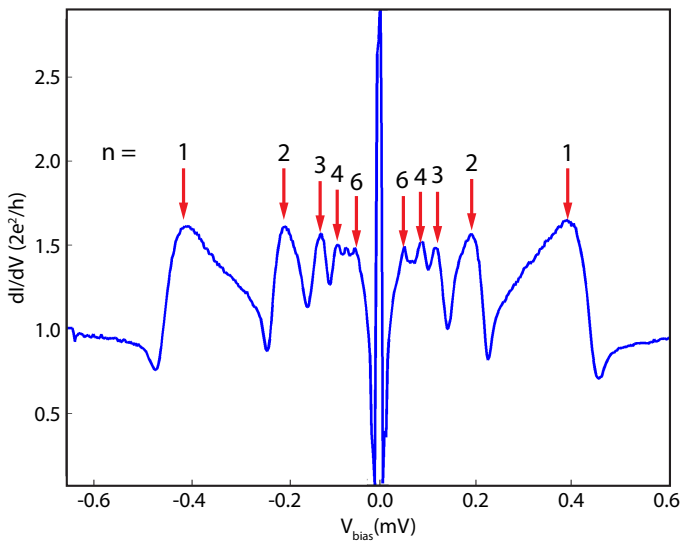

Figure 8.5 |Ti/Al contacts based on sulfur passivation, multiple Andreev reflection. A $\mathrm{d}I/\mathrm{d}V$ measurement at high device transmission is shown ($BG = +6$ V, outside the gate voltage range covered in Figure 8.4). MAR's up to order $n = 6$ are visible and indicated in the figure. The $n = 1$ peaks correspond to the edge of the superconducting gap, which has a size of $\Delta \sim 200$ μeV. At zero bias voltage, a sharp anomaly is present is due to supercurrent. $T \sim 100$ mK, $B = 0$ T.

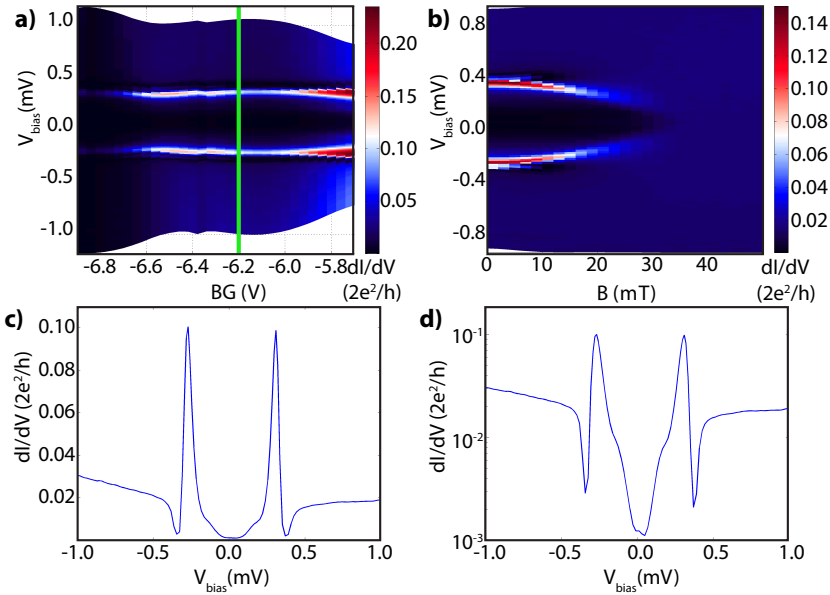

Figure 8.6 |Ti/Al contacts based on sulfur passivation, superconducting gap. a) zoom in of 8.4 at low gate voltage. b) $\mathrm{d}I/\mathrm{d}V$ versus magnetic field at $BG = -6.2$ V. c) and d) are linecuts in linear and log scale both at $BG = -6.2$ V and zero magnetic field. In a) the gate voltage at which b), c) and d) are taken is highlighted with a green line. From b), c) and d) $G_{\mathrm{inside}}/G_{\mathrm{outside}} \sim 0.1$, $\Delta \sim 200$ μeV and $B_{\mathrm{c}} = 32$ mT are extracted. In all measurements, $T \sim 100$ mK.

8

8.3.4 NBTI/NBTIN CONTACTS BASED ON SULFUR PASSIVATION AND SHORT AR ETCH

To achieve a high critical B field, but avoid the problems related to Ar etching, we combine sulfur passivation with a NbTiN contact. Unfortunately, combining sulphur passivation directly with NbTiN sputtering did not result in good contact quality. We found that the Ti sticking layer in the sulfur passivated Ti/Al contact plays a crucial role (see appendix). This inspired us to make a sulfur passivated NbTiN contact with a NbTi sticking layer, resulting in improved, but still insufficient, contact quality (see appendix).

In the final contact deposition recipe, we incorporate a very short, low power Ar RF plasma etch, between sulfur passivation and superconducting film deposition. The motivation for this is the observation that the lowest possible two-terminal device resistance after sulfur passivation is a bit higher compared to Ar etched contacts (~4 kΩ vs ~2 kΩ). This may indicate the presence of a small tunneling barrier at the interface, possibly caused by the sulfur passivation layer, or by some residual water after sulfur passivation, or by some reoxidization during sample transfer.

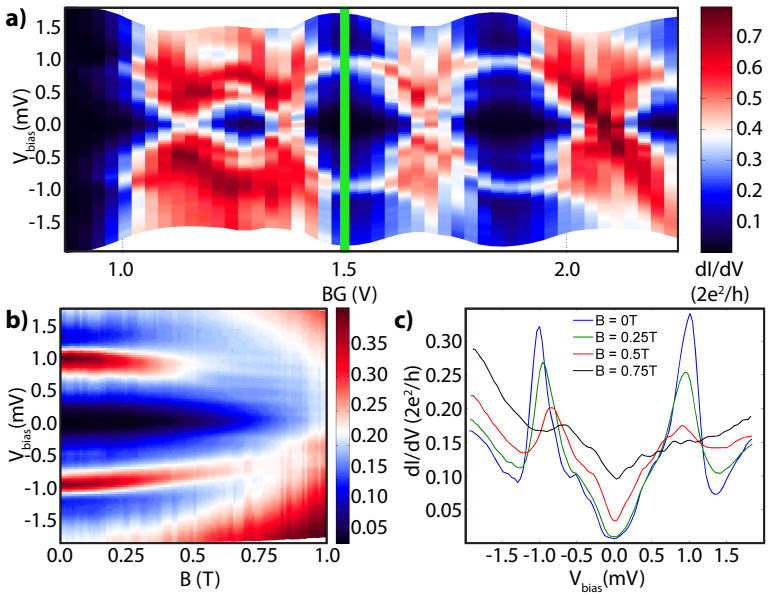

Figure 8.7 |NbTi/NbTiN contacts based on sulfur passivation and short Ar etch. A $\mathrm{d}I/\mathrm{d}V$ measurement as a function of backgate is shown. Coulomb blockade features are visible, this happens often near pinch-off in two-terminal, globally gated devices, regardless of contact preparation method. The horizontal lines at ± 1 mV indicate the superconducting gap, which has a size of 0.5 meV. b) B dependent $\mathrm{d}I/\mathrm{d}V$ measurement at $BG = 1.5$ V, indicated with a green line in a). The superconducting gap survives to about 1 T. c) linecuts from b) at different magnetic fields. $\Delta \sim 0.5$ meV and $G_{\mathrm{inside}}/G_{\mathrm{outside}} \sim 0.1$ are extracted at $B = 0$ T from the measurements. In all measurements, $T \sim 250$ mK.

8

The final contact consists of a sputtered NbTi/NbTiN 5/80 nm film deposited after sulfur passivation and short Ar etch (see appendix for details).

Typical results obtained with this type of contact are shown in Figure 8.7. Figure 8.7a shows a $\mathrm{d}I/\mathrm{d}V$ measurement as a function of global gate voltage. The device is in a Coulomb blockade regime, however, a clear induced gap of size $\Delta = 0.5$ meV and the $n = 2$ MAR are visible. At higher conductance (not shown) also the $n = 3$ MAR is visible. More importantly, upon measuring $\mathrm{d}I/\mathrm{d}V$ as a function of B, as shown in Figure 8.7b, a clear gap is visible up to ~750 mT, while weaker gap like features are present up to at least 1 T. This is also revealed in the $\mathrm{d}I/\mathrm{d}V$ traces shown in Figure 8.7c. A conductance ratio of ~10 is observed inside and outside the gap, showing a comparable conductance suppression to the sulfur passivated Ti/Al contact, although the shape of the induced gap is clearly less ideal (Figure 8.7c vs Figure 8.6c).

The data shown in Figure 8.7 corresponds to the best superconducting gap found at B field values around ~500 mT, the typical B regime in which a topological superconductor with MBS's may appear in the system. It is important to remark that typical experiments detecting a potential MBS are carried out in our coldest setups, with effective temperatures around 25 mK, a factor of 10 smaller compared to the temperature at which the data in Figure 8.7 was taken. It is therefore expected that the quality of the induced gap will improve even more in an actual tunneling spectroscopy experiment performed in a dilutions refrigerator. On the other hand, although the results presented here are a significant improvement over the poor quality induced gaps obtained by using purely Ar etching, still the contact quality is not as good as the sulfur passivated Ti/Al contact, indicating that further improvements may be possible.

8.4 SUMMARY

In this work we show the optimization of the interface between a superconducting contact and an InSb nanowire. We found that the details of the nanowire surface preparation prior to superconducting contact deposition are extremely important in this respect.

More specifically, for different types of contact preperation, we have studied the differential conductance as measured in the tunneling regime of two-terminal S-NW-S devices with global gate. Evidence for several important conclusions has been presented. Firstly, Ar etching as a cleaning method is shown to be detrimental for obtaining high quality induced superconducting gaps in the nanowire. Secondly, a non-invasive contact preparation method based on sulfur passivation of the nanowire surface, followed by thermal evaporation of Ti/Al, shows the best superconducting properties at zero magnetic field. Unfortunately, this type of contact results in a very low critical magnetic field of ~ 40 mT, not suitable for the purpose of studying topological superconductivity in this system. Finally, it has been shown that good contacts can be made by combining sulfur passivation with sputtering of a thin layer of NbTi before sputtering NbTiN. Here the best results were obtained by applying a very short Ar etch prior to contact deposition. This superconducting contact deposition recipe developed here results in a well developed, sizeable (~0.5 meV) superconducting gap surviving up to magnetic fields of order of 1 T.

In conclusion, it is clear that sulfur passivation based contact recipes give a much better developed superconducting gap compared to Ar etching based contact recipes. We believe this is directly related to preserving the nanowire crystal much better in the first case, a scenario which is also indicated by results obtained by others on epitaxially grown Al on InAs [1].

8.4.1 RECOMMENDATIONS

The results presented here may indicate that the short Ar etch, likely necessary to remove a thin tunneling barrier layer after sulfur passivation, still softens the induced gap. In order to develop the induced gap better with the NbTi/NbTiN recipe,

alternative ways of removing such a possible layer should be pursued. Possibilities include: a) in situ heating of the sample prior to contact deposition [14], b) in situ exposure to UV light prior to contact deposition [15] or c) in situ chemical etching such as exposure to hydrogen radicals [16]. This last option may remove the native oxide as well and thus prevent from the necessity of sulfur passivation altogether.

As an alternative cause of the more rounded superconducting gap observed with the final NbTiN based contacts presented here, the bulk NbTiN film quality is very important. If the material itself is non-ideal, no hard induced gap can be expected in the proximitized nanowire. We have not focussed on NbTiN film quality in this study and this may be the topic of future device optimization.

An interesting alternative contact deposition method, which could not be investigated here, is the combination of thermal evaporation of a thin Ti layer, with sputtering of NbTi/ NbTiN on top, in the same deposition chamber. This way, the excellent properties of sulfur passivation + thermally evaporated Ti sticking layer may be combined with the high critical field of the NbTiN film. The effect on the induced gap size and its survival in magnetic field is not known, however.

Finally, our results motivate also in the case of InSb nanowires the epitaxial growth of superconductors directly onto the nanowire crystal. We believe the primary focus in this should be on superconductors such as Nb, because of their good magnetic field compatibility, a crucial ingredient in creating a topological superconductor in the InSb nanowire system.

8.5 APPENDIX

8.5.1 DEVICE FABRICATION DETAILS

Device are fabricated on a p++ doped Si substrate covered by 285 nm thermal SiO_2 as dielectric, the substrate serves as a global backgate in the experiments. Nanowires are deposited deterministically, as discussed in chapter 3. Contacts are defined with standard e-beam lithography, using PMMA as resist. In case of sputtered (e.g. NbTiN) contacts, a 200 nm thick single layer mask is applied; while for thermal evaporation, a double layer PMMA mask with undercut is used.

Ti and Al are thermally evaporated in the same vacuum chamber. NbTi and NbTiN are sputterred in a different chamber, which is also used for the Ar RF plasma etching.

AR RF PLASMA ETCHING DETAILS

The recipe used for devices shown in Figure 8.2b, resulting in a smooth nanowire surface under SEM imaging, was obtained by etching for 200 s, at a power of 25 W and a Ar pressure of 3 mTorr.

To achieve low ohmic contact to NbTiN by using Ar RF plasma etching, regardless of the specifics of the etching, at least an etch depth of ~20 nm is necessary. This is much more than the typical thickness of the native oxide layer ($\leq$ 5 nm). It is unclear why this is the case. A possibly relevant process is back deposition of material during sputtering. This may also be the cause of the formation of pillars under particular etching conditions.

SULFUR PASSIVATION DETAILS

Prior to sulfur passivation, after development of the PMMA mask, a short O_2 RF plasma etch is applied, to remove organic residues of the PMMA in the developed areas. Without this step, no good contact could be obtained using sulfur passivation (this step is not necessary in the case of Ar etching).

The sulfur passivation solution is prepared by first over saturating an ammoniumsulfide solution with sulfur (290 mg of sulfur powder in 3 mL ammoniumsulfide), this solution is stirred at room temperature for 15 min. Next, this solution is diluted in demi water by a factor 200. The actual sulfur passivation is done by placing the developed and oxygen rf plasma cleaned sample in a small beaker containing ~10 mL of this solution, the sulfur passivation process is at 60 C and has a duration of 30 min **include original reference**. Since exposure to air degrades the solution, it is important for the yield of the process to close the beaker as airtight as possible. After this, the sample is taken out and rinsed in water, followed by a N2 blowdry and quick transfer into the deposition tool.

DEPOSITION DETAILS OF NBTI/NBTIN CONTACTS BASED ON SULFUR PASSIVATION AND SHORT AR ETCH

The standard sulfur passivation recipe is applied. Before film deposition, an Ar RF plasma etch at 25 W and 3 mTorr is applied for 20 s (10 times shorter compared

to contacts purely based on this same Ar RF plasma etch). After this, first 5 nm of NbTi is sputtered (no N_2 is present in the chamber, otherwise same conditions are applied as for NbTiN sputtering), subsequently 80 nm of NbTiN is deposited.

Instead of simply swithing on the N_2 flow during sputtering of NbTi to change to NbTiN, we found it crucial in obtaining a good contact to first shut down the plasma after NbTi sputtering, introduce a N_2 flow, let it settle for ~ 10 s, and then switch on the plasma again to continue NbTiN sputtering.

8.5.2 INTERMEDIATE STEPS TO ARRIVE AT THE FINAL CONTACT PREPARATION METHOD

Here we describe intermediate steps between the sulfur passivated Ti/Al contact described in the main text (section 8.3.3 and the final NbTi/NbTiN contact based on sulfur passivation and short Ar etch described in the main text (section 8.3.4).

INFLUENCE OF TI STICKING LAYER

A possible origin of the low critical magnetic field of the Ti/Al contact may be the presence of the Ti sticking layer, since Ti is a weaker superconductor compared to Al. To get a better understanding of the effect of Ti on the induced gap and its survival in B, a device has been made with purely Al contacts. The fabrication is exactly the same as in the case of the Ti/Al contacts, except that no Ti sticking layer is evaporated. The room temperature contact resistances are very high with pure Al contacts (order of MΩ's). Such high contact resistances at room temperature indicate that improper contact formed to nanowire. This finding is important, because it shows that Ti plays a crucial role as a sticking layer on a sulfur passivated InSb nanowire surface.

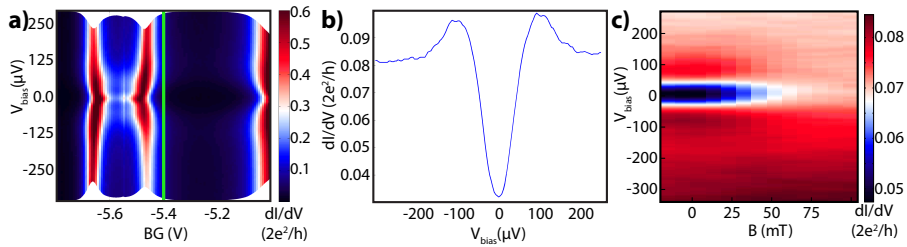

Figure 8.8 |Ti contacts based on sulfur passivation. a) $\mathrm{d}I/\mathrm{d}V$ measurement as a function of global gate voltage. The device is in a Coulomb blockade regime near pinch off. An induced gap of size $\Delta = 50$ μeV is weakly visible. b) Linecut at gate voltage of -5.4 V, highlighted in a), where $G_{\mathrm{inside}}/G_{\mathrm{outside}} \sim 0.4$. Softening of the gap is predominantly caused by thermal broadening. c) $\mathrm{d}I/\mathrm{d}V$ measurement as a function of B. Critical field of the induced gap is around 50 mT. In all measurements, $T \sim 100$ mK.

To further investigate the role of Ti, we fabricated devices with pure Ti contacts,

keeping sulfur passivation treatment the same. Ti is deposited via thermal evaporation. Figure 8.8 shows a dI/dV measurement as a function of global gate voltage. In the gate range shown here, the device is in a Coulomb blockade regime, as happens often in globally gated devices near pinch off. The induced gap in the data is well visible, but is also quite soft. However, given the small critical temperature of Ti of ~400 mK, this can be explained by thermal broadening (electron temperature ~ 100 mK). In the case of Ti/Al based contacts, the superconducting film probably behaves mostly like Al because the Ti is proximitized, thus thermal broadening plays a less important role (effective T_c is ~1.3 K). In Figure 8.8c, the critical magnetic field B_c of the gap is measured, which is around 50 mT.

The good superconducting contact quality observed when involving Ti, either as sticking layer or as the dominant contact material, suggests that it has a crucial role in forming good contact to the sulfur passivated InSb nanowire surface. No understanding of the microscopic details can be obtained from these observations, however.

SULFUR PASSIVATED TI/AL/NBTIN CONTACTS

In a first attempt to increase B_c of the sulfur passivated Ti/Al contact, we directly proximitized it with a NbTiN top layer. A drawback, however, is that NbTiN has to be sputtered in a different vacuum chamber. As a consequence, vacuum has to be broken between the thermal evaporation of Ti/Al and the sputtering of NbTiN, leading to oxidation of the Al. This AlO_x has to be removed in order to make good electrical contacts with NbTiN, which is done here by Ar RF plasma etching before sputtering of NbTiN.

The device is fabricated by first thermally evaporating a layer of 5/30 nm Ti/Al after sulfur passivation. Then the sample is transferred to the sputtering chamber, where prior to deposition of 100 nm NbTiN, the AlO_x is etched by Ar rf plasma etching at 25 W, 3 mTorr for 5 min.

A dI/dV measurement as a function of global gate voltage is shown in Figure 8.9a. A clear induced gap, about twice the size as in the Ti/Al case, is present; furthermore the the $n = 2$ MAR is visible. However, as visible in Figure 8.9c, the induced gap is softer compared to the sulfur passivated Ti/Al contact (see Figure 8.6).

Due to the low background pressure during thermal evaporation, this deposition process is highly anisotropic. The nanowire side facets are therefore not completely covered at a film thickness of 35 nm, which is much smaller than the typical wire diameter of ~ 100 nm. In contrast, the Ar RF plasma etch is much more isotropic due to the relatively high Ar pressure. Consequentially, part of the nanowire side facets, not covered by the Ti/Al layer, can still be damaged by the Ar etching. This may result in the softening of the induced gap. Note that the ratio between inside and outside gap conductance is very similar to the Ti/Al contact, if the conductance in the middle of the gap is taken.

Despite the softer gap, the B_c of the film increased by about a factor of 10 to ~ 300 m, as shown in Figure 8.9c. Both the doubling in size of the induced gap

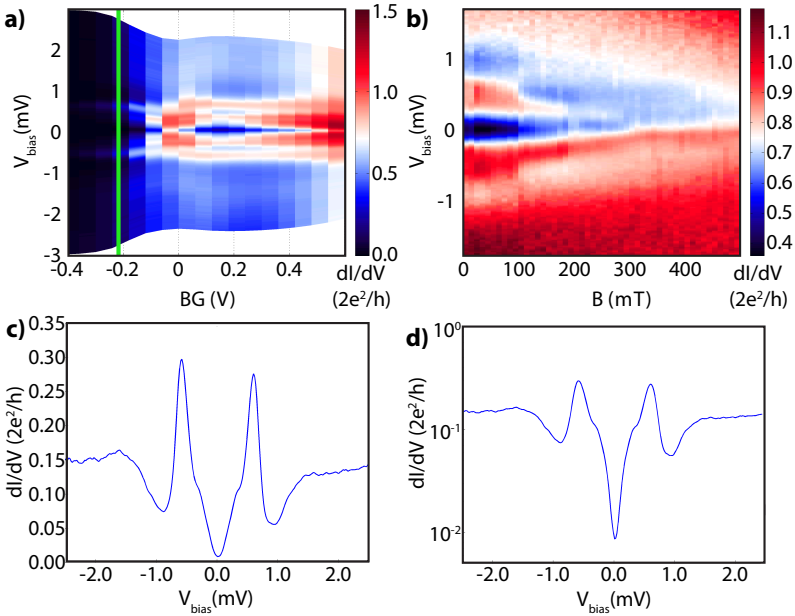

Figure 8.9 |Ti/Al/NbTiN contacts based on sulfur passivation. After sulfur passivation, Ti/Al is evaporated first and then covered by NbTiN after Ar RF plasma etching of the Ti/Al surface. a) $\mathrm{d}I/\mathrm{d}V$ as a function of global gate voltage. Both induced gap and $n = 2$ MAR are visible. b) $\mathrm{d}I/\mathrm{d}V$ as a function of B, showing $B_\mathrm{c} \sim 300$ mT. c) and d) are a $\mathrm{d}I/\mathrm{d}V$ trace at BG = -0.22 V and $B = 0$ T, both in linear and log scale. The gate voltage of b), c) and d) is indicated by a green line in a). From c) and d) $\Delta \sim 0.3$ meV and $G_\mathrm{inside}/G_\mathrm{outside} \sim 0.1$ are extracted. $T = 250$ mK.

and the significant increase of B_c clearly show that the Ti/Al layer was successfully proximitized by the NbTiN top layer.

However, $B_\mathrm{c} \sim 300$ mT is still low for being relevant to creating a topological superconducting state and studying MBS. Nevertheless, this result proves the more general point that the proximity effect indeed may improve the gap size and its B_c.

SULFUR PASSIVATED NBTI/NBTIN CONTACTS

Earlier we established the importance of the Ti sticking layer in the sulfur passivated Ti/Al contact. Since NbTiN is sputtered from an alloyed target containing 30% Ti, using a thin NbTi layer containing a significant amount of Ti, to replace the Ti/Al layer used before, could be a good choice. Importantly, this option avoids one of our fabrication limitations, namely the deposition of the sticking layer in a different vacuum chamber from the NbTiN deposition chamber. This is possible since

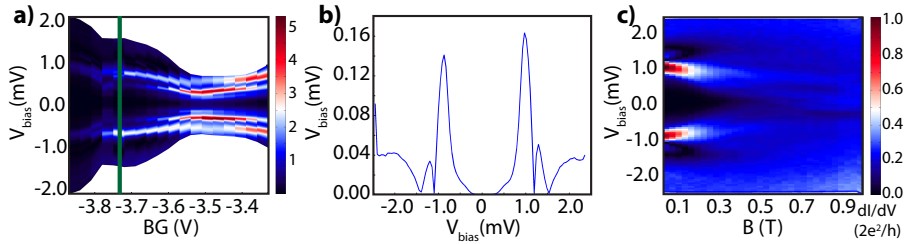

Figure 8.10 |NbTi/NbTiN contacts based on sulfur passivation. a) $\mathrm{d}I/\mathrm{d}V$ as a function of global gate voltage. A clear induced gap and several MAR's are visible. b) linecut from a) at the indicated gate position in a). c) B dependence of the induced gap. The critical magnetic field $B_c \sim 500$ mT is visible. The gap here has a shape very close to the Ti/Al gap shown in Figure 8.6. $T = 250$ mK.

switching between NbTi and NbTiN deposition simply depends on the absence or presence of a N_2 flow into the chamber.

Using this type of process, a device is fabricated by doing sulfur passivation followed by sputtering 6 nm of NbTi and 80 nm of NbTiN afterwards. Note that the comment made before (see 8.5.1 on stopping sputtering between the two layers is also essential here, first the N_2 flow and pressure has to settle.

A $\mathrm{d}I/\mathrm{d}V$ measurement as a function of global gate voltage is shown in Figure 8.10. A clear induced gap is visible, with a size $\Delta \sim 0.5$ meV, comparable to the induced gap size of the Ti/Al/NbTi/NbTiN contact and about a factor 2 larger compared to the induced gap of the Ti/Al based contact. Such a superconducting gap corresponds to a topological phase transition at a minimum magnetic field of ~ 350 mT.

For higher device transparencies, MAR's appear up to order $n = 3$, which is an improvement compared to the Ti/Al/NbTi/NbTiN case where only the $n = 2$ MAR was visible. The gap obtained in the tunneling regime is quite sharp, close to the observations for the Ti/Al contact.

A B dependent $\mathrm{d}I/\mathrm{d}V$ measurement is shown in Figure 8.10c. A clear induced gap is visible up to ~ 400 mT and weaker gap features are visible up to a field of ~ 1 T. This means the contact may already be good enough for potential topological superconductivity.

It is important to remark here that the results discussed above strongly depend on layer thickness of the NbTi layer. We found for a 20 nm thick NbTi layer poor results (not shown) compared to the results discussed here. We therefore stick to a NbTi layer thickness between 5 and 10 nm.

As discussed in the main text, since sulfur passivated contacts result in a lowest possible two point device resistance always a bit larger compared to Ar etched contacts, we decided to incorporate a short Ar etch in between sulfur passivation and NbTi/NbTiN deposition, this is the final contact recipe discussed in the main text

(section 8.3.4).

REMARKS ON CONTACT OPTIMIZATION

Here we discuss a few more detailed remarks regarding the optimization procedure that are not presented in the main text. Firstly, in case a thin film deposition tool has to be chosen, we strongly recommend: i) to use a tool dedicated to the deposition of superconductors only, since this will help maintaining a high quality NbTi/NbTiN film, and ii) to use a tool in which thermal evaporation and DC magnetron sputtering can be combined in a single vacuum chamber. This allows for combination of both evaporated and sputtered films without breaking the vacuum. Typical materials to have in such a deposition chamber are Ti, Al for evaporation and Ti, Al, Nb, NbTi for sputtering.

Secondly, the short Ar etching before superconducting film deposition in the sulfur passivation recipe can be optimized further. It may be possible to use even lower RF power of order 10 W and reduce the etch time further.

Thirdly, we attempted to sputter a Ti layer after sulfur passivation, but no good results were found. However, in that case, the Ti sputtering recipe was not optimized well and this observation is therefore inconclusive. Nevertheless, there is a possibility that the difference between thermal evaporation and DC magnetron sputtering matters, this could be relevant to investigate.

Lastly, upon combining Ti with NbTiN, it is likely important to incorporate a thin NbTi layer in between. Otherwise, an insulating TiN surface may form. This could be important in view of the good contact properties obtained with a thin thermally evaporated Ti sticking layer. This contact recipe could not be investigated here, but it may result in a good quality superconducting gap surviving up to B fields of order 1 T. With the current knowledge, a typical contact recipe would consist of: sulfur passivation, followed by ~5 nm thermally evaporated Ti, followed by ~5 nm sputtered NbTi, and a final layer of 80 nm sputtered NbTiN.

REFERENCES

[1] W. Chang, S. Albrecht, T. Jespersen, F. Kuemmeth, P. Krogstrup, J. Nygård, and C. Marcus, "Hard gap in epitaxial semiconductor–superconductor nanowires," *Nature nanotechnology*, vol. 10, no. 3, pp. 232–236, 2015.

[2] S. R. Plissard, D. R. Slapak, M. A. Verheijen, M. Hocevar, G. W. Immink, I. van Weperen, S. Nadj-Perge, S. M. Frolov, L. P. Kouwenhoven, and E. P. Bakkers, "From insb nanowires to nanocubes: looking for the sweet spot," *Nano letters*, vol. 12, no. 4, pp. 1794–1798, 2012.

[3] Y.-J. Doh, J. A. van Dam, A. L. Roest, E. P. Bakkers, L. P. Kouwenhoven, and S. De Franceschi, "Tunable supercurrent through semiconductor nanowires," *science*, vol. 309, no. 5732, pp. 272–275, 2005.

[4] J. A. Van Dam, Y. V. Nazarov, E. P. Bakkers, S. De Franceschi, and L. P. Kouwenhoven, "Supercurrent reversal in quantum dots," *Nature*, vol. 442, no. 7103, pp. 667–670, 2006.

[5] H. Nilsson, P. Samuelsson, P. Caroff, and H. Xu, "Supercurrent and multiple andreev reflections in an insb nanowire josephson junction," *Nano letters*, vol. 12, no. 1, pp. 228–233, 2011.

[6] T. Nishio, T. Kozakai, S. Amaha, M. Larsson, H. A. Nilsson, H. Xu, G. Zhang, K. Tateno, H. Takayanagi, and K. Ishibashi, "Supercurrent through inas nanowires with highly transparent superconducting contacts," *Nanotechnology*, vol. 22, no. 44, p. 445701, 2011.

[7] E. J. Lee, X. Jiang, R. Aguado, G. Katsaros, C. M. Lieber, and S. De Franceschi, "Zero-bias anomaly in a nanowire quantum dot coupled to superconductors," *Physical review letters*, vol. 109, no. 18, p. 186802, 2012.

[8] E. J. Lee, X. Jiang, M. Houzet, R. Aguado, C. M. Lieber, and S. De Franceschi, "Spin-resolved andreev levels and parity crossings in hybrid superconductor-semiconductor nanostructures," *Nature nanotechnology*, vol. 9, no. 1, pp. 79–84, 2014.

[9] M. Deng, C. Yu, G. Huang, M. Larsson, P. Caroff, and H. Xu, "Anomalous zero-bias conductance peak in a nb–insb nanowire–nb hybrid device," *Nano letters*, vol. 12, no. 12, pp. 6414–6419, 2012.

[10] M. Deng, C. Yu, G. Huang, M. Larsson, P. Caroff, and H. Xu, "Parity independence of the zero-bias conductance peak in a nanowire based topological superconductor-quantum dot hybrid device," *Scientific reports*, vol. 4, 2014.

[11] J. Paajaste, M. Amado, S. Roddaro, F. Bergeret, D. Ercolani, L. Sorba, and F. Giazotto, "Pb/inas nanowire josephson junction with high critical current and magnetic flux focusing," *Nano letters*, vol. 15, no. 3, pp. 1803–1808, 2015.

[12] G. E. Blonder, M. Tinkham, and T. M. Klapwijk, "Transition from metallic to tunneling regimes in superconducting microconstrictions: Excess current, charge imbalance, and supercurrent conversion," *Phys. Rev. B*, vol. 25, pp. 4515–4532, Apr 1982.

[13] N. Tajik, "Sulfur passivation of iii-v semiconductor nanowires," 2013.

[14] J. Klem, J. Tsao, J. Reno, A. Datye, and S. Chadda, "Thermal desorption of insb surface oxides," *Journal of Vacuum Science & Technology A*, vol. 9, no. 6, pp. 2996–2998, 1991.

[15] H. Simchi, G. Sareminia, A. Shafiekhani, and G. Valizadeh, "Passivation of insb surface for manufacturing infrared devices," *Infrared physics & technology*, vol. 51, no. 3, pp. 263–269, 2008.

[16] R. Tessler, C. Saguy, O. Klin, S. Greenberg, E. Weiss, R. Akhvlediani, R. Edrei, and A. Hoffman, "Oxide-free insb (100) surfaces by molecular hydrogen cleaning," *Applied physics letters*, vol. 88, no. 3, p. 031918, 2006.

9

TUNNELING SPECTROSCOPY IN A INSB NANOWIRE DEVICE WITH IMPROVED SUPERCONDUCTING CONTACTS

In this chapter we report a preliminary study of tunneling spectroscopy measurements in a superconductor-InSb nanowire device using contacts prepared with the sulphur passivation method developed in chapter 8. A zero bias conductance peak is found against a much cleaner background conductance compared to data shown in chapters 5 and 7 based on Ar etched contacts. The measured zero bias conductance peak splits upon varying a gate voltage underneath the superconducting contact, but is independent on the gate voltage away from the superconducting contact. Furthermore, using a gate 100 nm away from the superconducting contact as tunnel barrier, we can create states similar to data reported by others [2], sometimes resulting in a zero bias conductance peak as well. This distinguishes the original robust zero bias peak in our data from zero bias peaks of of a clear non-topological origin.

[1] Kun Zuo performed sample fabrication, measurements and data analysis. Kun Zuo was mainly responsible for reporting of the results, with comments and assistance of Vincent Mourik.
[2] In collaboration with D. Car, E. P. A. M. Bakkers, L.P. Kouwenhoven

9.1 INTRODUCTION

Based on the device improvements achieved, especially the improved superconducting contact quality as reported in chapter 9, a preliminary tunneling spectroscopy study is presented here.

A three terminal device is fabricated as shown in Figure 9.1. Two normal contacts (N) are attached to each end of the nanowire with a superconducting contact (S) in the middle. The S contact is deposited following the optimized recipe as discussed in chapter 8, using a NbTi/NbTiN film deposited after sulfur passivation and short Ar etch. The S contact has a length of 500 nm and covers only half the nanowire diameter. Between S and each N contact, there are three small local gates, one of these being at edge of the S contact. A single wide gate is used to tune the chemical potential underneath the S contact. In the following, only the left NS-junction is investigated, while the right NS junction was made non-conducting by applying a negative voltage to its local gates. All measurements are done in a dilution refrigerator with a base temperature of ~ 25 mK.

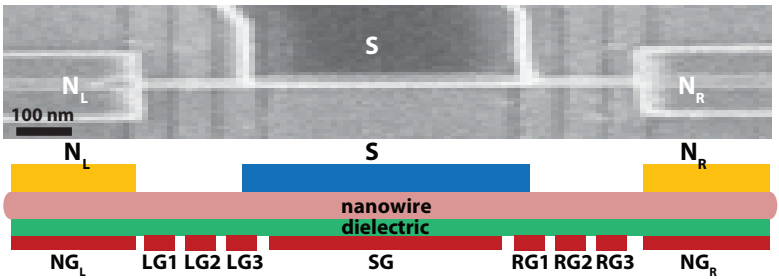

Figure 9.1 |Improved three-terminal tunneling spectroscopy device. Top: SEM image of the device. Bottom: device schematic. Normal contacts (N) made from gold (Au) are made to the nanowire at both ends and a superconducting contact (S) made from NbTiN is deposited in the middle of the nanowire. Electrostatic potential can be controlled locally with the individual gates. In this experiment, the right junctions N_RS is made non-conducting by applying negative voltages to gates RG1,2,3 and NG_R. All measurements are done on the left junction N_LS.

9.2 DEVICE CHARACTERIZATION

A typical dI/dV measurement as a function of the tunnel barrier gate LG3 is shown in Figure 9.2. A clear superconducting gap Δ is visible of size $\Delta \sim 0.4$ meV. Furthermore, no spurious resonances are visible, indicating that both N and S contact are of good quality. In the tunneling spectroscopy, a ratio of conductance inside and outside the gap is around 0.2, showing an improved conductance suppression inside the superconducting gap with the optimized S contact.

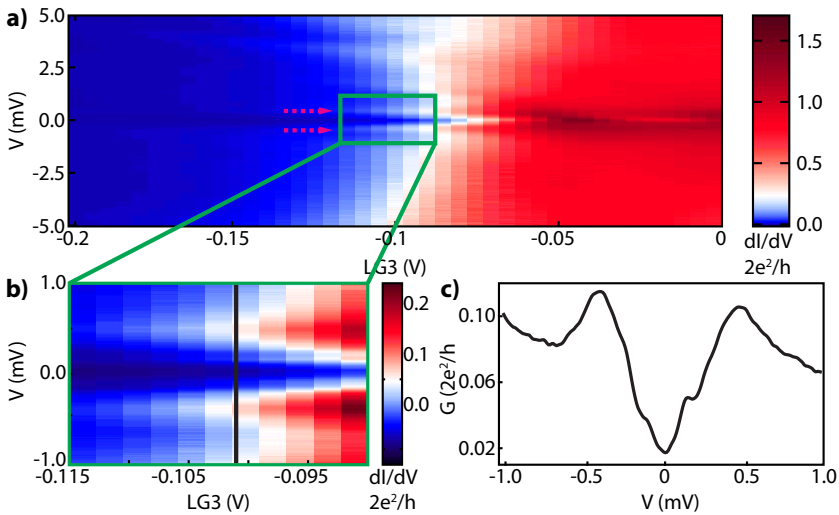

Figure 9.2 |Device characterization. a)$\mathrm{d}I/\mathrm{d}V$ as a function of tunnel barrier gate LG3. A superconducting gap of size $\Delta \sim 0.4$ meV, indicated by pink arrows, is clearly visible. b) Zoom in on tunneling regime, indicated with green box in a). Note that no spurious resonance are present in both a) and b). c) is a linecut from b) at the indicated position. The ratio of conductance inside and outside the superconducting gap is ~ 0.2.

9.3 TUNNELING SPECTROSCOPY AT FINITE MAGNETIC FIELD

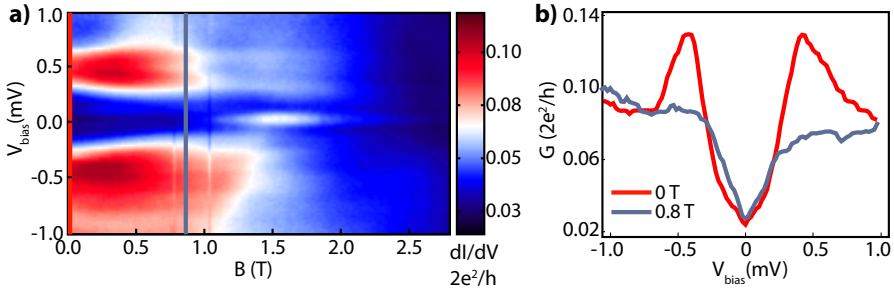

Figure 9.3 |Tunneling spectroscopy as a function of magnetic field. a) $\mathrm{d}I/\mathrm{d}V$ vs B. A clear superconducting gap is visible up to $B = 1$ T, and a weaker superconducting gap is still present up to ~2 T. Around 1.1 T, a ZBP arises, present up to the highest investigated B of 2.8 T. Importantly, no other subgap states or resonances are present near the ZBP. b) Linecuts at indicated positions in a) of 0 T and 0.8 T, showing a well-developed superconducting surviving up to high B. For ZBP linetraces, see Figure 9.4. A negative voltage of -9 V is applied to gate SG, gate LG3 has a potential comparable to Figure 9.2c)

Next we focus on B dependent tunneling spectroscopy, as shown in Figures 9.3 and 9.4. Here gate LG3 is operated in a regime similar to Figure 9.2c. Two aspects are important.

Firstly, upon applying significant magnetic fields of order 1-2 T, still a clear superconducting gap is visible. For increasing B, no spurious subgap states or resonances moving down in energy, are visible. This is a significant improvement to our earlier measurements (chapter 5, [1]) and a direct consequence of the improved superconducting contact quality.

Secondly, at about 1.1 T, a zero bias conductance peak emerges (ZBP), lasting for more than 1 T. This feature is also clearly visible in the linetraces of Figure 9.4. Different from our previous observations, this ZBP has a larger width of ~100 μV, although the temperature of the set-up (~25 mK) and the tunneling strength ($G < 0.1G_0$, $G_0 = 2e^2/h$) are very similar. Another striking difference is the much larger onset B field of the ZBP. Based on $\Delta \sim 0.4$ meV, a possible topological phase transition happens at a minimum field of $B \sim 0.3$ T (taking $g = 50$). In the context of Majorana bound states (MBS's), the large onset B field of the ZBP implies a significant non-zero chemical potential.

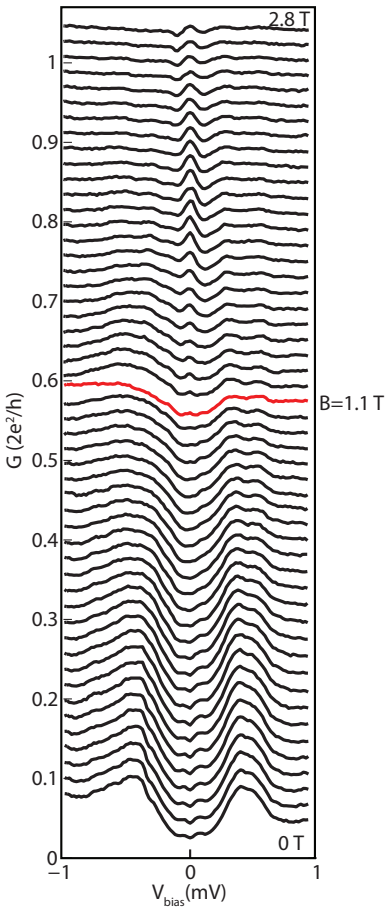

Figure 9.4 |Tunneling spectroscopy as a function of magnetic field. $\mathrm{d}I/\mathrm{d}V$ traces from Figure 9.3 are plot above each other. The lowermost trace corresponds to $B = 0$ T, each subsequent trace corresponds to an increase in B of 40 mT and is offset for clarity by $0.02G_0$. The red curve corresponds to the ZBP onset field of 1.1 T.

9.3.1 GATE DEPENDENCE AT FINITE MAGNETIC FIELD

The dependence of the ZBP on the different gates in the device has been investigated and is shown in Figure 9.5. In these measurements, B is kept constant at 1.2 T. The ZBP strongly depends on the gate SG underneath the superconducting contact, as is visible in Figure 9.5a. The ZBP is only present for very negative gate voltages below ~ -7 V. Here it extends to the lowest gate voltage of -10 V investigated here (Figures 9.3 and 9.4 correspond to SG = -9 V). For less negative gate voltages, SG> -7 V, only a pair of split peaks is observed, lasting throughout the gate range investigated here (up to SG = -5 V). Importantly, no tuning effect on the ZBP by tunnel barrier gate LG3 or the gates at the normal side of the tunnel barrier is observed.

Unfortunately, due to instability of the device, the experiment had to be terminated before a more complete dataset could be taken. The observations on the ZBP discussed are therefore a preliminary to a full investigation. In particular, the large ZBP onset B field, its larger peak width and its very negative SG gate voltage range, are not fully understood and investigated as of yet. Nevertheless, the gate dependent behavior observed confirms our earlier findings of a ZBP crucially depending on the gate potential underneath the S contact, but not depending on other gates.

9.4 SPURIOUS SUB-GAP RESONANCES CREATED WITH LOCAL GATES

A last aspect we discuss is the position of the tunnel barrier. In the preceding results, the gate LG3, placed at the edge of the S contact, was used to induce a local tunnel barrier. However, any of the local gates LG1,2,3 can be used to create a tunnel barrier, here we show some results obtained by using LG2 as tunnel barrier gate.

B dependent tunneling spectroscopy measurments with LG2 as tunnel barrier are shown in Figure 9.6. In these measurements, spurious resonant sub-gap states are clearly visible, being symmetric around zero bias. Furthermore, as a function of B, these states disperse, crossing zero bias at finite B, thus resulting in a ZBP. This ZBP extends over a B range roughly corresponding to the life-time broadening of the crossing resonances. By slighlty varying the gate settings near the tunnel barrier, the exact crossing point and ZBP extension in B change significantly. However, a robust ZBP extending over large B field ranges is not present.

In several aspects this type of ZBP differs from the previously discussed type of ZBP. Firstly, it clearly originates from the crossing of two states, whereas the previous ZBP shows up as an isolated ZBP. Secondly, these crossing states are present upon placing the tunnel barrier away from the S contact edge, but absent in case the tunnel barrier is placed right at the S contact edge. Thirdly, the ZBP onset B field and extension in B are very sensitive to the specific gate settings around the tunnel barrier region, whereas the other type of ZBP is robust in these gates and instead is tuned by the gate underneath the S contact.

All these aspects show that the resonances and corresponding ZBP created here have a spurious, non-topological origin and are most likely not caused by a MBS. A

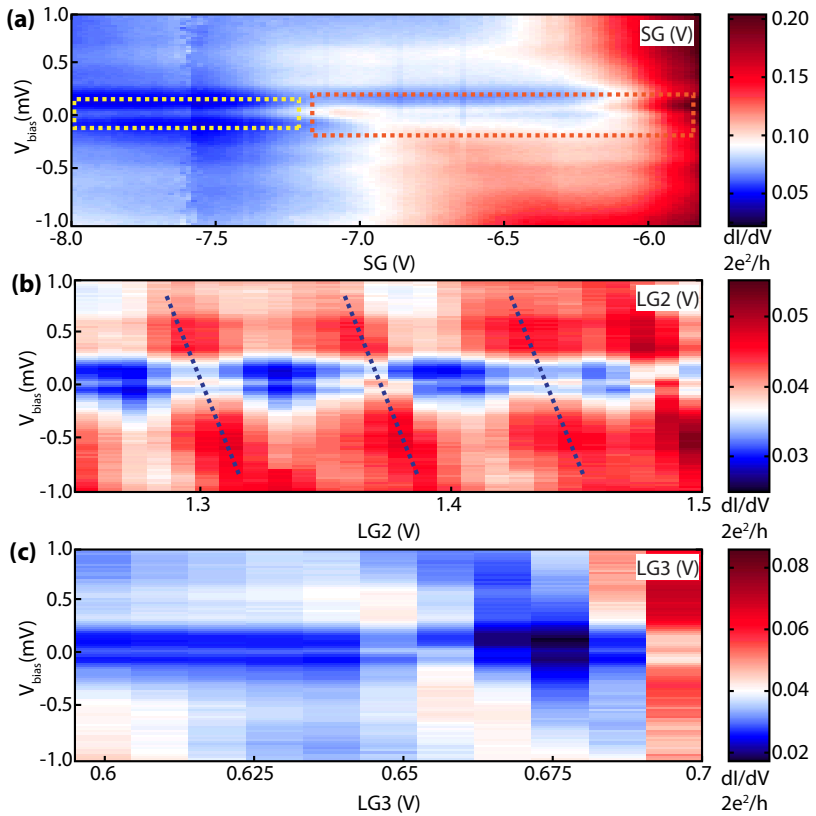

Figure 9.5 |Dependence of ZBP on different gates. In all panels, $B = 1.2$ T. a) Dependence on gate SG underneath superconducting contact. Below ~ -7 V, a ZBP is visible (indicated by yellow box), which extends to the lowest gate voltages investigated. For larger SG potentials, the ZBP splits into a pair of parallel running peaks (indicated by green box), this behavior is found between -10 V and -5 V. The change in background conductance is caused by SG coupling to the tunnel barrier. b) Tunnel barrier gate LG3 dependence. In the conductance regime investigated here $(0.01-0.1G_0)$, no tuning effect of LG3 on the ZBP is observed. c) Dependence on gate LG2 at normal side of tunnel barrier. Again no tuning effect of LG2 on the ZBP is observed, although several slight variations in background conductance are visible (indicate with dashed lines). In both b) and c), SG = -10 V.

likely explanation of this type of ZBP is the presence of trivial Andreev states within the section between tunnel barrier and S contact, as also reported by other groups [2]. In our setup, to create a local tunnel barrier gate with LG2, a positive voltage is applied to LG3, such that the nanowire section controlled by LG3 may contain

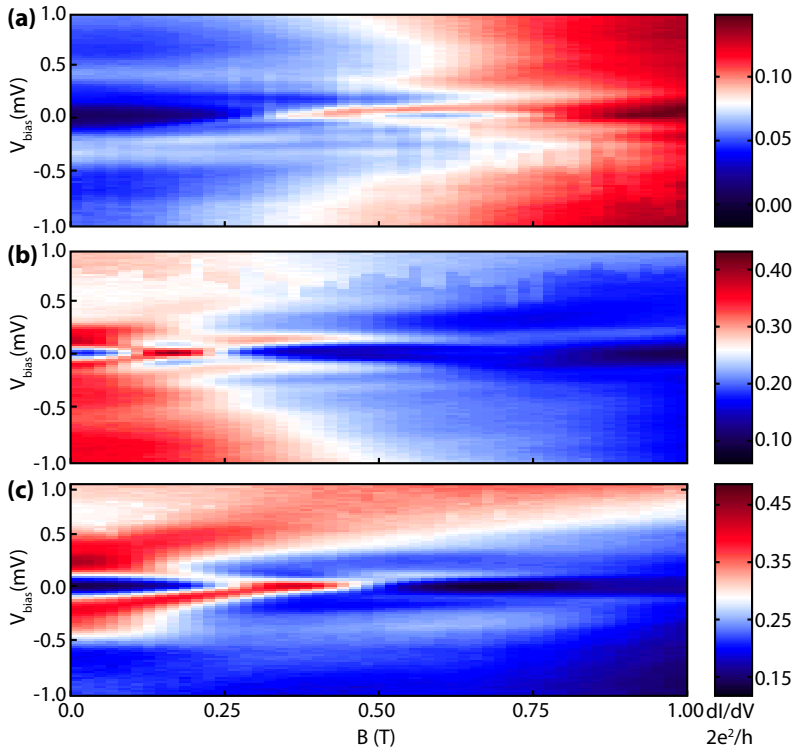

Figure 9.6 |Spurious sub-gap resonances and ZBP's created with local gates. All panels show a $\mathrm{d}I/\mathrm{d}V$ measurement as a function of B. LG2, 80 nm away from the S contact edge, is used as tunnel barrier gate and positive voltages are applied to LG1 and LG3. In all panels, a pair of subgap states originating at finite energy for $B = 0$ T moves down upon increasing B. Upon crossing a ZBP is formed, extending for a period in B similar to the life-time broadening of the crossing resonances. This extension in B, typically ~ 100 mT, is more than 1 order of magnitude less compared to the type of ZBP shown in Figure 9.3. The different panels correspond to slightly different combinations of the gate potentials of LG1,2,3. This significantly alters the B value at which the states cross and form a ZBP. Details of gate potentials: a) LG1 = 1.5 V, LG2 = -0.215 V, LG3 = 1.5 V; b) LG1 = 1.425 V, LG2 = -0.19 V, LG3 = 1.5 V; c) LG1 = 1.475 V, LG2 = -0.215 V, LG3 = 1.39 V. In all panels, SG = 0 V.

confined electronic states. These states have an Andreev character, since they not only normally reflect at the tunnel barrier, but also undergo Andreev reflection at the S interface.

Concluding, by placing the tunnel barrier away from the S contact edge, spuri-

ous subgap resonances, resulting in ZBP's most likely not originating from a MBS, are created. This underlines the importance of i) using a tunnel barrier right at the S contact edge and ii) the necessity of carefully establishing the robustness in B, and in gates away from the S contact, of a ZBP potentially caused by a MBS.

9.5 CONCLUSION

Preliminary results of tunneling spectroscopy in a device with an optimized superconducting contact are shown. An improved superconducting gap at $B = 0$ T was observed compared to our previous works, which survives in B up to field strengths of order 2 T. Sub-gap resonances dispersing in B are no longer present.

Furthermore, above 1 T, we observed a ZBP long lived in B and not tuned by any gates, except the gate underneath the superconductor. Although this feature could not be investigated fully due to limited device stability, the preliminary observations presented here are very promising for identifying such a ZBP as caused by a MBS.

Lastly, we deliberately created spurious resonances inside the superconducting gap by placing the tunnel barrier further away from the superconductor. Upon crossing, these resonances result in a short lived ZBP in B, which is sensitive to all gates around the tunnel barrier. This ZBP is likely not caused by a MBS, but by a crossing of trivial Andreev states, living between tunnel barrier and S contact. This observation shows we are capable of distinguishing a robust ZBP possibly caused by a MBS from a ZBP caused by a trivial level crossing.

The results presented here show great promise for future tunneling spectroscopy experiments in similar device designs. Once a stable device with similar contact quality to the current device is obtained, a systematic investigation of the robust ZBP observed here should be possible. Furthermore, fully exploiting the three terminal N-S-N geometry and correlating local measurements from two sides of the S contact, seems within reach.

REFERENCES

[1] V. Mourik, K. Zuo, S. Frolov, S. Plissard, E. Bakkers, and L. Kouwenhoven, "Signatures of majorana fermions in hybrid superconductor-semiconductor nanowire devices," *Science*, vol. 336, no. 6084, pp. 1003–1007, 2012.

[2] E. J. Lee, X. Jiang, M. Houzet, R. Aguado, C. M. Lieber, and S. De Franceschi, "Spin-resolved andreev levels and parity crossings in hybrid superconductor-semiconductor nanostructures," *Nature nanotechnology*, vol. 9, no. 1, pp. 79–84, 2014.

10

SPECTROSCOPY OF SPIN-ORBIT QUANTUM BITS IN INSB NANOWIRES

Double quantum dot in the few-electron regime is achieved using local gating in an InSb nanowire. The spectrum of two-electron eigenstates is investigated using electric dipole spin resonance. Singlet-triplet level repulsion caused by spin-orbit interaction is observed. The size and the anisotropy of singlet-triplet repulsion are used to determine the magnitude and the orientation of the spin-orbit effective field in an InSb nanowire double dot. The obtained results are confirmed using spin blockade leakage current anisotropy and transport spectroscopy of individual quantum dots.

[1] KZ contributed to sample fabrication, measurements, data analysis and reporting of the results. VM was not involved in this research.

[2] In collaboration with S. Nadj-Perge, V. S. Pribiag, J. W. G. van den Berg, S. R. Plissard, E. P. A. M. Bakkers, S. M. Frolov, L.P. Kouwenhoven. This chapter is published in *Physical Review Letters*

10.1 INTRODUCTION

The spin-orbit interaction (SOI) describes coupling between the motion of an electron and its spin. In one dimension, where electrons can move only to the left or to the right, the SOI couples this left or right motion to either spin-up or spin-down. An extreme situation occurs in what is called a helical liquid [1] where, in the presence of magnetic field, all spin-up electrons move to the left and all spin-down electrons to the right. As proposed recently [2, 3], a helical liquid in proximity to a superconductor can generate Majorana fermions [4]. The search for Majorana fermions in 1D conductors is focused on finding the best material in terms of a strong spin-orbit interaction and large Landé g-factors. The latter is required for a helical liquid to exist at magnetic fields that do not suppress superconductivity. High g-factors of the order 50, strong SOI and the ability to induce superconductivity put forward InSb nanowires [5, 6] as a natural platform for the realization of 1D topological states.

The SOI can be expressed as an effective magnetic field $\vec{B}_{\mathrm{SO}}$ that depends on the electron momentum. An electron moving through the wire undergoes spin precession around $\vec{B}_{\mathrm{SO}}$ with a π rotation over a distance l_{SO} called the spin-orbit length (see Fig. 1(a)). The length l_{SO} is a direct measure of the SOI strength: a stronger SOI results in a shorter l_{SO}. In this letter, we use spin spectra of single electrons in quantum dots [7] to extract l_{SO} and the direction of $\vec{B}_{\mathrm{SO}}$. In quantum dots, the SOI hybridizes states with different spin [5, 8, 9]. For a single electron, the SOI-hybridized spin-up and spin-down states form a spin-orbit qubit [10, 11]. For two electrons SOI hybridization induces level repulsion between singlet and triplet states. The resulting level-repulsion gap between the well-defined qubit states can be used to measure the SOI: the gap size is determined by l_{SO} [5, 8, 9] and the gap anisotropy indicates the direction of $\vec{B}_{\mathrm{SO}}$ [12–14].

10.2 DEVICE AND READOUT

Double quantum dots in InSb nanowires are defined by local gating (Figs. 1(b),1(c)). A finite voltage is applied across the source and drain electrodes; and the current through the nanowire is measured. Five gates underneath the wire create the confinement potential and control the electron number on the two dots [9, 15]. We focus on the (1,1) charge configuration (Fig. 1(d)), in which both the left and the right dot contain exactly one electron, each of them representing a qubit [10, 11, 16–18].

The qubit eigenstates are described by the Kramers spin-orbit doublet $\Uparrow$ and $\Downarrow$. These two states are superpositions of spin-up and spin-down, and of several of the lowest orbital states [20]. Similar to the case of pure spin states, a magnetic field B induces a Zeeman splitting $E_Z = g\mu_B B$ between the Kramers doublets, where g is the effective Landé g-factor for a given direction of $\vec{B}$, and μ_B is the Bohr magneton. The two qubits in the (1,1) configuration can either form a Kramers singlet state S(1,1) or one of the three triplets $\mathrm{T}_+(1,1)$, $\mathrm{T}_0(1,1)$ and $\mathrm{T}_-(1,1)$. The states of the qubits are prepared using Pauli spin blockade [10, 11, 17, 18, 21] (Fig. 2(a)), which

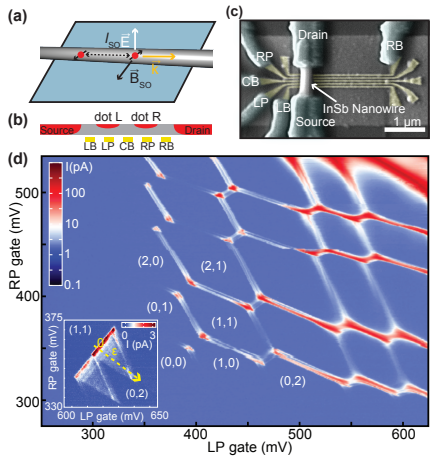

Figure 10.1 |(color online) (a), An electron moving with momentum $\vec{k}$ through the wire experiences a spin-orbit field $\vec{B}_{SO}$ which rotates the spin by π after a distance l_{SO}. Vector $\vec{E}$ indicates likely direction of the electric field. In the case of spin-orbit coupling due to structural inversion asymmetry, $\vec{B}_{SO} \propto \vec{E} \times \vec{k}$ [19]. (b), Schematic of a double quantum dot in an InSb nanowire. Red color indicates regions of the nanowire which are not depleted by gates. Gates LB, CB, and RB define the left, central and right barriers. Gates LP and RP are the left and right plungers used to control the electron number on each dot. (c), Scanning electron microscopy of a nanowire device similar to the one used in the measurements. (d), Charge stability diagram of the double dot for source-drain voltage V_{sd}= 1 mV. Typical charging energy is 10 meV. Numbers in brackets correspond to the charge occupation on the left and the right dots. The inset shows the charge stability diagram near the (1,1) → (0,2) charge transition for V_{sd}= 5 mV. The detuning axis ε is indicated by the dashed arrow.

relies on the tunneling process from (1,1) to the (0,2) spin singlet S(0,2) (note that T(0,2) state is at 5 meV above S(0,2) and therefore inaccessible for $B = 0$). When the two electrons form a triplet state, tunneling of the left electron to the right dot is prohibited by selection rules. This absence of tunneling initializes the qubits in the so-called blocked (1,1) state and thereby suppresses the current of electrons passing through the double dot. Leakage current can occur due to hybridization of T(1,1) states with S(0,2) induced by SOI and by spin mixing between T(1,1) and S(1,1) due to hyperfine interaction [8, 15, 22, 23].

10.3 ELECTRIC DIPOLE SPIN RESONANCE

Transitions between qubit states are induced by a.c. electric fields via electric dipole spin resonance (EDSR) [10, 11, 16, 25–27]. Voltages at microwave frequencies are

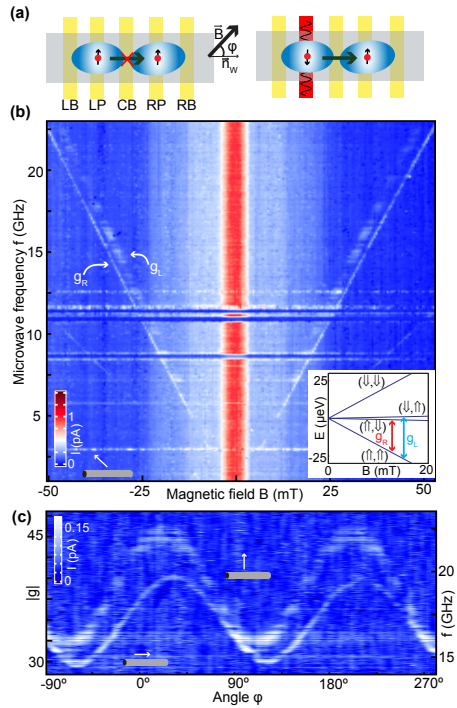

Figure 10.2 |(color online) (a), Left: blocked parallel configuration. φ is the angle between nanowire axis $\vec{n}_W$ and $\vec{B}$. Right: microwaves applied to LP gate (red) induce EDSR. Tunneling to the right dot is allowed when the left qubit is rotated to antiparallel configuration. (b) V-shaped EDSR resonances with slopes providing g_L and g_R for φ =130 ° and $V_{sd} = 8$ mV. Larger g-factor was assigned to the larger dot, i.e to the dot with smaller orbital energy (orbital energy is 5 meV for the left dot and 7.5 meV for the right dot). V-shaped lines with half the slope are two-photon transitions. Enhanced current around B= 0 is due to spin mixing in the absence of microwaves (see [24] section S2). Resonances at constant f are due to photon-assisted tunneling enhanced by cavity modes. (At each frequency the maximum current is normalized to 1pA and a constant offset is subtracted for clarity.) Inset shows energy spectrum of weakly coupled double dots with arrows illustrating the observed transitions. (c), Current versus f and φ for $B = 35$ mT. Vertical axis on the left is rescaled to g=$hf/\mu_B B$. (At each field a constant current offset is subtracted for clarity.) White arrows over grey cylinders indicate B-field orientation with respect to nanowire in panels (b) and (c).

applied to the left plunger (LP) gate (Fig. 2(a)). The oscillating electric field wiggles the electronic orbits. This periodic motion results, via SOI, in a rotation of the spin [10, 11]. When the microwave frequency is on resonance with the double dot level

transitions, EDSR can assist in overcoming spin blockade thereby increasing the current through the double dot. We map out this current increase as a function of microwave frequency f and $\vec{B}$ (Fig. 2(b)).

10.4 EDSR IN THE WEAK COUPLING REGIME

For weak interdot tunnel coupling the spectrum is determined by the energies of individual qubits. At *B=0* all four states are degenerate and non-blocked due to fast decay to singlet state induced by hyperfine interaction [22]. At finite *B*, parallel configurations ($\Uparrow, \Uparrow$)= $T_+(1,1)$ and ($\Downarrow, \Downarrow$) = $T_-(1,1)$ split in energy and become blocked, while the other two configurations ($\Downarrow, \Uparrow$) and ($\Uparrow, \Downarrow$) remain non-blocked. EDSR induces transitions between 'parallel' and 'anti parallel' configurations, resulting in an on-resonance current as observed in Fig. 2(b). The slopes of the two "V" shaped resonances determine the g-factors of the right and left dots, $|g_R| = 29.7 \pm 0.2$ and $|g_L| = 32.2 \pm 0.2$ for this plot. Moreover, the g-factors of both dots are highly anisotropic as revealed by the EDSR spectroscopy for different field orientations (Fig. 2(c)). The observed anisotropy is likely determined by the details of confinement [28, 29] since the g-factor in bulk zincblende InSb is expected to be isotropic.

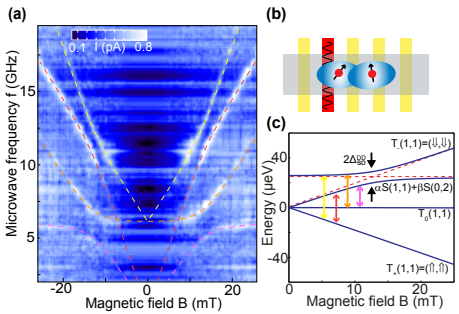

Figure 10.3 |(color online) (a), Current, in color, versus f and B for detuning $\varepsilon \approx 0.5$ meV (V_{sd} =-5 mV). Dashed lines are fits to a model described in the [24] section S4. Line colors match transitions indicated in panel (c). (At each frequency a current offset is subtracted for clarity.) (b), Diagram illustrating a strongly coupled double quantum dot realized by applying a more positive voltage to the central gate. (c), Energy diagram deduced from (a) and used to extract the S-T spin-orbit gap Δ_{SO}^{DD}. Arrows indicate transitions observed in (a). In the absence of coupling, the triplet and the singlet state would simply cross as indicated by dashed lines.

10.5 EDSR IN THE STRONG COUPLING REGIME

When we increase the interdot tunneling (Fig. 3(b)), the (1,1) states hybridize with S(0,2) resulting in level repulsion between spectral lines. In the absence of SOI, only

states with the same spin can hybridize *e.g.* S(1,1) with S(0,2). SOI, however, also enables hybridization between the singlets and the triplets [7, 9, 23, 30] (Fig. 3; see also Fig. 4(e)). All observed transitions in Fig. 3(a) can be identified using a simple model which takes into account the hybridization between the (1,1) triplets and S(0,2) (see [24] section S4). The four avoided crossings observed in Fig. 3(a) correspond to the same double dot spin-orbit gap Δ_{SO}^{DD} between $T_-(1,1)$ and the singlet, as illustrated in Fig. 3(c). The quantitative comparison with the model allows us to estimate the spin-orbit length $l_{SO} = 230 \pm 40$ nm (see [24] section S5).

10.6 ANISOTROPY OF THE SPIN-ORBIT GAP

The observed singlet-triplet gap is highly anisotropic (Fig. 4). The gap Δ_{SO}^{DD} is largest when $\vec{B}$ is parallel to the nanowire axis $\vec{n}_W$: Δ_{SO}^{DD} shrinks as the direction of $\vec{B}$ is rotated in the sample plane (Fig. 4(b) and 4(c)). Finally for $\vec{B} \perp \vec{n}_W$ the gap disappears (Fig. 4(d)). For this orientation the resonance line corresponding to the $T_+(1,1)$ to singlet transition becomes straight indicating the absence of level repulsion between $T_-(1,1)$ and singlet. In addition, the visibility of the $T_+(1,1) \rightarrow T_-(1,1)$ transition vanishes, suggesting that both $T_+(1,1)$ and $T_-(1,1)$ states are completely blocked for this field orientation.

The observed anisotropy of Δ_{SO}^{DD} confirms the spin-orbit origin of the singlet-triplet level repulsion (see also [24] section S3). The gap Δ_{SO}^{DD} is expected to be proportional to $|\vec{B}_{SO} \times (\vec{B}/B)|$ [23, 31, 32]. When the two fields are aligned, singlet and triplet states cannot mix and therefore the spin-orbit gap closes (Fig. 4(d)). From the observed anisotropy we conclude that $\vec{B}_{SO}$ points perpendicular to the nanowire and is parallel to the substrate plane (Figs. 4(i) and 4(a)).

The knowledge of $\vec{B}_{SO}$ orientation provides a substantial increase in the fidelity of the initialization and readout of spin-orbit qubits [10]. The fidelity is presently limited due to unwanted transitions from $T_+(1,1)$ and $T_-(1,1)$ to S(0,2) induced by SOI. When $\vec{B}$ and $\vec{B}_{SO}$ are misaligned, $T_+(1,1)$ and $T_-(1,1)$ are coupled to S(0,2) (Fig. 4(e)) [23]. The unwanted transitions are manifest in the d.c. current through the double dot at finite magnetic fields (Figs. 4(f), 4(g), 4(h)) [15, 30]. For an ideal readout and initialization no current flows after either $T_+(1,1)$ or $T_-(1,1)$ state is occupied. When $\vec{B}$ is aligned with $\vec{B}_{SO}$, $T_+(1,1)$ and $T_-(1,1)$ become decoupled from S(0,2) and d.c. current is expected to vanish. This dramatic suppression of d.c. current is observed for $\vec{B} \perp \vec{n}_W$(Fig. 4(h)). Importantly, both Δ_{SO}^{DD} and I show almost identical angle dependence further confirming that the singlet-triplet hybridization due to SOI is absent when $\vec{B} \parallel \vec{B}_{SO}$ (Fig. 4(i)).

Given the direction of $\vec{B}_{SO}$ we can analyze the origin of the spin-orbit interaction in InSb nanowires. The field $\vec{B}_{SO}$ depends on the electron momentum $\vec{k}$. In a simple physical picture, during the interdot tunneling, the momentum $\vec{k}$ is along the nanowire, which is grown in the [111] crystallographic direction. In zincblende InSb the spin-orbit interaction has two contributions, the bulk-inversion asymmetry term (BIA) and the structure-inversion asymmetry term (SIA). However, for $\vec{k}$

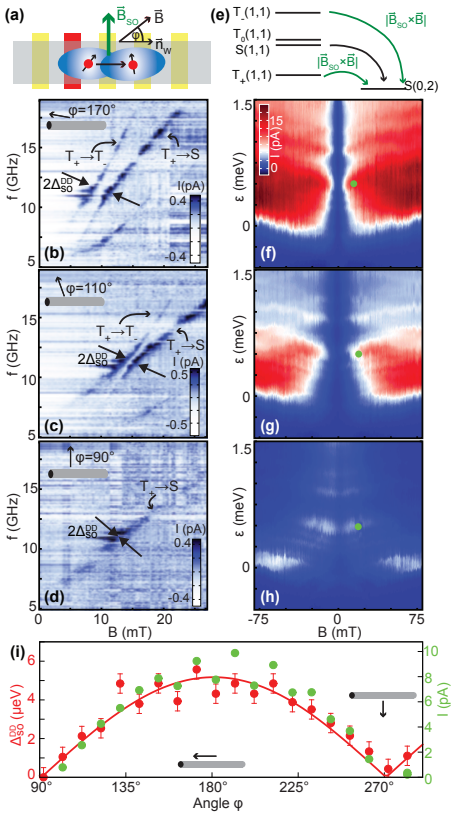

Figure 10.4 |(color online) a, As the left electron tunnels to the right it experiences a field $\vec{B}_{SO}$. (b-d) The avoided crossing in the EDSR spectrum as in Fig. 3(a) for three directions of $\vec{B}$: φ =170°; φ = 110°; and φ = 90° (V_{sd}=-5 mV). (At each magnetic field an offset is subtracted for clarity.) (e), Transitions between (1,1) states and S(0,2) at finite B. The two singlet states are hybridized due to tunnel coupling. $T_+(1,1)$ and $T_-(1,1)$ are coupled to S(0,2) due to $\vec{B}_{SO}$. This SOI induced coupling scales as $|\vec{B}_{SO} \times \vec{B}|$ for small $\vec{B}$ [23]. (f-h), I versus ε and B for the same orientations of $\vec{B}$ as in (b-d) with microwaves off. (i), Extracted values of Δ_{SO}^{DD} (see [24] section S6) and I at B = 20 mT and ε = 0.5 meV (green dot in panels (f-h)) as a function of φ. Solid line is a fit to $\Delta_{SO}^{DD} = \Delta_{SO}|\cos(\varphi - \varphi_0)|$ with Δ_{SO}=5.2±0.3 μeV and φ_0 = 1°±5° . The error bars are determined by the width of EDSR resonance.

10

|| [111] the BIA term is expected to vanish [19], and therefore the SIA contribution should dominate. The field $\vec{B}_{SO}$ due to SIA is orthogonal to both the momentum and the external electric field (Fig. 1(c)). The electric field is likely perpendicular to

the substrate since the symmetry of confinement in the nanowire is broken by the substrate dielectric and voltages on the gates. Therefore the direction $\vec{B}_{SO} \perp \vec{n}_W$ and in the substrate plane is consistent with the SIA spin-orbit interaction.

We compare the results obtained from EDSR spectroscopy with the spectrum of (0,2) states (Fig. 5(a)) [5, 9, 30]. The SOI hybridization of S(0,2) and T_+(0,2) states leads to a single dot spin-orbit gap Δ_{SO}^{SD}. Since the energies of the (0,2) states are too large to be accessed with microwaves ($\Delta_{ST} \approx 5$ meV at B=0), we use the lowest energy T_+(1,1) level as a probe of the (0,2) spectrum. By changing detuning we move T_+(1,1) with respect to the (0, 2) levels. When T_+(1,1) is aligned with either S(0,2) or T_+(0,2), an increase in d.c. current is observed (Fig. 5(b)) [8]. The level repulsion between T_+(0,2) and S(0,2) is observed at $B \approx 2$T (Fig. 5(c)). The single dot gap is also strongly anisotropic reaching the smallest value for $\vec{B} \perp \vec{n}_W$ (Figs. 5(d), 5(e) and 5(f)). The spin-orbit length $l_{SO} = 310 \pm 50$ nm estimated from Δ_{SO}^{SD} is in agreement with the value obtained using EDSR.

Recent proposals for experimental detection of Majorana bound states in hybrid nanowire-superconductor devices require wires with strong spin-orbit coupling [2, 3]. Besides InSb, indium arsenide (InAs) and p-type silicon/germanium (Si/Ge) nanowires [33] are among most promising material systems for this purpose. Majorana states are expected to appear at the boundaries of the topological superconducting phase. The topological phase is predicted to occur if: (i) $E_Z > \Delta$ and (ii) $E_{top}, \Delta > T$. Here Δ is the superconducting gap, E_{top} is the gap of the topological phase and T is the temperature. Due to large g-factors in InSb nanowires first requirement is satisfied at low magnetic fields even if large gap superconductors such as niobium are used ($\Delta \sim 5$K). This is a clear advantage since low magnetic fields are preferential in order not to suppress superconductivity. The size of the topological gap $E_{\text{top}} \approx 2\sqrt{E_{SO}\Delta}$ is determined by the bulk SOI splitting $E_{SO} = \hbar^2/(2m_e^* l_{SO}^2)$ [1]. Here $\hbar$ is the Planck constant and $m_e^* \approx 0.015\, m_e$ is the effective electron mass (m_e is the electron mass). We can estimate $E_{SO} \approx 0.5$ K and $E_{top} \approx 3$ K for the case of ballistic one-dimensional transport. While E_{SO} is expected to be an order of magnitude larger for p-type Si/Ge wires [33] the $E_{SO} \approx 0.1$-0.3 K is similar for InAs wurtzite nanowires [24] ($m_e^* \approx 0.042$-$0.06\, m_e$ for wurtzite InAs [34]). Note however that besides strength of SOI experimental details such as quality of semiconductor-superconductor interface as well as disorder may in the end determine the most promising material system. Finally we note that the anisotropy measurements (Fig. 4 and 5) suggest the orientation $\vec{B} || \vec{n}_W$ to be optimal for observing Majorana states since the maximum mixing of the SOI-split bands occurs for $\vec{B} \perp \vec{B}_{SO}$ and the superconductivity is suppressed least when $\vec{B}$ is in the substrate plane.

We would like to thank J. Danon, Y. Nazarov, M. Rudner, D. Loss, F. Hassler and J. van Tilburg for discussions and help. We acknowledge help with the measurement software from R. Heeres and P. de Groot. This work has been supported by ERC, NWO/FOM Netherlands Organization for Scientific Research and through the DARPA program QUEST.

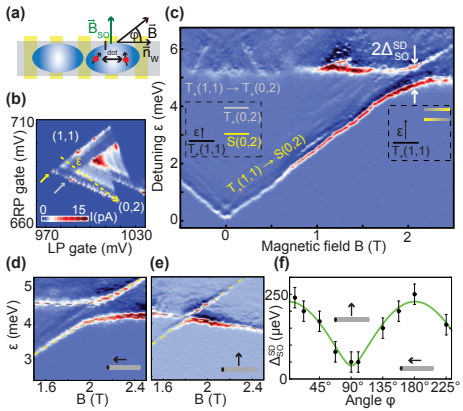

Figure 10.5 |(color online) (a), Two electrons in the right quantum dot. The separation of the two electrons in the triplet state is of the order of the dot size. (b), Charge stability diagram close to (1,1) → (0,2) transition at B= 1.4 T, for V_{sd}= 7 mV and $\vec{B}||\vec{n}_W$. Transitions $T_+(1,1) \rightarrow S(0,2)$ and $T_+(1,1) \rightarrow T_+(0,2)$ are indicated by yellow and gray arrows. (c), Resonances corresponding to $T_+(1,1) \rightarrow S(0,2)$ and $T_+(1,1) \rightarrow T_+(0,2)$ as a function of B for φ=180°. Colors from dark blue (low) to red (high) in panes (c), (d) and (e) indicate values of $dI/d\varepsilon$ in arbitrary units. (d) and (e), Avoided crossing for φ=180° and φ=90°. The dashed lines are fits to the model from Ref. [9]. (f), The gap Δ_{SO}^{SD} as a function of φ. Solid line is a fit to $\Delta_{SO}^{SD} = \Delta'_{SO}\sqrt{\cos^2(\varphi-\varphi_0)\cos^2\theta+\sin^2\theta}$ with Δ'_{SO}= 230 ± 10 μeV, $\varphi_0 = 2° \pm 5°$ and θ=10° ± 3°. The error bars are determined by average linewidth corresponding to $T_+(1,1) \rightarrow S(0,2)$ and $T_+(1,1) \rightarrow T_+(0,2)$ transitions. Note that the anisotropy of Δ_{SO}^{SD} depends on the relative positions of the two electrons in the right dot which may be different from nanowire axis. Out-of-plane $\vec{B}_{SO}$ angle θ therefore may be non-zero due to confinement details of the right quantum dot. Measurements at the (1,1) → (2,0) transition yielded the same in-plane anisotropy for the left dot (data not shown).

REFERENCES

[1] Středa, P. and Šeba, P., *Phys. Rev. Lett.* **90**, 256601 (2003).

[2] Lutchyn, R. M., Sau, J. D., and Das Sarma, S., *Phys. Rev. Lett.* **105**, 077001 (2010).

[3] Oreg, Y., Refael, G., and von Oppen, F., *Phys. Rev. Lett.* **105**, 177002 (2010).

[4] Kitaev, A. Y., *Phys. Usp.* **44**, 131 (2001).

[5] Nilsson, H. A., Caroff, P., Thelander, C., Larsson, M., Wagner, J. B., Wernersson, L.-E., Samuelson, L., and Xu, H. Q., *Nano Lett.* **9**, 3151 (2009).

[6] Nilsson, H. A., Samuelsson, P., Caroff, P., and Xu, H. Q., *Nano Lett.* **12** 228 (2012).

[7] Schreiber, L. R., Braakman, F., Meunier, T., Calado, V., Danon, J., Taylor, J. M., Wegscheider, W., and Vandersypen, L. M. K., *Nature Commun.* **2**, 556 (2011).

[8] Pfund, A., Shorubalko, I., Ensslin, K., and Leturcq, R., *Phys. Rev. B* **76**, 161308 (2007).

[9] Fasth, C., Fuhrer, A., Samuelson, L., Golovach, V. N., and Loss, D., *Phys. Rev. Lett.* **98**, 266801 (2007).

[10] Nadj-Perge, S., Frolov, S. M., Bakkers, E. P. A. M., and Kouwenhoven, L. P., *Nature* **468**, 1084 (2010).

[11] Nowack, K. C., Koppens, F. H. L., Nazarov, Y. V., and Vandersypen, L. M. K., *Science* **318**, 1430 (2007).

[12] Takahashi, S., Deacon, R. S., Yoshida, K., Oiwa, A., Shibata, K., Hirakawa, K., Tokura, Y., and Tarucha, S., *Phys. Rev. Lett.* **104**, 246801 (2010).

[13] Kanai, Y., Deacon, R. S., Takahashi, S., Oiwa, A., Yoshida, K., Shibata, K., Hirakawa, K., Tokura, Y., and Tarucha, S., *Nature Nanotech.* **6**, 511 (2011).

[14] Golovach, V. N., Khaetskii, A., and Loss, D., *Phys. Rev. B* **77**, 045328 (2008).

[15] Nadj-Perge, S., Frolov, S. M., van Tilburg, J. W. W., Danon, J., Nazarov, Y. V., Algra, R., Bakkers, E. P. A. M., and Kouwenhoven, L. P., *Phys. Rev. B* **81**, 201305(R) (2010).

[16] Pioro-Ladriere, M., Obata, T., Tokura, Y., Shin, Y. S., Kubo, T., Yoshida, K., Taniyama, T., and Tarucha, S., *Nature Phys.* **4**, 776 (2008).

[17] Petta, J. R., Johnson, A. C., Taylor, J. M., Laird, E. A., Yacoby, A., Lukin, M. D., Marcus, C. M., Hanson, M. P., and Gossard, A. C., *Science* **309**, 2180 (2005).

[18] Koppens, F. H. L., Buizert, C., Tielrooij, K. J., Vink, I. T., Nowack, K. C., Meunier, T., Kouwenhoven, L. P., and Vandersypen, L. M. K., *Nature* **442**, 766 (2006).

[19] Winkler, R., *Spin-Orbit Coupling Effects in Two-Dimensional Electron and Hole Systems.* Springer, Berlin, (2003).

[20] Flindt, C., Sorensen, A. S., and Flensberg, K., *Phys. Rev. Lett.* **97**, 240501 (2006).

[21] Ono, K., Austing, D. G., Tokura, Y., and Tarucha, S., *Science* **297**, 1313 (2002).

[22] Koppens, F. H. L., Folk, J. A., Elzerman, J. M., Hanson, R., van Beveren, L. H. W., Vink, I. T., Tranitz, H. P., Wegscheider, W., Kouwenhoven, L. P., and Vandersypen, L. M. K., *Science* **309**, 1346 (2005).

[23] Danon, J. and Nazarov, Y. V., *Phys. Rev. B* **80**, 041301 (2009).

[24] Supplementary Material accompanies this paper. It can be downloaded at http://link.aps.org/supplemental/ 10.1103/PhysRevLett.108.166801

[25] Bell, R. L., *Phys. Rev. Lett.* **9**, 52 (1962).

[26] Golovach, V. N., Borhani, M., and Loss, D., *Phys. Rev. B* **74**, 165319 (2006).

[27] Laird, E. A., Barthel, C., Rashba, E. I., Marcus, C. M., Hanson, M. P., and Gossard, A. C., *Phys. Rev. Lett.* **99**, 246601 (2007).

[28] Pryor, C. E. and Flatté, M. E., *Phys. Rev. Lett.* **96**, 026804 (2006).

[29] Schroer, M. D., Petersson, K. D., Jung, M., and Petta, J. R., *Phys. Rev. Lett.* **107**, 176811 (2011).

[30] Pfund, A., Shorubalko, I., Ensslin, K., and Leturcq, R., *Phys. Rev. Lett.* **99**, 036801 (2007).

[31] Nowak, M. P., Szafran, B., Peeters, F. M., Partoens, B., and Pasek, W. J., *Phys. Rev. B* **83**, 245324 (2011).

[32] Stepanenko, D., Rudner, M., Halperin, B. I., and Loss, D., *Phys. Rev. B* **85**, 075416 (2012).

[33] Kloeffel, C., Trif, M., and Loss, D. *Phys. Rev. B* **84**, 195314 (2011).

[34] De, A., and Pryor, C. E., *Phys. Rev. B* **81**, 155210 (2010).

11

OUTLOOK - KUN ZUO

Since the first proposal of Majorana fermions, pursuit of them in solid state physics has never stopped. Progresses in nanowire system are constantly made both experimentally and theoretically, especially after the report of the signatures of Majorana fermions in chapter 5. In this chapter I will first summarize the results achieved in this thesis work followed by the possible directions of ongoing researches. The future experiments to establish Majoranas are discussed in a separate section, and finally topological quantum computation based on Majoranas will be presented.

11.1 CONCLUSIONS

Following the propositions by Oreg and Das Sarma [1, 2], proper engineered systems with the required elements to create Majoranas are investigated.

- In chapter 4, superconductivity is successfully induced in InSb nanowires by proximity effect from superconductor NbTiN. Oscillation of supercurrent as a function of magnetic field is observed in Josephson junctions based on InSb nanowires and NbTiN contacts. Moreover in some cases, at 0 T, anomalous supercurrent is found.

- In chapter 5, signatures of Majorana fermions were detected in tunnelling spectroscopy measurements. A ZBP was found when a finite magnetic field B is applied along the InSb nanowires. Gate dependence and magnetic field orientation dependence support the hypothesis of Majorana fermions at the ends of superconducting contacts in the hybrid devices.

- In chapter 7, tunneling spectroscopy with the improved Majorana device structure have been explored. Similar ZBP as in chapter 5 is reproduced. In addition, more features that follows the predictions of Majorana fermions are observed, i.e. oscillations of ZBP as a function of magnetic field B, the onset field of the ZBP changes as the change of gate settings. In addition, it is demonstrated that the ZBP lives underneath the superconducting lead, which confirms the ZBP has a superconducting origin.

- In chapter 8 and 10, the superconducting gap induced in the InSb nanowires are optimized and the properties of SOI are measured. These two results are important for the future realization of Majorana fermions for braiding and quantum computation.

11.2 DEVICE IMPROVEMENTS

Devices, based on which the first signature of Majorana fermions was reported, have been optimized continuously. With the accumulated improvements over years, better data are obtained as in chapter. However, due to the limit time and manpower, not all possible directions are implemented, here I will discuss some of them.

11.2.1 CONTACTS

In order to induce optimal superconducting gap, it is essential to achieve highly transparent superconducting contacts. Therefore, a lot of efforts have been put in in this respect. The improved contacts investigated in Chapter 8 indeed lead to better data in Chapter 9, however, the interface between the two materials is never perfect with the contact based on etching away surface oxide. The best way of forming a perfect contact is to avoid the surface oxidation. Therefore epitaxial

grown superconducting contact *in situ* is put forward. Marcus lab demonstrated the initial results [3], a relatively hard gap was found in the InAs nanowire junction.

However, as it is suggested, the InAs combined with Al contacts might not be adequate for braiding Majorana fermions in the future (low Tc, hard to get rid of quantum dot features), systems based on InSb and high T_c superconductor is still preferable. Since the first signature has already been detected in the NbTiN devices, combination of InSb with epitaxially grown Nb/NbTi shell would be optimum. Attempts of this type of expitaxial core-shell wires are in progress and should be investigated further.

11.2.2 TUNNEL BARRIER

In all of the epxeriments done so far, the tunnel barriers are created by applying negative potential on the gate underneath the InSb nanowires. However due to the finite width and the distance from the gate to the nanowires, the effective tunnel barriers are not perfect, i.e. finite height and finite width. As discussed in chapter 6, these non-ideal tunnel barriers might induce some uncertainties in the measured tunneling spectroscopy. Therefore it is preferable to have a tunnel barrier closer to the ideal case, to at least eleminate the uncertainty, if not to imporve the measurements quality. One of the interesting way of creating such tunnel barrier is by growing a heterojunction in the nanowire itself.

11.2.3 GATES

If the electrical coupling between gates and the nanowires are very strong, the drawback of the current gate design will magnify itself as a bigger problem later on. When the gates have different heights, nanowires do not touch with the dielectric everywhere as shown in Figure 11.1a) and b), this forms air voids between nanowires and the dielectric. Due to the difference in dielectric constants between the dielectric (HfOX) and the air, a large variation in potential landscape is expected. Situation is worse if the nanowires is tilted, see Figure 11.1b)

One solution to this problem is to use the so called SWAP gates. Schematic of the fabrication of such gates is shown in Figure 11.1. As we can see, because the gates were evaporated on a flat surface and then flipped upside down. All the gates are as flat the as the first substrate. Measurements on these gates show that the variation is even smaller than 1nm. More importantly, compared to the alternative solutions of using BrN as dielectric, this type of gates are suitable for scaling up.

11.2.4 SOI

Strength of Spin Orbit Interaction in InSb nanowires has been measured in three different systems as of now ([4, 5]). The very first one is measured in QD as we quoted in chapter[], another one is measured in a system similar to the Majorana devices using weak anti-localization. However both methods have their limits, none of them provides full understanding of the SOI effect, especially in term of Majorana's. The third method probes the helical gap in InSb nanowires show a di-

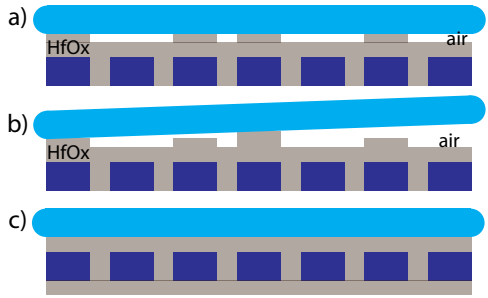

Figure 11.1 |Formation of air voids between gates and nanowires due to the variation of gate heights. a) In the ideal case, all gates covered by the dielectric have equal height, nanowires lies on the dielectric surface flatly. However in reality with the conventional gate fabrication, the height of gates are different, this leaves the air voids between lower gates and the nanowires, as in b). Due to the difference in dielectric constant, the coupling of the adjacent gates can be very different, such an effect can lead to a variational potential landscape that causes the non-uniform topological protection. c) is the new type of gates by flip gates upside down and bond to a new wafer. In this case all gates are as flat as the surface of the substrate.

rect measure of SOI in InSb nanowires, an more accurate estimation of SOI could be made if in an improved helical gap experiment that mimics the Majorana device.

Better understanding of SOI in the InSb nanowires is very important in advance in Majorana physics, however what is equally important is to control the orientation of the SOI. Due to the fact that braiding of Majoranas is in 2D structure (T-junctions), not all nanowires are aligned in the same direction. Because of the restricted effective angle of magnetic field where Majoranas present, it is therefore much simpler if the direction of SOI can be manipulated individually at different sections. Experiments from [5] already showed that gating effect could change the strength of the SOI, it is possible to explore this aspect further to use the gate to control the direction of the SOI filed.

11.3 EXPERIMENTS BASED ON CURRENT DEVICES

The primary goal of the 3-terminal devices is to demonstrate the correlation of appearance of the Majorana pairs at both ends of the superconducting contact. However the design of 3-terminal devices are suitable for many other interesting experiments, such as cross Andreev reflection and non-local effect with the presence of Majorana fermions.

11.3.1 CROSS-ANDREEV REFLECTION

Uniform superconductivity across the whole superconducting contact is one of the crucial ingredients leading to uniform topological protection. However, due to the

contact preparation, it is unclear at the moment how homogeneous the interface between contact and the nanowire is. One of the relevant experiments to check this property is the cross-Andreev reflection. If the induced superconductivity is equal within the superconducting lead, an electron incidents from the left end will generate a hole going out from the right end. The measurable effect would be the negative current from the normal lead to the right end of the device [6], as indicated in the Figure 11.2.

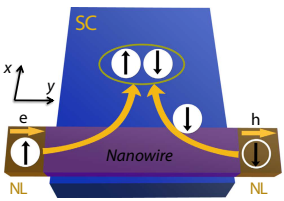

Figure 11.2 |Cross Andree resonant tunneling in a Majorana based device. Two normal leads are attached to the two ends of a wire with finite length. In a crossed AR process, an electron from the left lead is reflected as a hole in the right lead. As a result, two electrons are injected into the superconductor to form a Cooper pair. Figure from [6].

Not only to check the superconductivity, Cross-Andreev reflection can also be applied to measure the correlation of the two Majorana fermions at the ends of a 1D topological superconductor. One should be able to measure both correlation in spin current but also in the short noises generated due to the tunnelling. Correlations of both signals are a stronger evidence to the existence of Majorana fermions, see paper [7].

11.3.2 NON-LOCAL EFFECT OF MAJORANA FERMIONS

As we have elaborated before, the 3-terminal device is capable of probing the non-local effect of Majoran fermions. One of the very interesting experiments is the controlling of the splitting and oscillations. If a pair of Majorana fermions emerge at the end of the superconducting contact, due to the overlap of wavefunctions, the tunnelling spectroscopy will give rise to a pair of split conductance peaks. However, if one of the two sides of the device is opened up, the Majorana localized at the side will leak into the lead, and therefore less overlap of two Majoranas and less splitting. Hence one should observe the recover of ZBP by tuning the gates at the opposite side of the contact.

11.3.3 EXPERIMENTS IN A LONG TERM

Though tunnelling spectroscopy with ZBP is the simplest method to probe Majorana fermions in the 1D nanowire system, different signals and different detecting schemes are also proposed. With the increased complexity of fabrication and the

availability of T-shape nanowires [8, 9], many of these alternative proposals are possible to be realized in the future.

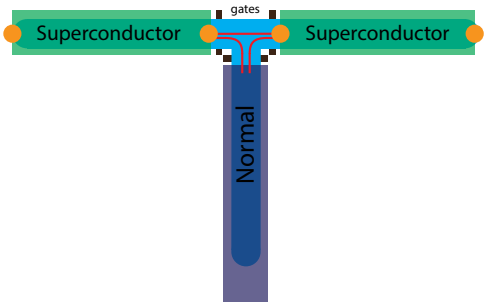

Figure 11.3 |T-junction Majorana devices. A T-junction nanowire is contacted with two superconducting contacts as indicated in the figure. The third branch is contacted with a normal lead. In front of each lead there is a gate to create potential barriers. Firstly The middle gate serves as the tunnel probe to detect Majorana fermions separately of each superconducting branch. While measuring, keep the other superconducting branch pinched off with the gate in front. Once both superconducting branches are in Majorana region, only the gate in front of the normal lead is left pinched off as a tunnel probe, the other two are open. So that the Andree bound states in the middle branch with the presence of Majorana bound states could be probed.

One of the very relevant schemes [10] is shown in Figure 11.3. A T-shape nanowire is contacted at two far ends with superconducting leads, and in the middle a normal contact. The idea of this scheme is to combine both ZBP ([11]) and Majorana Josephson junction ([12–14]) measurements together.

First, one tunes two side branches subsequently to topological states where Majorana fermions emerge at the end of the superconducting contacts. This could be individually confirmed by measuring ZBPs using the middle contact as tunnel probe. While tuning one superconducting branch, the other superconducting branch is totally pinched off. As soon as both branches host Majorana fermions, two superconducting branches could be operated as a Josephson junction, therefore one could probe the Andreev bound states in the Majorana Josephson junction with the middle tunnel probe. Moreover, this geometry could be combined with the 4π periodicity measurements as in ([15]).

11.4 BRAIDING

It is reasonable to expect that with all the improved gate design and the interfaces between superconducting contacts and InSb nanowires, the Majorana bound states could be fully established. The ability to fully control the MBSs in the system enables the demonstrating the unique non-Abelian statistics with braiding, which is, in turn, the ultimate way to prove the existence of Majorana fermions. Several proposals on braiding Majorana fermions and demonstrating the non-abelian statistics are developed, here we will briefly discuss three of them [16–19].

KEYBOARD SCHEME

The very first braiding scheme is also called keyboard scheme [20], as it uses a set of keyboard like gates to manipulate Majorana bound states in the 1D nanowire system as shown in Figure 1. If the gating effect is strong enough, by tuning the gate voltage, exchange of two Majorana fermions is possible in a T-junction as depicted in the Figure 11.4.

The keyboard scheme is rather simple and easy to understand, however due to the fact that the electrical gating underneath superconducting contacts are too weak to fully shift Majorana fermions around and the T-junction is not readily available, the realization of such scheme is rather hard. Two different solutions from two different groups resolved this problem.

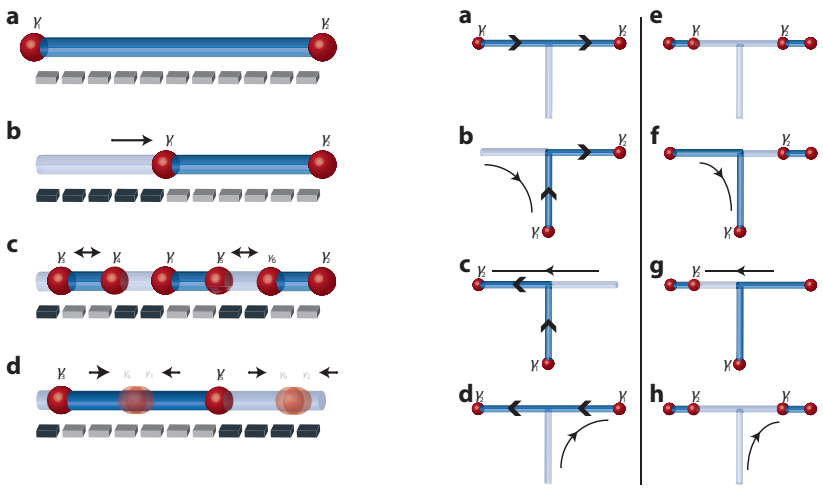

Figure 11.4 |Schematic of the keyboard braiding scheme. Left column shows how Majorana fermions are controlled via gates, and the right column demonstrates how to braid Majorana fermions step by step in a T-junction nanowire system

TUNNEL COUPLING

J. Sau at.el [18] showed that exchange of two Majorana fermions could be realized by sequential tunnel coupling and decoupling of Majorana bound states as shown in the schematic of Figure 11.5.

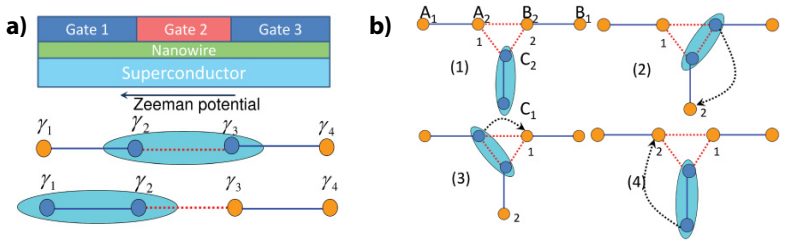

Figure 11.5 |Exchange of Majorana fermions with the tunnel coupling tuned by gates. a) Nanowire segments in the TS phase are shown as blue lines. Orange (light) and blue (dark) circles indicate unpaired and paired MFs, respectively. MFs are paired by tunnelling across the TS or NTS segments denoted by the light blue oval. Decreasing the tunnelling amplitude between $\gamma_1$and γ_3 and simultaneously increasing the tunneling amplitude between γ_1 and γ_2 can effectively transfer MF γ_1 to γ_3. b) is the exchange subsequence to realize the braiding of Majorana fermions.

FLUX CONTROL

Similar to previous proposal,Van Heck at. el [17] found that coupling of Majorana fermions on the island of a Cooper pair box depends strongly on the energy ratio of E_j/E_c. By tuning the coupling strength via flux through the Cooper pair box, the two Majorana fermions could be exchanged. The braiding procedure is similar to the tunnel coupling scheme and is described in Figure 11.6.

11.5 TOPOLOGICAL QUANTUM COMPUTATION

Essentially, braiding of Majorana fermions is a generic quantum gate [21]. Therefore, any system that can demonstrate braiding and read out the initial and final state (parity) could be applied as topological quantum computer. One of the most realistic read out schemes is to combine Majorana fermions with transmon qubits. A simple scheme of this type is shown in Figure 11.7 [19].

The setup consists of two blocks of Cooper pair boxes as in Figure 11.6 embedded in a resonator that forms a transmon qubit. After the topological phase transition, two Majorana fermions are localized on the ends of each nanowires on the superconducting islands. In the T-junction, where 3 Majorana fermions meet and form effectively a single Majorana fermion. Coulomb coupling of Majorana fermions is controlled by the flux Θ_x. The braiding of Majorana fermions is the

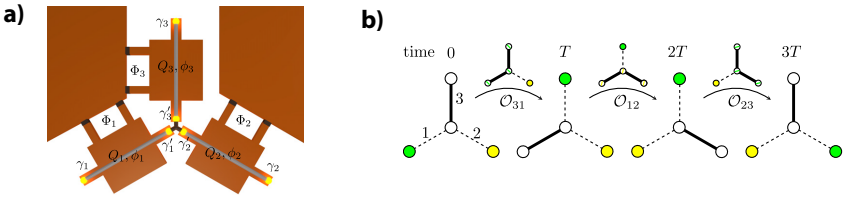

Figure 11.6 |Braiding scheme based on flux controlled Cooper pair box. a)Three Cooper pair boxes connected at a tri-junction via three overlapping Majorana fermions. The island contains Majorana fermions (yellow) at the end points of a nanowire (gray). These are coupled by the Coulomb charging energy, tunable via the flux 8 through the Josephson junction. b) a walking through braiding scheme as in Figure 11.5b). Figure is adapted from [ref]

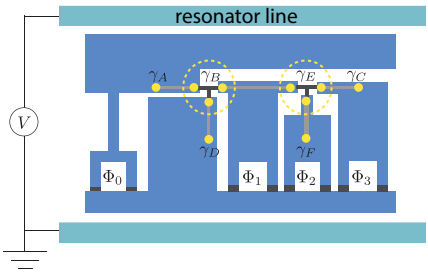

Figure 11.7 |Minimal circuit for flux-controlled demonstration of non-Abelian Majorana statistics. Two large superconducting plates form a Cooper pair box in a transmission line resonator, i.e., a transmon qubit. Three smaller superconducting islands are embedded between the two transmon plates. Each superconducting island contains a nanowire supporting two Majorana bound states. Adapted from [19]

same as in Figure 11.6, before and after the braiding, parity of the island is measured by the transmon qubit.

During the Majorana exchange process, the system is tuned to E_j dominant regime, so that the parity is fully protected. After exchange, Cooper pair box is brought back to E_C dominant regime where parity could be measured [22].

REFERENCES

[1] R. M. Lutchyn, J. D. Sau, and S. D. Sarma, "Majorana fermions and a topological phase transition in semiconductor-superconductor heterostructures," *Physical review letters*, vol. 105, no. 7, p. 077001, 2010.

[2] Y. Oreg, G. Refael, and F. von Oppen, "Helical liquids and majorana bound states in quantum wires," *Physical review letters*, vol. 105, no. 17, p. 177002, 2010.

[3] W. Chang, S. Albrecht, T. Jespersen, F. Kuemmeth, P. Krogstrup, J. Nygård, and C. Marcus, "Hard gap in epitaxial semiconductor–superconductor nanowires," *Nature nanotechnology*, vol. 10, no. 3, pp. 232–236, 2015.

[4] S. Nadj-Perge, V. Pribiag, J. Van den Berg, K. Zuo, S. Plissard, E. Bakkers, S. Frolov, and L. Kouwenhoven, "Spectroscopy of spin-orbit quantum bits in indium antimonide nanowires," *Physical review letters*, vol. 108, no. 16, p. 166801, 2012.

[5] I. van Weperen, B. Tarasinski, D. Eeltink, V. Pribiag, S. Plissard, E. Bakkers, L. Kouwenhoven, and M. Wimmer, "Spin-orbit interaction in insb nanowires," *Physical Review B*, vol. 91, no. 20, p. 201413, 2015.

[6] J. J. He, J. Wu, T.-P. Choy, X.-J. Liu, Y. Tanaka, and K. T. Law, "Correlated spin currents generated by resonant-crossed andreev reflections in topological superconductors," *Nature communications*, vol. 5, 2014.

[7] J. Liu, F.-C. Zhang, and K. Law, "Majorana fermion induced nonlocal current correlations in spin-orbit coupled superconducting wires," *Physical Review B*, vol. 88, no. 6, p. 064509, 2013.

[8] S. R. Plissard, I. van Weperen, D. Car, M. A. Verheijen, G. W. Immink, J. Kammhuber, L. J. Cornelissen, D. B. Szombati, A. Geresdi, S. M. Frolov, *et al.*, "Formation and electronic properties of insb nanocrosses," *Nature nanotechnology*, vol. 8, no. 11, pp. 859–864, 2013.

[9] D. Car, J. Wang, M. A. Verheijen, E. P. Bakkers, and S. R. Plissard, "Rationally designed single-crystalline nanowire networks," *Advanced Materials*, vol. 26, no. 28, pp. 4875–4879, 2014.

[10] S. Valentini, R. Fazio, and F. Taddei, "Andreev levels spectroscopy of topological three-terminal junctions," *Physical Review B*, vol. 89, no. 1, p. 014509, 2014.

[11] K. Law, P. A. Lee, and T. Ng, "Majorana fermion induced resonant andreev reflection," *Physical review letters*, vol. 103, no. 23, p. 237001, 2009.

[12] A. Y. Kitaev, "Unpaired majorana fermions in quantum wires," *Physics-Uspekhi*, vol. 44, no. 10S, p. 131, 2001.

[13] L. Fu and C. L. Kane, "Josephson current and noise at a superconductor/quantum-spin-hall-insulator/superconductor junction," *Physical Review B*, vol. 79, no. 16, p. 161408, 2009.

[14] C. Beenakker, "Search for majorana fermions in superconductors," *arXiv:1112.1950*, 2011.

[15] E. B. Hansen, J. Danon, and K. Flensberg, "Phase-tunable majorana bound states in a topological n-sns junction," *arXiv preprint arXiv:1511.03877*, 2015.

[16] J. Alicea, Y. Oreg, G. Refael, F. von Oppen, and M. P. Fisher, "Non-abelian statistics and topological quantum information processing in 1d wire networks," *Nature Physics*, vol. 7, no. 5, pp. 412–417, 2011.

[17] B. Van Heck, A. Akhmerov, F. Hassler, M. Burrello, and C. Beenakker, "Coulomb-assisted braiding of majorana fermions in a josephson junction array," *New Journal of Physics*, vol. 14, no. 3, p. 035019, 2012.

[18] J. D. Sau, D. J. Clarke, and S. Tewari, "Controlling non-abelian statistics of majorana fermions in semiconductor nanowires," *Physical Review B*, vol. 84, no. 9, p. 094505, 2011.

[19] T. Hyart, B. van Heck, I. Fulga, M. Burrello, A. Akhmerov, and C. Beenakker, "Flux-controlled quantum computation with majorana fermions," *Physical Review B*, vol. 88, no. 3, p. 035121, 2013.

[20] J. Alicea, "Majorana fermions in a tunable semiconductor device," *Physical Review B*, vol. 81, no. 12, p. 125318, 2010.

[21] L. H. Kauffman and S. J. Lomonaco Jr, "Braiding operators are universal quantum gates," *New Journal of Physics*, vol. 6, no. 1, p. 134, 2004.

[22] F. Hassler, A. Akhmerov, C. Hou, and C. Beenakker, "Anyonic interferometry without anyons: how a flux qubit can read out a topological qubit," *New Journal of Physics*, vol. 12, no. 12, p. 125002, 2010.

12

OUTLOOK - VINCENT MOURIK

This chapter contains a short reflection on the research done within the scope of this thesis. Next, I will discuss future directions of the research, in a narrow sense relevant to tunneling spectroscopy on Majorana bound states, but also more general future directions relevant to Majorana bound states research in nanowires are discussed.

12.1 INTRODUCTION

As a starting point of the discussion on future perspectives for Majorana bound state (MBS) related research, I summarize what I believe to be the main findings of this research:

- The observation of a zero bias peak (ZBP) in the differential conductance of a hybrid superconducting-semiconducting nanowire device. This ZBP behaves in accordance to the MBS hypothesis, but cannot be explained, as of yet, by any known alternative theory.
- The observation that furthering our understanding of this ZBP and its likely origin, a MBS, critically depends on obtaining devices of improved quality. In particular, improving the superconductor-semiconducting nanowire interface is crucial in this. We have shown this can be achieved by carefully engineering the nanowire surface preparation and superconductor deposition techniques.

Based on these conclusions, several aspects of future research directions are discussed in the following. Section 12.2 contains a discussion of direct follow up experiments on the research presented in this thesis. Material developments in nanowire growth, relevant to MBS research, are discussedn in section 12.3. Section 12.4 discusses experiments beyond tunneling spectroscopy, relevant to MBS research in semiconducting nanowires. Lastly, section 12.5 contains a short more general discussion of future perspectives regarding establishing non-abelian statistics and its possible usage for quantum computing purposes.

12.2 PERSPECTIVES ON FUTURE TUNNELING SPECTROSCOPY EXPERIMENTS

Although the observed ZBP presented in this thesis fits well to the MBS hypothesis, new observations further establishing this conjecture are of uttermost importance, especially given the controversy created by the proposal of a disorder induced ZBP. We argued earlier in this thesis that the latter type is not fitting well to the observations, however, only more conclusive and extensive experimental results can resolve this debate. Obtaining these was the aim of the research in the second part of this thesis. Although impossible to fully realize within the scope of the thesis research, it seems enough progress has been made to enable such measurements in the near future.

More specifically, in chapter 8 it has been shown that devices can be obtained with a better developed superconducting gap, of larger size and surviving up to larger magnetic field B. Furthermore, spurious resonances are virtually absent in such improved devices. Lastly, gentler contact preparation seems to result in more stable devices, with less random charge switches. These developments pave the way for future tunneling spectroscopy experiments potentially capable of a more conclusive identification of the ZBP as a MBS signature.

The first step is to obtain a full understanding of the emergence of the ZBP in parameter space. We have already shown clear trends, such as the tunability of the ZBP with gates underneath the superconducting nanowire section, and the absence of such a tuning effect with gates outside this section. These trends have to be confirmed further by completely mapping out the ZBP in (B, V_{gate})-space for the different gates in a device. Furthermore, the B-field angle dependence of the ZBP has to be investigated in more depth.

Rigorously establishing the ZBP parameter space has not been possible before, but may lead to vital insights regarding the topologically non-trivial phase. The shape of such a ZBP phase diagram may shed light on crucial aspects like the role of disorder, the role of orbital effects [1], and the gating effect underneath the superconducting region [2]. Importantly, such a study needs a relatively simple device geometry, a nanowire atop local gates, contacted with a single normal and a single superconducting contact will suffice.

Fully establishing the ZBP phase diagram seems within reach with the current device technology, the results shown in chapter 9 already present a preliminary study along those lines. Such a research should be accompanied by more involved numerical studies focusing on a realistic modeling of the electro- and magnetostatics of the relevant device geometry, i.e., a continuation of studies such as [1, 2].

12.2.1 SUPERCONDUCTING CONTACT GEOMETRY

A second crucial aspect to investigate is the role of the superconducting contact geometry. Two important, basic questions regarding MBS's are related to this. Firstly, the degree of control over the chemical potential underneath the superconducting contact by varying local gate potentials is crucial to the existence of MBS's. This depends on the amount of coverage of the nanowire by the superconductor [2]. Secondly, the MBS's at each end of the superconducting nanowire section should be far enough apart, such that coupling between them is negligible, an aspect directly dependent on the superconducting contact length.

I propose therefore two future studies:

1. A variation of the degree of nanowire coverage by the superconducting contact. The control over the nanowire coverage is set by electron beam lithography alignment precision. We obtained throughout our research precise location of the nanowire on a predefined local gate array within a ten's of nanometer range. This corresponds to about one half of the nanowire diameter. Consequentially, it is most realistic to aim for a partial coverage corresponding to roughly one quarter of the nanowire's circumference. Natural spread due to alignment precision may create additional coverage angles, although reproducibility I expect to be correspondingly poor. Such a partial coverage can be compared to full coverage of the nanowire atop substrate. Measurements on a few good quality devices of each category should suffice.

   Regarding measurements, I propose to use the same tunneling spectroscopy method as employed before. Once a ZBP similar to the type reported here is

found, its gate dependence should be investigated. Crucial in this is to use a local gate design consisting of several, independently tunable gates underneath the contact. This way, the problem of a gate underneath the contact influencing the tunnel barrier gate (see 7) can be avoided by using a separate gate several hundred's of nanometers away from the tunnel barrier region. Expected signatures are the (dis)appearance of the ZBP as a function of gate, and/or the (dis)appearance of a splitting in the ZBP as a function of gate due changing coupling of the MBS's. If this happens while the background tunneling conductance does not change significantly, it is a clear indication that locally, deep underneath the superconducting contact, chemical potential tuning is possible. Comparison between the two device categories of partial and full nanowire coverage should reveal how important a role electrostatic screening plays in chemical potential tunability and what is ideal, from this perspective.

A further very relevant aspect in this context is the dependence of the quality of the superconducting gap induced in the nanowire on degree of coverage. Best superconducting proximity is expected for largest possible degree of coverage, this may however not be the optimum for gate tunability since it corresponds to maximal electrostatic screening. Directly comparing the shape of the superconducting gap in a tunneling spectroscopy measurement, and its survival in magnetic field, should suffice to answer this question.

The outcome of the measurements proposed here can be used to standardize the degree of nanowire coverage by the superconducting contact in future, more complex device geometries.

2. A variation of the superconducting contact length. As explained before, one of the characteristic parameters determining the degree of coupling of a pair of MBS's is their physical separation length. In a given device, the upper limit of this is the length of the superconducting section of the nanowire, which in turn is set by the superconducting contact length. This aspect is crucial for any future, more complex device design: the smallest possible superconducting contact size is the one at which MBS's are just not significantly coupled.

   Again tunneling spectroscopy measurements focusing on the behavior of a ZBP as reported before should suffice. It is expected that for strongly coupled MBS's, for most of the parameter range the two states are at finite energy, and only incidentally move to zero energy. At the other end of the spectrum, for MBS's not significantly coupled, it is expected that the two states are at zero energy. Hence I expect a trend in tunneling spectroscopy measurements upon increasing superconducting contact length: going from observing mostly a pair of states at finite energy and only sometimes a short lived ZBP, towards a long lived, robust ZBP, all as a function of relevant system parameters other than the contact length.

   Such an observation would be a clear signature of coupled MBS's, especially if

no, or very few, other discrete states are observed within the superconducting gap. Such an observation in itself may even serve as a further disapproval of a disorder induced ZBP scenario. More importantly, it will inform the agenda of future experiments on MBS's in nanowires, by setting a minimal superconducting contact length for which MBS's are not expected to couple significantly over a parameter range large compared to energy scales such as disorder and temperature.

Once gate tunability and a basic understanding of minimum device length are established, a combination offers an interesting playground. Having several local gates underneath the superconducting contact should then allow for in situ tuning in and out of the topologically non-trivial phase. This way, for example MBS's initially not coupled may be brought close enough to result in coupling, which may be observed in tunneling spectroscopy as a splitting of the ZBP. Such experiments should allow for comparison between the estimated size of a topologically non-trivial phase based on the gate geometry and their potentials, and based on the superconducting contact length, thus possibly resulting in evidence for in situ shortening and expanding a topologically non-trivial phase.

Lastly, I emphasize once more that all measurements proposed so far require the simplest possible, two-terminal tunneling spectroscopy geometry, combined with a variation of superconducting contact lay-out. Regardless of its relative simplicity, this set-up is capable of answering some crucial questions regarding the possible MBS's in our set-up.

12.2.2 THREE TERMINAL NORMAL-SUPERCONDUCTOR-NORMAL GEOMETRY

An almost trivial expansion of the previously discussed two-terminal tunneling spectroscopy geometry is to add a second normal terminal at the other side of the superconducting contact. This geometry constitutes a three-terminal normal-superconductor-normal device (NSN-device), which, atop local gates, consists of two individually controllable NS-junctions. We briefly explored this geometry already in this research, but results so far are truly preliminary.

Before proposing some possible measurements in this set-up, it is important to realize that by applying a negative voltage to the local gates underneath one NS-junction, this part of the nanowire can be made effectively into an insulator, thus restoring the previously discussed two-terminal geometry. This implies that all previously proposed experiments for the two-terminal geometry can be performed in a three-terminal geometry as well, making this layout very flexible and versatile.

Many types of measurements are possible in the three-terminal geometry. Without attempting to be complete, I discuss these I consider most straightforward and/or interesting.

1. It seems natural to first explore and establish a ZBP at one of the two NS-junctions. Once this stage is reached, the next step is to also explore the sec-

ond NS-junction. Several strategies can be followed. Firstly, simply turning off one NS-junction via its local gates while measuring the other may already be interesting and important. Observing a ZBP at both sides for similar gate ranges for the superconducting gates, having comparable behavior as a function of B-field and its angle, would be fully in line with the predictions for a topologically non-trivial state with a MBS localized at each end.

A slightly more complex variation of these measurements would be by performing tunneling spectroscopy simultaneously at both NS-junctions, either by biasing both N-terminals simultaneously, while current is drained via the S-terminal, or while biasing the S-terminal and draining current into both N-terminals. In both cases, the N-terminals should contain a current meter. The advantage of this set-up is that 'global' parameters such as B-field and its angle and gates underneath S have to be varied only once to obtain data from both junctions. A potential disadvantage is that reaching a truly equal voltage bias across both tunnel barriers is complicated. This depends for example on the series resistance of each branch in the circuit, which may differ for each junction, e.g. due to a different carrier density in each junction's section before the tunnel barrier. Furthermore, thermoelectric voltages may slightly differ for each terminal and its corresponding refrigerator bias line. Such effects could easily lead to 10-20% difference in effective voltage bias, and its offset, across the individual tunnel barriers. This should however not lead to any different features being present in the tunneling spectroscopy measurement, making this concern only relevant at the quantitative level.

An important remark should be made here. The basic theory is clear in its predictions regarding the topologically non-trivial phase in a nanowire: it should be accompanied by a localized MBS at each end. This leads to the experimental expectation of a strong correlation in the occurrence of ZBP's in individual tunneling spectroscopy measurements as a function of relevant system parameters. More realistically, however, if the system is disordered or inhomogeneously gated, parts of the superconducting nanowire may undergo the topological phase transition, while other parts stay trivial. This may lead to a discrepancy in the ZBP occurrence upon comparing the two NS-junctions. A further complication in this respect are non-ideal tunnel barriers, which may lead to different tunnel coupling strengths and related ZBP visibility at each junction. Furthermore, having multiply occupied nanowire subbands, additional, strongly coupled MBS's may be present locally if combined with a smooth tunnel barrier [3, 3, 4]. This may lead to additional discrepancies upon comparing the differential conductance measurements at each junction. To work around such practical limitations, a geometry in which the MBS's are weakly coupled may be ideal. Upon identifying similar ZBP features at each NS-junction, tuning the interaction strength of the MBS's via a local gate and/or the B-field should result in a strict correlation of a ZBP splitting observed at each NS-junction.

2. After establishing a correlation in the occurrence of ZBP's at each NS-junction, several interesting gate dependencies are expected. The necessary layout for this is to have several, individually addressable gates underneath the S contact, with 3 being the likely minimum amount. Given a correlation between the two sides, it is interesting to destroy such a correlation by varying these gates.

   Firstly, by changing the middle gate such that the piece of nanowire above it is driven into the trivial phase, the MBS's at each end are no longer belonging to the same topologically non-trivial phase. As a consequence, a possible previous coupling between them is now gone, and replaced by two individual pairs of MBS's which are stronger coupled (since their corresponding non-trivial phase is shorter) compared to the previous situation. Also, varying the interaction strength no longer results necessarily in a correlated ZBP splitting at each side. Such a situation assumes weakly coupled MBS's to start with. Alternatively, going from a non-interacting pair of MBS's one may create two individual, interacting pairs of MBS's. Experimentally this would show as the replacement of a single ZBP by split peaks sometimes crossing zero as a function of relevant parameters, with no necessary correlation between these patterns upon comparing both NS-junctions.

   Secondly, by changing the gate nearest to one of the NS-junctions such that the system is locally driven out of the topologically non-trivial phase, the MBS effectively moves inwards. This leads to a) an increased coupling between the MBS's, showing as the occurrence of a ZBP splitting at the other NS-junctions, or an increased splitting, depending on the dimensions, and b) to the disappearance of the ZBP or split peaks at the first NS-junction. Increasing the ZBP splitting this way was already proposed above, the three-terminal geometry allows for monitoring the disappearing MBS at the other side as well.

   Note that such gating effects all rely on having weakly, or non-coupled, MBS's to result in clear experimental signatures of increasing coupling strength.

3. A slightly different type of experiment related to the previous gate dependencies may be performed. A MBS interacting with a continuum of states of a normal metal results in a hybridization, the MBS moves away from zero energy due to this interaction. Such an interaction may be turned on in situ by lowering the tunnel barrier in the NS-junction and coupling the MBS to the (quasi-)continuum of states in the normal part of the nanowire.

   This offers an interesting possibility in the three terminal geometry. The starting point is observing a split ZBP at both NS-junctions. The first NS junction may be used to perform tunneling spectroscopy, while the second NS junction may be used to turn on/off an interaction between normal states in the junction and the MBS at that end. In the tunneling spectroscopy measurements of the first junction, this should result in a decreasing or vanishing splitting of the ZBP, since the far away MBS 'leaks out' into the junction and

hybridizes there. Reversing the order of the NS junctions should result in a similar find.

Such observations would be in line with having a pair of coupled MBS's, and having a controllable interaction of one of them with a nearby (quasi-) continuum of normal states.

12.2.3 CONCLUDING REMARKS

The proposed experiments are direct follow up experiments to the results presented in this thesis. None of them is truly original or new and all rely on the interplay between gate control and device geometry in a two- or three-terminal tunneling spectroscopy set-up. Nevertheless, I believe this type of experiments to be crucial. Vital insights regarding the typical length scale and the gate tunability of possible MBS's may be gained. Although in a realistic scenario the tunneling spectroscopy method employed is far from perfect, at a qualitative level the features and trends I discussed above should be observable.

The bottleneck in all this is device quality and stability: can devices be engineered which reproducibly allow for a robust topologically non-trivial phase enabling the experiments proposed? If yes, any other alternative explanation to the ZBP reported here becomes unlikely. If not, discussion will always remain, and I do not see perspective for more complex and involved experiments towards achieving braiding of MBS.

As a final remark I emphasize that the geometry discussed above allows for many types of different measurements related to MBS's, such as studying tunneling into a MBS via a quantum dot [5], studying spin texture of MBS's [6], etc. Although many of these are interesting and will result in new insights, it is my opinion that the proposed series of experiments is the most simple and potentially results in crucial insights. After being successful in these, perhaps the time is ripe to move to systems with a higher degree of complexity.

12.3 PERSPECTIVES ON MATERIAL DEVELOPMENTS OF SEMICONDUCTING NANOWIRES

In the recent past, important developments from the material growth perspective have taken place, e.g. deposition of superconductors on semiconducting nanowires within a single growth chamber and the development of crossed nanowires. Although not part of this thesis research, these aspects deserve discussion here, since I believe them to be highly relevant to future research on MBS's in semiconducting nanowires.

12.3.1 EPITAXIAL GROWTH OF SUPERCONDUCTORS ON SEMICONDUCTING NANOWIRES

Recent work of the Copenhagen research groups [7] has resulted in the epitaxial growth of aluminum on InAs nanowires in a single molecular beam epitaxy (MBE) chamber. Without breaking the vacuum, after MBE growth of the InAs nanowires, MBE sidegrowth of Al is possible, which results in a crystalline thin layer of Al covering the nanowire, either fully (upon rotating the growth substrate) or partially. This result is exciting from a material growth perspective since the two material types are epitaxially combined in a single heterostructure.

What does this imply for MBS related research? An epitaxial interface between superconductor and semiconducting nanowire represents the most pure and best quality interface possible. According to the authors of [7], this results in an excellent proximity induced superconducting gap, as inferred from tunneling spectroscopy measurements obtained by electrical transport through such a nanowire. This is of course highly desirable in creating a topologically non-trivial phase, since low energy quasi-particle states inside the superconducting gap are highly suppressed. As a consequence, these findings potentially represent a true breakthrough for MBS research in semiconducting nanowires.

Without lessening the importance of this find, which is clearly evident in my opinion, a few cautious notes regarding its relevance to MBS research seem appropriate:

1. A serious point of discussion is the interpretation of the transport data. It is believed that in InAs nanowires band bending happens at the nanowire surface, causing the charge carriers to be located near the nanowire surface. After Al is deposited on top, further redistribution of the charge density in the nanowire may happen. As a consequence, it is not clear to what extend the electronic wavefunction is located in the nanowire or in the superconductor. This raises the question if the superconducting properties observed in transport measurements so far actually represent the proximity effect in the nanowire, or are more representative of the superconducting Al layer on top of the nanwoire. In other words, what superconducting gap is probed, the bulk Al gap, the proximity induced gap in InAs, a blend of those? Resolving this is crucial in determining the relevance of this material system to MBS research.

2. The results on a top-down approach to improve the superconductor-semiconductor nanowire interface, as reported in this thesis, are not that different regarding the transport properties. In fact, the best results obtained by optimizing the superconducting contact deposition method result in the observation of a superconducting gap with a conductance suppression rather similar to a comparable measurement for an epitaxially grown superconducting contact. Especially since more elaborate contact preparation techniques can still be pursued, possibly resulting in better quality contacts, this ques-

tions the true necessity of the usage of an epitaxially deposited superconductor, without questioning the elegance of the latter method.

3. In the context of braiding, a quasi two-dimensional system is required, e.g. a network of nanowires (see section 12.5). It is expected that the direction of spin-orbit interaction of semiconducting nanowires lies in the transverse plane of the nanowire, and in, or close to, the substrate plane. As extensively discussed in chapter 2, an external B-field orthogonal to this direction is demanded to establish a topologically non-trivial phase. Any network of nanowires demonstrated so far has angles of order 90° between its branches. Using an external B-field applied within the substrate plane therefore results in an angle of several tens of degrees between external B-field and spin-orbit interaction, to achieve an external B-field component orthogonal to spin-orbit interaction in both nanowire branches. This situation is highly non-desirable, if any topologically non-trivial phase is possible at such a large relative angle between the two, which is unlikely in itself, it will be short lived in B-field magnitude, making the non-trivial phase fragile.

   A solution to this seems straightforward: apply the B-field out of the substrate plane. This, however, is very demanding towards the superconducting properties of the system: a significantly sized superconducting gap in the nanowire is required in a perpendicular B field of order 0.5 T. Here Al as a material fails, since the typical perpendicular critical B field of its superconductor phase in a thin film is of order tens of mT's. This makes the material combination of Al and InAs a dead end in the long run. Attempts to achieve similar epitaxial contacts based on Nb as a superconductor have not been successful as of yet.

In summary, I believe the development of epitaxially grown superconductors on semiconducting nanowires to be very important as a demonstrating find from a materials growth perspective. Its relevance to MBS research is not fully clear, however, and for long term goals, the current superconductor used, Al, is insufficient and should be replaced by a superconductor capable of withstanding the significant magnetic fields required to establish a topologically non-trivial phase in semiconducting nanowires.

12.3.2 EPITAXIAL GROWTH OF SEMICONDUCTING NANOWIRE CROSSES

It is evident from the discussion in chapter 2 that braiding of MBS's requires a two dimensional system. This seems irreconcilable with the inherently one-dimensional nature of semiconducting nanowire's. Fortunately, a quasi two-dimensional network of nanowires, in which MBS's can be exchanged in position, also fulfills the requirements for braiding [8].

In this light, the recent development of crossed InSb nanowires of the type used in this thesis is exciting. Since InSb nanowires naturally do not grow orthogonal to

the growth substrate, but under a slightly different angle, by placing catalyst particles next to each other (using electron beam lithography), nanowires can grow towards each other. It has been shown that this way crosses made out of two individual nanowires touching each other can be formed [9, 10]. Furthermore, it has been shown that these crosses have good electrical properties across their junction, a low resistance junction can be formed upon applying gate potentials. Most relevant to braiding proposals involving small networks of nanowires is that supercurrent has been demonstrated across such a junction. This will be discussed in more detail in section 12.5, but it implies that individual MBS's at different sides of the nanowire junction may couple to each other, or possibly even be transported across the junction. Therefore, the essential geometry to do braiding of MBS's in semiconducting nanowires is readily available at this stage.

As discussed above, it is highly unlikely that an external B field applied in the substrate plane will work. In case of the InSb nanowire crosses, the angle corresponding to a purely crystalline junction is 70°, which implies a 35° relative angle to each nanowire 'arm' of such a structure [10, 11]. This is not compatible with establishing a robust topologically non-trivial phase, and hence an external B field perpendicular to the substrate plane is required, with the related challenge of maintaining good superconducting properties in a realistic structure.

12.4 PERSPECTIVES ON FUTURE EXPERIMENTS IN SEMICONDUCTING NANOWIRES

So far in the discussion the main focus was on probing the possible existence of a MBS via tunneling spectroscopy. Since such a measurement happens in a open system, with the superconductor directly connected to ground, no parity is defined. As a consequence, non of the non-abelian aspects of such a state can be accessed in such a way. A possible quantized conductance plateau at $2e^2/h$ in a superconducting quantum point contact containing a MBS can only be explained by the presence of a topologically non-trivial state, according to [12]. We argued in chapter 6 that such a measurement is very hard under realistic conditions and will most likely not succeed. Several alternative measurements, not relying on tunneling spectroscopy, may probe different aspects of the possible MBS's in the system. A vast body of literature exists by now describing many different types of measurement to probe MBS's. I focus on two directions I consider particularly interesting: the 4π-Josephson effect and the degeneracy of parity states in a superconducting island containing MBS's.

12.4.1 4π-JOSEPHSON EFFECT

For an introduction to the 4π Josephson effect, see chapter 2. This effect was in fact one of the original predictions of Kitaev in his first work on the Kitaev chain. Observing this is widely considered as an important independent signature of MBS's. In relation to InSb nanowire Josephson junctions we already reviewed this effect

in chapter 4. There we concluded that both DC supercurrent measurements and Shapiro step measurements are not very likely to result in clear siqnatures of this effect. How to probe this effect more clearly?

It seems to me the best way forward is by somehow directly detecting the Josephson radiation coming from a topologically non-trivial Josephson junction. In the spectrum of this radiation, upon entering the topologically non-trivial phase, appearance of a peak at half the Josephson frequency is expected. In principal, no intrinsic aspects of the Josephson effect are expected to result in such a signal, only higher frequencies due to possible higher harmonics are expected. Nevertheless, it may happen that under certain conditions Landau-Zener transitions may occur between nearby ABS's and/or the continuum outside the gap, thus creating an apparent 4π behavior which is not related to topological superconductivity. Therefore, as with the zero bias conductance peak, the 4π periodic signal should correlate with the conditions for the sytem being expected to be in the topological phase: it should appear at finite B field only, and show the expected dependence on gate potentials and B field angle. Ideally, in a single device one combines this measurement with simultaneous tunneling spectroscopy into one, or both, of the outermost MBS's not directly involved in the 4π-Josephson effect. Such a dataset would be extremely hard to explain with any known alternative scenario possibly resulting in zero bias conductance peaks and a 4π Josephson effect, if such a scenario exists at all.

I believe at least two possibilities for such measurements exist. Firstly, one could implement an on-chip noise detector, based on photon assisted tunneling (PAT), capacitively coupled to the topologically non-trivial Josephson junction, e.g. as was employed by Deblock et al. [13]. As a noise detector, a conventional superconducting tunnel junction may be used because of its sharply non-linear current-voltage characteristic at the gap edge. The signal would be a PAT current below the gap edge, up to a voltage of $\hbar\omega_J$ below the gap value. Note that this tunnel junction should preserve its attractive characteristics (sharp current onset at gap edge) well upon applying B field, a challenging requirement. The 4π-Josephson effect would show up as an extra step in PAT current which onsets at a voltage of half the Josephson frequency below the gap. Josephson radiation from the topologically non-trivial junction can be generated by voltage biasing the junction.

A secondly possibility is to place a topologically non-trivial Josephson junction into a resonator, likely an on-chip superconducting coplanar waveguide resonator is the most natural choice. Voltage biasing the Josephson junction will generate Josephson radiation, which can only couple resonantly to the resonator, resulting in a microwave signal from the resonator at its resonance frequency. Again, this maps the discrete frequencies in the junction's spectrum directly onto a power spectrum of the resonator as a function of junction voltage bias. The 4π-effect should show up as a peak at half the Jopsephson frequency in such a measurement. Alternatively, one can also expect interesting behavior when sending microwave power into the resonator at its resonance frequency. The Josephson junction should be

on resonance as well, either by matching its Josephson frequency, or that of the higher harmonics, or, most interestingly in our context, matching half the Josephson frequency. Such a system is highly non-linear, and it seems therefore difficult to anticipate what would happen for example to the junction's current as a function of microwave power, this deserves proper theoretical attention. Some measurable response in this latter case is not unexpected, however, this may provide a means as well to detect the 4π-Josephson effect.

Both schemes possibly allow for combination with tunneling spectroscopy in a more complex device geometry. In the noise detection experiment this is not very straightforward, because it requires an extra pair of terminals allowing to voltage bias a gate induced tunnel probe in the nanowire and to measure the corresponding tunneling current. This is not very compatible with having relatively high resistance leads, as required to 'guide' the microwave signal towards capacitors coupling it to the noise detector. A resonator based measurement is possibly more forgiving in this respect, although there the limited available space inside the resonator may be problematic.

I believe that experiments along the lines of what I describe here have a lot of potential in detecting the 4π-Josephson effect. A more fundamental bottleneck, in my opinion, is that to get the 4π-Josephson effect, two pieces of a nanowire should be brought into a topologically non-trivial phase simultaneously; and these phases should be reasonably robust and uninterrupted such that the MBS's at both ends of an individual piece are uncoupled. This is a rather stringent demand, which may prove challenging to meet. This emphasizes once more the importance of gathering evidence via more simple tunneling spectroscopy measurements for a reproducible, gate controllable topologically non-trivial phase in an optimized geometry.

12.4.2 DEGENERACY OF PARITY STATES

As discussed in the theory chapter, a pair of MBS's contains a single fermionic degree of freedom, which is degenerate: the pair may be occupied, or unoccupied, with a single fermion, at no energy cost. It may be possible to probe this peculiar property directly.

A possibly suitable set-up for this is a superconducting single electron transistor (SET), build from the nanowire. The SET consists of a small superconducting island, contacting the nanowire. The SET is further defined by defining local tunnel barriers in the nanowire at both ends of the superconducting island. The ends of the nanowire are contacted by normal metallic leads, allowing for transport via tunneling through the SET.

Normally, the parity effect shows in this context by the so called 'even-odd'-effect: in case the original charge occupation of the SET is even, an energy equaling the charging energy plus the superconducting gap is required to place an extra charge on the island, whereas in the odd case, only the charging energy is required, since the two charges can recombine into a cooper pair. Disappearance of this difference in energy between the even and odd state could signal the topological

phase transition, since now a pair of states is available at the Fermi level which can host a single quasi-particle. Such an effect should be present whenever the system is expected to be in the topologically non-trivial phase.

The parity effect is typically shown by gate dependent tunneling spectroscopy through the SET, which would show alternating, unequal sized Coulomb diamonds. Reconfiguration of this spectrum to a continuous sequence of small diamonds would indicated disappearance of the parity effect. An important caveat in all this is that any trivial state moving down in energy towards the Fermi level will have a similar effect, and one has to be very careful in establishing that a disappearance of the parity effect is truly related to the emergence of topologically non-trivial phase. If this is possible, one of the defining properties of MBS's is tested, namely their origin from normal fermionic excitations and their corresponding fermionic occupation number.

12.4.3 CONCLUDING REMARKS

As pointed out in the introduction of this section, many proposals are out to probe different aspects of MBS's. I have not discussed any phase dependent measurements. All experiments described so far may in principal be combined with control over the superconducting phase degree of freedom. This would for sure lead to more complex experiments, but possibly also to more striking evidence for the MBS scenario.

12.5 PERSPECTIVE ON ESTABLISHING THE NON-ABELIAN EXCHANGE STATISTICS OF MAJORANA BOUND STATES

This outlook chapter would not be complete with a short discussion of perspectives for establishing and controlling the non-abelian exchange statistics of MBS's. Achieving this is the true motivation behind any MBS's related research, and represents the 'holy grail' in this field. I focus here on braiding proposals relevant to semiconducting nanowires.

12.5.1 BRAIDING IN QUASI TWO-DIMENSIONAL NANOWIRE NETWORKS

We discussed in chapter 2 what a braiding operation is in two spatial dimensions. Based on the discussion there, it is reasonable to expect the possibility of braiding in a quasi two-dimensional network, build from one dimensional wires, as long as the MBS's in it are far enough apart not to interact. This idea was put forward and rigorously proven for the first time in the work of Alicea et al. [8]. In this initial proposal, MBS's were moved through the structure, around each other, by adiabatically changing electrostatic gate potentials. The minimum nanowire structure necessary for this is a tri-junction.

A drawback of this initial proposal for braiding MBS's in nanowires is the sensitivity of this scheme to microscopic details. Continuously changing gate potentials to shift topologically non-trivial phases through nanowires is likely to generate charge noise, or even leakage current between gates and nanowire. Ideally, once the topologically non-trivial phases are created, gate potentials are left untouched to keep the device tuning the same. Especially for first demonstration experiments this is crucial, since possible topologically non-trivial phases cannot be expected to be very robust: this would demand a very high degree of control over all material and device aspects which is not likely to be the case at that stage.

A first important step was provided in the work of Sau et al. [14], where it was shown that exchange of MBS's may be achieved by performing a sequence of turning on and off a tunnel coupling between the different topologically non-trivial phases in the three pieces of a nanowire tri-junction. Control over the tunnel couplings is still via gates in this proposal.

This idea is taken a step further by combining it with phase-controllable coupling between MBS's [15–17]. Each arm of the tri-junction is build from a superconducting island, with a phase bias loop attached to it. By varying the phase bias, MBS's belonging to an individual island may be (de)coupled. Now a static tunnel coupling connecting the three arms of the tri-junction suffices. By varying fluxes through the individual phase bias loops, effectively a braiding operation may be implemented. This proposal completely removed the necessity to alter a gate potential during the braiding operation. Furthermore, it is actractive since the architecture of superconducting islands with a phase bias is very close to the existing transmon architecture used in superconducting qubit research.

In all schemes, initialization and read-out consists of a parity measurement on one of the pairs of MBS's, to check its fermionic occupation number. Again, the last scheme mentioned offers a rather natural solution to this by employing existing transmon architecture. A complication for this scheme, however, is that several phase bias loops closely spaced need to be controlled individually, which may prove challenging.

A more recent proposal [18] avoids this issue, but instead relies on gate tunable Josephson couplings. This may prove challenging in itself, since at least in the InSb based Josephson junctions no significant supercurrent was observed at the magnetic fields necessary for establishing a topologically non-trivial phase. On the other hand, the fact that some small supercurrent is still present is a hopeful sign, by optimizing the junction further this may become large enough for implementation of that particular scheme. It is premature at this stage to judge which particular braiding scheme is the best, since all currently available options require significant engineering efforts with unknown outcome.

12.5.2 TOWARDS TOPOLOGICAL QUANTUM COMPUTING

Demonstrating braiding would only be a first step in a larger scheme. The simplest braid operation implements certain single qubit rotations. Although MBS's

are a type of non-abelian anyons not allowing for universal quantum computing, schemes have been put forward suggesting a 'hybrid' approach, relying on a clever combination of topological and 'conventional' quantum computing. In this respect a combination of flux controlled topological quantum computing, combined with the transmon architecture (as suggested in [17]) seems particularly attractive.

'Conventional' quantum computing efforts are currently focused on reaching milestones such as demonstration of quantum error correction and establishing a surface code architecture. On the other hand, topological quantum computing is in its true infancy: only the first signatures of its main constituent, MBS's, have been observed. This completely different level at which both experimental efforts operate make it seem unlikely that MBS's will be a principal constituent of a possible first quantum computer. However, given its elegance in avoiding many sources of decoherence, topological quantum computing may become very important in a future further ahead, enabling alternative, more powerful quantum computing schemes. This underlines the relevancy of MBS or other non-abelian anyon research to the ongoing effort of realizing quantum computing.

The research on MBS's in semiconducting nanowires is in a crucial phase at the moment in my opinion. Either the near future will result in more and clearer signatures of MBS's, and more control will be shown, or other candidate systems for realizing MBS may start to catch up. If non of this happens, the research may even slowly fade out. Nevertheless, a clear agenda is available: 1) gather more MBS signatures, 2) integrate a superb superconductor-semiconductor interface and suppress environmental quasi-particles 3) develop a magnetic field compatible Josephson junction. Combining and integrating all these will allow for braiding in semiconducting nanowires. Since results or clear solution directions on all these aspects are available, semiconducting nanowires are currently at a clear advantage over other material systems for establishing non-abelian exchange statistics, and it is not unrealistic to have high expectations of the system towards demonstrating braiding in the future.

REFERENCES

[1] B. Nijholt and A. R. Akhmerov, "Orbital effect of magnetic field on the majorana phase diagram," *arXiv preprint arXiv:1509.02675*, 2015.

[2] A. Vuik, D. Eeltink, A. Akhmerov, and M. Wimmer, "Effects of the electrostatic environment on the majorana nanowire devices," *arXiv preprint arXiv:1511.08044*, 2015.

[3] P. W. Brouwer, M. Duckheim, A. Romito, and F. von Oppen, "Topological superconducting phases in disordered quantum wires with strong spin-orbit coupling," *Physical Review B*, vol. 84, no. 14, p. 144526, 2011.

[4] G. Kells, D. Meidan, and P. W. Brouwer, "Near-zero-energy end states in topo-

logically trivial spin-orbit coupled superconducting nanowires with a smooth confinement," *Phys. Rev. B*, vol. 86, p. 100503, Sep 2012.

[5] M. Leijnse and K. Flensberg, "Scheme to measure majorana fermion lifetimes using a quantum dot," *Phys. Rev. B*, vol. 84, p. 140501, Oct 2011.

[6] N. Sedlmayr and C. Bena, "Visualizing majorana bound states in one and two dimensions using the generalized majorana polarization," *Phys. Rev. B*, vol. 92, p. 115115, Sep 2015.

[7] W. Chang, S. Albrecht, T. Jespersen, F. Kuemmeth, P. Krogstrup, J. Nygård, and C. Marcus, "Hard gap in epitaxial semiconductor–superconductor nanowires," *Nature nanotechnology*, vol. 10, no. 3, pp. 232–236, 2015.

[8] J. Alicea, Y. Oreg, G. Refael, F. von Oppen, and M. P. Fisher, "Non-abelian statistics and topological quantum information processing in 1d wire networks," *Nature Physics*, vol. 7, no. 5, pp. 412–417, 2011.

[9] S. R. Plissard, D. R. Slapak, M. A. Verheijen, M. Hocevar, G. W. Immink, I. van Weperen, S. Nadj-Perge, S. M. Frolov, L. P. Kouwenhoven, and E. P. Bakkers, "From insb nanowires to nanocubes: looking for the sweet spot," *Nano letters*, vol. 12, no. 4, pp. 1794–1798, 2012.

[10] D. Car, J. Wang, M. A. Verheijen, E. P. Bakkers, and S. R. Plissard, "Rationally designed single-crystalline nanowire networks," *Advanced Materials*, vol. 26, no. 28, pp. 4875–4879, 2014.

[11] S. R. Plissard, I. van Weperen, D. Car, M. A. Verheijen, G. W. Immink, J. Kammhuber, L. J. Cornelissen, D. B. Szombati, A. Geresdi, S. M. Frolov, *et al.*, "Formation and electronic properties of insb nanocrosses," *Nature nanotechnology*, vol. 8, no. 11, pp. 859–864, 2013.

[12] M. Wimmer, A. Akhmerov, J. Dahlhaus, and C. Beenakker, "Quantum point contact as a probe of a topological superconductor," *New Journal of Physics*, vol. 13, no. 5, p. 053016, 2011.

[13] R. Deblock, E. Onac, L. Gurevich, and L. P. Kouwenhoven, "Detection of quantum noise from an electrically driven two-level system," *Science*, vol. 301, no. 5630, pp. 203–206, 2003.

[14] J. D. Sau, D. J. Clarke, and S. Tewari, "Controlling non-abelian statistics of majorana fermions in semiconductor nanowires," *Physical Review B*, vol. 84, no. 9, p. 094505, 2011.

[15] F. Hassler, A. Akhmerov, and C. Beenakker, "The top-transmon: a hybrid superconducting qubit for parity-protected quantum computation," *New Journal of Physics*, vol. 13, no. 9, p. 095004, 2011.

[16] B. Van Heck, A. Akhmerov, F. Hassler, M. Burrello, and C. Beenakker, "Coulomb-assisted braiding of majorana fermions in a josephson junction array," *New Journal of Physics*, vol. 14, no. 3, p. 035019, 2012.

[17] T. Hyart, B. van Heck, I. Fulga, M. Burrello, A. Akhmerov, and C. Beenakker, "Flux-controlled quantum computation with majorana fermions," *Physical Review B*, vol. 88, no. 3, p. 035121, 2013.

[18] D. Aasen, M. Hell, R. V. Mishmash, A. Higginbotham, J. Danon, M. Leijnse, T. S. Jespersen, J. A. Folk, C. M. Marcus, K. Flensberg, *et al.*, "Milestones toward majorana-based quantum computing," *arXiv preprint arXiv:1511.05153*, 2015.

SUMMARY

Majorana fermions are exotic elementary particles predicted in 1937 by Ettore Majorana. Although heavily searched for, they have never been found in nature up to date. In the past decades, with progressing insights, theoretical physicists predicted that Majorana fermions may emerge in certain exotic classes of condensed matter systems, where they show up as 'quasi-particles': a particle like state which is a result of the collective behavior of all atomic nuclei and electrons in the system. Because of their special exchange statistics, Majorana fermions in condensed matter are expected to find application as building blocks of topological quantum computers, a new type of quantum computing which is robust against perturbations.(chapters 1 and chapter 2)

This thesis is about creating and detecting Majorana fermions in one of these special systems. The system consists of a semiconducting Indium Antimonide nano-wire in contact with a superconductor (Niobium Titanium Nitride). At very low temperatures below 100 milliKelvin and in the presence of a strong magnetic field, Majorana fermions are expected to emerge. After successfully engineering the device (chapter 3), in a first series of experiments the striking feature of a robust conductance peak at zero energy has been found, indicating the existence of Majorana fermions (chapter 5).

Since our publication of these signatures of Majorana fermions, the theoretical understanding of Majorana fermions in our nanowire system rapidly developed. A summary of these theory developments relevant to our research is given in chapter 6.

In the second half of the project, the initial findings were reproduced and new behavior was found explainable by a model of interacting Majorana fermions (chapter 7). Furthermore, it became clear that the interface between superconductor and semiconducting wire is the most crucial aspect in obtaining high quality Majorana devices. As a consequence, a large effort has been put in optimizing this interface (chapter 8), resulting in improved devices paving the way for currently ongoing experiments (chapter 9). This second half of the project has led to a deeper and more detailed understanding of our devices and the signatures of Majorana fermions found in them.

Two important side tracks related to the main research topic are part of this thesis. Firstly, the study of spin-orbit interaction in quantum dots (chapter 10) gives an indication of the strength of spin-orbit interaction in the Indium Antimonide nanowire, and was crucial in judging the feasibility of the material to realize Majorana fermions. Secondly, the study of the Josephson effect in Indium Antimonide nanowire based Josephson junctions (chapter 4) has shown new types of behaviors in

magnetic field, highly relevant to both Majorana fermion research in nanowires, and the research on the Josephson effect in general.

SAMENVATTING

Majorana fermionen zijn exotische deeltjes voorspeld in 1937 door Ettore Majorana. Ondanks een intense zoektocht zijn ze tot op heden nooit gevonden in de natuur als elementaire deeltjes. In de afgelopen decennia voorspelden theoretisch natuurkundigen dat Majorana fermionen mogelijk ontstaan in bepaalde klasses van materialen in vaste stof systemen. Hier zouden ze verschijnen als 'kwasi-deeltjes': een deeltjesachtige toestand, die veroorzaakt wordt door het collectieve gedrag van alle atoomkernen en elektronen in het systeem. Vanwege hun bijzondere, niet-abelse deeltjes statistiek, is de verwachting dat deze vaste stof Majorana fermionen een nieuwe manier van kwantum berekeningen mogelijk maken die zeer robust is tegen verstoringen (hoofdstuk 1 en 2).

Dit promotieonderzoek gaat allereerst over het creëren van één van deze speciale systemen waarin mogelijk Majorana fermionen verschijnen. Vervolgens wordt geprobeerd deze te detecteren. Het systeem bestaat uit een halfgeleidende nanodraad met zeer kleine dimensies: een lengte van enkele micrometers en een diameter van ongeveer 100 nanometer. Het is de verwachting dat Majorana fermionen verschijnen in dit systeem bij zeer lage temperaturen, onder de 100 milliKelvin, en in de aanwezigheid van een sterk magneetveld, wanneer een speciaal materiaal gekozen wordt voor de draad (Indium Antimonide) en deze in contact gebracht wordt met een supergeleider (Niobium Titaannitride). Na het succesvol realiseren van deze nanostructuur (hoofdstuk 3) werd in een eerste reeks experimenten een markante waarneming gedaan van een robuste geleidingspiek bij nul energy tijdens het meten van de elektronische toestanden in de nanostructuur. Dit geeft een sterke indicatie voor het bestaan van Majorana fermionen (hoofdstuk 5 en 6), en heeft geleid tot de sleutelpublicatie van dit onderzoek in het blad Science (2012).

In de tweede helft van dit project zijn de eerste metingen gereproduceerd en is nieuw gedrag gevonden wat past in een model van wisselwerkende Majorana fermionen (hoofdstuk 7). Daarnaast werd duidelijk dat het grensvlak tussen supergeleider en halfgeleidende nanodraad het meest cruciale aspect is om een hoge kwaliteit van de nanostructuur te realiseren. Er is daarom sterk gefocust op het optimaliseren van dit grensvlak (hoofdstuk 8), wat resulteerde in verbeterde nanostructuren die nog voortdurende experimenten mogelijk hebben gemaakt (hoofdstuk 9). Deze tweede helft van het promotieonderzoek heeft geleid tot een dieper, meer gedetailleerd inzicht in het gedrag van onze nanostructuren en de aanwijzingen voor het bestaan van Majorana fermionen die daarin gevonden zijn.

Twee belangrijke zijpaden gerelateerd aan het hoofdonderwerp zijn onderdeel van dit proefschrift. Allereerst gaf de studie van spin-baan koppeling in kwantum dots een eerste indicatie van de sterkte van de spin-baan koppeling in Indium An-

timonide nanodraden (hoofdstuk 10), en was daarmee cruciaal in het beoordelen van de geschiktheid van dit materiaal om Majorana fermionen te realiseren. Daarnaast heeft de studie van het Josephson effect in Josephson juncties gebaseerd op Indium Antimonide nanodraden geleidt tot de observatie van nieuw gedrag in magneet veld (hoofdstuk 4), sterk relevant voor zowel Majorana fermion onderzoek in nanodraden, als ook voor onderzoek naar het Josephson effect in het algemeen.

CURRICULUM VITÆ

Kun ZUO

Oct. 06, 1985	Born in Anhui, China.
2000-2003	Qingyang High School, Anhui, China
2003-2007	BSc Applied Physics Nanjing University of Aeronautics and Astronautics
2008-2009	MSc Applied Physics Katholieke Universiteit Leuven
2009-2010	MSc Applied Physics Delft University of Technology Thesis advisor: Prof. dr. ir. L.P. Kouwenhoven *Anisotropies of g-factor and spin blockade in InAs nanowire quantum dots.*
2010 - 2015	PhD research, Delft University of Technology Promotor: Prof. dr. ir. L.P. Kouwenhoven, Quantum Transport Group and QuTech Advanced Research Centre *Signatures of Majorana Fermions in Hybrid Superconductor Semiconductor Nanowire Devices.*

CURRICULUM VITÆ

Vincent MOURIK

21 Maart 1987	Born in Capelle aan den IJssel, The Netherlands
1991-1999	Primary school, PCB Groen van Prinsterer, Capelle aan den IJssel
1999-2005	Secondary school, Wartburg College, Rotterdam
2005-2008	BSc. Applied Physics Delft University of Technology
2008-2010	MSc Applied Physics Delft University of Technology
2010 - 2015	PhD research, Delft University of Technology Promotor: Prof. dr. ir. L.P. Kouwenhoven Quantum Transport Group an QuTech

List of Publications — Kun Zuo

1. V. Mourik*, **K. Zuo***, S. M. Frolov, S. R. Plissard, E. P. A. M. Bakkers, L. P. Kouwenhoven. *Signatures of Majorana Fermions in Hybrid Superconductor Semiconductor Nanowire Devices*, Science. 336. 6084. 1003-1007.

2. S. Nadj-Perge, V. S. Pribiag, J. W. G. van den Berg, **K. Zuo**, S. R. Plissard, E. P. A. M. Bakkers, S. M. Frolov, and L. P. Kouwenhoven *Spectroscopy of Spin-Orbit Quantum Bits in Indium Antimonide Nanowires*, Phys. Rev. Lett. 108, 166801

3. S. M. Frolov, J. Danon, S. Nadj-Perge, **K. Zuo**, J. W. W. van Tilburg, V. S. Pribiag, J. W. G. van den Berg, E. P. A. M. Bakkers, and L. P. Kouwenhoven *Suppression of Zeeman Gradients by Nuclear Polarization in Double Quantum Dots*, Phys. Rev. Lett. 109, 236805

4. **K. Zuo***, V. Mourik*, D.J. van Woerkom, D. Car, S. R. Plissard, E. P. A. M. Bakkers, L.P. Kouwenhoven. *Tunnelling spectroscopy in 3-terminal superconducting InSb nanowire devices.*
   In preparation

5. V. Mourik*, **K. Zuo***, S. M. Frolov, D.J. van Woerkom, S. R. Plissard, E. P. A. M. Bakkers, L.P. Kouwenhoven. *Supercurrent oscillations in InSb nanowires.*
   In preparation

6. V. Mourik*, **K. Zuo***, O. Gul, F.K. de Vries, D.J. van Woerkom, D.B. Szombati, D. Car, S. R. Plissard, E. P. A. M. Bakkers, L.P. Kouwenhoven. *Optimization of the superconductor-nanowire interface for improving superconducting proximity effect in InSb nanowires.*
   In preparation

∗ equal contribution

List of Publications — Vincent Mourik

1. **V. Mourik***, K. Zuo*, S. M. Frolov, S. R. Plissard, E. P. A. M. Bakkers, L. P. Kouwenhoven. *Signatures of Majorana Fermions in Hybrid Superconductor Semiconductor Nanowire Devices*, Science. 336. 6084. 1003-1007.

2. K. Zuo*, **V. Mourik***, D.J. van Woerkom, D. Car, S. R. Plissard, E. P. A. M. Bakkers, L.P. Kouwenhoven. *Tunnelling spectroscopy in 3-terminal superconducting InSb nanowire devices.*
In preparation

3. **V. Mourik***, K. Zuo*, S. M. Frolov, D.J. van Woerkom, S. R. Plissard, E. P. A. M. Bakkers, L.P. Kouwenhoven. *Supercurrent oscillations in InSb nanowires.*
In preparation

4. **V. Mourik***, K. Zuo*, O. Gul, F.K. de Vries, D.J. van Woerkom, D.B. Szombati, D. Car, S. R. Plissard, E. P. A. M. Bakkers, L.P. Kouwenhoven. *Optimization of the superconductor-nanowire interface for improving superconducting proximity effect in InSb nanowires.*
In preparation

∗ equal contribution